



ES9700322



Ciemat

Centro de
Investigaciones Energéticas,
Medioambientales
y Tecnológicas

Miner

III Workshop on Microwave Reflectometry for Fusion Plasma Diagnostics

J. Sánchez
E. de la Luna

Informes Técnicos Ciemat

29 - 01

838

Noviembre 1997

R K

III Workshop on Microwave Reflectometry for Fusion Plasma Diagnostics

J. Sánchez

E. de la Luna

Toda correspondencia en relación con este trabajo debe dirigirse al Servicio de Información y Documentación, Centro de Investigaciones Energéticas, Medioambientales y Tecnológicas, Ciudad Universitaria, 28040-MADRID, ESPAÑA.

Las solicitudes de ejemplares deben dirigirse a este mismo Servicio.

Los descriptores se han seleccionado del Thesaurus del DOE para describir las materias que contiene este informe con vistas a su recuperación. La catalogación se ha hecho utilizando el documento DOE/TIC-4602 (Rev. 1) Descriptive Cataloguing On-Line, y la clasificación de acuerdo con el documento DOE/TIC.4584-R7 Subject Categories and Scope publicados por el Office of Scientific and Technical Information del Departamento de Energía de los Estados Unidos.

Se autoriza la reproducción de los resúmenes analíticos que aparecen en esta publicación.

Depósito Legal: M-14226-1995

NIPO: 238-97-001-5

ISSN: 1135-9420

Editorial CIEMAT

CLASIFICACIÓN DOE Y DESCRIPTORES

700320

PLASMA DIAGNOSTICS; PLASMA MICROINSTABILITIES; PLASMA DENSITY; ELECTRON DENSITY; FLUCTUATIONS; PROCEEDINGS

"Proceedings of the III Workshop on Microwave Reflectometry for Fusion Plasmas"
CIEMAT, Madrid (Spain) May 5-7 1997
Organised in collaboration with IAEA
Sánchez, J.; Luna, E. de la
179 pp. 143 figs. 145 refs.

Abstract:

Microwave reflectometry is based on the analysis of the properties (phase delay, time delay, amplitude) of a millimeter wave beam which is launched and reflected at the plasma critical layer. Operation with a fixed frequency beam can be used to analyze the electron density fluctuations in the reflecting region. If several frequencies are launched, information about the density profile can be obtained.

In these proceedings, a collection of papers is presented on the issues of density fluctuation studies and profile analysis as well as a special contribution about the development of reflectometry for the ITER project.

**"Ponencias presentadas en el III Workshop on Microwave Reflectometry
for Fusion Plasmas"**
CIEMAT, Madrid (España) 5-7, Mayo 1997
Organizado en colaboración con la IAEA
Sánchez, J.; Luna, E. de la
179 pp. 143 figs. 145 refs.

Resumen:

La técnica de Reflectometría de Microondas se basa en el análisis de las propiedades (fase, tiempo de retardo y amplitud) de un haz de onda milimétrica que se envía y es reflejado en la capa crítica del plasma. Si se opera a frecuencia fija se obtiene información sobre las fluctuaciones de densidad electrónica en la zona de reflexión, mientras que si se envían varias frecuencias se obtiene información sobre el perfil de densidad electrónica.

En este informe se presenta una colección de trabajos sobre la medida de fluctuaciones de densidad y perfiles de densidad. Asimismo se incluye un apartado sobre el desarrollo de la técnica para el proyecto ITER.

Participants List:

Canada

G. Conway, University of Saskatchewan
e-mail : Garrard.Conway@jet.uk

D. Pinsonneault Centre Canadien de Fusion Magnétique, Varennes, Quebec
e-mail: pinsonneault@ccfm.ireq.ca

France

F. Clairet, Association EURATOM-CEA, Cadarache
e-mail: clairet@drfc.cad.cea.fr

C. Laviron, Association EURATOM-CEA, Cadarache
e-mail: laviron@drfc.cad.cea.fr

G. Leclert, LPMI, Univ. Henri Poincare Nancy I
e-mail leclert@lpmi.u-nancy.fr

P. Moreau, Association EURATOM-CEA, Cadarache
e-mail: pmoreau@drfc.cad.cea.fr

Germany

M. Hirsch, Max-Planck-Institut für Plasmaphysik, Garching
e-mail: Matthias.Hirsch@ipp-garching.mpg.de

D. Wagner, Institut fuer Plasmaforschung, Universitaet Stuttgart
e-mail: wagner@ipf.uni-stuttgart.de

Japan

A. Mase, Plasma Research Center, University of Tsukuba
e-mail: mase@prc.tsukuba.ac.jp

Portugal

L. Cupido, Centro de Fusao Nuclear, Instituto Superior Technico, Lisbon
e-mail: cupido@mail.ua.pt

M. E. Manso, Centro de Fusao Nuclear, Instituto Superior Technico, Lisbon
e-mail: emilia@cfm.ist.utl.pt

J. Santos, Centro de Fusao Nuclear, Instituto Superior Technico, Lisbon
e-mail: jsantos@cfm.ist.utl.pt

F. Serra, Centro de Fusao Nuclear, Instituto Superior Technico, Lisbon
e-mail: fserra@cfm.ist.utl.pt

A. Silva, Centro de Fusao Nuclear, Instituto Superior Technico, Lisbon
e-mail: silva@cfm.ist.utl.pt

P. Varela, Centro de Fusao Nuclear, Instituto Superior Technico, Lisbon
e-mail: pvarela@cfm.ist.utl.pt

Spain

B. Brañas, Asociación EURATOM-CIEMAT, Madrid
e-mail: lasala@ciemat.es

T. Estrada, Asociación EURATOM-CIEMAT, Madrid
e-mail: estrada@ciemat.es

C. Hidalgo, Asociación EURATOM-CIEMAT, Madrid
e-mail: hidalgoc@ciemat.es

E. de la Luna, Asociación EURATOM-CIEMAT, Madrid
e-mail: luna@ciemat.es

J. Sánchez, Asociación EURATOM-CIEMAT, Madrid
e-mail: Joaquin.Sanchez@ciemat.es

The Netherlands

A. J. H. Donne, FOM-Instituut voor Plasmafysica, Rijnhuizen, Nieuwegein
e-mail: donne@rijnh.nl

A. Hugenholtz, FOM Instituut voor Plasmafysica, Rijnhuizen, Nieuwegein
e-mail: hugenh@rijnh.nl

P. de Vries, FOM Instituut voor Plasmafysica, Rijnhuizen, Nieuwegein
e-mail: p.d.vries@kfa-juelich.de

USA

T. L. Rhodes UCLA, General Atomics, San Diego
e-mail: rhodes@gan.gav.com

G. Vayakis, ITER-JCT, San Diego Site
e-mail: vayakig@iterus.org

United Kingdom

N. Deliyakis, JET Joint Undertaking, Abingdon
e-mail: ndeli@jet.uk

INDEX (only first author given)	page num.
Garrard Conway, University of Saskatchewan Canada Reflectometer fluctuation and correlation studies at JET.	1
Atsushi Mase, University of Tsukuba Japan Density Profile and Fluctuation Measurements on GAMMA 10 Using FM Reflectometer.	11
Matthias Hirsch, IPP-Garching Germany Potential and limitations of reflectometry due to scattering from density fluctuations.	21
Fernando Serra, IST Lisboa Portugal A 2-D code for the analysis of microwave reflectometry measurements in fusion experiments.	29
Garrard Conway, University of Saskatchewan Canada 2D Physical optics simulation of fluctuation reflectometry: correlation and asymmetries.	39
Teresa Estrada, CIEMAT Madrid Spain Simulations of correlation reflectometry with a WKB 2-dim code.	49
Jorge Santos, IST Lisboa Portugal Data processing techniques for data evaluation from broadband reflectometry.	55
Maria E. Manso, IST Lisboa Portugal Density profile and fluctuation measurements with microwave reflectometry on ASDEX Upgrade.	65
Philippe Moreau, CEA Cadarache France Dual frequency O-Mode reflectometer for density profile measurements on Tore Supra.	77
Frédéric Clairet, CEA Cadarache France Reflectometry measurements on the Tore Supra tokamak.	85
Peter de Vries, FOM Rijnhuizen The Netherlands Investigation of density profile perturbations by means of Pulse Radar Reflectometry.	91
Albert Hugenholtz, FOM Rijnhuizen The Netherlands Multi-channel pulsed radar system for the TEXTOR tokamak.	99
Diane Pinsonneault, CCFM Varennes Canada AM reflectometer density profile measurements on TdeV.	109
Clément Laviron, CEA Cadarache France Automatic linearisation of swept microwave sources for density profile reflectometry.	119
Antonio Silva, IST Lisboa Portugal New developments of the ASDEX Upgrade tokamak microwave reflectometer.	127

Nicholas Deliyannis, JET Culham UK A novel fast frequency modulation scheme for the JET multi-channel reflectometer.	133
Joaquin Sánchez, CIEMAT Madrid Spain Effects of turbulence in profile reflectometry.	149
George Vayakis, ITER JCT San Diego USA The challenge of reflectometry in ITER.	157

Reflectometer fluctuation and correlation studies on JET

G.D.Conway†, G.Vayakis‡, D.V.Bartlett

JET Joint Undertaking, Abingdon, Oxon, UK

†*Plasma Physics Lab., University of Saskatchewan, Canada.*

‡*ITER-JCT, San Diego, USA.*

Abstract. Three X-mode, heterodyne, dual-channel correlation reflectometers (75GHz, poloidal/toroidal : 105GHz, pol/tor : 92-96GHz swept, radial) operating on the JET tokamak are described, together with recent results. A range of fluctuation phenomena (ELMs, coherent MHD modes etc.) are observed, as well as variations in core and edge turbulence during ohmic, L and H-mode plasmas. Radial correlation lengths are generally less than 5mm for turbulence but rise to 1cm or more for coherent modes. Toroidal correlation lengths range from 5 to 10cm. Large changes in toroidal rotation velocities are also observed (few km/s with ICRF, tens of km/s with neutral beam heating). Signal imbalances between channels - particularly in low axis and high triangularity discharges, are explained in terms of asymmetries in alignment of the antennas.

1. Introduction

A new reflectometer diagnostic has been operating on JET during the last two campaigns principally to measure simultaneously radial and (either) toroidal or poloidal correlation lengths of edge and core plasma turbulence. The diagnostic is actually three separate dual channel X-mode correlation reflectometers, one operating at a fixed frequency of 75 GHz (predominantly outboard edge and SOL), the second at a fixed frequency of 105 GHz (core or inboard edge), and a third swept frequency system at 92 to 96 GHz. All three reflectometers share a common waveguide and antenna cluster launching horizontally from the low field (outboard) side of the tokamak.

In this paper the reflectometer hardware will be described in detail together with the acquisition system and analysis techniques. The capabilities of the diagnostic will be illustrated with a selection of results from different operational conditions and plasma fluctuation effects, including coherent modes, broadband turbulence and ELMs. Finally, it will be shown how a defect in the antenna alignment can be used to advantage to provide additional information on plasma rotation.

2. Hardware - fixed frequency systems

The 75 GHz system (built in-house) and the 105 GHz system (IRE, Ukraine) are identical in operation and will be described first. Figure 1 shows a schematic of the microwave and electrical circuit for the 75 GHz system. There are two microwave channels, each with a separate transmitter and receiver horn antennas (see below). The two sources are Varactor tuned Gunn oscillators (about 50 mW o/p) locked together with a 10.7 MHz frequency difference by a phase locked loop (PLL). The two received signals undergo two-stage heterodyne down conversion, first to an IF of 10.7 MHz by mixing with a part (3 dB coupler) of the opposing transmitted signal, i.e. each source also acts as the local oscillator (LO) for the other channel's receiver. The two oscillator signals are also sampled with 10 dB couplers and mixed together to generate the 10.7 MHz reference signal for the PLL and the second stage 'incident and quadrature' (IQ) detectors. The mixer output (video) signals are first AC coupled to +30 dB wide-band amplifiers (to remove the homodyne component) and fed via isolating transformers to matched IQ demodulators (Pascal Ltd.) which generate (zero mean) $A \cos \phi$ and

$A \sin \phi$ signals for each channel. The IQ detectors and final stage amplifiers have an overall bandwidth of DC to 1 MHz. Both oscillators are temperature stabilised (and free-running) however the PLL ensures that any frequency drifts in the channel 1 master oscillator are tracked by the channel 2 slave.

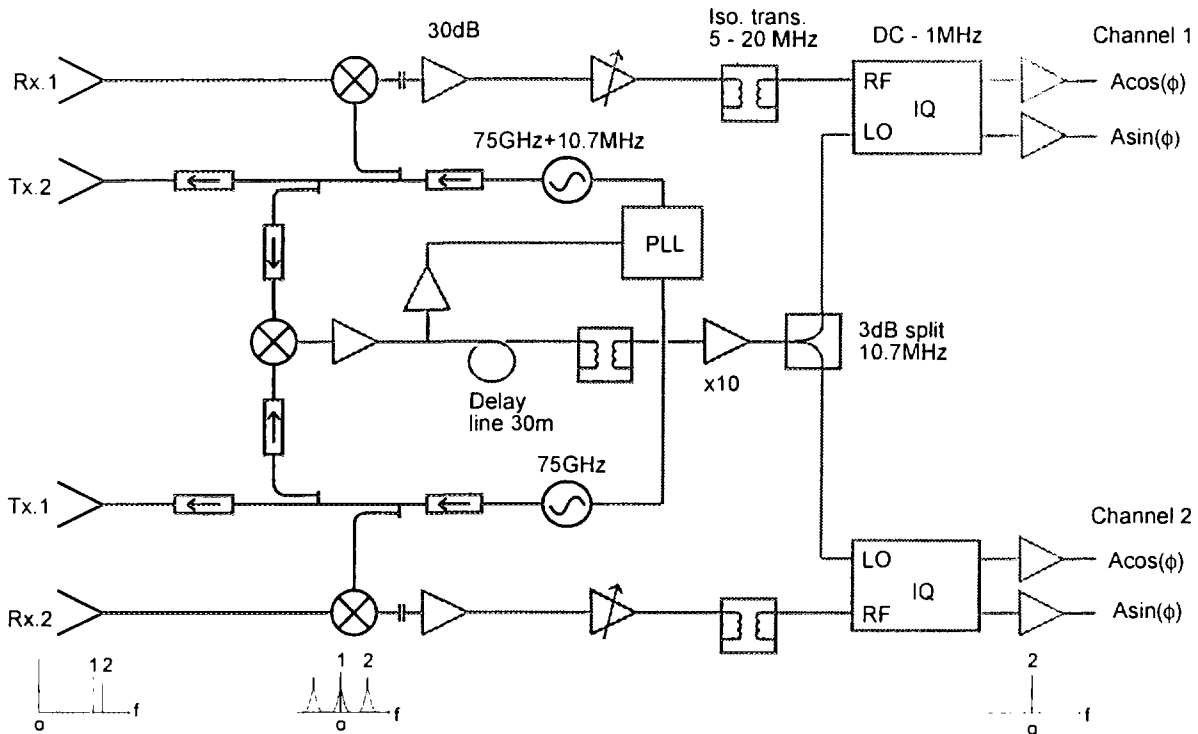


Figure 1: Schematic of the 75 GHz toroidal correlation reflectometer. Black lines represent waveguide, grey lines represent electronic circuitry.

3. Hardware - swept frequency system

The radial correlation reflectometer (ELVA-1 Ltd. St. Petersburg) is shown schematically in figure 2. The transmitter section has two oscillators, one fixed at 7.666 GHz and one tunable over 7.666 to 8.000 GHz via a digitally programmable frequency unit. The outputs are frequency multiplied ($\times 12$), amplified and then combined prior to launching. The receiver section has a single 90 GHz local oscillator (Impatt) which is heterodyne mixed with the received signal. The mixer output is amplified, split and then fed to the RF inputs of two IQ detectors. Part of the 90 GHz LO signal is also mixed with a sample of the 92 GHz and the 92 - 96 GHz launch signals to generate a 2 GHz and a 2 - 6 GHz reference signal (LO) for each of the IQ detectors. The resulting outputs are again a pair of $A \cos \phi$ and $A \sin \phi$ zero mean signals for the 92 GHz fixed channel and the 92 - 96 GHz swept channel.

4. Waveguide and antennas

The transmit and receive ports of the three systems are connected through a system of 3 & 5 dB couplers and tapers onto four oversized WG-12A waveguides. The waveguides are some 20 metres long and pass from the diagnostic hall through the biological shield wall and a series of E-plane bends to the mid-plane of the tokamak, figure 3. The oversized section has a typical single pass attenuation of about 9 dB. Tapers reduce the waveguide back to fundamental WG-27 guide which connects to the vacuum feedthroughs. These consist of a pair of horns either side of 15° tilted quartz double windows,

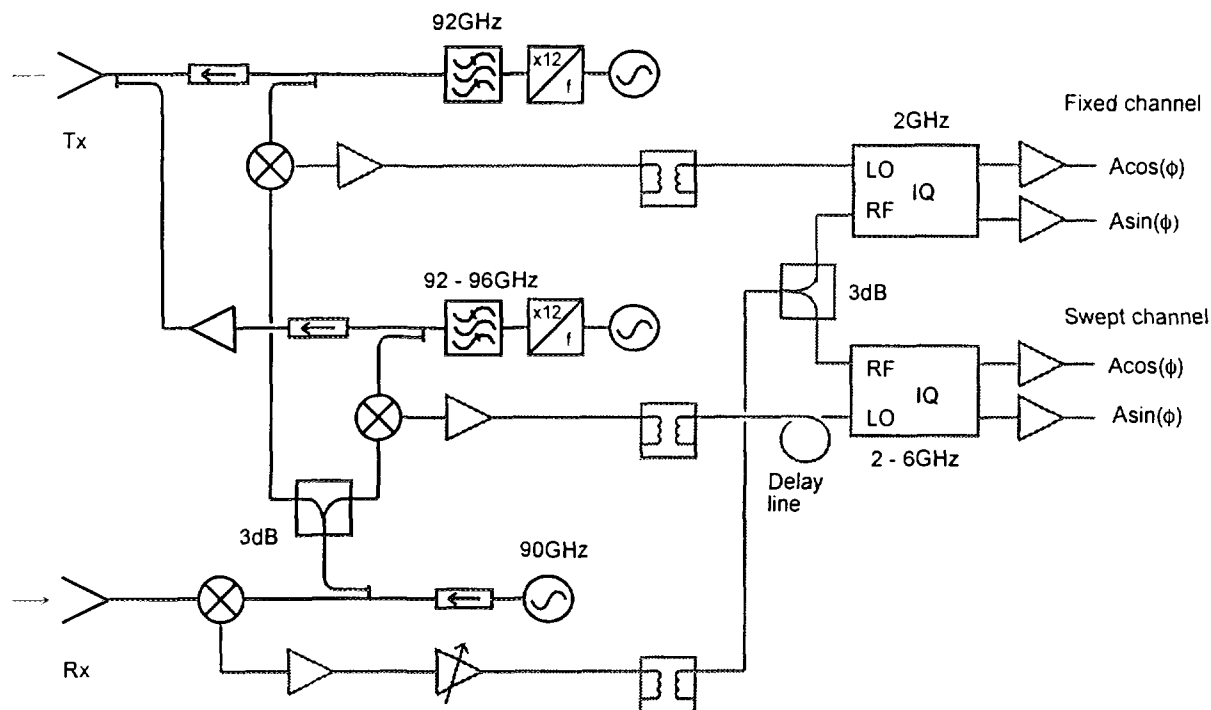


Figure 2: Schematic of the 92 - 96 GHz swept frequency radial correlation reflectometer.

surrounded by anti-cross-talk collars. Inside the vessel, 2 m lengths of fundamental waveguide (with several complex twists and bends) connect to (1 m long) 25 dB gain horn antennas. Figure 4 shows the rectangular configuration of the antenna cluster which is located on the tokamak low-field side and slightly above the typical height of the plasma magnetic axis. The orientation is X-mode and typically the spot size diameter is of the order of 12 cm at the separatrix. The two channels (75 and 105 GHz systems) transmit and receive on opposite diagonals of the rectangle. The antenna centres are separated by 4 cm toroidally and 2.5 cm poloidally. By switching the positions of the two receiving antennas (with special waveguide sections just prior to the mixers) the two channels can be configured to have either a toroidal or a poloidal separation. The 92 - 96 GHz system launches and receives via the channel 1 antennas.

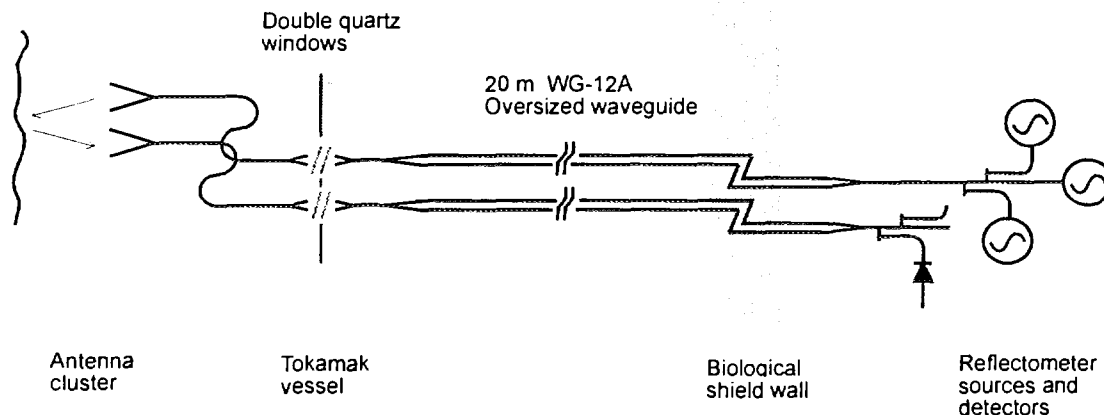


Figure 3: Layout of the waveguide path - only one channel shown.

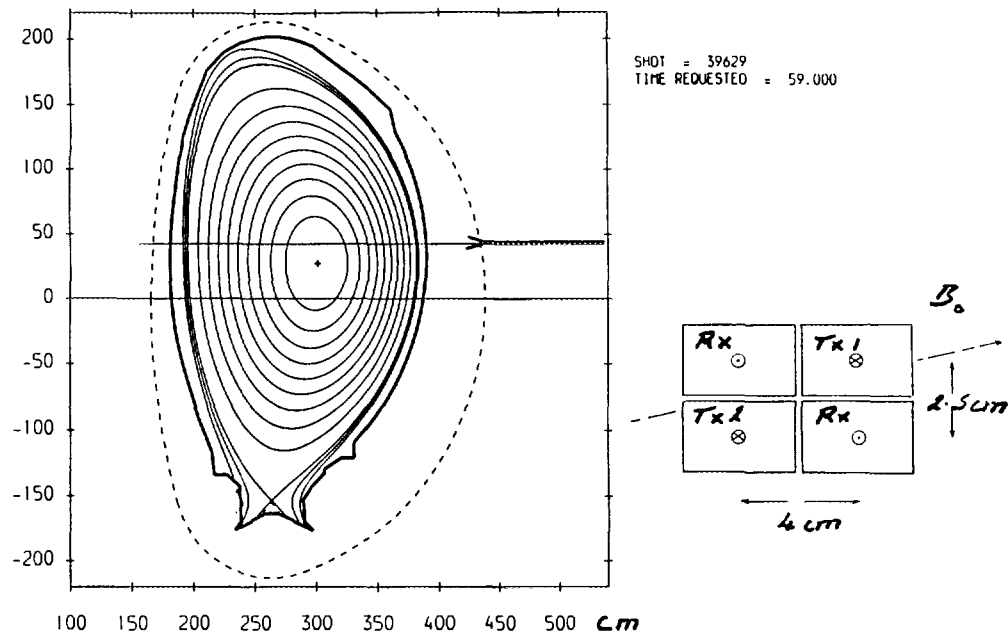


Figure 4: Flux surface plot for a typical low-axis JET discharge showing location of the antenna cluster. The inset shows the layout of the transmit and receive horns.

5. Data acquisition

There are 12 signals ($A \cos \phi + A \sin \phi \times 2$ channels \times 3 systems) which are digitised by three separate data acquisition systems - each with a different purpose. The first is a fast (up to 2 MHz) sample rate system with three parallel transputers (Sunnyside Ltd) controlled by a Pentium PC. The PC also controls the programmable frequency DAC for the radial correlation reflectometer. Up to 1 Mbyte of data per channel can be collected from up to 16 separately triggered time windows. This allows 'snap-shots' of the behaviour of the high frequency turbulence during a single plasma discharge. The second system is the Central Acquisition and Timing System (CATS) which digitises at 250/500 kHz. Signals from a variety of diagnostics (soft x-ray cameras, magnetics, ECE, D_α etc.) are all digitised simultaneously with a common clock for up to 3 seconds. This system is good for studying global events such as ELMs and coherent MHD modes. The third system is a slow (1 - 250 kHz) 32 kbyte CAMAC based digitiser. In this case the pairs of 'sin' and 'cos' signals first pass through analogue CRMS (complex root mean squarer) circuits, are then split in to a low-pass filter (DC - 10 kHz) and a high-pass filter (10 - 100 kHz). When operated at the slowest sample rate the system provides an indication of the level of reflected power and the overall level of fluctuations during the entire plasma discharge.

6. Signal conditioning

Prior to processing, each raw signal is corrected for DC offsets, gain inequalities, and phase delays in the amplifier chain. The phase and amplitude fluctuations are then separated using the quadrature nature of the signals. With the fastest sample rate (2 MHz) and mildly turbulent data it is just possible to track the phase beyond $\pm\pi$ and so automatically correct any phase jumps. Unfortunately in highly turbulent data phase run-away is a common occurrence which makes further processing difficult. However for roughly 90% of the data the phase jumps can be corrected by simply zeroing the phase mean and wrapping the phase at $\pm\pi$.

7. Plasma configuration

Figure 4 shows a typical JET plasma cross-section and flux surface plot for a low axis, high triangularity, divertor phase discharge. Because the antennas are located several cm above the plasma mid-plane, even the X-mode cut-off layers are tilted, scattering a substantial portion of the reflectometer beams away from antennas. The level of reflected power varies dramatically during the various ohmic, X-point and beam heated phases of the discharge, particularly during ELM events. The three favoured plasma configurations : ELMy H-modes, Hot-ion H-modes and Shear optimised discharges display different signatures and fluctuation characteristics. Two parameters in particular that affect the 'quality' of the signals are the plasma axis height and the plasma shaping, particularly triangularity.

8. Typical results

The following sections describe a range of typical results obtained with the diagnostic.

(a) Core and edge turbulence

Using multiple acquisition windows the behaviour of core and edge turbulence can be tracked through changes in confinement regimes. Figure 5 shows the evolution of the rms phase fluctuation level ϕ_{rms} during a Hot ion H-mode discharge #38369. During ohmic and L-mode the edge ($r/a > 0.9$) turbulence is dominated by low frequencies ($f < 100$ kHz), which collapse as the H-mode forms and then reappear with the step-down in NBI power - after the degradation in confinement. By contrast the core turbulence continues to rise in amplitude at all frequencies during the entire neutral beam heating phase - ie. beam driven. For Hot-ion H-modes the 'transport barrier' is close to the edge and it is evident that large amplitude low frequency fluctuations in the barrier region are linked to global confinement.

(b) Coherent modes

Coherent modes are mostly observed in the separatrix region at fairly well defined frequencies. These are a 10-20 kHz 'outer mode', a very common mode with a narrow peak frequency ranging between 35 and 70 kHz, and a series of high frequency harmonics in the 100 to 500 kHz range. The different modes sometimes occur simultaneously, and tend to appear in bursts, some lasting only a few ms. However in many cases the bursts switch on and off repeatedly for hundreds of ms. In this case the raw phase signals show the coherence modulated by a low frequency (200 - 500 Hz) oscillation. The modes propagate predominantly in the toroidal direction with the plasma and appear to be external kinks rather than ballooning modes, since in some cases they have been seen simultaneously on the 75 GHz system (outboard edge) and the 105 GHz system (inboard core/edge).

(c) ELMs

Edge Localised Modes (ELMs) are a prevalent feature in most plasmas; either giant/type-I, type-III or grassy ELMs. Figure 6 shows a contour plot of the time-delayed cross correlation coefficient of amplitude fluctuations, between two toroidally separated (4 cm) channels with the cutoff layer close to the separatrix. The upper trace is the D_α signal showing two giant ELM events. The narrow ridge of high correlation prior to the first ELM is broad band turbulence (see inset power spectra) propagating toroidally with a velocity of 2×10^4 m/s. During the ELM the coherence is completely disrupted and the turbulence level drops. There are also a large number of phase fringes indicating a very rapid (on

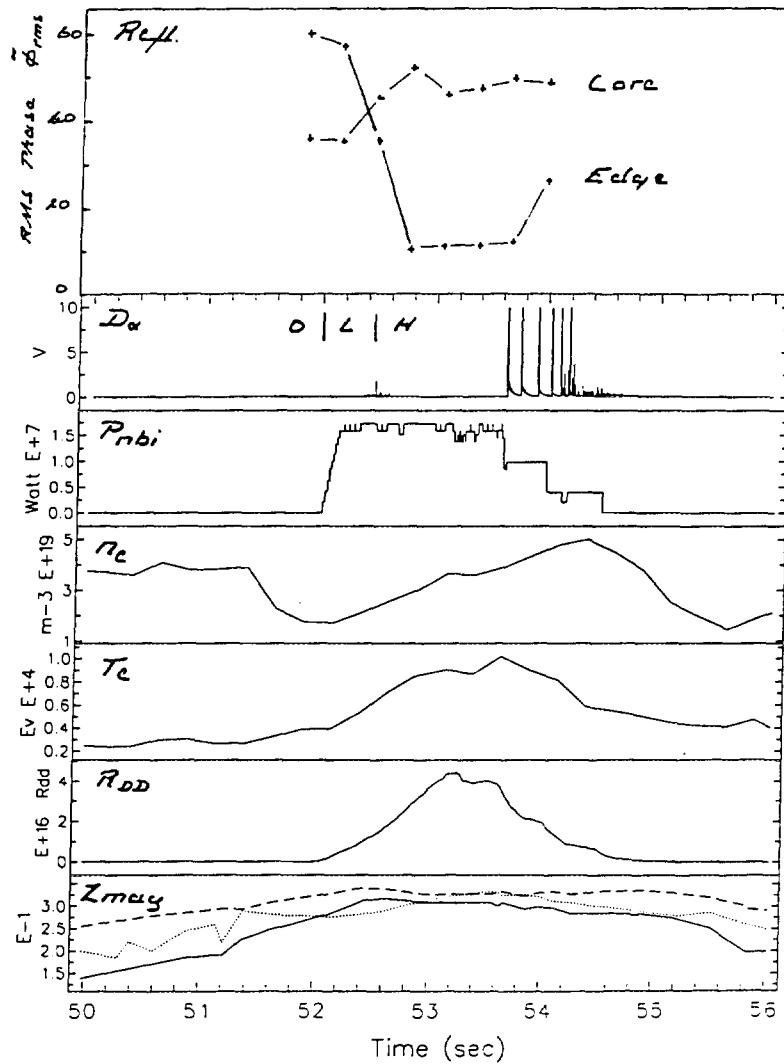


Figure 5: Variation of phase rms ϕ_{rms} levels from edge and core turbulence during a 16 MW NBI hot-ion H-mode discharge #38369.

the scale of microseconds) and a very large (several cm) inward movement of the cutoff layer, probably to the inside of the transport barrier where the turbulence level is lower. Afterwards the turbulence re-establishes over 3 - 4ms with low frequencies recovering first - reminiscent of energy cascading from longer to shorter wavelengths. The wide 'striation' in the correlation after the ELM corresponds to a 2 kHz oscillation (which is also seen on the SXR cameras) followed by a strong coherent post-cursor (or ringing) mode at 75 kHz lasting 12ms or more. Pre-cursor modes are hardly ever seen. The second ELM shows identical features.

(d) Correlation lengths

Both radial and toroidal correlation lengths have been measured simultaneously for turbulence, coherent modes, ELMs etc. Generally during H-modes the background broadband turbulence has very short correlation lengths, $L_r \sim 2 - 3$ mm, $L_t \sim$ a few cm. As expected during coherent modes correlation lengths increase by up to an order of magnitude, $L_r > 10$ mm, $L_t \sim$ several cms. Again ELMs are seen as disrupting both radial and toroidal coherence.

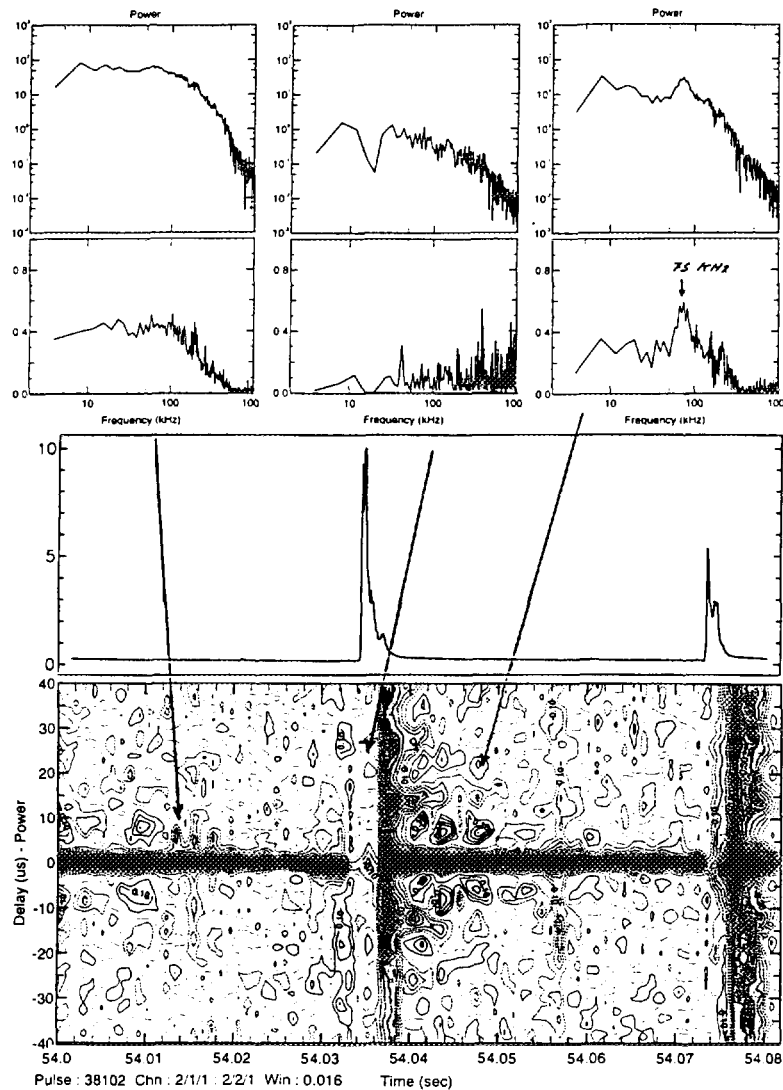


Figure 6: Contour plot of time-delayed correlation between two toroidal channels during two ELM events.

(e) Toroidal and poloidal velocities

Figure 7 shows two wavenumber - frequency spectra from edge turbulence during ohmic and ELM-free H-mode (6MW of RF only) phases of shot #38474. The linear dispersion regions show that the toroidal propagation velocity (lab frame) increases from around 18 km/s in the ohmic phase to over 40 km/s in the H-mode. The level of edge and core fluctuations also rise (the unusual increase in edge fluctuations during the H-mode is a side effect of the intense RF heating) and the toroidal correlation length decreases from over 6cm to less than 4cm. Edge velocities in excess of 70 km/s have been measured during NBI heating with toroidal correlation lengths approaching 10 cm. There is also some evidence of radial shearing in velocity. Generally edge propagation velocities match plasma velocities from the charge exchange diagnostic.

(f) Toroidal Alfvén Eigenmodes TAEs

TAEs are generally driven unstable when more than 4 MW of ICRF power is applied. A series of well defined peaks - sometimes narrow, sometimes broad - around 100 kHz are seen in the edge, and

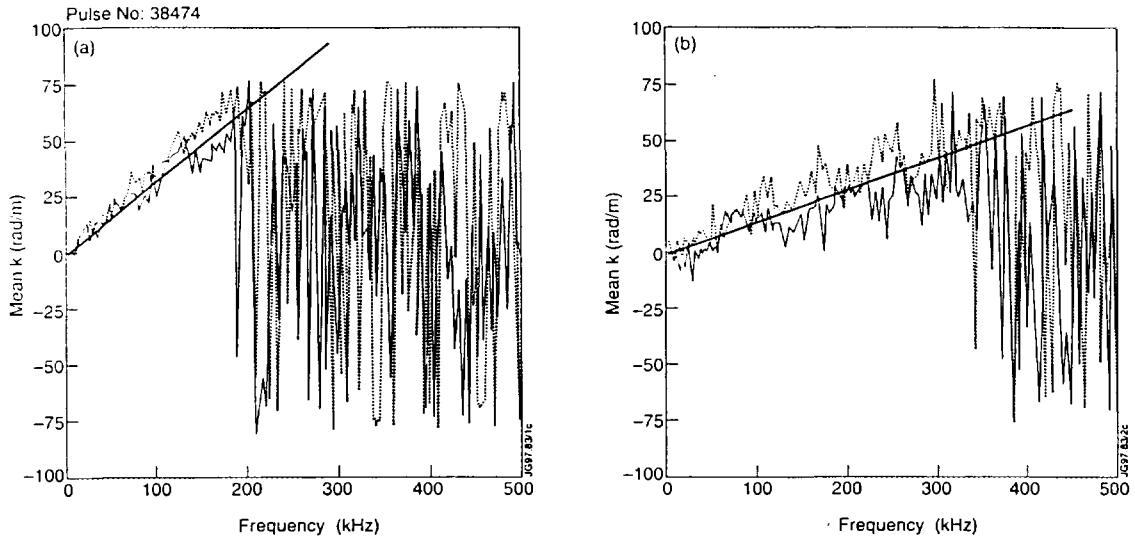


Figure 7: Wavenumber - frequency spectra of edge turbulence during (a) the ohmic and (b) 6 MW ICRF heated H-mode (#38474).

occasionally in the core. TAEs have also been recorded immediately after NBI switch-off. Figure 8 shows example spectra from two radial positions (left) $r/a = 0.85$ and (right) $r/a = 0.74$ (separated by 10 cm) just as the beams are switched off (shot #38882). The peak at about 120 kHz coincides with the predicted TAE frequency from theory. The second peak around 220 kHz is identified as an EAE (although possibly just a 2nd harmonic of the TAE). As yet there are no details on propagation.

9. Asymmetries in antennas

One striking feature evident in about 60 to 70% of the fluctuation data is a large difference in phase and power fluctuation levels between the two adjacent toroidal channels. Normally pre X-point ohmic phases give very similar ϕ_{rms} and P_{rms}/P_o values between the channels, but during divertor L and H-modes the levels for the two channels diverge; one channel shows a smaller ϕ_{rms} but a larger P_{rms}/P_o than the other. It seems the further out the cut-off layer and/or the higher the triangularity the greater the discrepancy. Nevertheless, even when asymmetry is evident, the high frequency fluctuations can still be highly correlated. Switching the antenna pairs simply reverses the channel asymmetry (on both 75 GHz and 105 GHz systems) which suggests there is a small mis-alignment (or possibly physical damage) to one of the horn antenna. Simulation studies show that an asymmetry of just a few degrees between the antenna pairs and the reflection layer can account for the observed discrepancies. Leakage between the reflectometer channels can not account for the observations.

In some instances an antenna asymmetry can be used to advantage. Edge data in shot #38791 shows a discrepancy of 50% in ϕ_{rms} and 30% in P_{rms}/P_o which from the simulation results, translates to an asymmetry of $\approx 5^\circ$. Both channels also show a high level of correlation between their respective phase and power fluctuations above 150 kHz with a relative phase difference of $\pi/2$ (figure 9) - two features predicted by simulations due to Bragg backscatter from a rippled cutoff layer. The coherence peaks result from TAEs starting around 172 kHz. From the asymmetry angle and the relative Doppler shifts a toroidal propagation velocity of 4 - 5 km/s is obtained.

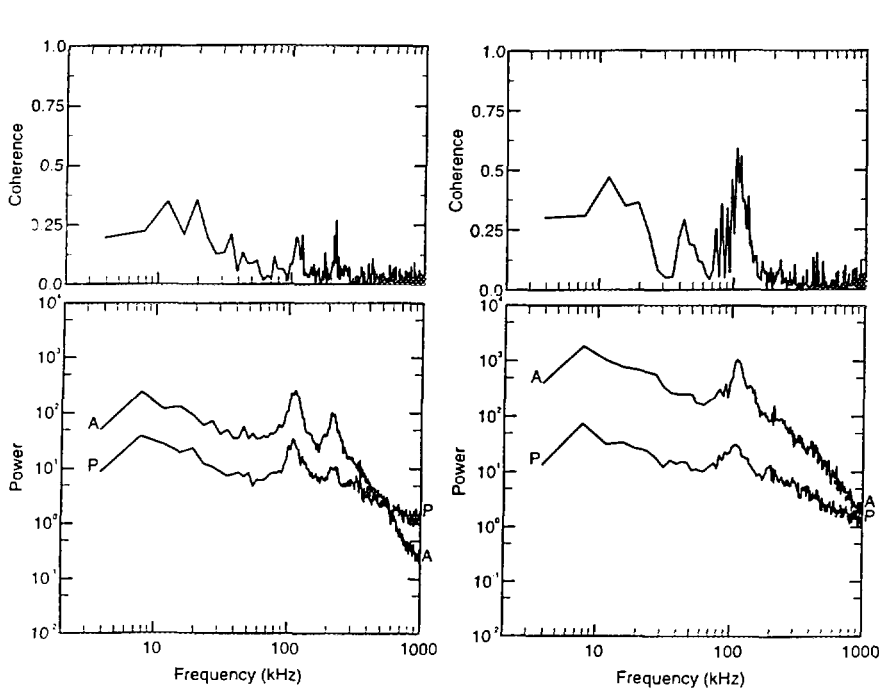


Figure 8: (left) Two spectra of phase and power fluctuations from (a) $r/a = 0.74$ and (b) $r/a = 0.85$ in JET shot #38882, just after NBI switch off. The peak around 120 kHz matches the TAE and peak around 220 kHz is identified as possibly an EAE.

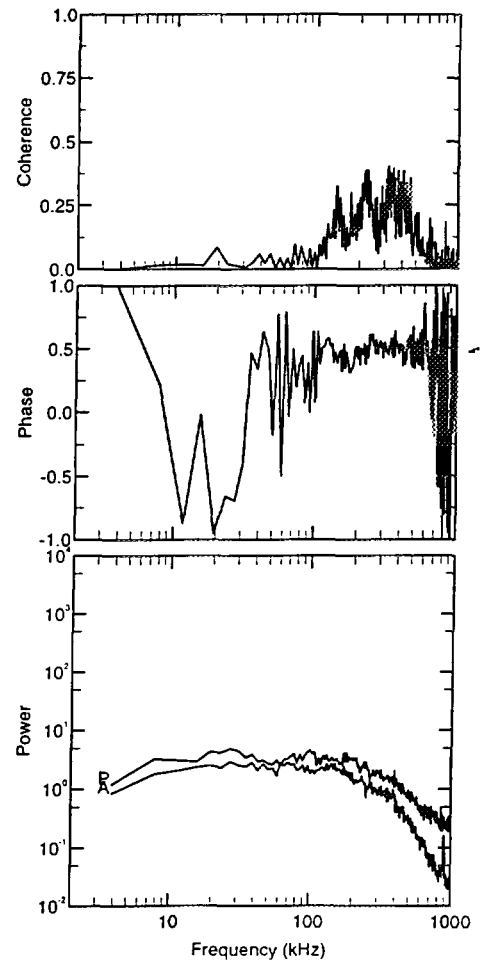


Figure 9: (right) Frequency spectra (lower), cross-phase (middle) and coherence (top) spectra between phase and power fluctuations from $r/a = 0.59$ in JET shot #38791, just after NBI switch off. Strong coherence and cross-phase of $\pi/2$ indicates asymmetry.

10. Conclusions

A vast range of fluctuation phenomena have been observed with the JET correlation reflectometers, just a few of which have been described in this paper. However the value of analysing the phase and power fluctuations separately is amply demonstrated by the fact that the phase and power do not always show the same features, for example sometimes there is good correlation in the phase but not in the power, and vice versa. Efforts will continue on the interpretation of such effects.

References

- [1] Vayakis G, 2nd IAEA Reflectometer Workshop (1994)
- [2] Conway G D, '2D physical optics simulation of fluctuation reflectometry', 3rd Intl. Reflectometer Workshop (1997)

Acknowledgements

Special thanks to N.Deliyanakis for assistance with diagnostic maintenance, J.Fessey for contributions to hardware design, and to members of the JET team during the 1996 experimental campaign.

**NEXT PAGE(S)
left BLANK**

Density Profile and Fluctuation Measurements on GAMMA 10 Using FM Reflectometer

A. Mase, T. Tokuzawa, L. G. Bruskin, Y. Kogi, N. Oyama,
A. Itakura, T. Tamano, and K. Yatsu

*Plasma Research Center, University of Tsukuba,
Tsukuba 305, Japan*

A broadband FM reflectometer was applied to the GAMMA 10 tandem mirror in order to measure density profile and fluctuations in the central-cell plasma. The clear fringes are observed during a plasma shot, when a fast-sweep oscillator is utilized and the resultant intermediate frequencies from the mixer output of the reflectometer are larger than the ion cyclotron range of frequency (ICRF). The density profile measurement is performed for various sweep times of the oscillator. The reliability of measurement seems to be improved when the sweep time is faster than $50\mu\text{s}$. The integrated value of many reconstructed density profiles agrees well with the profile obtained from a scanning interferometer. The several reconstruction algorithms are used to analyze the fast time-varying data, such as, the maximum-entropy method (MEM) spectral analysis and wavelet analysis.

The reflectometer was also applied to the measurement of fluctuations. The space and time resolving spectra of ICRF-driven waves as well as low-frequency instabilities are measured. The density and magnetic-field fluctuation levels are evaluated from both the reflectometer and cross-polarization scattering (CPS) diagnostic method. The CPS is related to the mode-conversion effect consisting of a polarization difference of a scattered wave with regard to an incident wave by the existence of magnetic fluctuations. It is observed that the Bragg resonance condition seems to be satisfied for the CPS similar to conventional Thomson scattering.

I. INTRODUCTION

Reflectometer has been expected to be one of the key diagnostics to measure density profiles and density/magnetic-field fluctuations in large fusion devices such as ITER. It provides good spatial and temporal resolution, while requiring a single viewing chord and minimal vacuum access in contrast to interferometry and Thomson scattering. One of the most serious problems in density profile measurement using conventional frequency-modulation (FM) reflectometer is caused by the existence of density fluctuations in plasmas, since the multifringe phase changes produced by a reflectometer are easily masked by those due to density fluctuations. Several methods have been proposed to avoid this problem such as amplitude-modulation (AM) reflectometry [1] or dual-frequency differential reflectometry [2] and pulsed radar reflectometry using moderate short pulse [3] or ultrashort pulse [4] as well as advanced data processing techniques based on Fourier spectrum analysis [5] and on maximum entropy method (MEM) [6].

We report here a broadband FM reflectometer system sweeping faster than the characteristic time scale of the density fluctuations. The high-frequency fringes due to the change of the cut-off layer can be distinguished from those due to the density fluctuations, since the fluctuation level with frequency larger than the ion cyclotron range of frequency (ICRF) is usually much smaller than the average density. Two types of data processing technique have been applied in order to reconstruct density profiles, that is, zero-cross

counting and MEM. Recently the wavelet transform is also applied for the reconstruction of the present FM reflectometer. Unlike the Fourier transform, which suffers from lack of temporal resolution, the wavelet transform possesses both time and frequency resolving capacities.

Diagnostics of plasma fluctuations are very important for transport study in magnetically-confined plasmas. Various techniques have been employed in order to measure the fluctuations, such as probes, electromagnetic wave scattering, reflectometry, and beam probe. In recent years, it has been mentioned that magnetic-field fluctuations as well as density and potential fluctuations are of importance for plasma transport. However, the direct measurement of internal magnetic field fluctuations remains a major issue in plasma diagnostics. A new application of electromagnetic wave scattering by magnetic fluctuations has been proposed recently. This is related to the mode conversion effect consisting of a polarization difference of a scattered wave from an incident wave called cross-polarization scattering (CPS) [7,8]. We have applied the CPS measurement to the waves in the ion cyclotron range of frequency (ICRF) [9]. In this paper, we report the observation of low frequency waves of less than 200 kHz. In magnetic confinement systems, the magnetohydrodynamic (MHD) wave and the electromagnetic drift wave can be excited in this frequency range.

II. DESCRIPTION OF THE EXPERIMENTAL ARRANGEMENTS

A. GAMMA 10 tandem mirror

The present experiment is performed in the hot-ion mode of GAMMA 10 [10]. The ICRF power with frequencies of 9.9 MHz (RF1) and 4.7-8.9 MHz (RF2) is employed to buildup a plasma and heat ions following gun-produced plasma injection. The frequency of 4.7-8.9 MHz corresponds to the ion cyclotron frequency near the midplane of the central cell, and 9.9 MHz corresponds to that of the anchor cells. Two separate 28 GHz gyrotrons are used in the plug/barrier cells in order to create the confining potentials. Fundamental electron cyclotron resonance heating (ECRH) occurs in the plug regions and second-harmonic ECRH occurs in the barrier regions. The central-cell plasma parameters are as follows: the line density $n_e l_c = 4-5 \times 10^{13} \text{ cm}^{-2}$ with an effective diameter of $l_c = 20-23 \text{ cm}$, the electron temperature $T_e = 60-80 \text{ eV}$, and the averaged ion temperature $T_i = 5-7 \text{ keV}$. The magnetic field strength at the midplane of the central cell is $B_c = 0.30-0.57 \text{ T}$, and the mirror ratio is 4.9.

B. FM reflectometer for Density profile measurement

The schematic of the reflectometer is shown in Fig. 1. It is installed in the central-cell midplane. A hyperabrupt varactor-tuned oscillator with 11.5-18 GHz and 40 mW output is used as a source. The separate transmitter and receiver horns are used to avoid the mixture of the spurious reflecting components in the waveguides and vacuum window. A focusing hog-horn antenna is used as a transmitter. The reflected wave picked up by a standard gain horn is mixed with the reference wave in a mixer through an 18 GHz low-pass filter. The homodyne-detected beat signals are then digitized at a sampling rate of 100 MHz with 128 kB memory using LeCroy 6841 digitizer or at a sampling rate of 50 MHz with 4 MB memory using Thamway AD-8H50II digitizer. In the present experiment the extraordinary mode propagation is adopted, since it covers a large portion of the density profile for the appropriate frequency range, 12-18 GHz.

We have applied and compared three reconstruction techniques in order to obtain the density profiles, zero-cross counting of the fringes, frequency analysis by means of the

MEM, and wavelet analysis [11,12]. A numerical algorithm to reconstruct the density profile is similar to the technique shown in the previous papers [13].

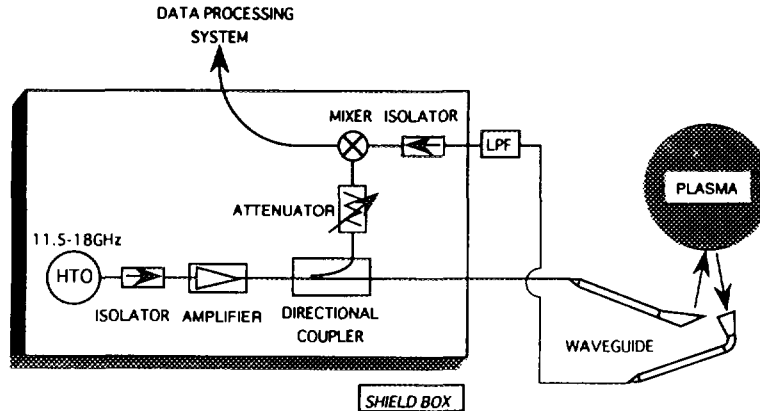


Fig. 1. A schematic diagram of the FM reflectometer system.

C. FM reflectometer and CPS system for fluctuation measurement

The CPS system as shown in Fig. 2 is located at the midplane of the central cell. Two pyramidal horns of ordinary (O) mode and extraordinary (X) mode are installed in the top and bottom ports respectively, and are used as transmitter or receiver for the CPS and reflectometric measurements. The systems utilize an 8-18 GHz, 100-150 mW output of a yttrium-iron-garnet (YIG) sweep oscillator as a source. The YIG oscillator is operated in a fixed frequency mode during a plasma shot. The scattered or reflected wave is mixed with the unperturbed local oscillator (LO) wave in a mixer. The intermediate frequency (IF) signal is amplified and separated into three ports by a power splitter. One of them is connected to a digitizer with 20 ns sampling time and 4 MB memory, while the others are fed to bandpass filters and rectified through detectors. The center frequencies of the bandpass filters are chosen to the frequencies of the RF2 and the self-excited instability identified as the Alfvén ion cyclotron (AIC) wave, respectively [14].

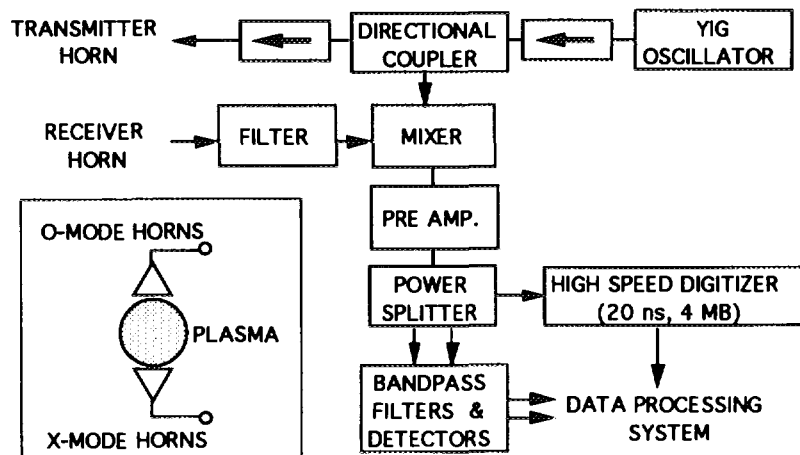


Fig. 2. A schematic diagram of the CPS Diagnostic system.

IV. EXPERIMENTAL RESULTS AND DISCUSSION

A. Density profiles

When the frequency of the incident wave is swept, multiradian phase change occurs due to the change of the cut-off layer and the path difference between the probe beam and the reference beam. The period of the fringes depends on the sweep speed of the source. Figure 2 shows a typical example of the density fluctuations obtained by the other fixed-frequency reflectometer installed in the central cell. The low-frequency components with frequency less than 100 kHz are identified to be flute-type and/or drift-wave instabilities by using the far-forward scattering system and probes. The high-frequency components with frequency 5-12 MHz are ICRF-driven waves such as the Alfvén ion cyclotron instability and the applied ICRF wave. The resultant intermediate frequencies (IF) between the reflected wave and reference wave for each sweep time of the HTO are also shown in Fig. 3. When the HTO is swept in 5 ms, the frequency spectrum of the IF signal lies in the range of 1-100 kHz, which is almost the same as that of the strong low-frequency fluctuations in the present experiment. Therefore, the fluctuations easily mask the information of the density profile.

The performance of the reflectometer system is investigated for various sweep times of the HTO. In Fig. 4, the density profiles are determined by two reconstruction methods using the zero-cross counting and the frequency analysis by MEM for several sweep times. It is seen that the reconstructed density profiles seem to be improved when the sweep time is faster than 33 μs for the MEM analysis, while the sweep time at least faster than 13 μs is necessary for the zero-cross counting method. The IF is in the range of 2-5 MHz and >20 MHz, respectively.

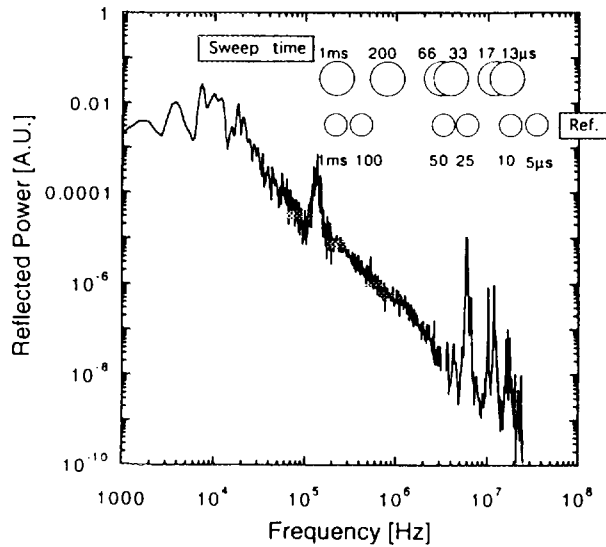


Fig. 3. A typical example of the density fluctuations in the central cell plasma of GAMMA 10.

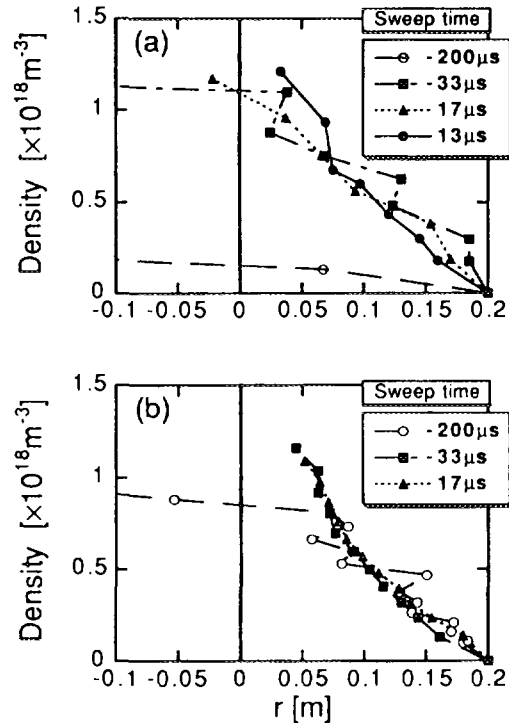


Fig. 4. Density profiles reconstructed by the zero-cross counting method (a) and the MEM analysis (b). The sweep time of the HTO is from 13 μs to 1 ms.

Figure 5 shows the density profiles measured with the reflectometer in every 7.5 μs . More than 100 density profiles are obtained in 1 ms. The thick solid line shows the profile averaged over 100 data, which corresponds to the time interval of 1 ms. Note that good agreement is obtained between the reflectometry and the interferometry.

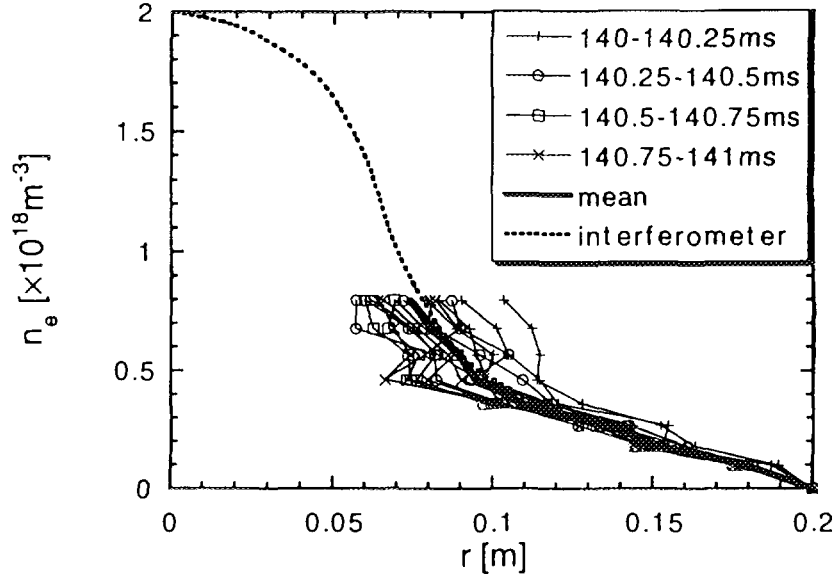


Fig. 5. Density profiles obtained by the reflectometer in every 7.5 μs and by the interferometer (dotted line). The thick solid line shows the density profile averaged over 100 data.

Recently, wavelet analysis is introduced as an alternative to zero-crossing and MEM analysis in order to improve the time-frequency resolution in signal processing. We have chosen the Gaussian wavelet as follows,

$$\psi_{\omega}(t) = \sqrt{\frac{\omega}{2\pi}} \exp(i\omega t) \exp\left(-\frac{\omega^2 t^2}{8\pi^2}\right) \quad (1)$$

Here, both the packet width and the wavelet frequency can be changed continuously by varying the value of ω . In order to determine the time-frequency dependence of the detected signal $s(t)$, we first normalize it in such a way that each data sequence of 100 points has a zero-average value and a constant variance, and obtain a convolution with a wavelet function for different ω

$$S(\omega, t) = \int s(\tau) q(\omega, t - \tau) d\tau \quad (2)$$

This gives the wavelet spectrum of the detected signal. It is possible to locate the maximum points and obtain the required time dependence of signal frequency. Typical density profiles obtained with present FM reflectometer are shown in Fig. 6. Here the sweep time of 20 μs is adopted. It was possible to obtain the density profiles for almost every sweep.

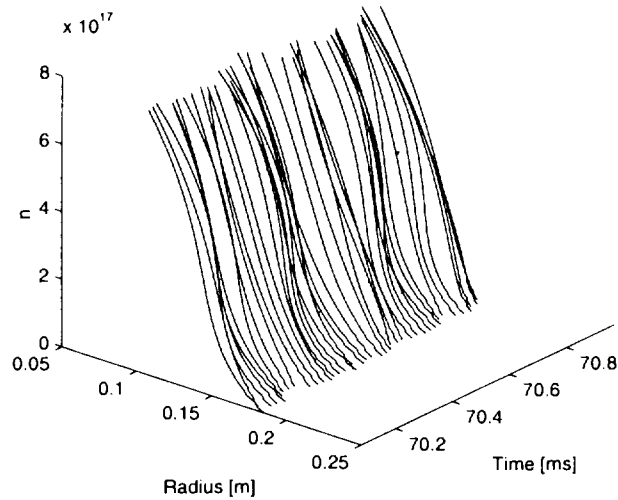


Fig. 6. Reconstructed density profiles for several subsequent sweeps.

C. Density and magnetic fluctuation

Two types of CPS can be observed by using horn antennas installed in the top and bottom ports: O- to X-mode ($O \rightarrow X$) scattering and X- to O-mode ($X \rightarrow O$) one. The time evolution of the frequency spectra is shown in Figs. 7 and 8. The frequency spectra of the CPS and the reflectometer signals show that the low-frequency waves less than 100 kHz is

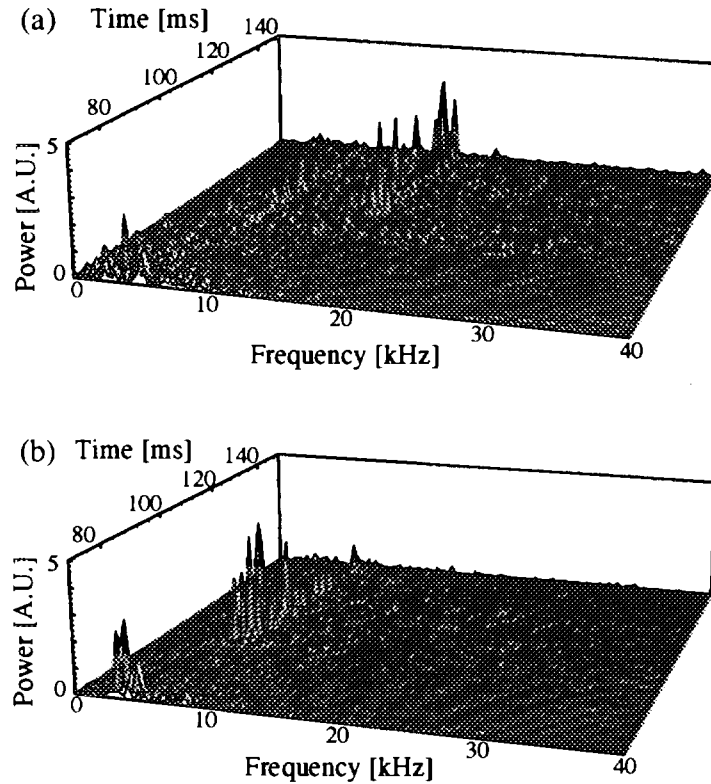


Fig. 7. Frequency spectrum of (a) CPS ($O \rightarrow X$) signal and (b) reflectometer ($X \rightarrow X$) signal.

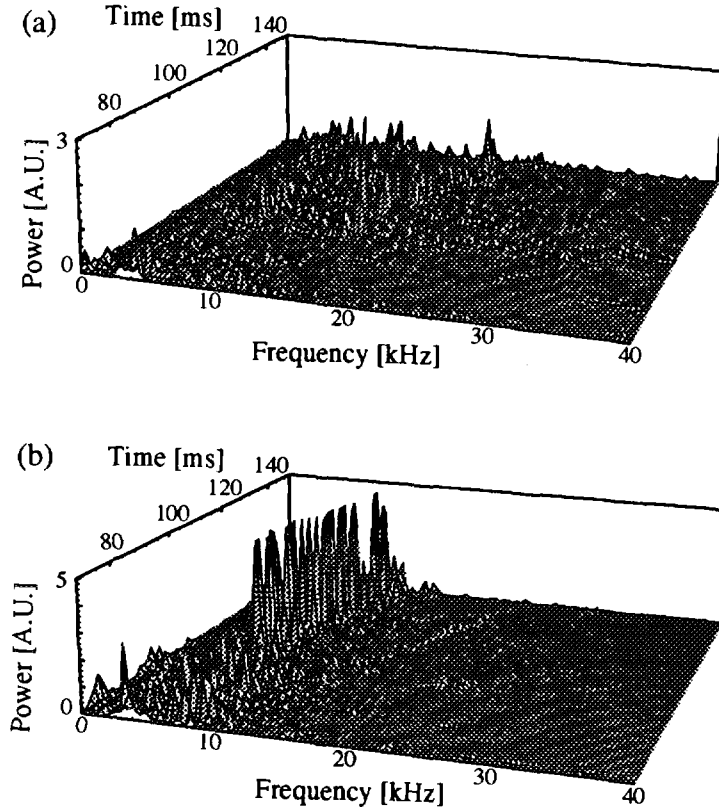


Fig. 8. Frequency spectrum of (a) CPS (X→O) signal and (b) reflectometer (X→X) signal.

strongly excited in a plasma. Figure 7 corresponds to the O→X mode CPS (incident frequency: 10.2 GHz) and the X-mode reflectometer (14.287 GHz) signals. On the other hand, the X→O mode CPS (11.46 GHz) and the X-mode reflectometer (11.159 GHz) signals are shown in Fig. 8. The incident frequencies are chosen so that both systems observe the similar radial positions of the plasma at the same shot. It is seen that the intensity

and spectra of the fluctuations are changed after the ECRH is applied, indicating the modification of the radial electric field due to the potential formation. Note that the frequency spectrum of the CPS signal is broader than that of the reflectometer signal.

The discrepancy of the spectra between the CPS and the reflectometer signals can be explained as follows. The refractive indexes of the O-mode and the X-mode propagations are given by

$$N_O = \frac{ck_O}{\omega_O} = \left(1 - \frac{\omega_{pe}^2}{\omega_O^2} \right)^{1/2}, \quad (3)$$

and

$$N_X = \frac{ck_X}{\omega_X} = \left(1 - \frac{\omega_{pe}^2}{\omega_X^2} \cdot \frac{\omega_X^2 - \omega_{pe}^2}{\omega_X^2 - \omega_{pe}^2 - \omega_{ce}^2} \right)^{1/2} \quad (4)$$

in the cold plasma approximation, where ω_{pe} and ω_{ce} are the electron plasma frequency and the electron cyclotron frequency, and ω_O and ω_X are the frequency of the O-mode and the X-mode incident waves, respectively.

In the CPS process, the incident O (X) wave is converted to the X (O) wave by the magnetic fluctuations until it reaches the cutoff layer of the plasma. The scattering process satisfies the Bragg condition $\mathbf{k} = \mathbf{k}_i - \mathbf{k}_s$, where \mathbf{k} , \mathbf{k}_i and \mathbf{k}_s are the wave-number vectors of the fluctuation, the incident wave and the scattered wave, respectively. Therefore, $k \cong 0$ in the transparent region of the plasma, since the scattering angle $\theta_s \cong 0$ for the present system and $k = 2k_i \sin(\theta_s/2)$, where $k_i \cong k_s$ is close to the wave number in the vacuum. At the cutoff region in the O \rightarrow X process, the wave number of the incident wave, k_O becomes 0 from Eq. (1), however, that of the mode-converted X wave, k_X becomes ω_X/c from Eq. (2). In the X \rightarrow O process, the wave number of the mode-converted O wave, k_O becomes $0.81\omega_O/c$ at the cutoff region from Eqs. (1) and (2) in the same manner. As a result, k varies from 0 to k_i for the O \rightarrow X process and from 0 to $0.81k_i$ for the X \rightarrow O process. On the other hand, the reflectometer always gives $k \cong 0$, since the wave numbers of the incident wave and the scattered wave equal to 0 at the cutoff layer. Since the frequency spectrum of the fluctuation are usually given by the relation $\omega = kv_p$, where v_p is the phase velocity of the wave, we should observe the higher frequency by the CPS measurement. The phase velocity of the fluctuations determined from the observed spectra, $v_p \cong 5 - 10 \times 10^3$ m is in agreement with the drift velocity $v_d \cong T_e/eBL_n$ using the present experimental conditions, where e is the charge of an electron and L_n is the density scale length. The magnetic field fluctuations may have significant influence in the drift-wave mode due to the finite- β effect and the shearless magnetic field of a tandem mirror, i.e. $(4\pi n_e T_e/B^2)(L_s^2/L_n^2) > 1$, where L_s is the shear length of the magnetic field [15].

V. SUMMARY

In summary, an ultrafast-swept reflectometer was applied to the central cell of the GAMMA 10 tandem mirror. The reliability of the density profile measurement is investigated for various sweep time of the source (HTO) from 13 μ s to 1 ms. It is observed that the reconstructed density profile is highly improved when the sweep time is faster than 33 μ s for the frequency analysis using the MEM, while it has to be faster than 10 μ s for the zero-cross counting method. A good agreement is obtained between the two profiles obtained by the reflectometry and the interferometry when the instantaneous density profiles from the reflectometry is averaged over many sweep periods. We have recently applied the wavelet transform to a problem of density profile reconstruction. It is demonstrated that it provides very good time-frequency resolution as well as having a denoising capability. It was possible to obtain the density profiles for almost every sweep.

The cross-polarization scattering diagnostic technique with frequency of 8-18 GHz was also applied to the central-cell plasma for measurement of electromagnetic plasma waves in the low-frequency region. The CPS process is identified by comparing the frequency spectra between the CPS and the reflectometer signals. The CPS signals (both O \rightarrow X and X \rightarrow O scattering) exhibit the broader frequency spectra than that of the reflectometer signals, which is considered to be the satisfaction of the Bragg resonance condition. This fact is considered to be the signature of the magnetic fluctuation measured using this method.

ACKNOWLEDGMENTS

The authors deeply acknowledge the GAMMA 10 group of the University of Tsukuba for their collaboration. This work was supported in part by a Grant-in-Aid for Scientific Research from the Japanese Ministry of Education, Science, Sports and Culture.

REFERENCES

- [1] J. Sánchez, B. Branas, T. Estrada, E. de la Luna and V. Zhuravlev, *Rev. Sci. Instrum.* **63**, 4654 (1992).
- [2] G. R. Hanson, J. B. Wilgen, T. S. Bigelow, I. Collazo, A. C. England, M. Murakami, D. A. Ramussen, and J. R. Wilson, *Rev. Sci. Instrum.* **66**, 863 (1995).
- [3] S. H. Heijnen, M. de Baar, A. J. H. Donné, M. J. van de Pol, C. A. J. Hugenholtz, and RTP team, *Rev. Sci. Instrum.* **66**, 419 (1995).
- [4] C. W. Domier, N. C. Luhmann, Jr., A. Chou, W-M. Zhang, A. J. Romanowsky, *Rev. Sci. Instrum.* **66**, 399 (1995).
- [5] K. W. Kim, E. J. Doyle, W. A. Peebles, A. Ejiri, N. C. Luhmann, Jr., and C. L. Rettig, *Rev. Sci. Instrum.* **66**, 1229 (1995).
- [6] M. Nagatsu, T. Hayashi, Y. Matsushita, and T. Tsukishima, *Jpn. J. Appl. Phys.* **33**, L45 (1994).
- [7] X.L.Zou, L.Colas, M.Paume, J.M.Chareau, L.Laurent, P. Devynck, and D.Gresillon, *Phys. Rev. Lett.* **75**, 1090 (1995).
- [8] L. G. Bruskin, A. Mase, and T. Tamano, *Plasma Phys. Control. Fusion* **37**, 255 (1995).
- [9] A. Mase, L.G.Bruskin, N.Oyama, T.Tokuzawa, H. Inutake, A.Itakura, H.Hojo, M.Ichimura, and T.Tamano, *Rev. Sci. Instrum.* **68**, 454 (1997).
- [10] T. Tamano, *Phys. Plasmas* **2**, 2321 (1995).
- [11] M. Nagatsu, A. Fuse, and A. Mase, *Plasma Phys. Control. Fusion* **38**, 1033 (1996).
- [12] L. G. Bruskin, A. Mase, T. Tokuzawa, N. Oyama, A. Itakura, and T. Tamano, *Jpn. J. Appl. Phys.* **36**, L632 (1997).
- [13] E. J. Doyle, T. Lehecka, N. C. Luhmann, Jr., W. A. Peebles, and the DIII-D Group, *Rev. Sci. Instrum.* **61**, 2896 (1990).
- [14] A. Mase, M. Ichimura, H. Satake, R. Katsumata, T. Tokuzawa, Y. Ito, H. Hojo, E. J. Doyle, A. Itakura, M. Inutake, and T. Tamano, *Phys. Fluids B* **5**, 1677 (1993).
- [15] S. J. Camargo, B. D. Scott, and D. Biskamp, *Phys. Plasmas* **3**, 3912 (1996).

NEXT PAGE(S)
left BLANK

Potential and limitations of reflectometry due to scattering from density fluctuations

M.Hirsch, E. Holzauer *

Max—Planck Institut für Plasmaphysik, EURATOM Ass., D-85748 Garching, FRG

** Institut für Plasmaforschung, Universität Stuttgart, D-70569 Stuttgart, FRG*

In collaboration with :

B. Kurzan, P. Amadeo (IPP-Garching)

B. Branas, M. Frances (CIEMAT -Madrid)

T. Grossmann (IST -Lisboa)

III Reflectometry Workshop on Fusion Plasma, CIEMAT, Madrid, Spain

May 5 - 7 , 1997

Introduction

Conventional reflectometry uses the phase of the reflected signal to monitor density fluctuations at the reflecting layer. However, in the presence of density fluctuations (e.g. in the L-mode or during ELMs) the nominal coherent reflection is strongly modified by refraction, diffraction and backscattering resulting from the small-scale turbulence-like density structures.

The reflected signal is determined by two effects [1] :

- (i) The *interferometric* term, described by a line-integral, which can be calculated with the WKB approximation.
- (ii) The *scattering* term, which is due to small-scale density structures which must be calculated from the full-wave solution.

As a consequence the wavefront of the reflected signal can be strongly distorted.

A number of experimental observations cannot be explained satisfactorily by 1-D models:

- Fluctuations in reflected signal power of up to 100 %.
- Loss of unshifted coherently reflected signal .
- Asymmetry of the reflected frequency spectrum (\Rightarrow phase runaway).
- Loss of radial coherence in 2-frequency reflectometer experiments.

In magnetically confined fusion plasma the variation of plasma parameters over the microwave beam cross-section in the toroidal direction can be neglected and the calculations are carried out in 2 dimensions. We use two different numerical codes to describe the propagation of electromagnetic waves in the plasma:

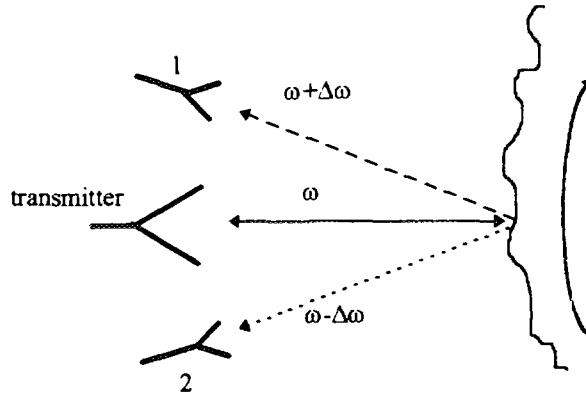
- (i) An equivalent electrical network (RLC - network) [2,3].
- (ii) A time-dependent finite difference method [4].

1-dimensional case:

A uni-directional Doppler shift can be produced by a density fluctuation propagating radially (i.e. along the line-of-sight), provided the Bragg condition for *backscattering* is fulfilled locally by the wavenumber of the fluctuation. This situation can be described by a 1-D model. Even if the fluctuation is nonpropagating (i.e. no Doppler shift) the total phase response of the reflectometer from interferometry and backscattering terms is modified which may lead to an error in density profile measurements.

2-dimensional case:

In fusion experiments one usually also observes fluctuations which propagate poloidally (i.e. transverse to the line-of-sight). The figure below (taken from [3]) illustrates the origin of zero-order and \pm first-order sidebands from a rotating periodic poloidal density fluctuation acting like a grating in reflection. Receiver antennas at viewing angles differing from perpendicular incidence onto the plasma surface allow to determine the poloidal propagation velocity and poloidal wavenumber of the density fluctuations. This type of reflectometry can be considered as a backscattering experiment with the radial resolution of a reflectometry system.



The resolution in poloidal wavenumber and the radial position both depend on the microwave frequency and the macroscopic density profile. The solution of this problem requires 2-D simulations. The question of poloidal rotation of plasma turbulence and its radial shear is related to the important problem of anomalous transport in magnetically confined fusion plasmas.

A special situation arises for a fixed antenna system if the plasma surface is tilted with respect to the incoming microwave beam. This is the case for the plasma in the W7-AS stellarator at IPP Garching with a tilt angle of ≈ 2.6 deg in the toroidal section of the original (unmodified) reflectometry system.

Recently an additional antenna has been installed which allows to vary the angle of the transmitter/receiving antenna with respect to the equatorial plane.

Nonlinear relationship between phasemeter output and density fluctuations

For finite density fluctuation levels n_e additional problems arise from the nonlinear relationship between phasemeter output and density fluctuation.

- (i) The signal phase depends on the refractive index n , which is a *nonlinear* function of n_e , which is especially important close to the reflecting layer. For O-mode propagation one obtains

$$n = (1 - n_e/n_{co})^{1/2},$$

where n_{co} is the cutoff density. If one expands this expression in a power series one gets

$$n \approx 1 - .5 n_e/n_{co} + .25(n_e/n_{co})^2 \pm \dots\dots\dots$$

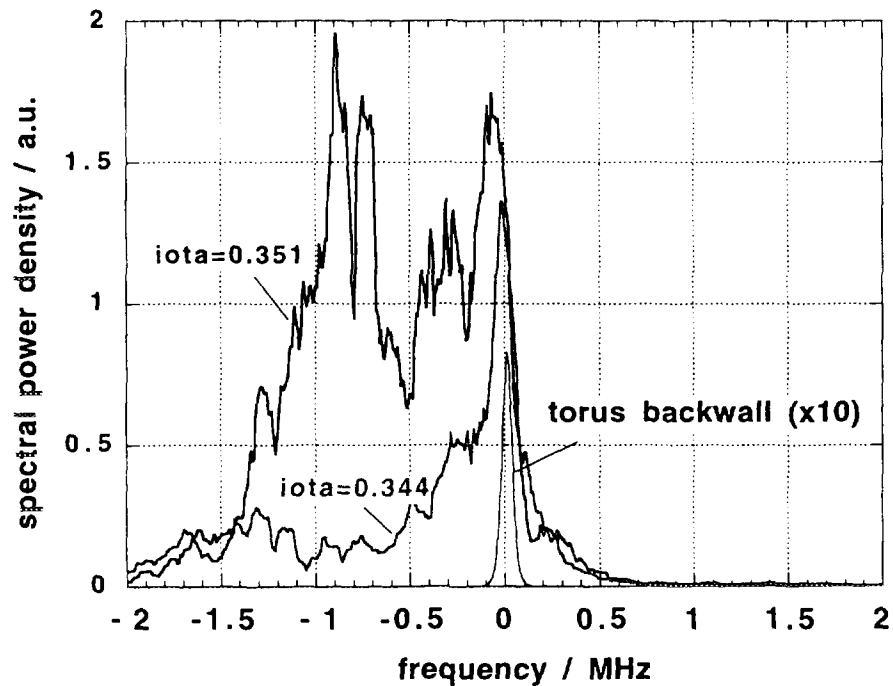
which yields both a *DC-term* and terms with higher harmonics. Although the harmonic terms seem small compared to the linear term, they may become important for (experimentally observed) frequency/wavenumber spectra which fall off steeply with frequency/wavenumber.

(ii) If the signal phase varies sinusoidally in time/space additional sidebands in frequency/wavenumber space appear, which are an intrinsic property of phase-modulated carriers. The power in the various harmonics (including the zero order) is given by Bessel functions and can be found in standard textbooks on rf-signal processing.

(iii) The output of a reflectometer comes from a phase detector which is a *nonlinear* device with respect to signal amplitude. If density fluctuations with different frequencies are present the information about the individual signal components at the receiver input can be lost. This can be easily demonstrated for the simple case of two signal components $a_1 \sin(\omega_1 t)$ and $a_2 \sin(\omega_2 t)$, for which the resulting phase $\phi(t)$ is given by

$$\phi(t) = \arctan [(a_1 \sin(\omega_1 t) + a_2 \sin(\omega_2 t)) / (a_1 \cos(\omega_1 t) + a_2 \cos(\omega_2 t))].$$

If one signal component dominates, the complete information about the second component will be increasingly suppressed with increasing amplitude of the first component. In addition, due to the nonlinearity of the above expression mixing products at new frequencies will appear. Therefore, to preserve the information about density fluctuations the received signals must be processed *before* the phase detector. An corresponding experimental result is given below. This figure shows the frequency power spectrum with a pronounced asymmetry in the Doppler shifted spectra analysed *before* the phase detector (and before the limiting amplifier). The system is thus operating as a *backscattering* experiment.

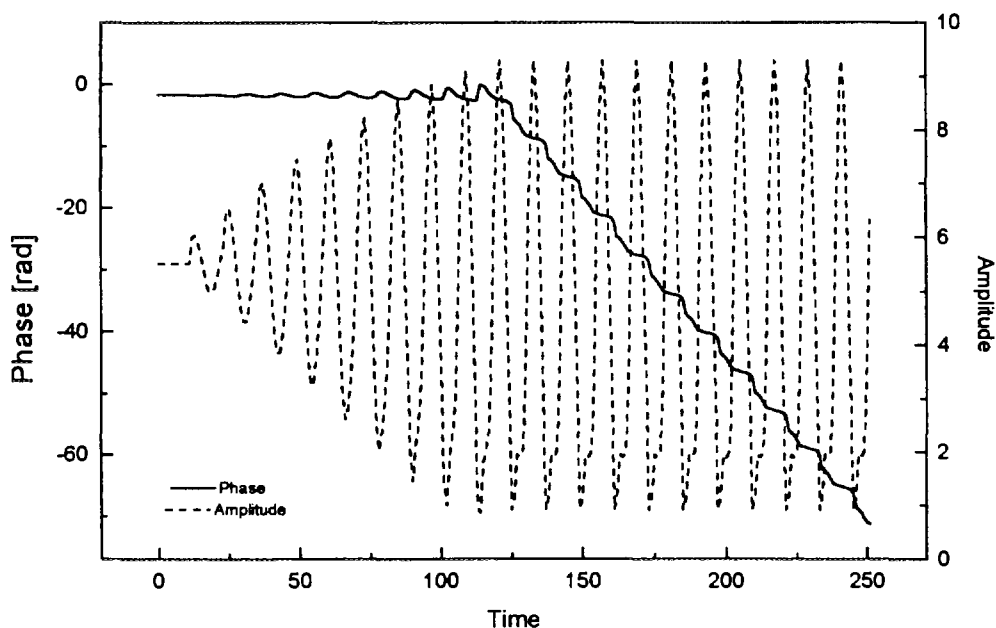


Analytic modelling of the phase-runaway

If the unshifted zero-order wave (coherent reflection) is not the dominant term at the input of the receiver antenna one observes transient destructive interference resulting in minima of the total wave amplitude associated with rapid changes of the phase. A simple *analytic* model allows to derive the origin of the phase runaway and the characteristic threshold for the fluctuation level needed for the onset of the phase runaway. This analytic model yields the resulting phase $\phi(t)$ due to the

- (i) unshifted zero-order signal with frequency ω ,
- (ii) frequency-shifted sidebands with frequency $\omega \pm \Delta\omega$.

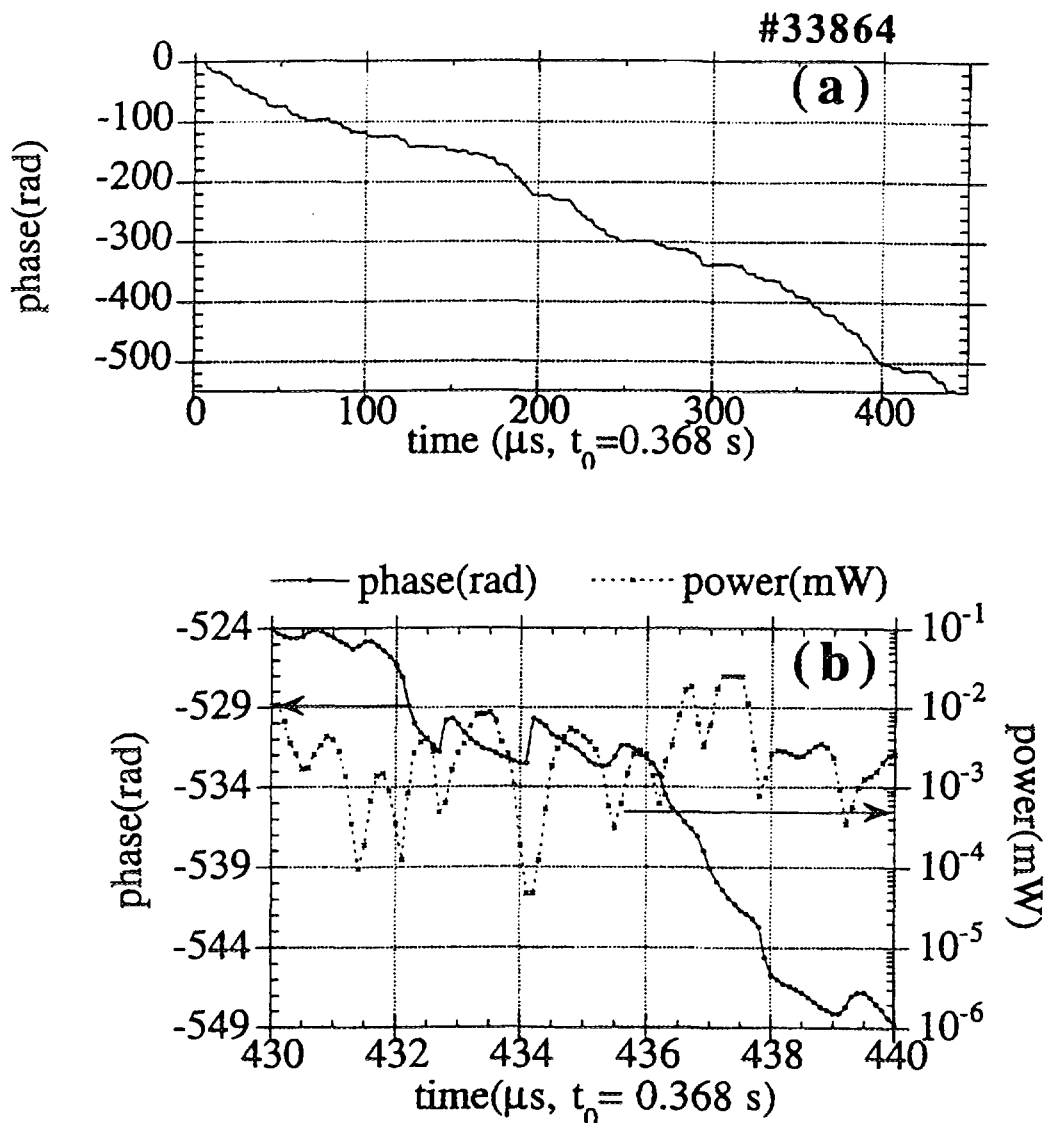
A detailed analysis can be found in [3] from which the following figure is taken, which shows the evolution of the phase for several cycles of a sinusoidal fluctuation for the case of one sideband. The amplitude of the sideband increases as a consequence of increasing fluctuation amplitude. For small sideband amplitude the phase oscillates around the mean value. Close to the threshold additional harmonics appear which result in a sawtooth-like time trace of the phase. The resulting $1/f$ -like frequency spectrum is observed in several experiments [5,6,7,8]. Once the threshold amplitude is reached the uni-directional drift of the phase starts.



Results regarding the phase runaway

Experimental observations of the phase runaway phenomenon have been observed in a number of fusion experiments (e.g. [5,6]). The next figure (taken from [5]) shows received signal power and phase detector output for a 10 μ s time window measured on W7-AS during ECRH (tilt angle of the plasma surface ≈ 2.6 deg.). On the average the phase drift runs in one direction. However, transiently the phase drift can stop or the direction of the drift can even reverse. The experimental results agree well with the predictions from the analytical model introduced above. Especially, the minima of the received signal power coincide with the maxima in the slope of the phase signal, which has also been observed in other experiments

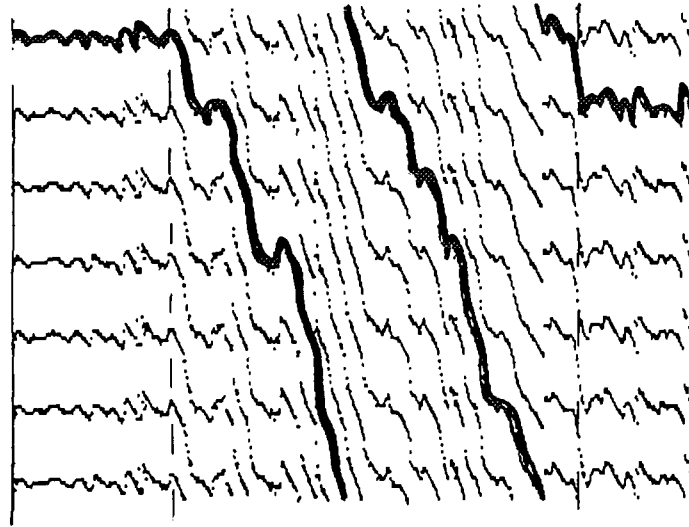
[7,8]. This can be understood as a result of intermittent destructive interference at the receiver antenna.



- (a) Experimental result showing the phase runaway at W7-AS.
- (b) Time window of 10 μs of the phase (solid line) and power (broken line) of the phase runaway.

For comparison we show in the next figure the time dependent phase signal obtained with the 2-D RCL-network code. The numerically generated turbulence (lower trace) corresponds to the typical fluctuation spectra observed during a burst of turbulence (e.g. ELM). As can be seen, there is a critical threshold amplitude for the onset and end of the phase runaway, in agreement with experimental observations at W7-AS and TFTR [9,6]. The intermittent reversal of the phase drift is also reproduced. The upper part of the plot shows the phase output modulo 2π . As a guide to the eye the temporal development of the phase is indicated by a thick line.

phasemeter response :

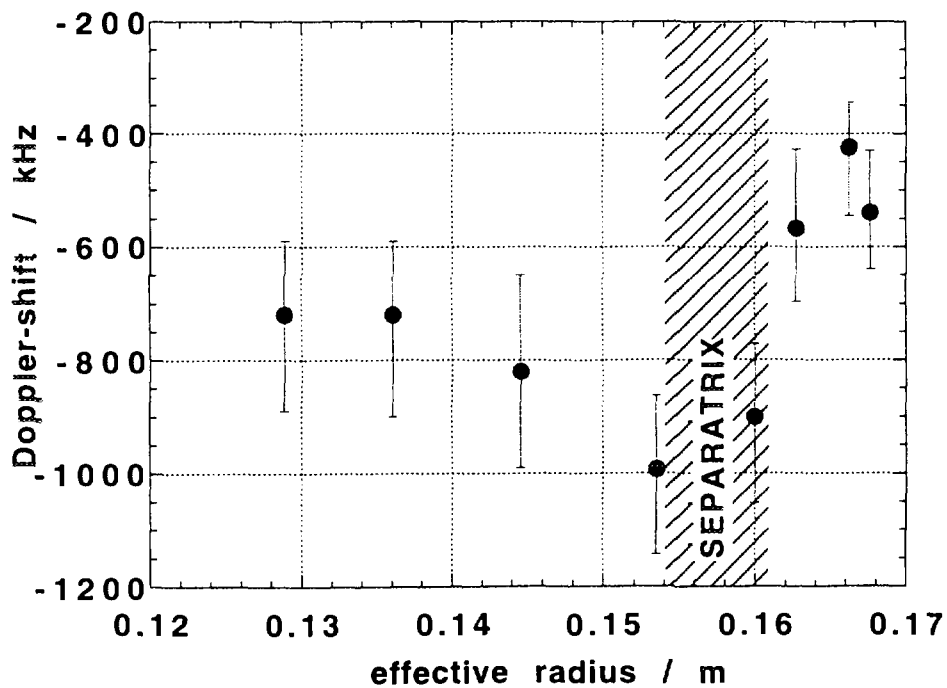


density fluctuations :



time

The radial resolution of the reflectometry system with respect to turbulent density fluctuations is demonstrated in the next figure obtained with a tilt angle of the probing beam with respect to the plasma surface ≈ 2.6 deg. during an ELMy H-mode at W7-AS. The radial shear in the poloidal propagation velocity and the achievable radial resolution can be clearly observed.



Problems to be solved

(i) The problems due to phase runaway in conventional reflectometry can be overcome by using AM-reflectometry. Numerical 2-D-code modelling of the influence of fluctuations on AM-reflectometers for the conditions at W7-AS are presently performed.

(ii) Which antenna geometry is best suited for poloidal propagation measurements?

First experiments with the new moveable antenna at W7-AS show a Doppler shift in excess of 1 MHz .

(iii) If and to what extent does the presence of density turbulence in fusion experiments modify the measured density profiles. Which antenna geometry is best suited for density profile measurements? What are the consequences for smoothing/averaging procedures for the reconstruction of density profiles?

(iv) To what extent is it possible to extract information about the radial correlation length of density fluctuations?

References

- /1/ E. Holzhauser, T.L. Rhodes, I. Reflectometry Workshop, IAEA TC-Meeting, JET (1993).
- /2/ E. Holzhauser, G. Rohrbach, I. Reflectometry Workshop, IAEA TC-Meeting, JET (1993).
- /3/ T. Grossmann, E. Holzhauser, M. Hirsch, F. Serra, M.E. Manso and I. Nunes, this workshop.
- /4/ J.H. Irby, S. Horne, I. H. Hutchinson, P.C. Steck, *Plasma Phys. Contr. Fusion*, 35, 601 (1993).
- /5/ B. Branas, M. Hirsch, V. Zhuravlev, J. Baldzuhn, J. Sanchez, T. Estrada, T. Geist, H.J. Hartfuss, this workshop.
- /6/ E. Mazzucato, S. Batha, M. Beer, M.G. Bell et al, *Phys. Rev. Lett.* 77, 3145 (1996).
- /7/ T.L. Rhodes, this workshop.
- /8/ G. Conway, this workshop.
- /9/ M. Hirsch, E. Holzhauser, J. Baldzuhn, B. Branas et al., 16th IAEA Fusion Energy Conf. , Montreal, 7 - 11 Oct. (1996).

A 2-D Code for the Analysis of Microwave Reflectometry Measurements in Fusion Experiments

M.T. Grossmann, E. Holzhauer¹, M. Hirsch², F. Serra,
M. E. Manso and I.Nunes

*Associação EURATOM/IST, Centro de Fusão Nuclear,
1096 Lisboa Codex, Portugal*

¹*Institut für Plasmaforschung, Universität Stuttgart, Germany*

²*Max-Planck-Institut für Plasmaphysik, EURATOM Association, D-85748 Garching,
Germany*

I - Introduction

Density fluctuations affect the group delay of electromagnetic waves probing the plasma and undergoing reflection from a cutoff layer. The purpose of the analysis of density fluctuations in reflectometry experiments is therefore two-fold: to deduce the spatial and spectral characteristics of the fluctuations and to understand their impact on the evaluation of density profiles.

Several theoretical studies have been undertaken recently in order to analyse the influence of density fluctuations on reflectometry signals. The reduction of the full-wave equation to a first-order Born approximation was treated analytically for the 1-D (Zou et al. 1990, Mazzucato and Nazikian 1991, Bretz 1992, Hutchinson 1992, Afeyan et al., 1995) and 2-D cases (Bruskin et al., 1995). Also several numerical codes were developed (using finite difference methods), for the direct solution of the wave equation in 2-D, with the Born single-scattering approximation (Fanack et al. 1996, Conway et al., 1996) or full-wave multiple scattering (Irby et al., 1993).

1-D solutions can provide insight about the interpretation of the measurements, namely in what concerns the localisation of the phase response of a reflectometer to radially propagating fluctuations: either due to the oscillation of the cut-off layer (for fluctuations with $k_f \ll k_0$) or to Bragg resonant scattering away from the cutoff layer (where $k_f = 2k(x)$, for $2k_A < k_f < 2k_0$, k_A being the finite wavenumber at the cut-off). The phase response is strongly influenced by the shape of the localised perturbation: for a damped wavetrain with sharp boundaries (broad spectrum) the phase response is dominant at cut-off for any value of the fluctuating wavenumber (Fanack et al. 1995, Grossmann et al. 1995), in agreement with experiments (Rhodes et al., 1992). Moreover the scattering process is roughly localised in the cut-off layer as long as the k-spectrum is concentrated below a critical value; this should be the case of tokamaks where usually the turbulence exhibits a spectrum rapidly decaying above $k = 5 \text{ cm}^{-1}$ (Fanack et al., 1995).

However, for a quantitative analysis of fluctuation measurements, 2-D effects (as refraction, diffraction, interference and beam divergence) have to be included in the scattering models, namely to account for poloidally propagating oscillatory modes: if $k_f < 2k_0$, the layer behaves as a "corrugated" surface that will scatter the incident beam, leading to Doppler-shifted components.

Here we present a 2-D numerical code based on spatially distributed RLC networks (Holzhauer and Rohrbach, 1992) to model the full-wave propagation in the density fluctuating plasma; it is easily adapted to different antennae-plasma configurations and to both O and X-modes. The code was applied to the study of the influence of

poloidal rotating structures in X-mode reflectometry measurements (with the AM and carrier phase system) on the W7-AS stellarator, taking into account the antennae-plasma geometry of the diagnostic: two poloidally separated antennae (emitter/receiver). The numerical simulations reveal the existence of an anomalous drift of the phase (“phase runaway”) above a given threshold of the perturbation, when a plasma tilting with respect to the symmetry axis of the two antennae is taken into account.

II - Numerical code

The code is based on spatially distributed RLC networks to model the full-wave propagation of electromagnetic waves ($\vec{E} = \vec{E}_0 \exp j(\vec{k} \cdot \vec{r} - \omega t)$) in a density fluctuating plasma. Using the Maxwell equations (where the plasma effects are included in the response of the current density \mathbf{J} to the wave electric field \mathbf{E}), in the cold plasma approximation and for O-mode propagation, one obtains for 1-D geometry ($\vec{k} \perp \vec{B}_0$ ($k_y = k_z = 0$), $\vec{E} \parallel \vec{B}_0$ ($\vec{E} = E_z$), with $\vec{B}_0 = B_0 \vec{e}_z$):

$$\frac{\partial E_z}{\partial x} \Delta x = j\omega \Delta x \mu_0 H_y \quad (1)$$

$$\frac{\partial H_y}{\partial x} \Delta x = \left(j\omega \epsilon_0 \Delta x + \frac{1}{j\omega \left(\frac{m_e}{\Delta x n_e e^2} \right) + \frac{v_{eff} m_e}{\Delta x n_e e^2}} \right) E_z \quad (2)$$

Δx is a plasma slice (with constant n_e) in the propagation direction. Applying Eq. 1 (corresponding to Ohm’s law) and Eq.2 (Kirchhoff’s current law) to an RLC circuit one obtains the basic model of Fig.1 (Holzhauer, Rohrbach, 1992):

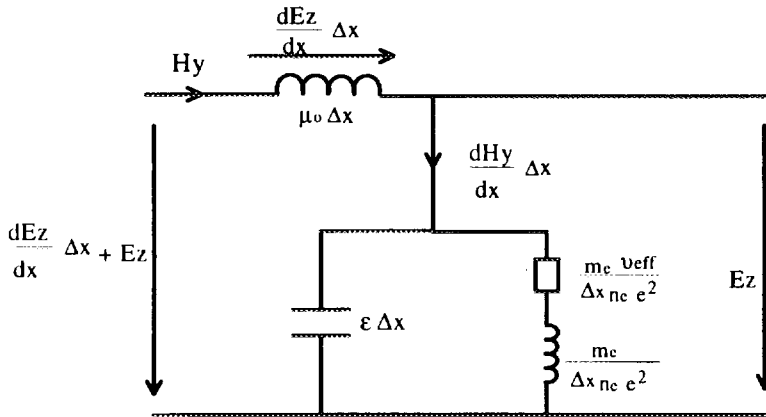
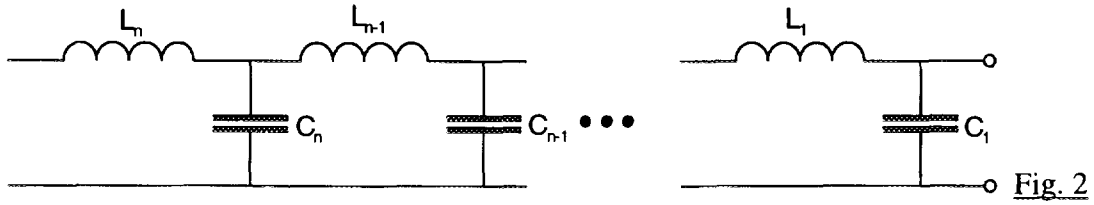


Fig.1

For frequencies in the GHz range the coil in parallel with the capacitor is deleted (coil impedance $j\omega m_e / \Delta x n_e e^2 \gg$ capacitive impedance $1/j\omega \epsilon \Delta x$) and collision effects are also disregarded (resistance set to zero). The complete circuit to model the plasma is obtained connecting in series several elementary circuits (Fig.2), where at least 12 elements per wavelength are considered ($\Delta x \leq \lambda_0/12$):



The characteristics of the plasma density profiles and of density fluctuations define the value of the network components. The capacitances for the two modes are:

$$(O - mode) \quad j\omega\epsilon(x)\Delta x = j\omega\Delta x\epsilon_0 \left(1 - \frac{\omega_{pe}^2(x)}{\omega^2} \right) \quad (3)$$

$$(X - mode) \quad j\omega\epsilon(x)\Delta x = j\omega\Delta x\epsilon_0 \left(1 - \frac{\omega_{pe}^2(x)(\omega^2 - \omega_{pe}^2(x))}{\omega^2(\omega^2 - \omega_{pe}^2(x) - \omega_{ce}^2(x))} \right) \quad (4)$$

Two - dimensional model: From the 1-D configuration the network can be extended in two directions as shown schematically in Fig.3

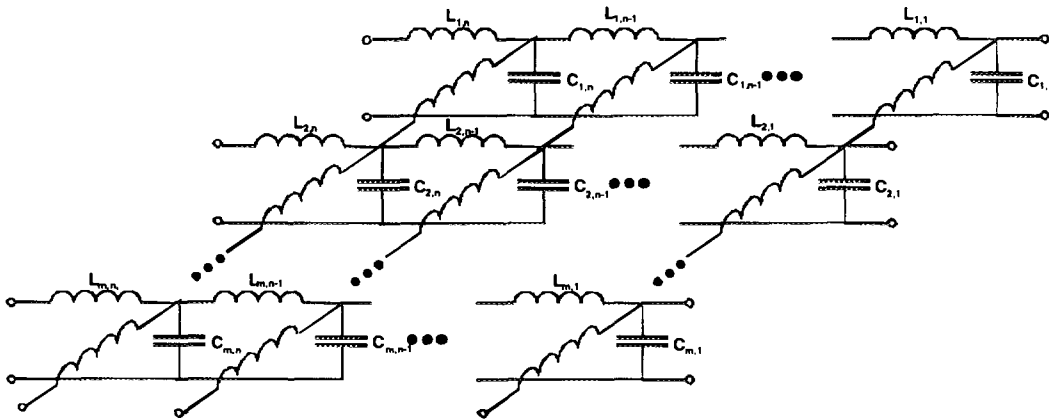


Fig. 3

In the 2-D model the antenna mouth is divided into several subareas to calculate the field distribution. Using the Huygens principle, the radiated field that arrives at the plasma edge is calculated applying the Fourier integral to each subarea. In order to find the plasma response to the incident field, the total impedance “seen” at the input is determined using $(2n \times 2n)$ matrixes (where n is the number of nodes that each row of the network contains). The voltages at the input (m^{th} row in Fig. 3) are related to the currents through the total impedance of the network that contains the plasma characteristics. The reflected field arriving at the plasma edge is then obtained.

At Asdex Upgrade reflectometry system the antennae are focusing hog-horn, simultaneously used for emission and reception (Silva et al.,1992). The code was applied to model the profile build-up at the L-H transition as detected with fixed frequency operation (Manso et al., 1997, this Workshop). Here we concentrate at the Stellarator W7-AS reflectometry system, using two conic antennae (one as emitter and one as receiver) and on the analysis of the phase runaway phenomena.

III - Phase runaway at the W7-AS reflectometry system

An anomalous drift of the phase, too large to be explained by a realistic radial movement of the cut-off layer is usually referred as “phase runaway” ($d\phi/dt \sim 100 - 200$ kHz at W7-AS). It has been detected in several reflectometry devices and attributed to the Doppler shift of the probing beam reflected from rotating cut-off layer disturbances (Sanchez et al., 1992; Bulanin, Korneev, 1994). First direct comparisons of the phase runaway with plasma rotation measurements have been recently reported at W7-AS, showing that the drift is inverted as the rotation is reversed (by inverting the magnetic field); using a 2-D WKB code numerical simulations have shown that for a net drift of the phase to appear it is necessary some asymmetry: in the geometry of the emitting/receiving horns and/or in the turbulent rotating structures (Brañas, Hirsch et al., 1997, this workshop). Here we describe briefly a theoretical approach for the occurrence of phase drift due to scattering, and compare it with numerical simulations using the 2-D RLC code adapted to the two-antenna geometry of the W7-AS reflectometry system.

(i) Theoretical analysis

A microwave of frequency ω which has been reflected from a plasma, in general contains a signal of the incident frequency and additional components at frequencies $\omega \pm \Delta\omega(t)$; the frequency shift is $\Delta\omega = \vec{k}_j \cdot \vec{v}_{pol}$, where \vec{v}_{pol} is the poloidal velocity of a rotating perturbation. The non-shifted signal corresponds to reflection and refraction in the stationary plasma. In contrast the frequency shifted components $\omega \pm \Delta\omega(t)$ result from the modulations of the optical properties due to temporal perturbations of the plasma (described either as moving structures on the surface of a mirror, or as temporal fluctuations of the refractive index in the propagating path), leading to scattering of the probing waves (Hirsch, Holzhauser et al., 1997, this Workshop). A combination of Doppler-shifted return signals might lead to a ramping of the phase detected at a receiver antenna in a different poloidal position with respect to the emitter, as shown with 2-D numerical simulations (Irby et al., 1993).

The perturbed received reflectometry signal (with heterodyne detection) is characterised by the amplitude $A(t)$ and a time dependent phase shift $\phi(t)$. In the following the reflected signal will be represented by three spectral components S^0 , S^+ and S^- , with frequencies ω , $\omega + \Delta\omega^+$ and $\omega - \Delta\omega^-$. Their interference at the receiving antenna will lead to a signal output:

$$S^0 + S^+ + S^- = \cos(\omega t) + a^+ \cos(\omega t) \cos(\Delta\omega^+ t) - a^+ \sin(\omega t) \sin(\Delta\omega^+ t) + a^- \cos(\omega t) \cos(\Delta\omega^- t) + a^- \sin(\omega t) \sin(\Delta\omega^- t) \quad (5)$$

where the phase of S^0 was set to zero, and the amplitudes (a^+ , a^-) have been normalised with respect to the amplitude of the non-shifted signal. Assuming that the signal at the output of the receiver antenna is $S(t) = A(t) \cos(\omega t + \phi(t))$, one obtains for the measured phase:

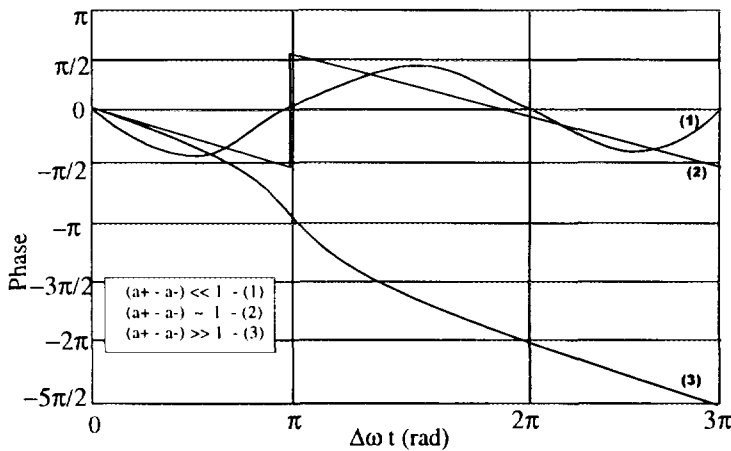
$$\tan \phi(t) = \frac{a^+ \sin(\Delta\omega^+ t) - a^- \sin(\Delta\omega^- t)}{1 + a^+ \cos(\Delta\omega^+ t) + a^- \cos(\Delta\omega^- t)} \quad (6)$$

and for the signal amplitude:

$$A^2(t) = (1 + a^+ \cos(\Delta\omega^+ t) + a^- \cos(\Delta\omega^- t))^2 + (a^+ \sin(\Delta\omega^+ t) - a^- \sin(\Delta\omega^- t))^2 \quad (7)$$

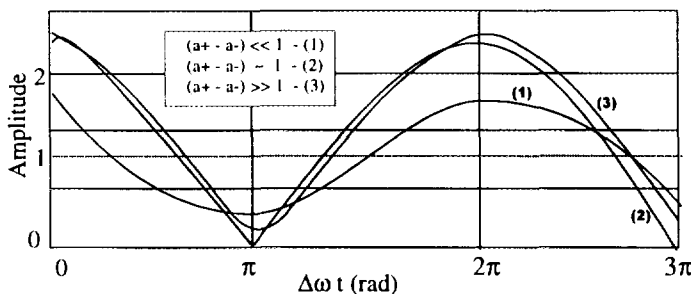
In order to explain an unidirectional phase drift some asymmetry is required: here it is assumed that the asymmetry is determined by the amplitude of the spectral components, $a^+ \neq a^-$, and that $\Delta\omega^+ = \Delta\omega^-$; in this case:

$$\tan \phi(t) = \frac{(a^+ - a^-) \sin(\Delta\omega t)}{1 + (a^+ + a^-) \cos(\Delta\omega t)}; \quad A^2(t) = (1 + (a^+ + a^-) \cos(\Delta\omega t))^2 + ((a^+ - a^-) \sin(\Delta\omega t))^2$$



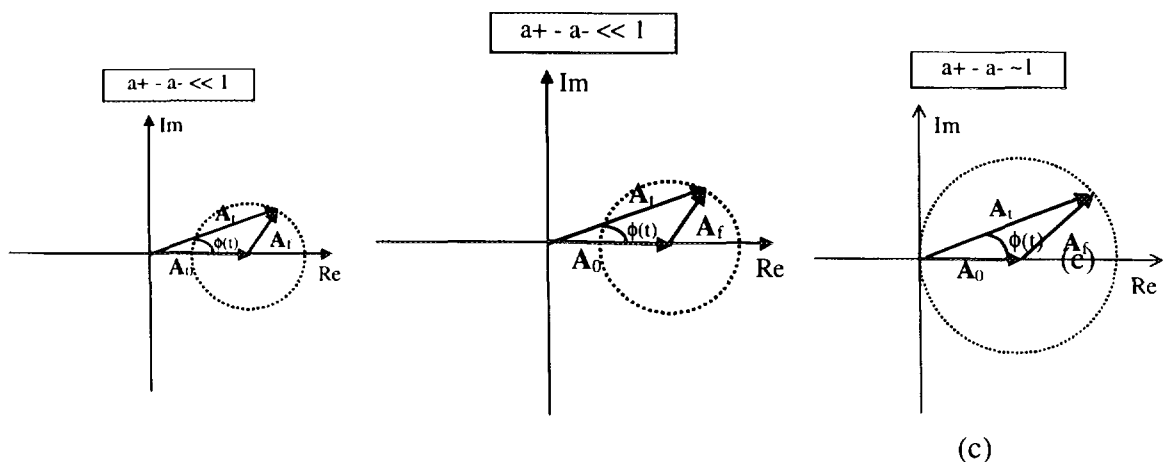
Taking the relative amplitude asymmetry ($a^+ - a^-$) as a parameter, the phase and amplitude evolution is shown in Fig.4 (a) and (b) respectively

(a)



(b)

Fig.4



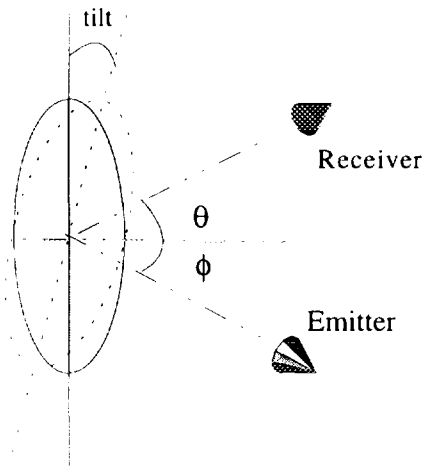
(c)

In the diagram of Fig. 4.c, A_0 and A_f are the complex amplitudes of the non-shifted and the shifted signals, shown for 3 typical situations. For $(a^+ - a^-) \ll 1$, the contribution of the fluctuation to the total complex amplitude A_t is small, and a phase which periodically changes around the phase of S^0 is obtained: $\phi(t) \equiv (a^+ - a^-) \sin(\Delta\omega t)$. For $(a^+ - a^-) \approx 1$ the threshold condition ($A_f = -A_0$) for the occurrence of Doppler shift in the phase occurs: $\phi(t)$ displays a “step” with a height of π ; simultaneously fully destructive interference of the signals imply the amplitude drop to zero. If $(a^+ - a^-)$ increases slightly above this level a periodic rapid change of the phase ($|\Delta\phi| \approx \pi$) is observed when the amplitude $A(t)$ has its minimum. Above the threshold the average slope of the phase change is independent of the specific value of $(a^+ - a^-)$. When $(a^+ - a^-) \gg 1$, the power of the unshifted signal component can be neglected. The amplitude of the received signal is dominated by the amplitude of the shifted component. The phase changes continuously as $\phi(t) = \Delta\omega t$, that is, the signal obtained at the antenna output is Doppler shifted by $\Delta\omega$ and therefore a continuous drift of the phase should be detected (“phase runaway”).

In a real experiment there are two possible sources for the asymmetry: a misalignment of the antenna with respect to the normal direction onto the plasma surface; a tilt angle of the plasma column which depends on the operating parameters of the plasma experiment and must be obtained from suitable diagnostic methods

(ii) 2-D simulation and comparison with experimental results

The reflectometry system installed at W7-AS [Hirsch et al., 1996] operates with X-mode in the W band (75-110) GHz. The two conical antennae use elliptical mirrors to produce a gaussian beam with a waist of 2cm focused near the plasma edge (at 55 cm from the antenna).



The antennas are oriented radially towards the centre of the torus centre and separated poloidally by 12° with their symmetry axis in the equatorial plane. The plasma major axis is not exactly perpendicular to the equatorial plane but slightly tilted: 2.6° . In Fig.5 it is shown schematically the antennae geometry considered in the 2D simulation: $\text{tilt} = 2.6^\circ$, $\theta + \phi = 12^\circ$

Fig. 5

The density and magnetic field profiles were modelled based on typical data. Fig. 6 shows an example with $n_e(0) = 5 \times 10^{19} \text{ m}^{-3}$, and a periodic density modulation (with fixed amplitude and wavelength) propagating in the poloidal direction, radially localised around the reflecting layer (at $r_{\text{eff}} \sim 14 \text{ cm}$, for $f = 85 \text{ GHz}$).

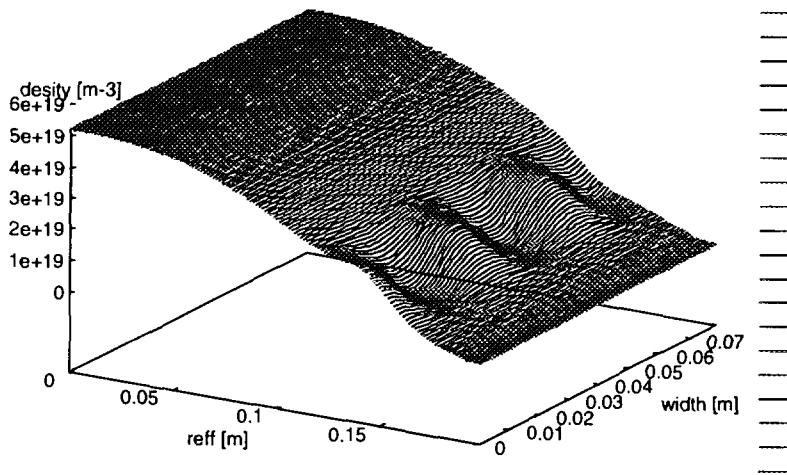


Fig.6

Fig.7 shows the evolution of the complex amplitude during one cycle of the perturbation, for increasing amplitude of the fluctuations (tilt=2.6°); a threshold amplitude for the fluctuation leading to phase runaway is found (normalised amplitude of 0.05).

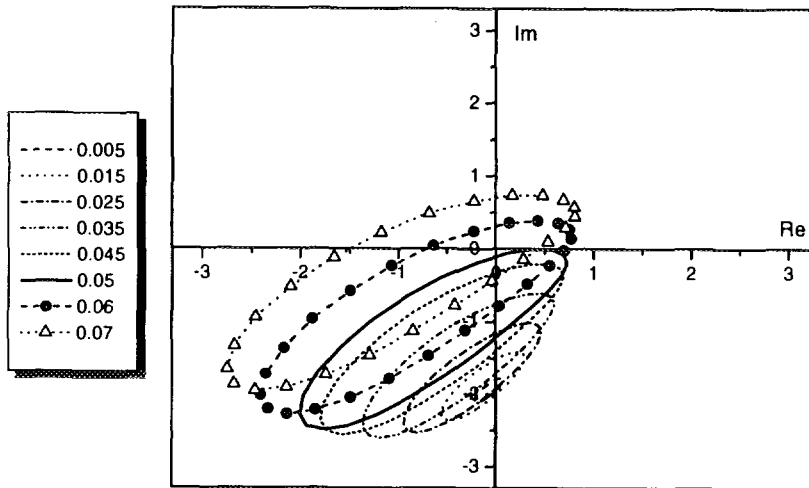


Fig. 7

As can be concluded from the evolution of the phase, when the fluctuation amplitude is 0.05 (threshold condition) a jump of π in the phase is observed (that should correspond to $(a^+ - a^-) \approx 1$). As the amplitude continues to increase above the threshold, the condition $(a^+ - a^-) \gg 1$ is fulfilled and the phase drifts, always in the same direction. The corresponding evolution of the phase and amplitude during one cycle of the perturbation are shown respectively in Figs. 8 and 9 :

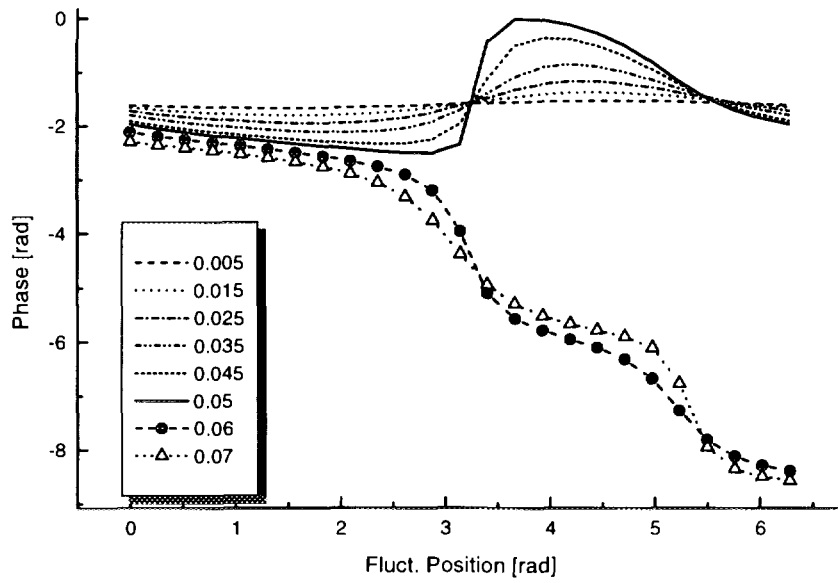


Fig.8

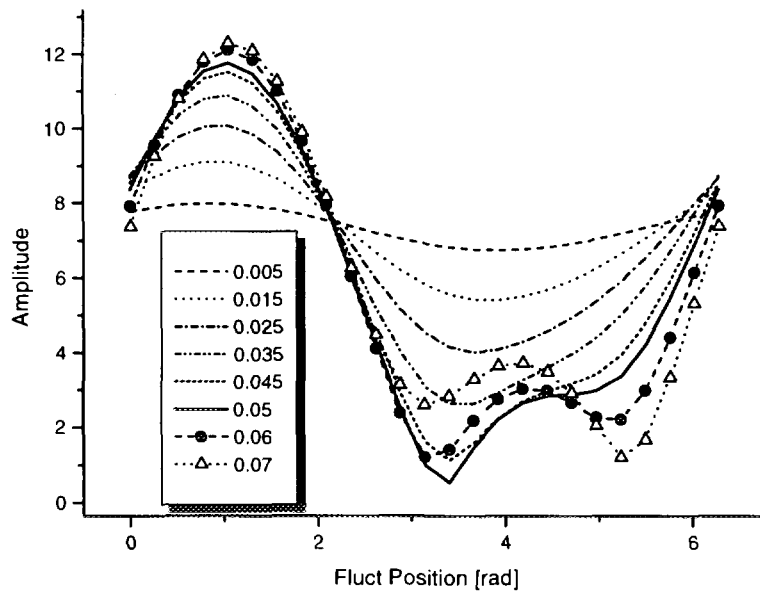


Fig.9

A good agreement with theoretical predictions is found: when the threshold condition is reached, the amplitude drops to a small value and the phase jumps by approximately π ; as the fluctuation amplitude continues to increase, instead of a periodic oscillation an unidirectional phase drift should be observed by the reflectometer . (When the tilt is not considered, no phase runaway is observed).

The evolution of the phase and amplitude over several cycles is shown in Fig.10. The amplitude of the fluctuation was increased by small steps and maintained constant when it reached the threshold ~ 0.06 .

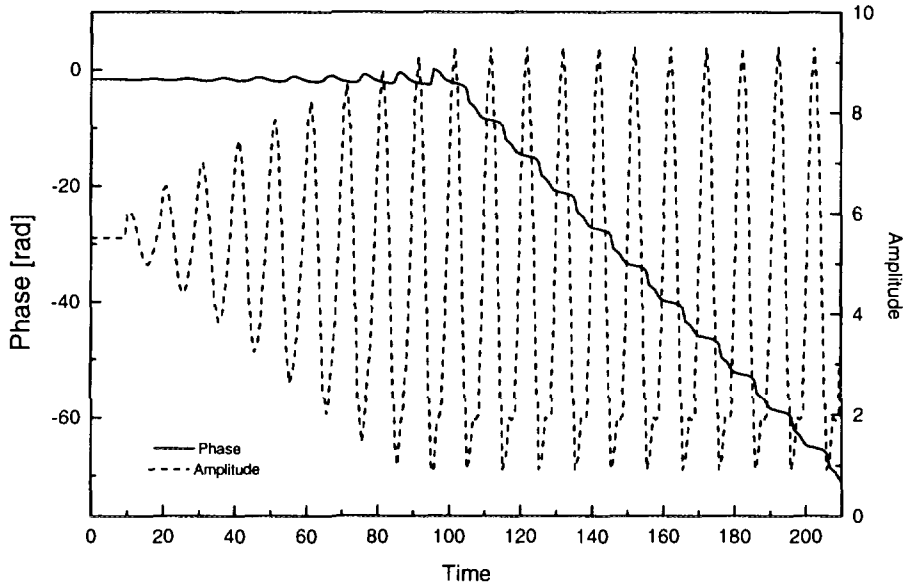


Fig.10

A value of $d\phi/dt \sim -100$ kHz is obtained with $k_f = 2 \text{ cm}^{-1}$, $V_{\text{pol}} \sim 3.2 \text{ Km/s}$. By continuously increasing the amplitude beyond the threshold (up to 0.1), the mean slope of the phase runaway ($d\phi/dt$) remains constant. This is shown in **Fig.11**, where the phase is also represented for symmetric (positive/negative) poloidal velocities.

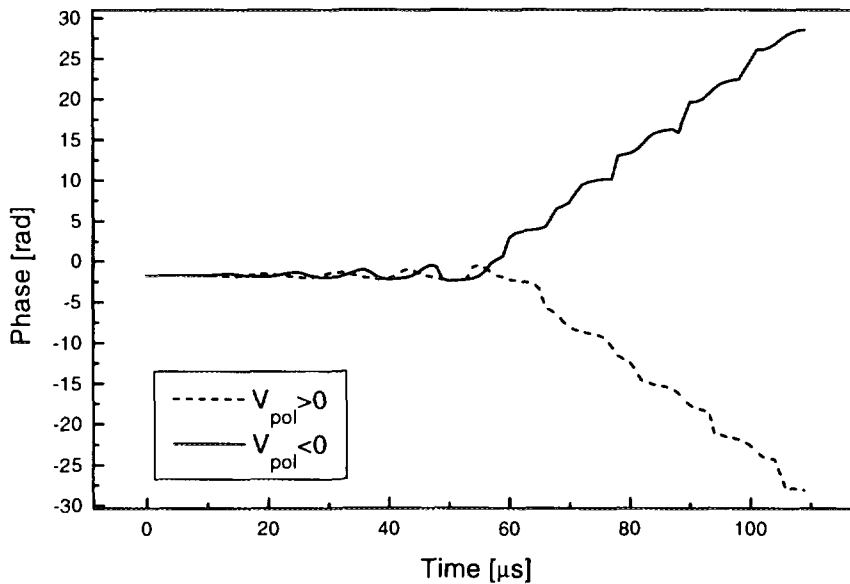


Fig.11

It is concluded that the slope of the phase drift changes from negative to positive when the poloidal velocity is reversed: this agrees with the experimental results where the inversion of the plasma poloidal rotation is accomplished by inverting the magnetic field.

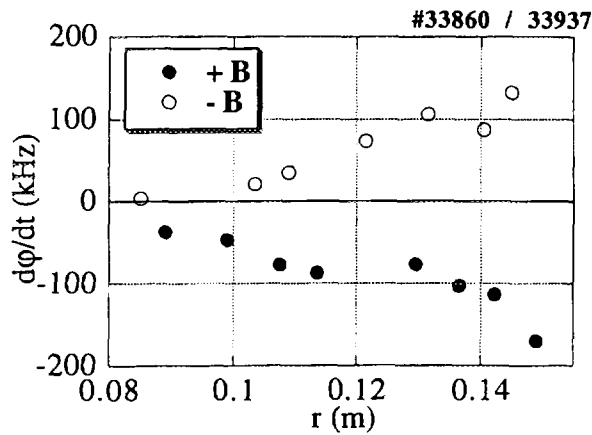


Fig. 12 shows the radial profile of the phase drift at W7-AS for positive and negative magnetic field, while all the other plasma parameters were kept constant (Brañas, Hirsch et al., this Workshop). The simulation results shown in Fig.11 fit the two symmetric experimental points obtained at $r_{\text{eff}} \sim 0.14\text{m}$.

Fig. 12

IV- Concluding Remarks

A 2-D code has been developed based on spatially distributed RLC networks to model the full-wave propagation in a density fluctuating plasma. It has the advantages of being easily adapted to different antennae-plasma configurations and to both the O and X-modes. The code was applied to the study of the influence of poloidal rotating structures in X-mode reflectometry measurements on the W7-AS stellarator. The results agree with experimental results and numerical simulations (with a 2-D WKB code) by Brañas et al. (this Workshop), and extend the analysis of the phase runaway for the two-antennae - plasma geometry. A plasma tilt of 2.6° (with respect to the symmetry axis of the two antennae) is suggested as the main cause of the phase runaway. The threshold for the amplitude of the perturbation triggering the phase runaway should correspond to (high) levels of turbulence, namely reached during L-mode regimes and with the occurrence of ELMs.

References

- B.Afeyan, A.Chou, B.Cohen, Plasma Physics and Controlled Fusion 37 315, 1995
- B.Brañas, M.Hirsch, V.Zhuravlev, J.Baldzuhn, J.Sánchez, T.Estrada, T.Geist, H.J.Hartfuß, submitted to Plasma Physics and Controlled Fusion, 1997
- N. Bretz, Phys. Fluids B 4 (8), August 1992
- L. Bruskin, A.Mase and T. Tamano, Plasma Phys. Contr. Fusion, 37,255, 1995
- V.Bulanin, D.O. Korneev, Plasma Physics Reports 20 (1) 14,1994
- G.D. Conway, L. Schott, and A. Hirose, Rev. Sci. Instrum. 67 (11), 1996
- C.Fanak, I.Boucher, F.Clairet, S.Heuroux, G.Leclert, X.L.Zou, 22nd EPS IV-409, Bournemouth, 1995
- T.Grossmann, F.Serra, E.Holzhauer and P.Varela, 6th European Fusion Theory Conference, P3-20,Utrecht, 1995
- M.Hirsch, H.Hartfuss, T.Geist, E. de la Luna, Rev. Sci. Instrum. 67 (5), 1807, 1996
- M.Hirsch, E.Holzhauer., IAEA TCM on Microwave Reflectometry, May 1997
- E.Holzhauer, G.Rohrbach, IAEA TCM on Microwave Reflectometry for Fusion Plasmas JET Joint Undertaking, March 1992
- J.Irby, S.Horne, I.Hutchinson, P.Steek, Plasma Physics and Controlled Fusion 35 601, 1993
- E.Mazzucato, R.Nazikian, Plasma Physics and Controlled Fusion 33 261-274, 1990
- J.Sánchez, T.Estrada, J.H.Hartfuß, 1st IAEA Tech. Comm. Meeting on Microwave Reflectometry for Fusion Plasma Diagnostics (Abingdon) 133, 1992
- F.Serra, A.Silva, M.Manso, J.Santos, B.Kurzan, W.Suttrop, 24th EPS, Berchtesgaden, 1997
- A.Silva, L.Cupido, M.Manso, F.Serra, F.X.Soeldner, P.Varela, C.Correia, C.Fernandes, C.Loureiro, A.Moreira, J.Neves, R.Pereira, J.Santos, Asdex Upgrade Team, 17th Symposium on Fusion Technology, Vol.1, p747 Rome, September 1992
- X.L.Zou, L.Laurent, J.M.Rax, Plasma Physics and Controlled Fusion 33 1091, 1991

2D Physical optics simulation of fluctuation reflectometry

G D Conway †

Plasma Physics Lab., University of Saskatchewan, Saskatoon, Canada.

†JET Joint Undertaking, Abingdon, Oxon, UK.

Abstract. The two-dimensional physical optics model of fluctuation reflectometry is reviewed and selected case studies presented comparing simulation with experimental results. The case studies include coherent modes, broadband turbulence, radial correlation lengths, correlation profiles and asymmetries in the launch - receive geometry.

1. Introduction

The two-dimensional (2D) physical optics model has been used to study several problems in fusion plasma fluctuation reflectometry [1,2]. These studies include quantifying the wavelength response to transverse propagating coherent modes [3]; the effects of broadband turbulence [4,5]; and more recently, the measurement of radial correlation lengths [6]. The results in each case show that the modulation of the reflectometer phase signal depends not only on the plasma fluctuation amplitude, but also on 2D effects such as the illumination spot size and the fluctuation wavelength or spectral content. Measured correlation lengths are also subject to 2D effects, however the model offers a means of reconciling the discrepancies between lengths measured from amplitude fluctuations (homodyne systems) and phase fluctuations (heterodyne systems). These, together with new results from simulating transverse correlation reflectometry, and the crucial effects of antenna misalignment (i.e. asymmetries in launch and receive geometry) will be summarised in this paper. Confirmatory experimental evidence from the JET correlation reflectometer will also be presented in each case as a validation of the model. With the inclusion of asymmetry effects the physical optics model now offers a comprehensive and (almost) complete picture of the behaviour of fluctuation reflectometry.

2. The model

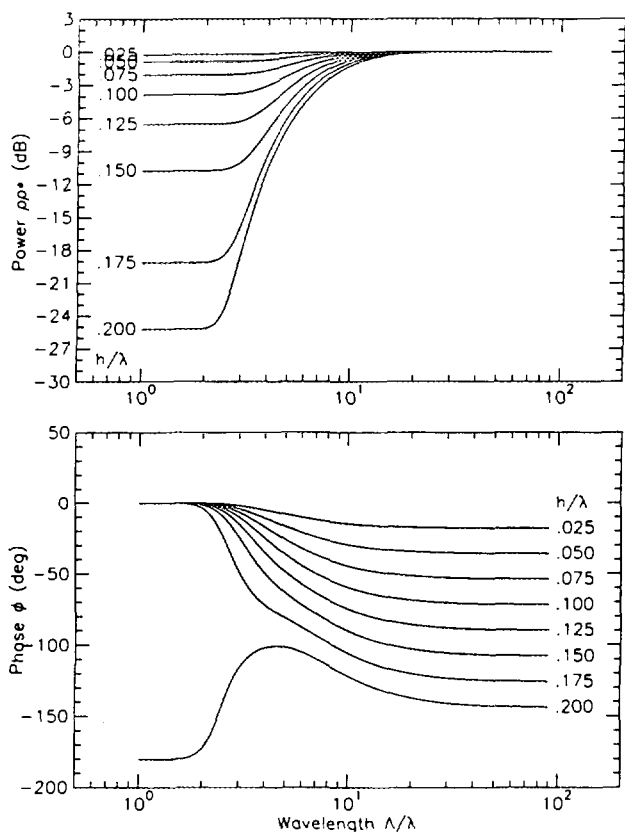
The principles and limitations of the model have been described in detail in the literature [3,6,7], but are briefly summarised as follows. The plasma cutoff layer is approximated to a thin distorted conducting surface. The phase and amplitude of the electric field of a microwave beam reflected or scattered from the surface are then calculated from the Helmholtz equation. General solutions are obtained using a far-field Greens function and a paraxial Gaussian incident microwave beam with a circular or elliptic cross-section. Plasma fluctuations are modelled as two-dimensional distortions in the surface. The two most important 2D effects, finite illuminated area and surface structure, are incorporated in the model together with basic reflectometer geometry parameters (i.e. launch and receive angles). For simple cases the Helmholtz equation can be solved analytically, but for a direct comparison with experimental results a numerical solution is more appropriate. Here, the reflection layer is moved past the reflectometer beam to generate simulated reflectometer time signals which are then processed as if they were real experimental signals using standard data analysis techniques.

3. Coherent modes

For the simple case of a coherent plasma or MHD mode the surface distortion is modelled as a sine wave with a normalised wavelength Λ/λ and peak amplitude h/λ , where λ is the microwave

wavelength. The simplest reflectometer geometry is assumed, that is normal incidence and backscatter $\theta_1 = \theta_2 = 0$ (i.e. a single launch/receive antenna, or monostatic configuration).

Simulation results. Figure 1 shows the maximum reflected power and phase shift as a function of Λ/λ for increasing mode amplitude with a fixed Gaussian beam width $w/\lambda = 2$. There are three distinct wavelength regions which scale with the reflectometer beam radius [3]:



(a) Long fluctuation wavelengths: $\Lambda/\lambda \gg 10w/\lambda$.

There is no attenuation, or modulation of the reflected power $\delta P = 0$. The phase shift replicates the shape of the mode, and the depth of phase modulation approaches the 1D geometric optics limit $\delta\phi = 4\pi h/\lambda$.

(b) Transition wavelengths: $w/\lambda < \Lambda/\lambda < 10w/\lambda$.

Phase $\delta\phi$ is no longer linear with h/λ . The reflected power is attenuated and there is large δP modulation at twice the phase modulation frequency, $f_P = 2f_\phi$.

(c) Short wavelengths: $\Lambda/\lambda < w/\lambda$.

Both $\delta\phi$ and $\delta P \rightarrow 0$ with decreasing Λ/λ . The reflected power is strongly attenuated, saturating at a value determined by h/λ .

Figure 1: Simulation: Reflected power and peak phase shift vs normalised coherent mode wavelength Λ/λ as a function of mode amplitude h/λ with $w/\lambda = 2$. At large Λ/λ the results approach the 1D geometric optics limit.

Experimental results. Figure 2 shows coherence spectra $\gamma^2(f)$ of phase and power signals from the JET correlation reflectometer (see accompanying paper for details [7]) with two beams separated by 40 mm toroidally and the X-mode cutoff close to the plasma separatrix ($R = 3.75$ m). The phase signal shows a coherent peak at 35 kHz while the power signal shows a single peak at twice this frequency - as expected in the transition region. The time delayed cross correlation of the phase fluctuations shows a sinusoidal correlation with a temporal shift from zero of $18 \mu s$ which gives a propagation velocity of $v = 0.04/18\mu s = 2.2 \pm 0.3$ km/s. The reflectometer wavelength $\lambda = 4$ mm and spot radius $w \sim 60$ mm give a fluctuation wavelength of $\Lambda \approx 80$ mm in the transition zone, and thus a propagation velocity of $v = \Lambda f = 2.8 \pm 0.6$ km/s. The close agreement of the calculated and measured velocities, together with the frequency doubling in the power signal validates the model.

4. Broadband turbulence

For broadband turbulence the surface distortions are simulated from Fourier components with a Gaussian wavenumber spectrum (normalised spectral width of k_w/k_o where $k_o = 2\pi/\lambda$) and an rms amplitude σ/λ . The reflectometer geometry is again a Gaussian beam normally incident on the reflection layer.

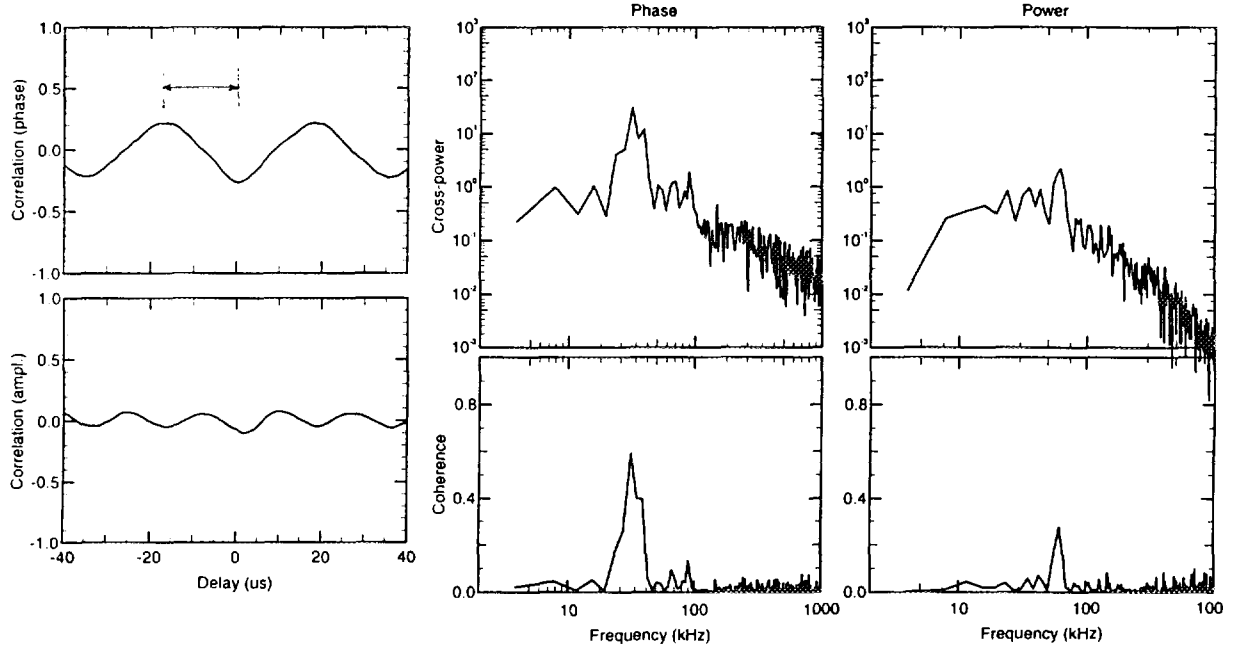


Figure 2: Experiment: Cross power and coherence spectra from JET edge showing coherent mode at 35 kHz in phase signal and 70 kHz mode in power signal. Phase cross correlation shows time delay of 18 μ s for 40 mm toroidal separation.

Simulation results. The random phase fluctuations in the reflected signal are symmetrically distributed (usually Gaussian) about the mean phase, but the power fluctuations are non-symmetrically distributed [5]. With increasing rms fluctuation amplitude σ/λ both the rms phase ϕ_{rms} and power P_{rms} levels initially increase and the mean reflected power level P_o decreases. For $\sigma/\lambda > 0.2$ the phase fluctuations become uniformly distributed between $\pm\pi$ and ϕ_{rms} goes to 0.6π . The spectral index also saturates at $n_\phi = -2$, i.e. a $1/f^2$ spectra; and P_{rms}/P_o approaches 1. Figure 3 shows the variation of ϕ_{rms} and P_{rms}/P_o as a function of the product of the beam radius and spectral width $(k_w/k_o) \cdot (w/\lambda) = k_w w/2\pi$ for various values of σ/λ . For very long wavelength fluctuations, and very small spot sizes, $k_w w/2\pi \ll 1$ the power fluctuations go to zero $P_{\text{rms}}/P_o \rightarrow 0$ and the phase ϕ_{rms} approaches the 1D geometric optics limit $\phi_{\text{rms}} = 4\pi\sigma/\lambda$. However, for $k_w w/2\pi > 1$ and $\sigma/\lambda \leq 0.1$ the phase is given by:

$$\phi_{\text{rms}} = 4\pi \frac{\sigma}{\lambda} \frac{1}{\sqrt{2}} \left(\frac{k_w w}{k_o \lambda} \right)^{-0.6} \quad (1)$$

If w is known then measuring the rms phase and power levels will give the fluctuation amplitude and spectral width, and hence the transverse correlation length. σ is effectively the physical displacement of the reflection layer and is related to the rms density fluctuations \tilde{n} (O-mode only) and magnetic field fluctuations \tilde{B} (X-mode reflectometer)

$$\sigma = L_n \frac{\tilde{n}}{n} \quad (\text{O - mode}) \quad \sigma = \frac{\tilde{n}/n + \tilde{B}/B(\omega_c \omega_o / \omega_p^2)}{L_n^{-1} + L_B^{-1}(\omega_c \omega_o / \omega_p^2)} \quad (\text{X - mode}) \quad (2)$$

Analysis of the signal spectra and distribution shape (skewness) of power fluctuations can also aid in determining plasma fluctuation properties.

Experimental results. Figure 4 shows a set of spectra and probability density functions (pdf) for reflectometer phase and power signals recorded during the ohmic and NBI heated H-mode phases from the JET edge ($r/a \sim 0.9$) region. As the edge turbulence decreases (predominantly low frequencies) in the H-mode, the ϕ_{rms} drops and the power pdf becomes more symmetric - exactly as predicted by the model [5]. All JET data follows the model, when the phase fluctuations increase the mean power decreases and visa versa. Using the curves in figure the edge σ/λ is seen to drop from 18% to around 6%.

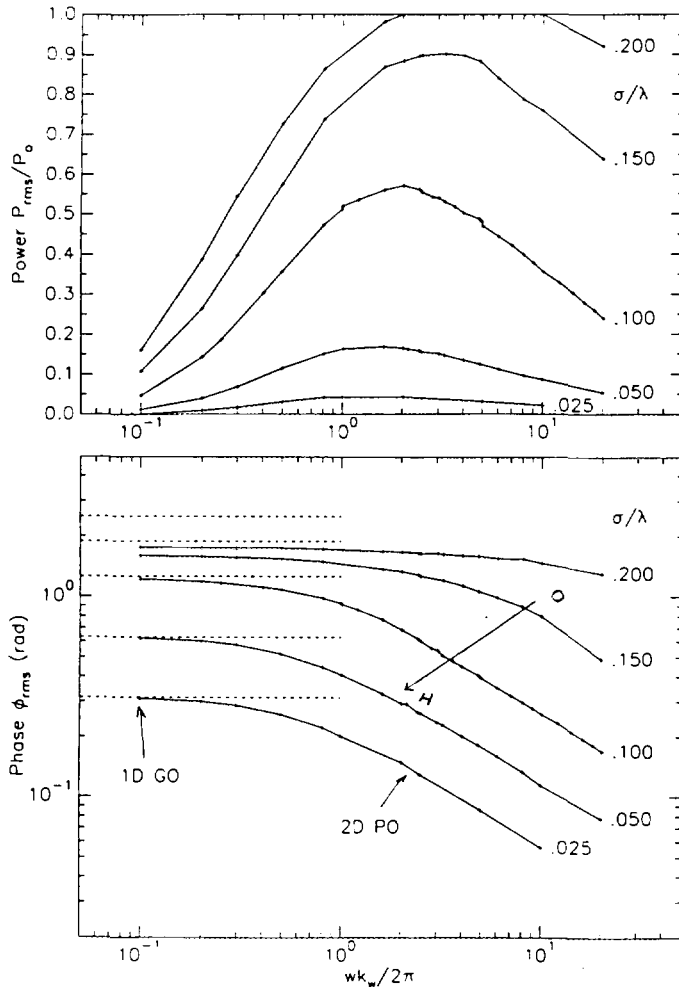


Figure 3: Simulation: rms phase and power from turbulent surface vs $k_w w/2\pi$ (beam width \times spectral width) for increasing rms fluctuation amplitude σ/λ .

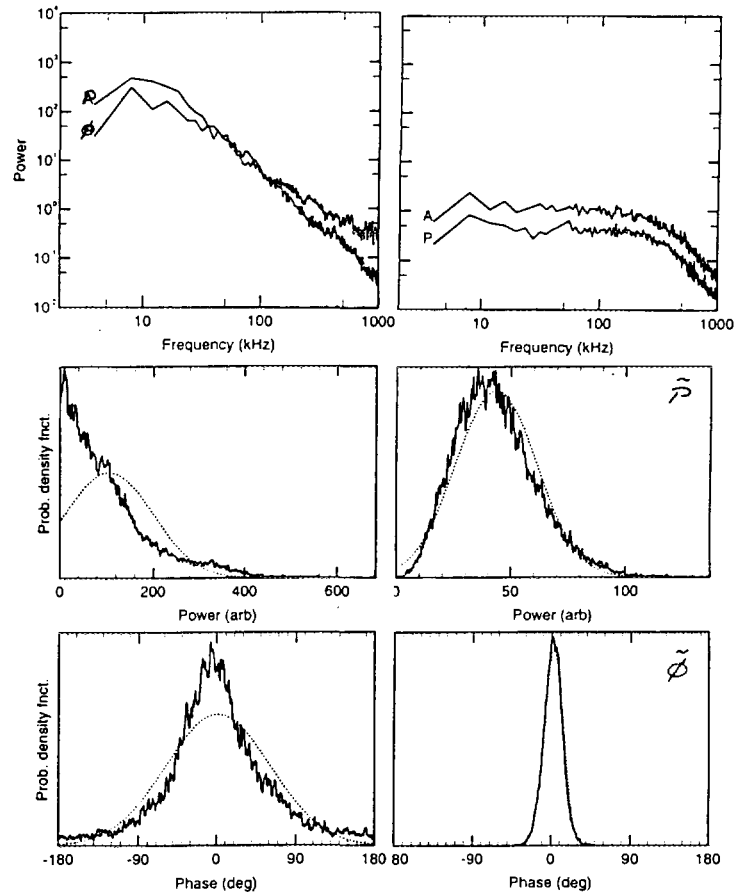


Figure 4: Experiment: Spectra and probability density functions (pdf) for JET edge fluctuations during ohmic (left) and NBI H-modes (right).

5. Radial correlation lengths

By extending the surface model to include a radial wavenumber component the model can be used to compare the radial correlation lengths of turbulence given by the phase signal $L_{r\phi}$ and the power signal L_{rP} . $L_{r\phi}$ is the value measured by heterodyne detection systems while L_{rP} is indicative of homodyne system results [6].

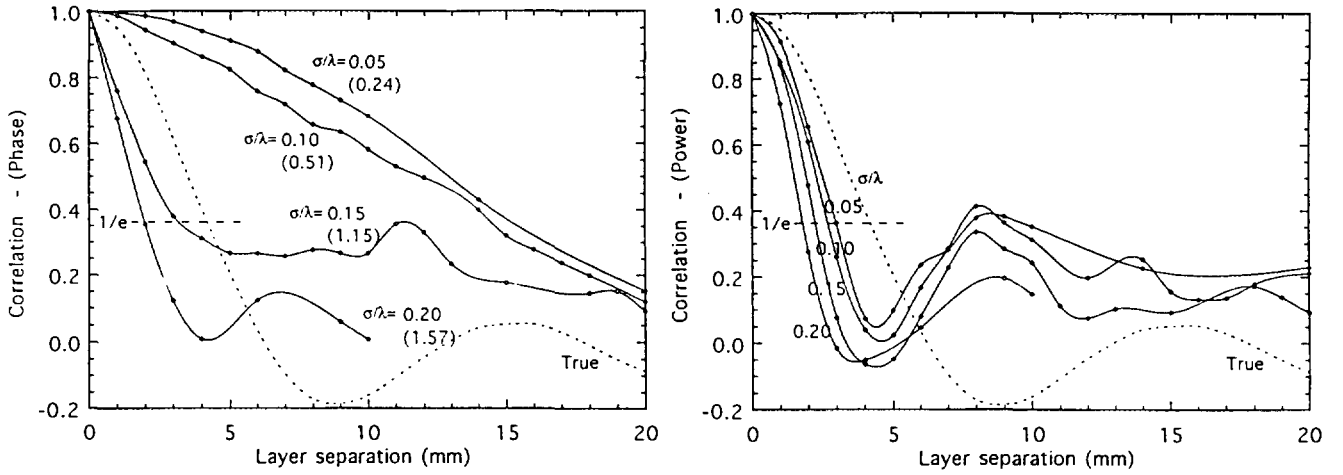


Figure 5: Simulation: Comparison of cross correlation coefficients vs radial separation from phase fluctuations (left) and power fluctuations (right) for increasing turbulence rms amplitude σ/λ . The dotted line is the true correlation function. $w/\lambda = 4$, $k_p/k_o = 0.35$, $k_r/k_o = 1.4$

Simulation results. $L_{r\phi}$ and L_{rP} are generally different and not equal to the true correlation length $L_{r\text{true}}$. Figure 5 shows the effect of increasing the fluctuation amplitude σ/λ on the radial cross-correlation functions from the phase fluctuations (left) and the power fluctuations (right).

(a) For phase signals, $L_{r\phi}$ depends on σ/λ , w/λ and k_w/k_o . However these parameters also change ϕ_{rms} resulting in an 'empirical' scaling relationship:

$$L_{r\text{true}} = L_{r\phi} \left(\frac{\phi_{\text{rms}}}{\phi_c} \right)^b \quad \text{where } \phi_c \approx \pi/3 \text{ and } b \approx \sqrt{3}. \quad (3)$$

(b) For power and homodyne signals, L_{rP} only depends only slightly on σ/λ . The scale factor S ranges from $\sqrt{2}$ for small σ/λ (5%) to 2 for large σ/λ (>20%).

$$L_{r\text{true}} = L_{rP} \times S \quad (4)$$

Experimental results. Figure 6 shows contour plots of coherence spectra $\gamma^2(f)$ and time histories of $\bar{\gamma}^2$ for phase and power signals from the 92 GHz JET radial correlation reflectometer with a constant layer separation of $\Delta r \approx 2.5$ mm. In this ELMy H-mode the background coherence is generally low, except for two bursts of coherent activity around 59.02 and 59.06 seconds. Assuming Gaussian turbulence the radial correlation length is given by: $L_r = \Delta r(1 - \bar{\gamma})^{-1/2}$, which gives the values shown in the figure. Applying the scaling relationships to the $L_{r\phi}$ and L_{rP} values with a measured $\phi_{\text{rms}} \approx 90^\circ$ give the corrected true correlation lengths of 10 mm and 7 mm for the two bursts.

6. Correlation profiles

The scaling laws derived above for the phase and power radial correlation lengths are also found to apply to correlation lengths for transverse separations, i.e. poloidal and toroidal correlation reflectometry with two separate microwave beams, and, to the time-delayed auto correlation functions, i.e. the phase and power auto-correlation times are different. All these effects are confirmed by experimental results. Another common feature in all correlation functions is the change in correlation profile of the phase fluctuations. For low fluctuation amplitudes $\sigma/\lambda \leq 0.1$ the phase signals have a Gaussian shape

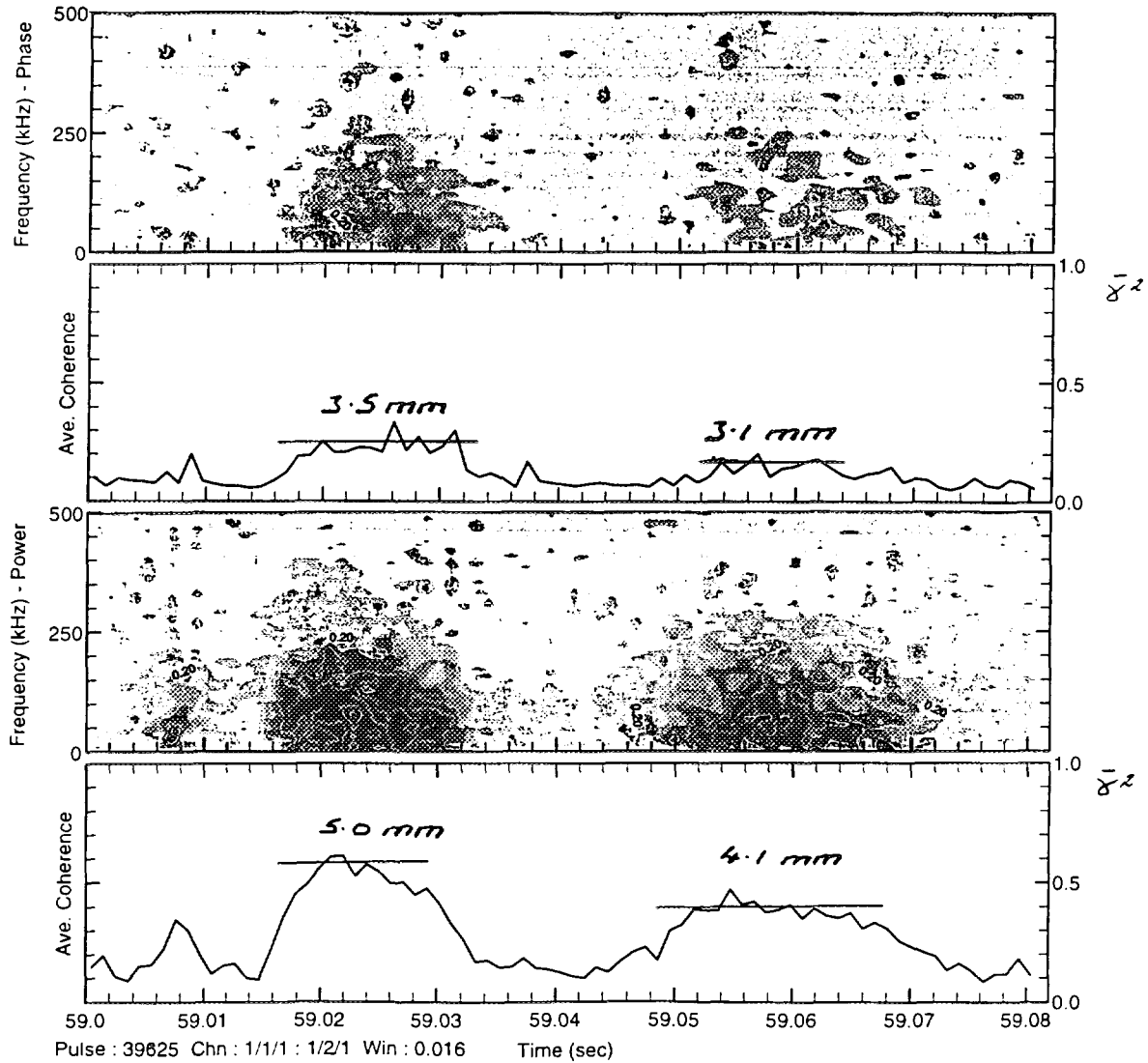


Figure 6: Experiment: Time evolution of $\gamma^2(f)$ coherence spectra for phase and power fluctuations from JET edge during two bursts of coherent mode activity (ELMy H-mode). $R = 3.7$ m, $\Delta f = 0.5$ GHz $\rightarrow \Delta r \approx 2.5$ mm.

$C(x) = \exp(-x^2/L^2)$ for the initial decay, figure 7, but this changes to Lorentzian $C(x) = \exp(-|x/L|)$ for $\sigma/\lambda > 0.12$ or for $k_w w/2\pi < 0.05$. The auto-correlation profile shape can therefore also be used as an indication of the fluctuation level.

7. Asymmetries

Asymmetry can take several forms, such as non-symmetric plasma perturbations (i.e. sawtooth structures, rotating islands, etc.) or from antenna mis-alignments. Experimentally it is very difficult to maintain perfect symmetry between the plasma reflection layer and the antenna beams - that is a normally incident, and hence normally reflected beam in a single antenna (monostatic) system, or symmetric incident and reflected angles (relative to the layer) in a dual antenna (bistatic) system. For instance tilting of the reflection layer by just a few degrees from an initially symmetric system introduces a range of new effects, many of which are interrelated.

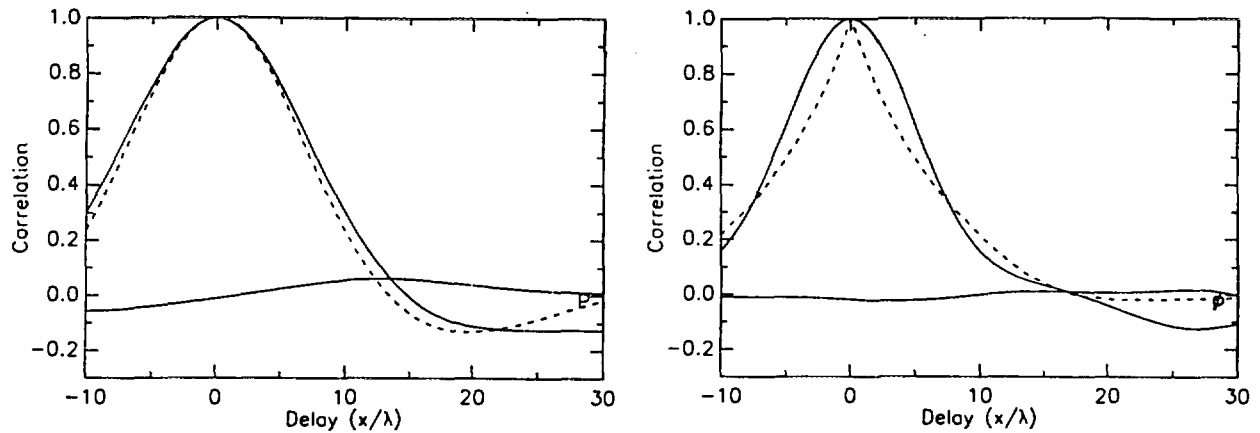


Figure 7: Simulation: Auto correlation functions of phase (dotted) and power (solid) fluctuations for $\sigma/\lambda = 0.05$ (left) and $\sigma/\lambda = 0.20$ (right). Normal incidence.

Simulation results. Extensive simulations with various asymmetries have been performed [8]. The following is just a brief summary of the more prominent features which appear with tilting the plasma reflection layer by an angle θ :

- (a) For coherent modes, phase run-away occurs when the fluctuation amplitude exceeds a critical value. This value varies with the tilt or mis-alignment angle θ and the fluctuation wavelength. Figure 8 shows phase run-away occurring for $h/\lambda > 0.12$ with a θ of only 2.5° .
- (b) The long wavelength Λ sensitivity is lost with increasing θ .
- (c) The phase shift ϕ no longer follows the surface but becomes distorted. This is evident in figure 8 as the perturbation moves through one period.
- (d) At large Λ/λ the reflected power is strongly modulated at the perturbation frequency.
- (e) Certain wavelength bands (centred on wavelengths given by $\Lambda/\lambda = m/(2 \sin \theta)$) give enhanced Bragg backscatter. Typically the mean power is a constant -6dB irrespective of the beam width.

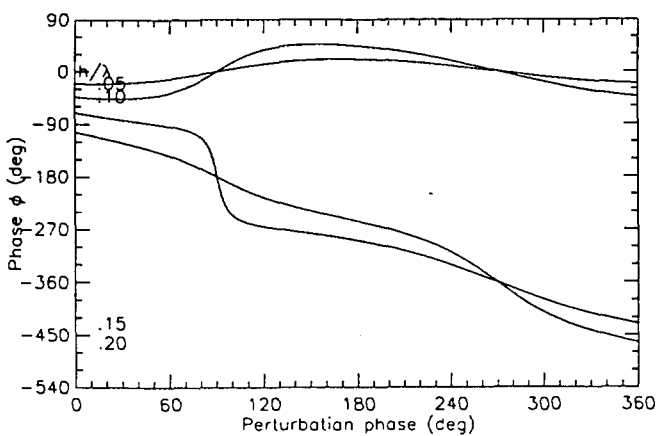


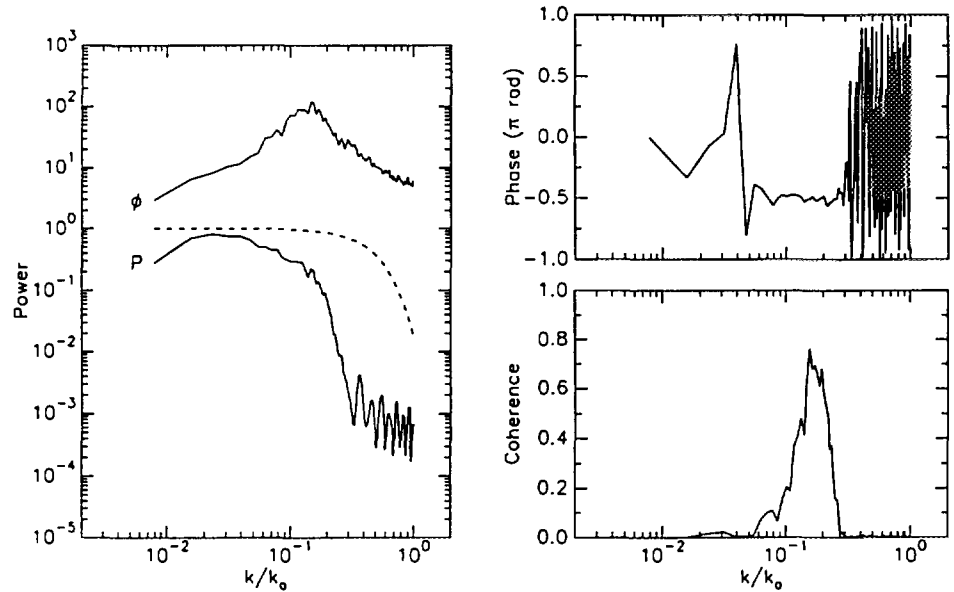
Figure 8: Simulation: Phase run-away occurring with a 2.5° tilt in mean plasma surface when the coherent mode amplitude h/λ exceeds 0.12, $w/\lambda = 2$, $\Lambda/\lambda = 5$.

- (f) For broadband turbulence, mis-alignment introduces a Doppler shifted spectral peak $f_D = 2f_0 v/c \sin \theta$ (the equivalent of phase run-away), figure 9.
- (g) Both the phase ϕ_{rms} and power P_{rms}/P_0 increase non-linearly with increasing θ , i.e. the signal

becomes more incoherent.

(h) $\tilde{\phi}$ and \tilde{P} are correlated (sometimes very strongly) over selected frequency bands (Bragg backscatter).

Figure 9: Simulation: Doppler shift in turbulence spectra with incident angle $\theta_1 = 0^\circ$ and scattered angle $\theta_2 = 8^\circ$. Note the strong coherence between phase and power fluctuations and relative phase shift of $\pi/2$. The dashed line is the input k-spectrum.



Experimental results. Data from the JET correlation reflectometer exhibits all of the above features at various times. Figure for example shows the $\gamma^2(f)$ coherence spectrum between $\tilde{\phi}$ and \tilde{P} from a single 75 GHz reflectometer channel around the plasma separatrix during an NBI H-mode. It shows a broad coherence from 50 to 200 kHz. With a tilt angle of only 2° the Doppler shift gives a propagation velocity in excess of 4 km/s. Asymmetries are more usually evident as differences in fluctuation levels between the adjacent toroidal reflectometer channels, such as the extreme case shown in figure for the 75 GHz reflectometer. The phase fluctuations of channel 2 are tiny compared to channel 1, yet the power signal still follows the low frequency oscillation. Note how in channel 1 when the phase rms goes up the mean power goes down. The discrepancies are consistent with an asymmetry of around 2 to 5° .

8. Conclusions

Several models for fluctuation reflectometry have been investigated, but as shown above, the physical optics model provides the first comprehensive explanation of a wide range of fluctuation effects. In fact all fluctuation phenomena observed with the JET correlation reflectometers can be explained and interpreted by the physical optics model. Of course for the JET diagnostic, the short microwave wavelengths, small antennas and large plasma distances make the far-field formulation appropriate. However smaller machines and divertor diagnostics may require near-field solutions - which may reveal new effects.

Acknowledgements

Thanks to J Howard, D V Bartlett, A Costley for stimulating discussions during the development of the model, and on the interpretation of experimental data. The JET data was obtained with the assistance of the members of the JET Task Forces during the 1996 experimental campaign.

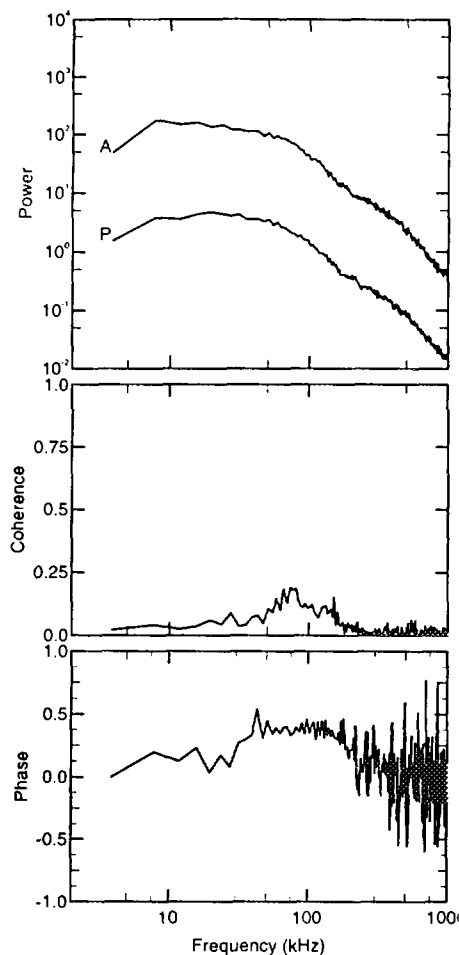
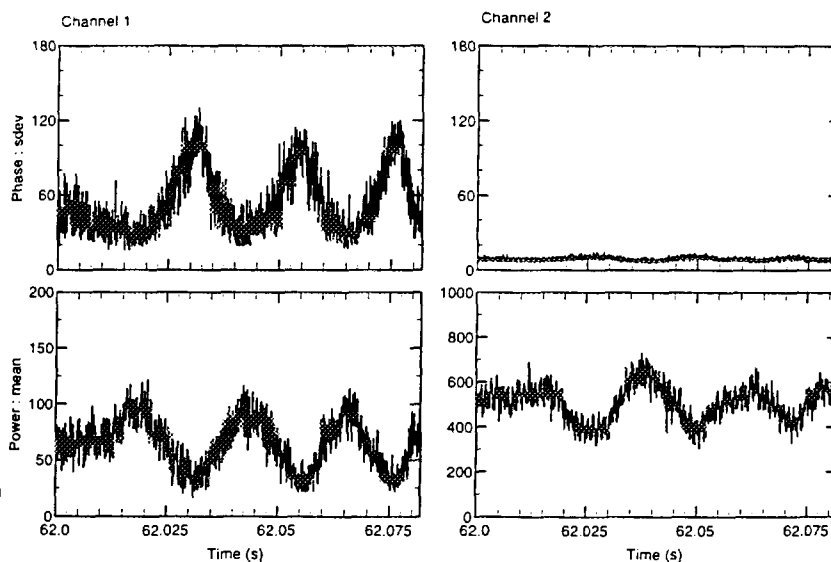


Figure 10: Experiment: $\gamma^2(f)$ coherence and cross-phase spectra between phase and power fluctuations from JET edge. No evident peaks in power spectra but note coherence from 50 to 200 kHz and $\pi/2$ phase difference. $\phi_{\text{rms}} = 17.3^\circ$, $P_{\text{rms}}/P_o = 0.51$

Figure 11: Experiment: Raw signals of rms phase and mean reflected power from two adjacent toroidal reflectometer channels showing evidence of asymmetries in antenna alignment.



References

- [1] Irby J H and Stek P, *Rev. Sci. Instrum.* **61** 3052 (1990)
- [2] Conway G D *et al*, 'Observations on Bragg backscatter from rippled surfaces via reflectometry.' *Bull. Am. Phys. Soc.* **37** 1453 (1992)
- [3] Conway G D, *Rev. Sci. Instrum.* **64** 2782 (1993)
- [4] Conway G D, Schott L and Hirose A, *Plasma Phys. Control. Fusion* **38** 451 (1996)
- [5] Conway G D, Schott L and Hirose A, *Rev. Sci. Instrum.* **67** 3861 (1996)
- [6] Conway G D, *Plasma Phys. Control. Fusion* **39** 407 (1997)
- [7] Conway G D, Vayakis G and Bartlett D V, 'Reflectometer fluctuation and correlation studies on JET.' 3rd Intl. Reflectometer Workshop, Madrid (1997)
- [8] Conway G D, 'Effects of asymmetries on reflectometer fluctuation measurements', To be submitted to: *Plasma Phys. Control. Fusion* (1997)

**NEXT PAGE(S)
left BLANK**

Simulations of correlation reflectometry with a WKB 2-dim code

T. Estrada, J. Sánchez, V. Zhuravlev, M. Francés, B. Brañas and E. de la Luna

Asociación Euratom-CIEMAT, 28040 Madrid, Spain.

Abstract

A two dimensional code [1] based on the WKB approximation is used to analyze the feasibility of reflectometry correlation measurements in a turbulent plasma.

Simulation results have been obtained for two fixed frequency beams reflecting simultaneously on a rotating turbulent structure in a plasma with ITER parameters. The results show that correlation measurements using the reflectometry signals provides information on radial correlation lengths of the turbulence only in cases in which the 2-dim effects are weak.

In addition to the use of these studies for turbulence analysis, the correlation measurements can be used as a robust method for the determination of the signal time delay and therefore of the density profile in highly turbulent plasmas with parasitic reflections.

Introduction

The knowledge of the turbulence structure is critical for modelling of reflectometry measurements because of the strong dependence of the results on the parameters of turbulence: amplitude, dominant wavelengths and correlation lengths. The spatial correlation of the reflectometry signals may be used to obtain information about these parameters, but there are still some difficulties in the interpretation of these type of measurements. In this work the possibilities of correlation reflectometry for turbulence studies are considered.

The reflecting layer for microwave frequencies in fusion plasmas shows a complex corrugated structure which can lead to destructive interference in the reflectometer beam, inducing intense amplitude oscillations and random-like phase behaviour. To simulate the plasma turbulence a combination of a two dimensional unperturbed density distribution with a set of interchanging hills and depressions has been considered. The hills and depressions amplitude and the distance between them change randomly within $\pm 50\%$ of the average values which define the amplitude, \tilde{n}/n , and wavelength, λ , of the turbulence. The average poloidal and radial wavelengths are equal. To ensure the applicability of the WKB approximation the ratio between the average wavelength of the turbulence and the vacuum wavelength of the probing beam is larger than four.

Simulations are done considering two incident frequencies reflecting simultaneously on a rotating turbulent structure for different values of \tilde{n}/n and λ_θ : from weak to strong interference

effects. The distance between the two cut-off layers is varied within the radial correlation length of the density fluctuations.

Simulation of correlation measurements

Simulation results compare cases with different perturbation parameters, average fluctuation level and poloidal wavelength, for a plasma with ITER parameters ($R=8.14$ m, $a=2.8$ m with $n(0)=5 \cdot 10^{14} \text{cm}^{-3}$). The dominant poloidal wavelength is varied between 1 and 6 cm and the relative density fluctuation level between 4 and 16 %, for a perturbation with a radial correlation length close to 1 cm. The beam size at the reflection layer is of the order of 2-3 cm and the incident frequencies are 75-77 GHz with o-mode propagation.

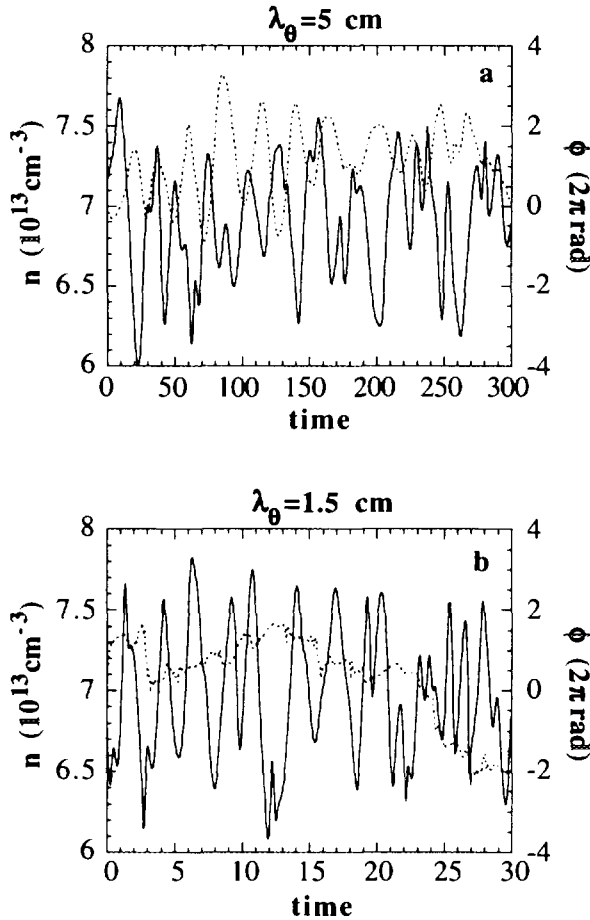


Fig. 1.- Time evolution of the phase (broken line) and density at the cut-off layer (solid line) for perturbations with $\bar{n}/n=8$ % and $\lambda_\theta=5$ cm (1a) and $\lambda_\theta=1.5$ cm (1b).

In the cases of long poloidal wavelengths (longer than the beam size) and low fluctuation levels, 2-dim effects are very weak and the phase fluctuations are similar to the density fluctuations. For shorter poloidal wavelengths and higher fluctuation levels, interference effects become stronger: simultaneous reflection from different poloidal points takes place and the phase variations do not follow the density fluctuations. In Fig. 1 the time evolution of the density at the reflecting layer and the phase are displayed for two cases with the same fluctuation level ($\bar{n}/n=8$ %) and different dominant wavelength: $\lambda_\theta=5$ cm (Fig.1a) and $\lambda_\theta=1.5$ cm (Fig.1b), corresponding to low and high destructive interference respectively.

The radial correlation of the phase is comparable to the radial correlation of the density in the cases of weak 2-dim effects but it drops faster than that as the interference effects become stronger. Fig. 2 displays the comparison between weak and strong 2-dim

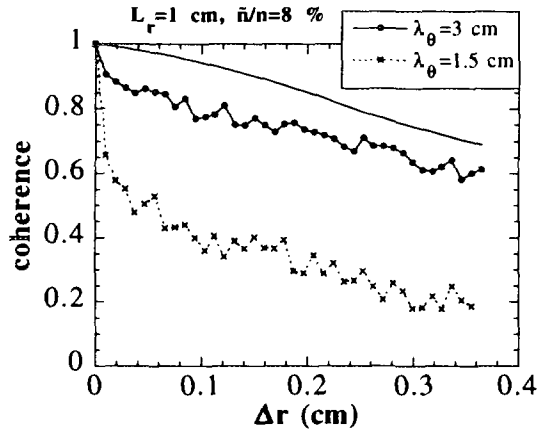


Fig. 2.- Radial correlation of the phase fluctuations for two cases with $\lambda_\theta=3$ and 1.5 cm ($\bar{n}/n=8\%$). Solid line: radial correlation of the density ($L_r=1$ cm).

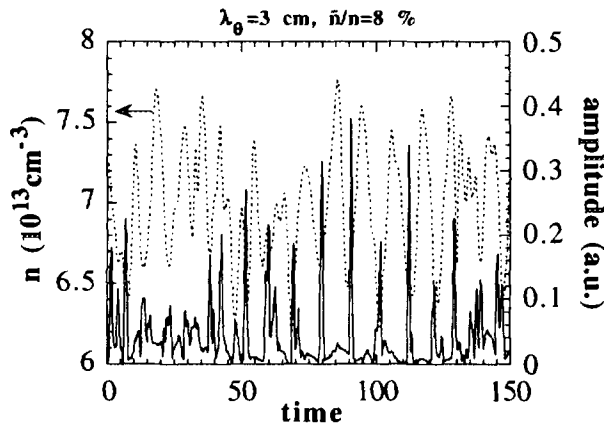


Fig. 3.- Time evolution of the density at the cut-off layer (broken line) and the amplitude of the reflected signal (solid line) for $\lambda_\theta=3$ cm and $\bar{n}/n=8\%$.

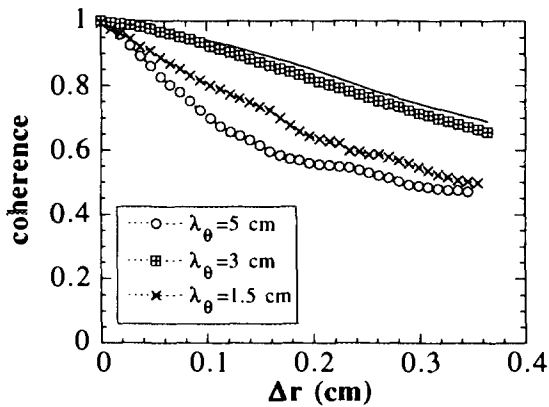


Fig. 4 Radial correlation of the amplitude for different perturbation wavelengths.

effects. The radial correlation length of the phase is much shorter than the real one in the short average wavelength case. As a consequence considering the phase signals big errors should appear in the radial correlation length determination.

The radial correlation of the amplitude of the reflected signals is very close to the radial correlation of the density fluctuations when the averaged poloidal wavelength and the beam size are of the same order. Under these conditions the poloidal structure of the cut-off layer acts like a lens: focusing the reflected beam when the layer has a concave shape and vice versa. As a result the amplitude of the reflected signal presents maxima associated with the minima in the density fluctuations during the poloidal rotation. Fig. 3 shows the time evolution of the density at the cut-off layer and the amplitude of the reflected signal for a perturbation with $\lambda_\theta=3$ cm and $\bar{n}/n=8\%$.

The behaviour of the amplitude is different when the averaged poloidal wavelength is shorter or longer than the beam size. For longer wavelengths the amplitude in average is higher and is almost independent of the density oscillations and for shorter wavelengths the amplitude falls due to destructive interference effects. In both cases the radial correlation of the amplitude drops faster than the radial correlation of the density. In Fig. 4 the radial correlation of the amplitude for the data of Fig. 3 is displayed together with the ones obtained for average wavelengths equal to 5 and 1.5 cm (in both cases: $\bar{n}/n=8\%$).

To properly measure the radial correlation with a homodyne detection reflectometer one of the frequencies has to be swept around the other one which is fixed. According to the 2-dim simulation the correlation of the homodyne signals shows a maxima-minima structure as the incident frequency is swept, being the maxima a good approach to the true values.

The simulations shows that the radial correlation measured with the homodyne signals is closer to the correlation of the density than the correlation of the phase in cases of high destructive interference.

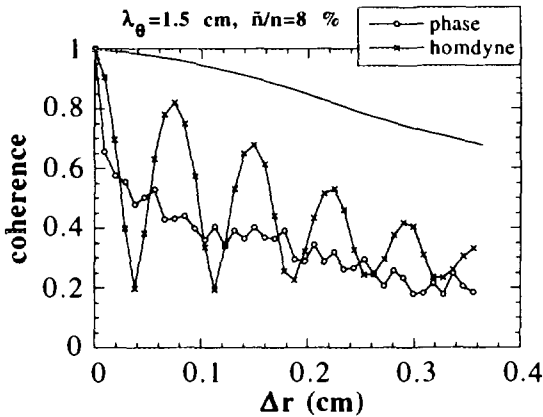


Fig. 5.- Radial correlation of the phase and homodyne signals for $\lambda_\theta=1.5$ cm and $\bar{n}/n=8$ %.

distance between consecutive maxima corresponds to increments of π in the phase offset of the reflectometer as the incident frequency is swept, thus, the time delay can be derived. Even in the cases of strong 2-dim effects, in which the maxima in the correlation of the homodyne signal are lower than the density correlation, this time delay is in very good agreement with the

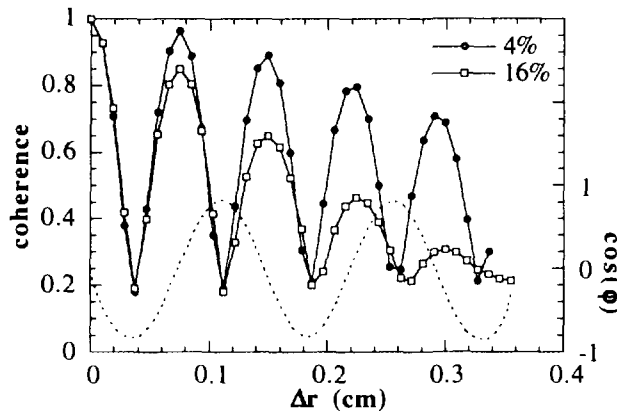


Fig. 6.- Correlation of the homodyne signals for $\bar{n}/n=4$ and 16 % ($\lambda=3$ cm) and phase delay from the unperturbed density profile (broken line)

time delay obtained from the unperturbed density profile. As an example two cases with the same average poloidal wavelength (3 cm) and different fluctuation level (4 and 16 %) are displayed in Fig. 6 together with the \cos of the phase delay of the unperturbed density profile.

The results presented up to now have been obtained considering the horn axis direction perpendicular to the reflecting layer. To study how they are modified in oblique reflection conditions we have tilted the angle of the antennas up to 15° . Phase

runaway appears being proportional to the tilted angle and making senseless the phase correlation results. Interference effects become stronger, as a consequence, the radial correlation of the reflectometry (amplitude and homodyne) signals decrease. To illustrate this effect we have

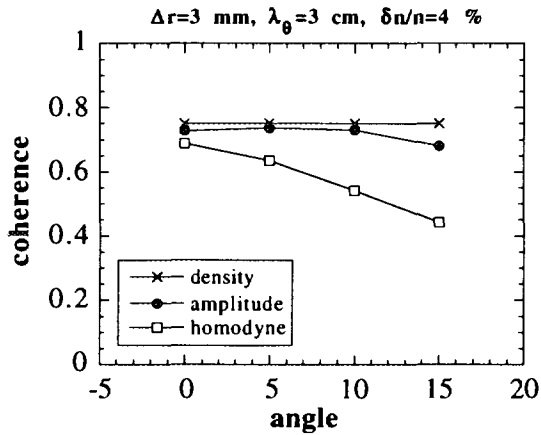


Fig. 7.- Correlation of the amplitude and homodyne signal (for two reflecting layers separated 3 mm) vs. the tilted angle of the antennas ($\lambda_\theta=3$ cm, $\tilde{n}/n=4$ %).

chosen a case in which for perpendicular reflection the radial correlation of the reflectometry signals reproduces the radial correlation of the density: low fluctuation level ($\tilde{n}/n=4$ %) and poloidal wavelength close to the beam size ($\lambda_\theta=3$ cm). Fig. 7 shows the correlation of the density, amplitude and homodyne signal (for two reflecting layers separated 3 mm in radial direction) as a function of the angle of tilting. The drop in the correlation as the tilted angle is increased is more pronounced in the homodyne signal than in the amplitude. A similar result is obtained with

perpendicular reflection for a fixed poloidal wavelength as the fluctuation level increases.

Conclusions

The 2-dim WKB code, able to compute interference effects, was used for qualitative investigation of the perturbations in reflectometry measurements induced by turbulence. Correlation measurements using the reflectometry phase signal may provide a useful tool to obtain information on radial correlation lengths of the turbulence only in cases in which the 2-dim effects are weak. In these cases and for average wavelengths similar to the beam size the correlation length of the amplitude signal also agrees with the correlation length of the density. The time delay deduced from the radial correlation of the homodyne signal is in very good agreement with the time delay obtained from the unperturbed density profile in all the conditions which have been studied. This kind of measurements can be used to obtain the density profile in turbulent plasmas with parasitic reflections due to poor access and complicated waveguides.

References

- [1] V. Zhuravlev, J. Sánchez, E. de la Luna. Plasma Phys and Control. Fusion **38** 2231 (1996).
- [2] J. Sánchez, B. Brañas, E. de la Luna and T. Estrada. Rev. Sci. Instrum. **64** (2) 487 (1993).

NEXT PAGE(S)
left BLANK

New Data Processing Techniques for Profile Evaluation from Broadband FM Reflectometry

J. Santos, M. Manso, F. Nunes, I. Nunes, A. Silva, P. Varela

Associação EURATOM/IST, CFN, Instituto Superior Técnico - 1096 Lisboa Codex

**MPI fuer Plasmaphysik, EURATOM Association, D-85748 Garching, Germany*

1. INTRODUCTION

Broadband FM reflectometry is used to obtain the plasma density profile. The profile is evaluated from the measured beat frequency (f_B) of the interference between a reference signal and the signal reflected from the plasma. Plasma fluctuations cause phase and amplitude perturbations in the reflected signal making the profile evaluation a difficult problem to solve. Different techniques have been developed to minimise this problem, namely AM [1], dual differential-phase reflectometry [2] and pulse radar [3]. In addition, very fast sweeping times ($\leq 10\mu\text{s}$) are presently being used to probe the plasma in time intervals shorter than the typical periods of plasma fluctuations, resulting in a significant decrease of the “noise” due to temporal fluctuations. In software, several data analysis methods have been implemented, including either digital filtering [4, 5] or spectral peak tracking using sliding Fast Fourier Transform algorithms [6] and the Maximum Entropy Method (MEM) [7].

Here we present a method based on the estimation of the power time-frequency distribution (TFD) of the reflectometry signals, that gives both the main beat frequency due to the average profile and the local energy scattered by plasma fluctuations.

The method was applied to O-mode broadband reflectometry signals obtained in ASDEX Upgrade. The reflectometry system probes the plasma in the density range of $n_e=0.4-6.5 \times 10^{19} \text{ m}^{-3}$, with very fast ($10-100\mu\text{s}$) simultaneous operation of several channels, both at the high and low field sides [8]. Here we present results from the high field side (HFS), during the H mode phase of shot #8180, obtained with four reflectometer channels covering the total frequency range 16-72 GHz.

2. METHOD OF ANALYSIS

2.1 Time-frequency distributions

The standard Fourier analysis allows us to separate a signal into its individual frequency components and establish the relative intensity of each component. Unfortunately, using the power spectrum, it is not possible to know when those frequencies occurred. To circumvent such limitations a joint function of time and frequency, i.e., a distribution is often employed. This mathematically more sophisticated approach is capable of higher resolution for a given length of data. In fact, no time-

frequency distribution can describe exactly the localised time-frequency energy density [9]. However, good approximations are obtained by selecting a suitable TFD, $P(t,f)$, according to the signal to be analysed.

The periodogram, the squared modulus of the Short-Time Fourier Transform (STFT), is the simplest form of $P(t,f)$. Its use, however, assumes the local quasistationary of the signal $s(t)$. When this condition cannot be fulfilled other TFDs (such as the Wigner-Ville Distribution) are better suited for these cases. These more sophisticated distributions may be useful to resolve very fast local changes of density, but as they are computationally quite complex we will investigate them only after we achieve a good understanding of the potentialities and limitations of the simplest distributions.

2.2 FFT and MEM estimators

In this study we used two spectral estimators: the Fast Fourier Transform (FFT) and the Maximum Entropy Method (MEM). These estimators require, as discussed above, that the signal is locally quasistationary.

In the FFT analysis the signal, considered as periodic, is decomposed into its sinusoidal Fourier series. MEM assumes that the signal is generated by an Autoregressive (AR) process and tries to model its transfer function. In the former case we have a spectral estimation problem, whilst in the latter we have a typical parameter estimation. The model must be an accurate representation of the random process, at least as far as the Power Spectral Density (PSD) is concerned. If this is the case, the resulting spectral estimator will be less biased (higher resolution) and will exhibit lower variance. The TFDs of Fig. 2.2.1 were obtained for a K Band signal [16-24.3 GHz] using FFT and MEM estimators. The PSD plots of a time window centred at $F_p=20.7$ GHz are compared, for both cases, in Fig. 2.2.2, where we can observe MEM's higher resolution.

It should be noted that while the FFT is a fairly straightforward method, MEM requires a careful choice of the parameters adequate to the particular characteristics of the signals under analysis.

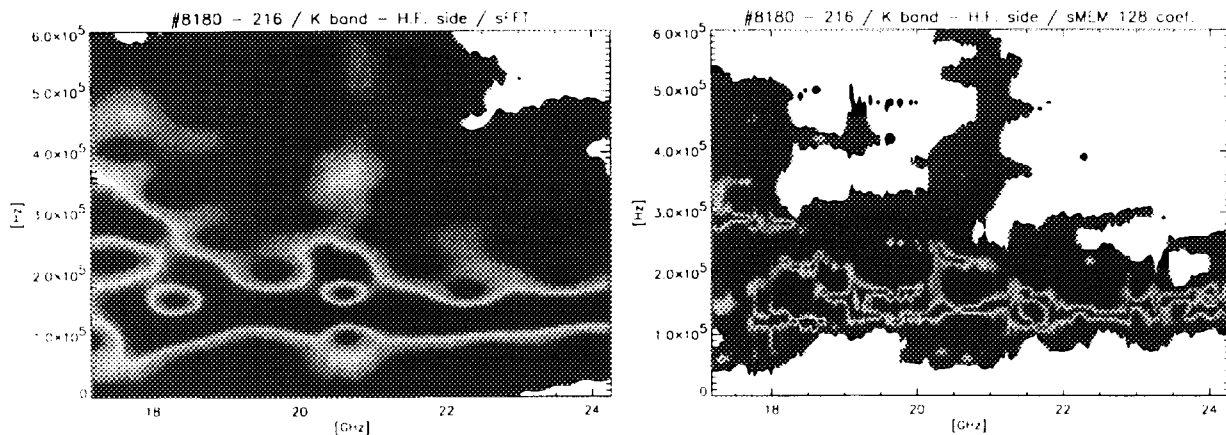


Figure 2.2.1

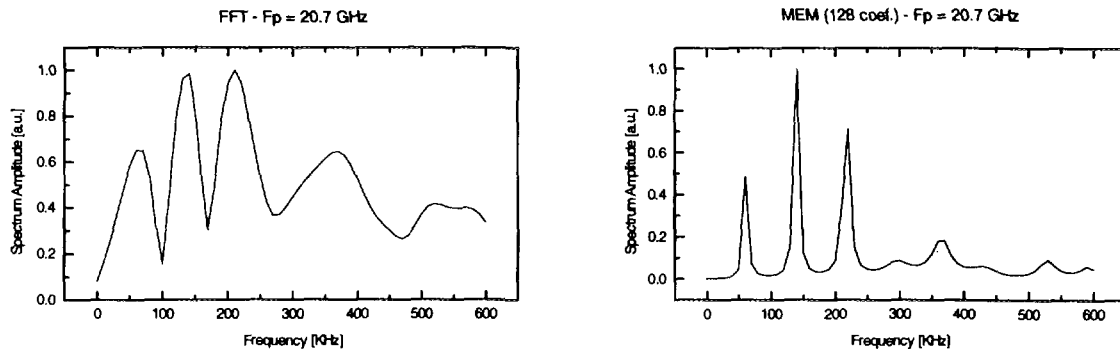


Figure 2.2.2

2.3 TFD average frequency

One way of estimating automatically the beat frequency evolution, needed for profile inversion, is to calculate the first moment of the TFD. This average frequency curve is calculated using the following expression:

$$\hat{f}_B(t) = \frac{\int_{-\infty}^{+\infty} f P(t, f) df}{\int_{-\infty}^{+\infty} P(t, f) df}$$

In Fig. 2.3.1 (a) is shown the periodogram of a Ka Band signal [25-36 GHz], and in (b) the f_B and the maximum spectral peak curves of the periodogram. The former curve averages the effects of the signal perturbations, this effect being particularly evident in the neighbourhood of $F_p = 31$ GHz, where it takes into account the spectral components of the perturbations at ≈ 100 KHz (Fig. 2.3.1 (a)), whilst the maximum peak curve ignores them.

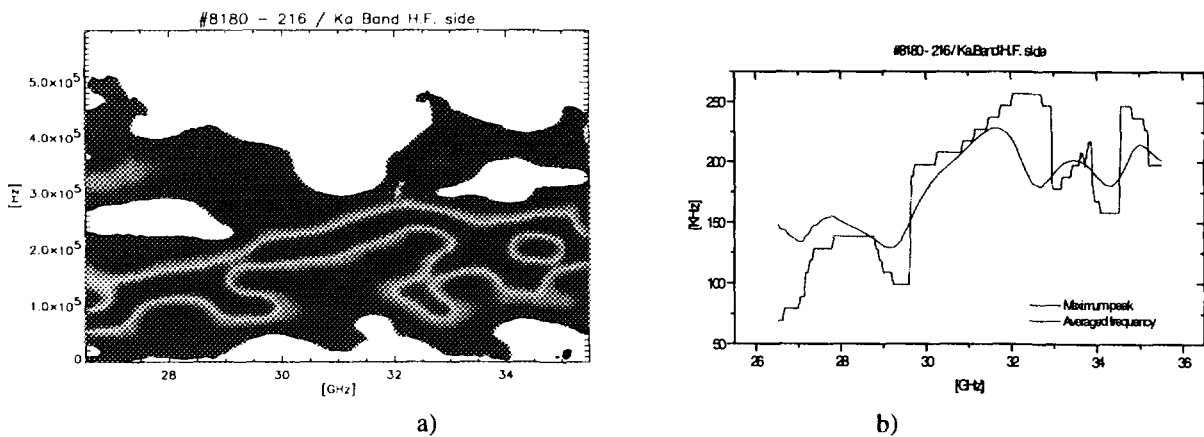


Figure 2.3.1

3. PARAMETER ADJUSTEMENT

There are two main parameters to set when using sliding window based TFDs. The first one is the window size and the second the degree of overlap between consecutive windows. For MEM an additional parameter has to be set: the number of coefficients.

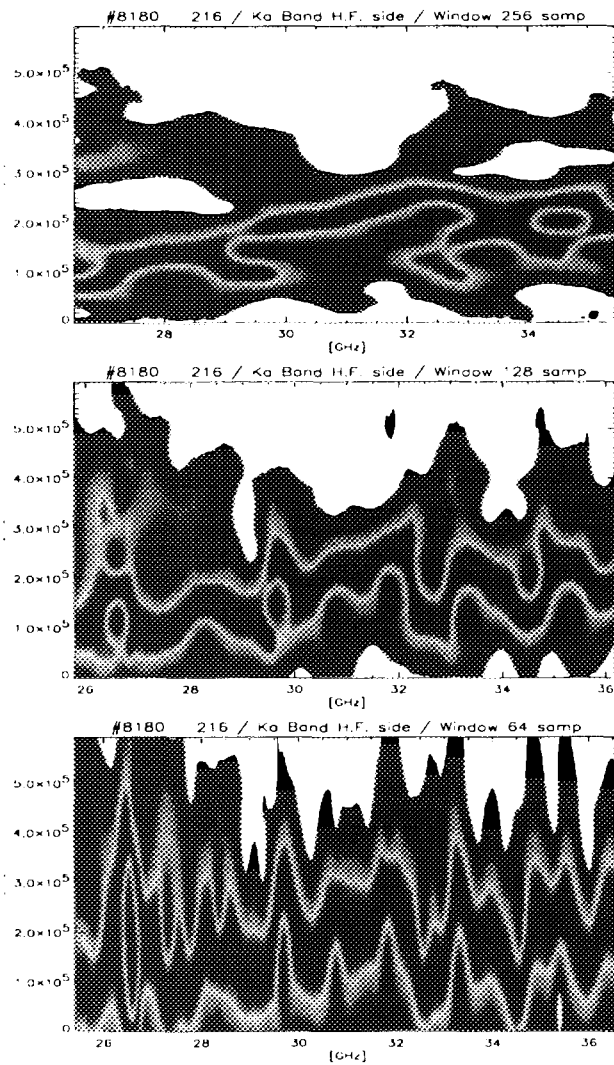


Figure 3.1.1

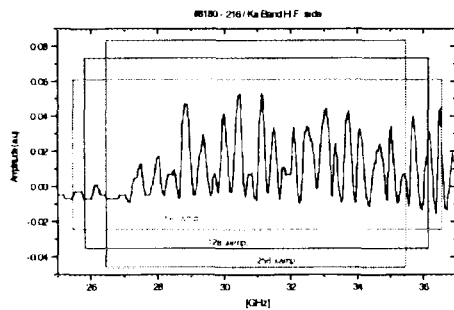


Figure 3.1.2

3.1 Window size

The window size depends directly on the signals to be analysed. Longer windows capture the changes that the signal might endure, weighting more the stronger frequency components during that time period. On the other hand, shorter windows will increase the probability of analysing the signal in locally stationary periods. Figure 3.1.1 shows the result of using different window sizes (256, 128 and 64 samples) to estimate the spectral evolution of the reflectometry signal. In Fig. 3.1.2 is shown the raw data signal used to generate the previous TFDs. The window size is directly related to the length in time (probing frequency) of the calculated TFD. Superimposed in the graphic are the resulting TFD ranges that correspond to the three window sizes. The size of the windows determines the detail of the beat frequency versus time estimation. Long windows tend to smooth the details of f_B and if the size of the window tends to a dirac pulse the resulting spectral estimation will tend to the instantaneous frequency [9]. The final choice should be determined by the physical process under study.

3.2 Overlap factor

With the overlap factor we control the amount of samples that the sliding windows will overlap in consecutive spectral estimations. For time varying signals the overlap factor has to be adjusted in order to track the changes of the local spectral content. In Fig. 3.2.1 is shown that an increasing overlap factor applied to a K band reflectometry signal results in an increased detail, as expected. The calculated TFDs present greater detail if an increasing overlap factor is used. The resulting f_B history

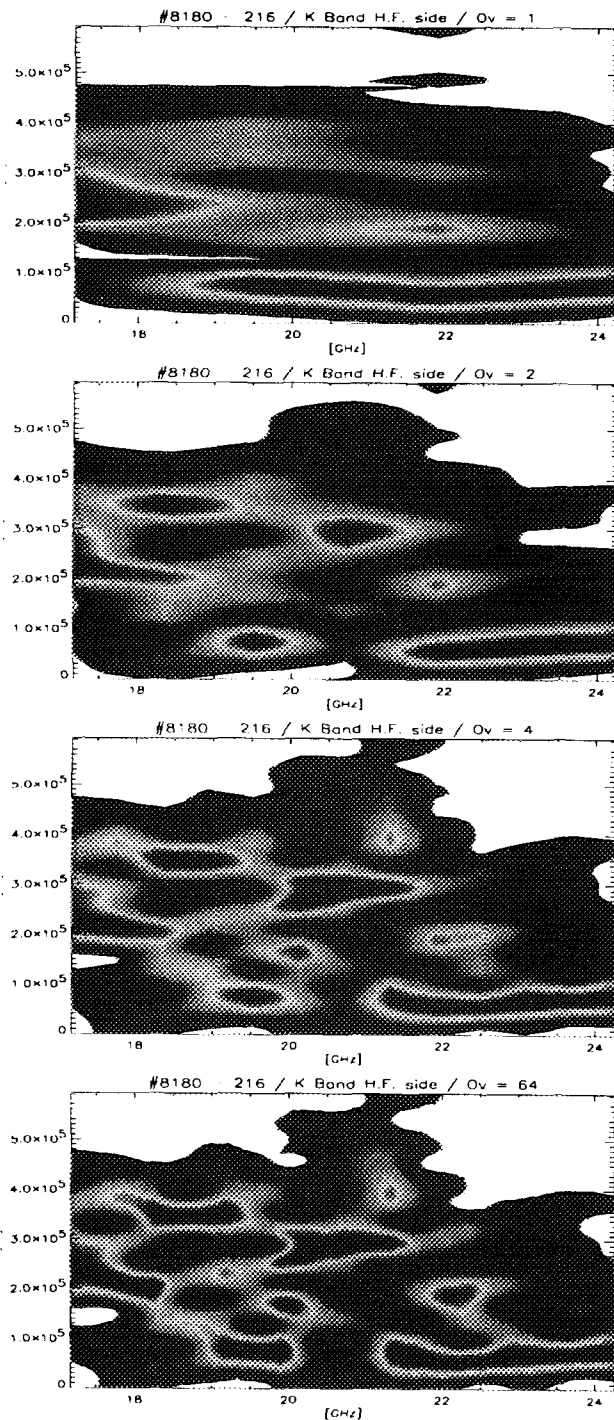


Figure 3.2.1

obtained from the first moment of the TFD (Fig. 3.2.2) reveals that the variations observed between 19.5 and 22.5 GHz cannot be detected without overlapping, ($Ov=1$), and are better resolved for the highest overlap factor ($Ov=64$).

3.3 Choice of MEM coefficients

One of the difficulties of using parametric spectral estimators like MEM is to select the right number of coefficients. In order to model a signal with N sharp spectral peaks the AR model must have at least $2N$ poles. Decreasing the number of coefficients will produce an averaging of neighbouring spectral peaks, whereas an excessive number of coefficients will result in a noisy spectrum with many spurious peaks. Figure 3.3.1 shows the TFDs of the K band signal, calculated with the FFT and with MEM with $k=32, 64, 128$ and 200 coefficients. Using the FFT time-frequency distribution of Fig. 3.3.1 as a reference, we observe that with $k=32$, the spectral peaks around 17.5 and 20.5 GHz are averaged. With 64 coefficients the TFD is very close to the FFT result and for $k=128$ and 200 an increasing number of spurious peaks appear. In Fig. 3.3.2 is shown the beat frequency evolution obtained from these MEM distributions. The noisy behaviour of these curves is particularly obvious for the case of $k=200$.

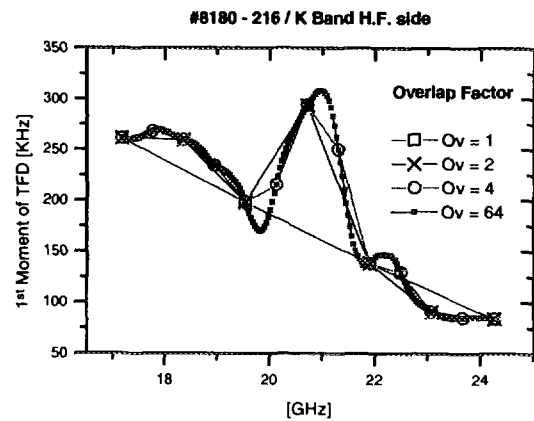


Figure 3.2.2

Figure 3.2.2

obtained from the first moment of the TFD (Fig. 3.2.2) reveals that the variations observed between 19.5 and 22.5 GHz cannot be detected without overlapping, ($Ov=1$), and are better resolved for the highest overlap factor ($Ov=64$).

3.3 Choice of MEM coefficients

One of the difficulties of using parametric spectral estimators like MEM is to select the right number of coefficients. In order to model a signal with N sharp spectral peaks the AR model must have at least $2N$ poles. Decreasing the number of coefficients will produce an averaging of neighbouring spectral peaks, whereas an excessive number of coefficients will result in a noisy spectrum with many spurious peaks. Figure 3.3.1 shows the TFDs of the K band signal, calculated with the FFT and with MEM with $k=32, 64, 128$ and 200 coefficients. Using the FFT time-frequency distribution of Fig. 3.3.1 as a reference, we observe that with $k=32$, the spectral peaks around 17.5 and 20.5 GHz are averaged. With 64 coefficients the TFD is very close to the FFT result and for $k=128$ and 200 an increasing number of spurious peaks appear. In Fig. 3.3.2 is shown the beat frequency evolution obtained from these MEM distributions. The noisy behaviour of these curves is particularly obvious for the case of $k=200$.

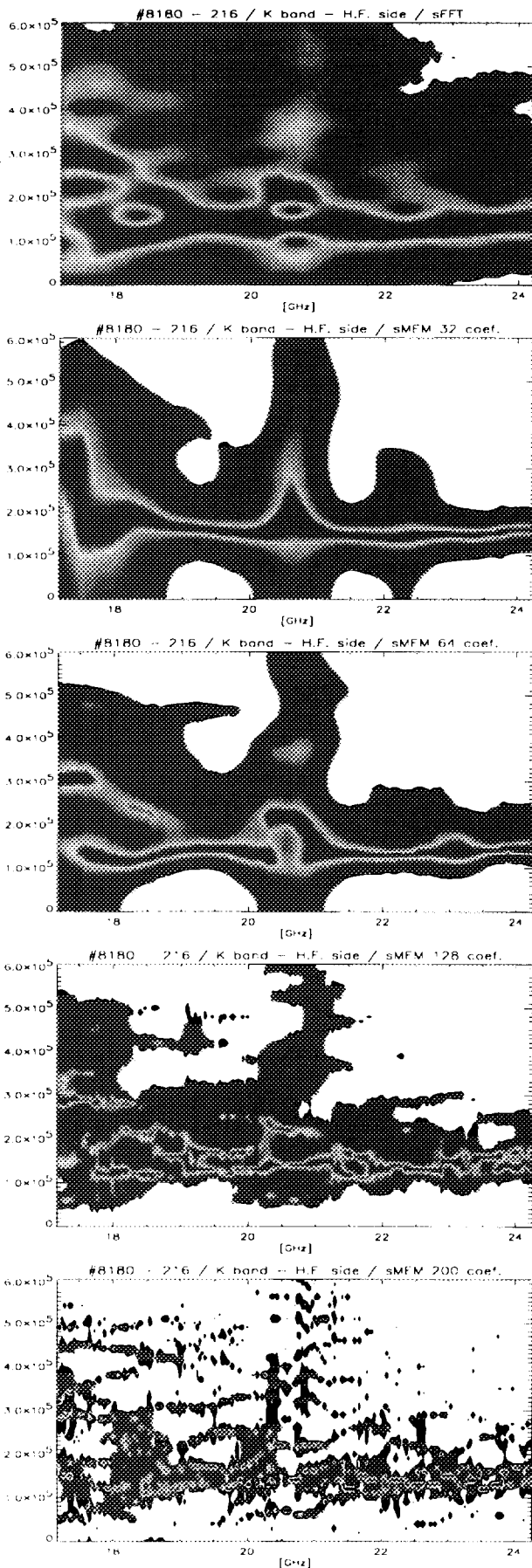


Figure 3.3.1

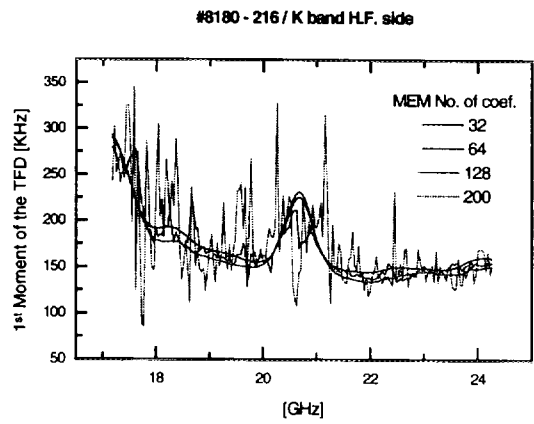


Figure 3.3.2

4. CROSSPOWER SPECTRUM

If the plasma profile does not change significantly from one sweep to the other (which is likely to occur in consecutive sweeps when the time between sweeps is very short, $\Delta t \approx 10\mu\text{s}$), the fast small perturbations of the beat frequency can be averaged by computing the cross-power spectrum. This results from the enhancement of the common characteristics of the individual power spectra and from the partial cancellation of the perturbations, that affect the sweeps differently.

In Fig. 4.1 are shown the power distributions of two consecutive samples (sweeps 216 and 217). Each distribution, containing information from K (17 -25 GHz), Ka (25 - 36 GHz), Q (36 - 50 GHz) and V band (50 - 70 GHz) reflectometers, presents similar variations of the main beat frequency (slow variation) due to the average density profile and a spread around f_B due to the plasma fluctuations. In the cross-power spectrum (Fig. 4.2) the small-scale perturbations are smoothed. In particular, the high frequency

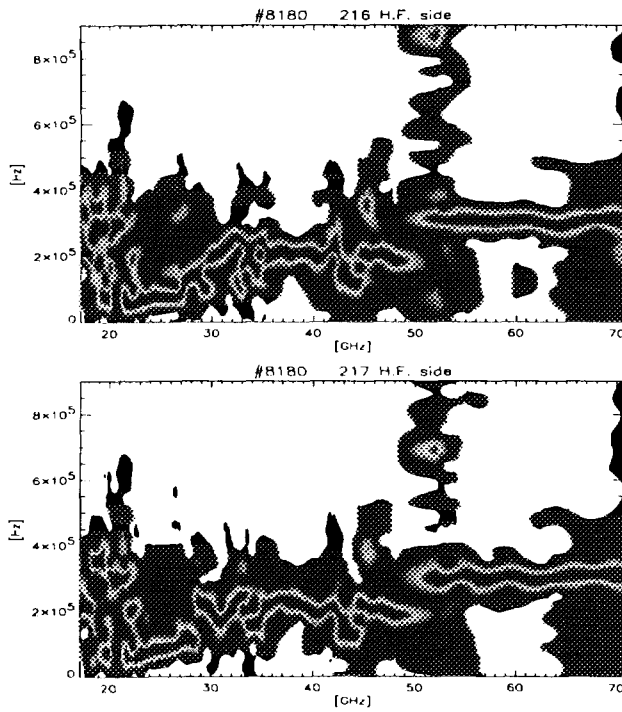


Figure 4.1

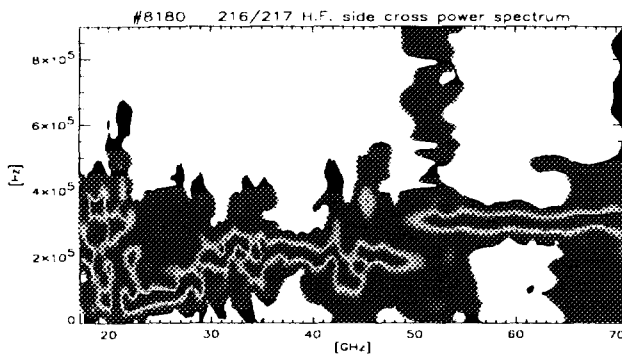


Figure 4.2

perturbation around probing frequency 54 GHz, observed in sweep 216 (at $F \approx 880$ KHz) and in sweep 217 (at $F \approx 700$ KHz), is cancelled. This has a great impact in profile evaluation because the effect of cancelling the spurious peaks at $F = 54$ GHz, and the averaging in the ranges 25-35 and 54-67 GHz, result in the smoothing of the beat frequency curve. In the plots of Fig. 4.3 the above averaging effect is more evident. This method was applied to signals that are correlated but it can also be used to enhance common characteristics of two different

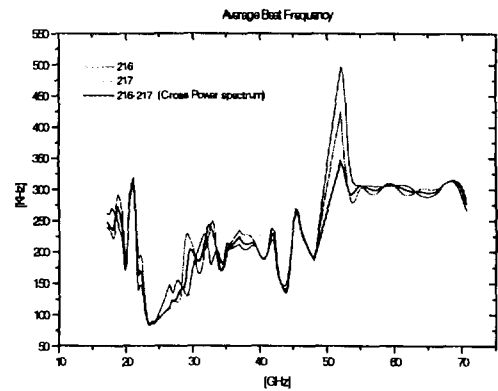


Figure 4.3

signals.

5. EVALUATION OF DENSITY PROFILES AND SPATIAL MAPPING OF PLASMA FLUCTUATIONS

5.1 Numerical results

One interesting application of the TFDs is the mapping of regions where the plasma perturbations affect the reflectometry signal. By inverting the profile we obtain the correspondence between the probing frequency F ($F \propto \sqrt{ne}$) and the location of different density layers. It is therefore possible to map the probing frequency axis into radial distance to estimate the spatial localisation of the plasma disturbed regions.

To investigate this possibility we simulated a K band Low Field Side (LFS) signal. The raw data was modulated with a perturbation, both in phase and amplitude between 18.5-21.5 GHz ($ne: 0.42 - 0.57 \times 10^{19} \text{ m}^{-3}$), Fig 5.1.1 (a). This corresponds to localise the perturbation in the simulated profile (Fig. 5.1.2) between 43.4-44.2 cm as can be seen in the spatial representation of the TFD (Fig. 5.1.1 (b))

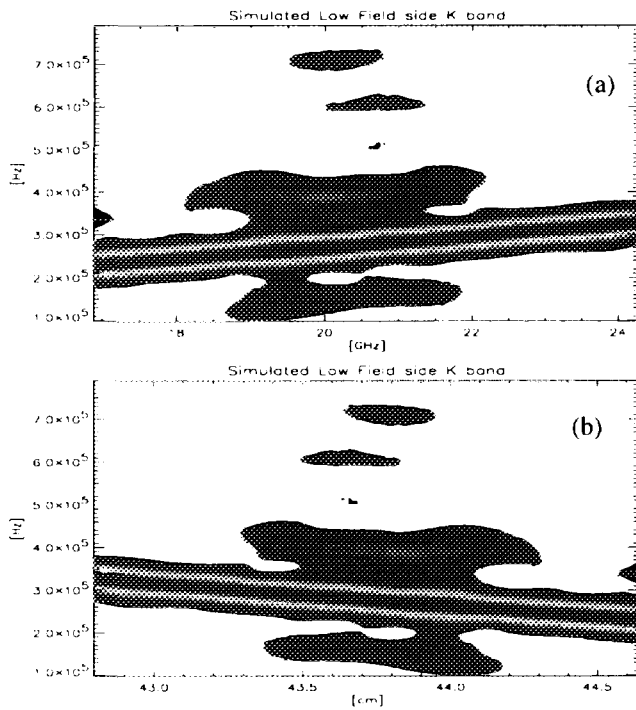


Figure 5.1.1

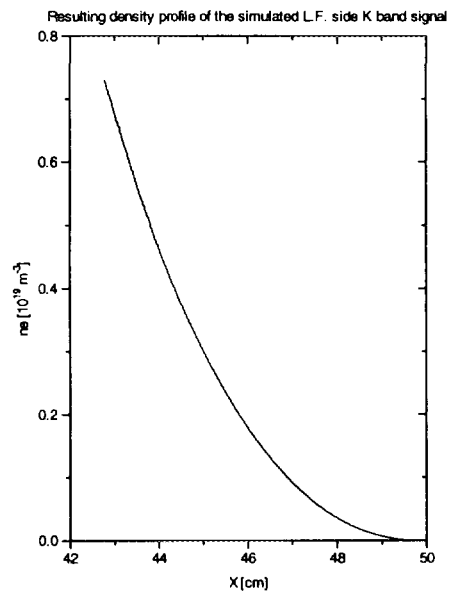


Figure 5.1.2

5.2 Experimental results

Using the same procedure to the ASDEX Upgrade reflectometry data of shot #8180, (sweep 123) we obtain the density profile from the first moment of the TFD (Fig. 5.2.1, dashed line). A moving average was applied to the profile in order to obtain the monotonically increase of distance versus density (Fig. 5.2.1, solid line) necessary to compute the spatial representation. This study showed that the perturbations in the temporal plot (Fig. 5.2.2 (a)) in frequency ranges: 17.5-21 GHz and 42-55 GHz are located (Fig. 5.2.2 (b)) between 109.7-110 cm and 113.2-115 cm. The accuracy of the localisation depends on the accuracy of the density profile used to map the probing frequency (GHz) into radial distance (cm). Please note that line contour plots were used in figure 5.2.2 in order to make the graphical representation of the mappings more clear.

6. CONCLUSIONS

The data analysis technique described in this paper, which estimates the evolution of the local power spectrum of non-stationary signals, is particularly adequate to process broadband reflectometry signals. In the resulting time-

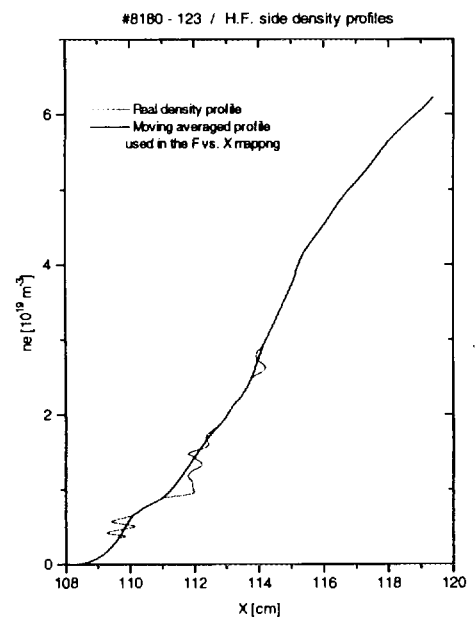


Figure 5.2.1

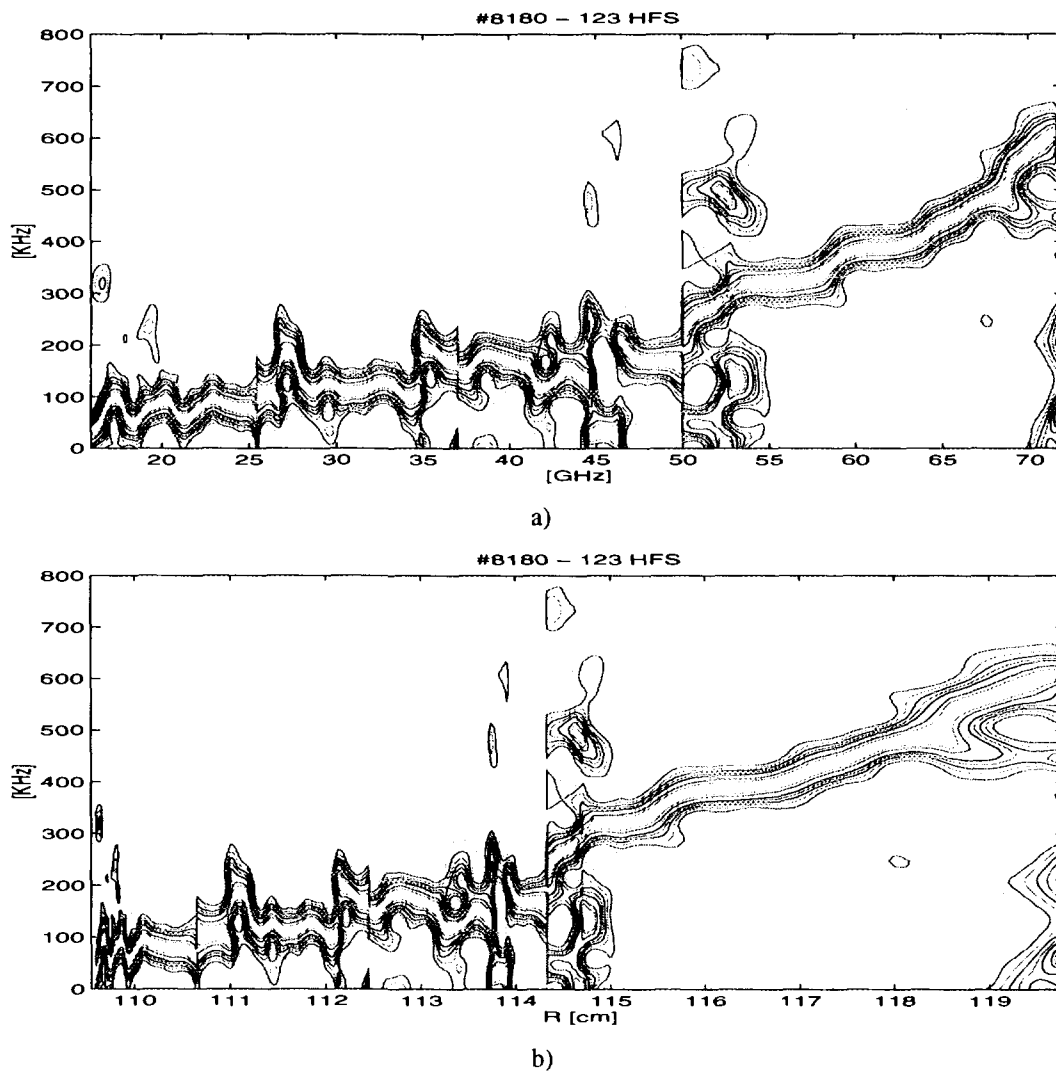


Figure 5.2.2

frequency distributions is contained the information due to the mean density profile and to the plasma fluctuations. By estimating the beat frequency evolution from the first moment of the distribution, the effect of fluctuations is averaged which is particularly important for profile evaluation. On the other hand, understanding the effect of fluctuations on profiles should clarify the meaning of the average profile and, ultimately, improve its accuracy. The technique can also be used to identify and map disturbed regions and therefore contribute to the study of the underlying physical phenomena causing density fluctuations.

Acknowledgements - This work has been carried out in the frame of the Contract of Association between the European Atomic Energy Community and "Instituto Superior Técnico" and has also received financial support from JNICT and PRAXIS XXI.

References

[1] J. Sanchez et al. 1992 *Review of Scientific Instruments* **63** pp. 4654

- [2] G. R. Hanson et al. 1992 *Review of Scientific Instruments* **63** pp. 4658
- [3] A. Huggenholtz et al. 1991 *Review of Scientific Instruments* **62** pp. 1100
- [4] K. W. Kim et al. 1995 *Review of Scientific Instruments* **66** pp. 1229
- [5] A. Silva et al. 1995 *Proc. 22nd Eur. Conf.* Vol. 19C Part IV pp. 413
- [6] F. Claret et al. 1994 *Proc. 21st Eur. Conf.* Vol. 18B Part III pp.1172
- [7] M. Nagatsu et al. 1996 *Plasma Phys. Control Fusion* **38** pp. 1033.
- [8] A. Silva et al. 1996 *Review of Scientific Instruments* **67** pp. 4138
- [9] B. Porat et al. 1994 *Digital Processing of Random Signals*, Prentice-Hall, Englewood Cliffs

Density profile and fluctuation measurements with Microwave Reflectometry on ASDEX UPGRADE

M. Manso, F. Serra, J. Santos, I. Nunes, A.Silva, B. Kurzan*, P.Varela, S.Vergamota,
T.Grossmann, W. Suttrop*

Associação EURATOM/IST, CFN, Instituto Superior Técnico - 1096 Lisboa Codex

**MPI fuer Plasmaphysik, EURATOM Association, D-85748 Garching, Germany*

1. Introduction

The microwave reflectometry system on ASDEX Upgrade uses O-mode at high-field (HFS) and low-field (LFS) sides, X-mode (low-field) and can operate at broadband ultrafast sweep ($\geq 20 \mu\text{s}$) and at fixed frequency, probing densities up to $\sim 6.5 \times 10^{19} \text{ m}^{-3}$ [1]. Broadband reflectometry view the plasma continuously in space at narrow time slots, and fixed frequency in narrow space slots (density layers) along large time windows. Here we present results obtained during H - mode discharges in ASDEX Upgrade where broadband and fixed frequency results are used in a complementary way to analyse profile changes and fluctuations.

2. Broadband swept operation

Plasma fluctuations “print” their signature on the reflectometry signals but for profile inversion only the average beat frequency f_B is extracted and the perturbations due to fluctuations are regarded (together with the noise from the system) as problems to the profile evaluation. Here we apply a method based on the estimation of the time-frequency distribution (TFD) of the energy of the reflectometry signals, that gives both f_B and the profile perturbations. The broadband signals are nonstationary because their spectral characteristics vary along the sweep and the method uses the concept of instantaneous frequency (f_i) that was introduced to describe the frequency of nonstationary signals at a particular time [2]. The f_i is the first moment of the TFD with respect to the frequency [2]. Several TFD’s can be used to estimate the f_i , in our study we used the simplest one which is the periodogram. This can be computed with a sliding

window Short-Time-Fourier Transform (STFT), being applicable as long as the signals are locally (in each window) quasistationary; the method and its application to broadband reflectometry is described in [3]. The analysis contributes to the study of the physical phenomena underlying plasma fluctuations and to the understanding of the effect of fluctuations on the profile which will improve the accuracy of profile measurement from reflectometry.

2.1 L/H transition

The ASDEX Upgrade plasma was probed with the simultaneous operation of several O-mode reflectometry channels in the frequency range F : 17-72 GHz, corresponding to densities n_e : $0.4 - 6.5 \times 10^{19} \text{ m}^{-3}$. The measurements were performed at the high field side (HFS) during the ELM phase of shot #8180. The interval between consecutive sweeps was 5 ms and the sweeping time 100 μs .

The distribution of energy in time and frequency (periodograms) of the reflectometry signals is shown in Fig. 1 for the L and H phases; signals were obtained at the LFS with three channels (K, K_a , Q bands) and at the HFS with four channels (K, K_a , Q, V bands). The maps show that the line where the energy is mainly concentrated, corresponding to the average density profile, is disturbed due to the density fluctuations; in some regions the main peak is reduced or even disappears because the energy is scattered by fluctuations, (for example for $F > 45$ GHz in Fig. 1b). In other cases sidebands of the main peak arise (for example, Fig. 1b at $F \approx 35$ GHz) indicating that a perturbation with a well defined frequency occurs. The observed patterns reveal the complexity of the interaction between the incident beam and the fluctuating plasma. Here the performance of the reflectometry system plays a major role because when the reflected signal is weak the characteristic of the system (seen for example at very low f_B in Fig. 1a, for $F > 38$ GHz), may become dominant preventing τ_g measurements in the corresponding frequency range. For this reason an heterodyne detection system is being implemented that will improve the S/N in some 30 dB (according to the laboratory tests).

The above periodograms are a useful tool not only for profile evaluation but also to study plasma fluctuations due to the wide spatial window of probing and high temporal resolution of broadband reflectometry measurements. After the L/H transition it is observed that fluctuations

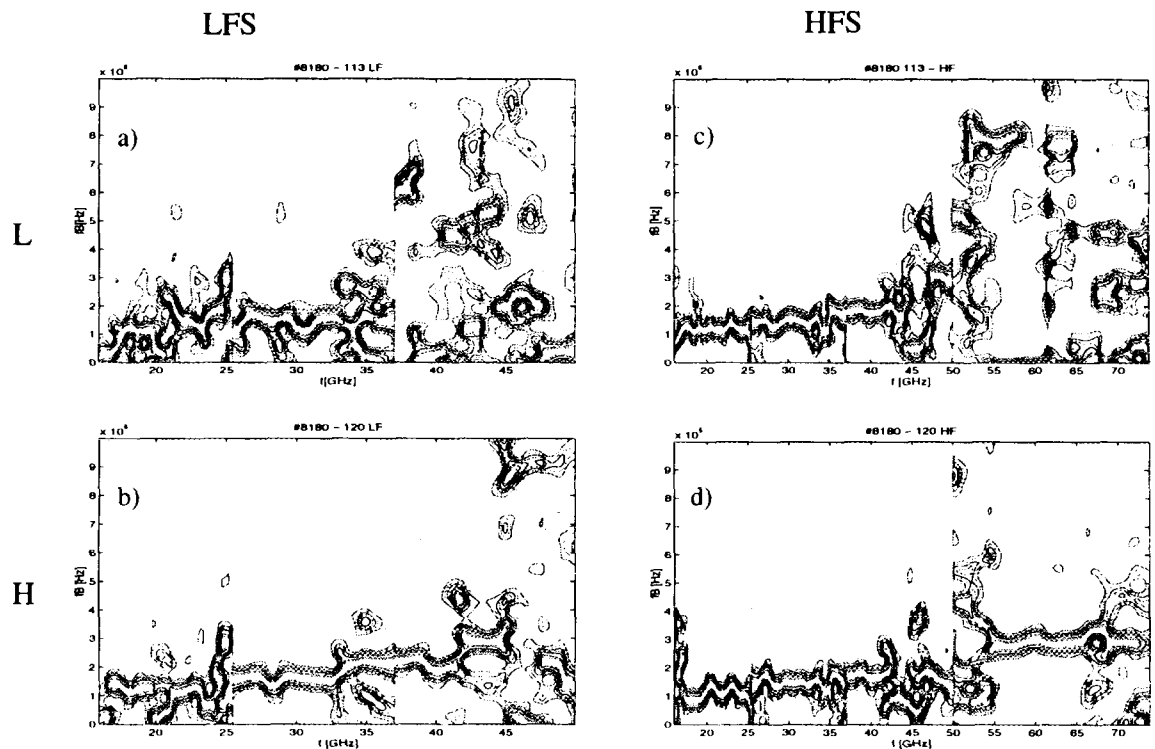


Figure 1

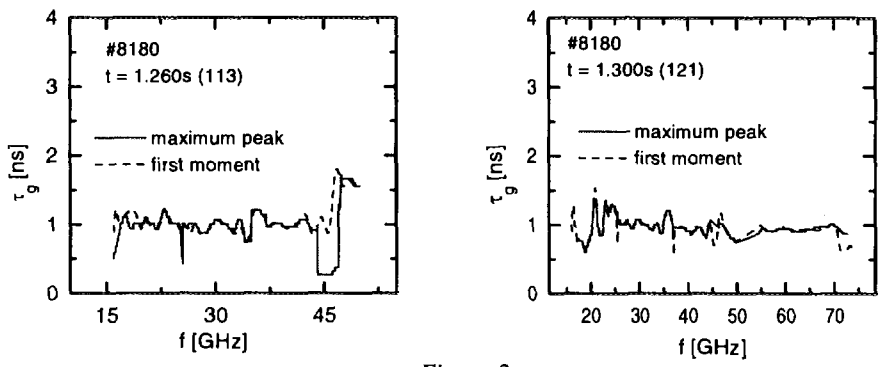


Figure 2

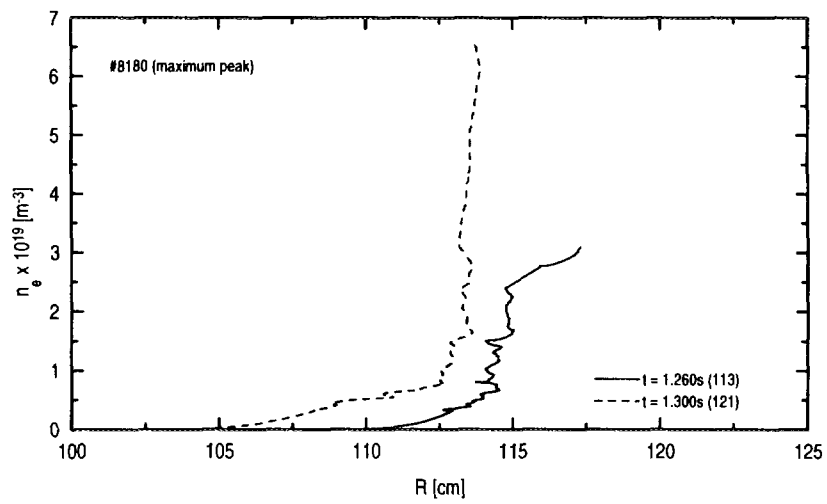


Figure 3

are reduced (specially at the LFS) with particularly emphasis at inner density layers (higher probing frequencies), where the main line due to the plasma profile can now be clearly seen (Fig. 1 b,d).

In spite of the observed perturbations the group delay history can be extracted directly from the maximum peak at each window of analysis or from the first moment of the periodogram (see Fig.2). It is now a question of understanding the meaning of the corresponding τ_g curves and its correspondence to the average density profile. In the curves obtained from the first moment of the TFD the perturbations are average but in the example below (Fig.3) the density profiles obtained from the two τ_g curves are consistent with expectations from other diagnostics namely concerning the radial shift of the magnetic separatrix from L to H-phase (~ 2.5 cm). However, a deviation of some 2 cm in the absolute position of the profiles seems to exist, probably due to calibration errors that are being checked.

Note that the performance of some reflectometry channels were improved after the measurements presented here were made by optimising some microwave paths inside the machine. In this respect the results in this paper when compared with data from experiments to be performed in the next measuring campaign on ASDEX Upgrade (June 1997) will give a good idea of the potentialities of the new method of analysis to extract the τ_g information when the system performance difficult the profile evaluation. Our efforts shall also aim at understanding the role of turbulence on broadband signals in order to improve the profile accuracy.

2.2. Evolution of density profile and fluctuations during ELMs

The first time window under analysis is between 1.31 s (sweep 123) and 1.315 s (sweep 124) corresponding to the beginning of the ELM phase ($\overline{n_e} \cong 6 \times 10^{19} \text{ m}^{-3}$). The periodograms obtained at the peak of the first ELM (Fig. 4, sweep 123) and after the ELM (Fig. 4, sweep 124), reveal that the plasma layers are mainly disturbed for n_e below $2.5 \times 10^{19} \text{ m}^{-3}$ ($F_1 < 45 \text{ GHz}$). The profile shape can be inferred from the evolution of f_B , by taking into account that $F \propto \sqrt{ne}$, (horizontal axis) and f_B (vertical axis) can be converted into distance after integration in F . During the ELM (Fig.4, 123) the profile flattens for $F > F_1$ (large increase of f_B), and it peaks (Fig.4,124) in the same region after the ELM (very small increase of f_B).

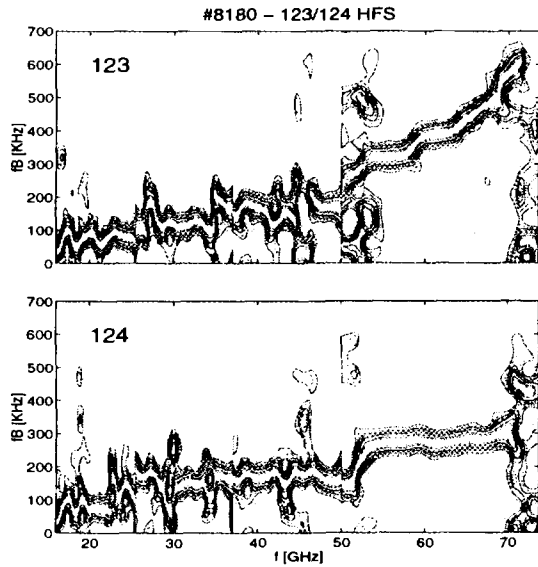
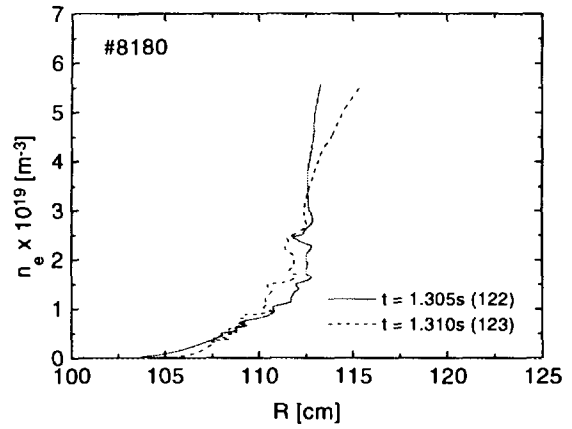
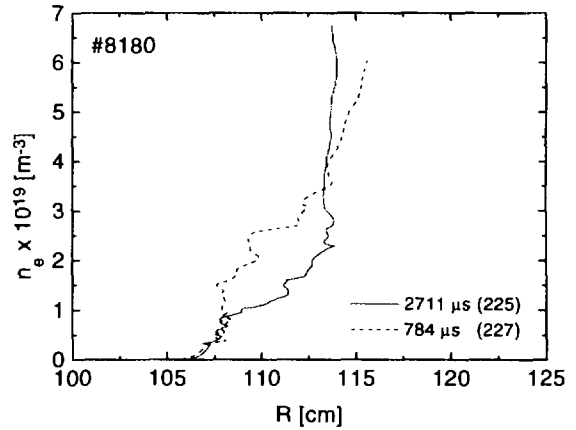


Figure 1

The density profiles (Fig.5.a) obtained directly from the first moment of the periodograms show that the profile flattening occur close and inside the magnetic separatrix, $n_{es} \cong 1.5 \times 10^{19} \text{ m}^{-3}$. Outside the separatrix the changes in the profile are very small, the plasma moves only slightly outward during the ELM. In Fig. 5b two profiles are shown for a different window in the ELMy phase, for $\overline{n_e} \cong 9 \times 10^{19} \text{ m}^{-3}$ and $n_{es} \cong 4.1 \times 10^{19} \text{ m}^{-3}$; $t = 1.82 \text{ s}$ (sweep 225) is between ELMs and $t = 1.83 \text{ s}$ (227) is during one ELM (see Fig.6). The crossing point of the profiles during an ELM and between ELMs in both studied cases, Fig. 5 (a,b), occur at a density close to n_{es} , suggesting therefore that the separatrix region acts as a kind of “joint” for profile movements.



a) $n_{es} \cong 1.5 \times 10^{19} \text{ m}^{-3}$



b) $n_{es} \cong 4.1 \times 10^{19} \text{ m}^{-3}$

Figure 2

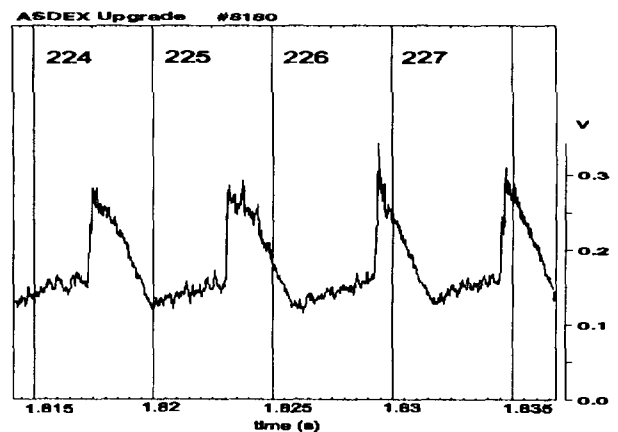


Figure 3

3. Fixed frequency operation

With fixed frequency specific plasma density layers are probed at a rate of 1 μ s (sampling frequency: 1 MHz). A technique to track the plasma position of fixed density layers is presented and demonstrated for the density profile build-up during L- to H- transitions.

The temporal evolution of the frequency spectra of the reflected signals (with 300 kHz maximum imposed by the data acquisition rate) shows an abrupt reduction of the turbulent fluctuations at the L - H transition. The reduction is observed both at the high and low-field sides and permits to identify the time of transition (aside from the decrease of the D_α signal) with high temporal resolution. In the spectral content of the reflected signals a clear low-frequency oscillation (≤ 500 Hz) is also observed around the L-H transition, due to the radial displacement outwards of the reflecting layer as the edge density gradient increases. From the corresponding phase and amplitude variations the incremental shift of the position of the reflecting layers can be inferred, with an accuracy (in the millimetre range) defined by the high temporal resolution of the detected fringes (3 μ s). Therefore, the profile build-up following the L-H transition can be tracked revealing the temporal development of the transport barrier.

3.1. Analysis of turbulence during an H-mode discharge

In a homodyne system the detected signal is sensitive to amplitude and phase fluctuations, such that $V(t) = A(t) \cos \phi(t)$, where $\phi(t)$ is the phase difference between the signals from the plasma and the reference arm. A reflection layer at a fixed equilibrium position leads to a constant phase angle. Density fluctuations will cause displacements and corrugations of the refractive index surfaces, leading to amplitude and phase variations that will have impact on the spectral components of the detected signal.

The temporal evolution of the power spectra is obtained using a FFT sliding technique. Fig. 7 c-e shows the contour plots, corresponding to three probing frequencies: 22.7 GHz ($n \sim 0.64 \times 10^{19} \text{ m}^{-3}$, at the HFS), 31.7 GHz ($n \sim 1.24 \times 10^{19} \text{ m}^{-3}$, close to the magnetic separatrix, at the LFS), 45.7 GHz ($n \sim 2.58 \times 10^{19} \text{ m}^{-3}$, LFS), for # 8595; it is a discharge with unfavourable gradB drift direction (away from the X-point), where the H-mode is attained through ctr-NBI with high heating power

(Fig. 7a). An abrupt reduction in the power spectrum of the turbulent fluctuations is observed both at the high and low field sides, that permits to identify the time of the L-H transition ($t=1.704s$) aside from the decrease of the $D\alpha$ signal (Fig. 7b).

Although the reduction of density fluctuations occurs at the transition (simultaneously) for all the probed layers (that should therefore be located inside the suppression zone where the transport barrier builds-up), there is a distinct behaviour when analysing the discharge from the OH to the H phases: at the HFS, outside the separatrix, the frequency spectrum extends up to ~ 100 kHz (Fig. 7e); at the LFS, close to the separatrix, it extends to ~ 150 kHz (Fig. 7d) with

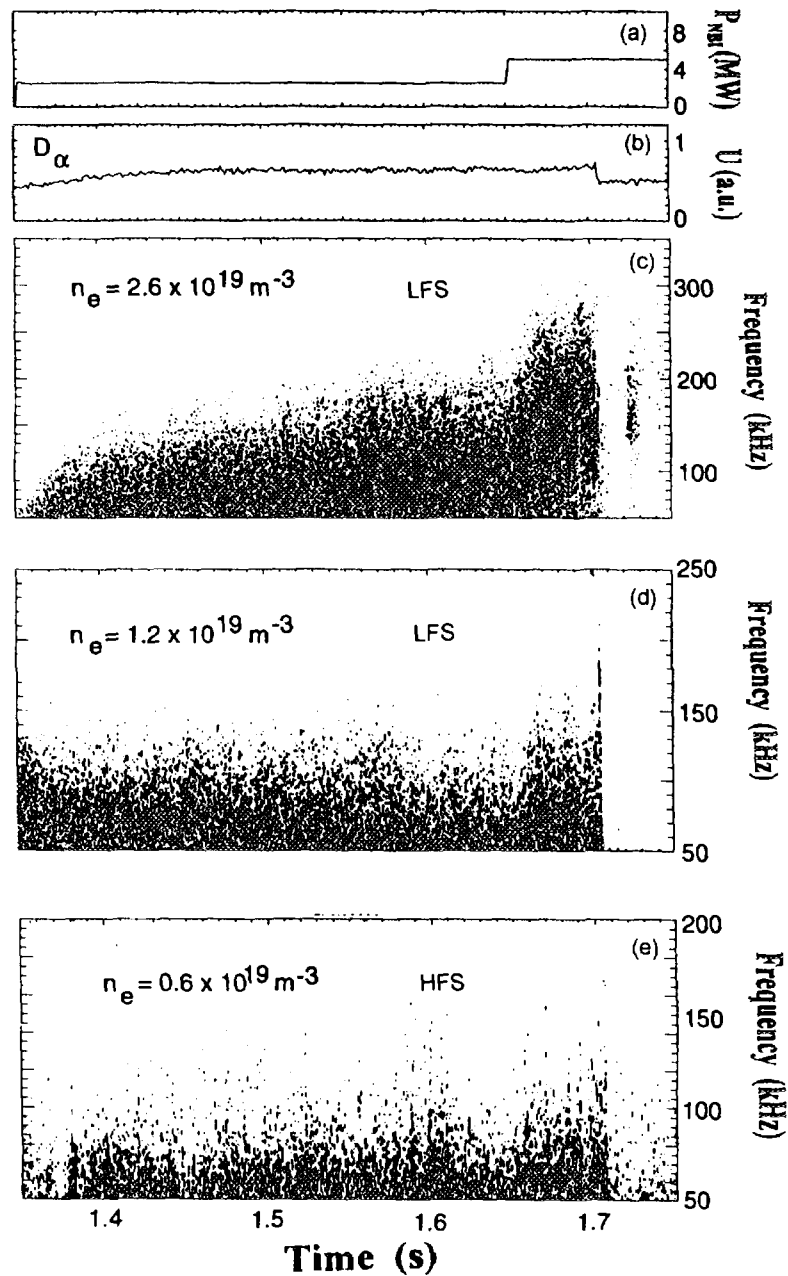


Fig.7

an almost constant temporal behaviour until the transition; in contrast, inside the separatrix, at LFS, a broadening of the frequency spectrum occurs correlated with NBI, specially with high heating power (after 1.65 s) and reaching ~ 300 kHz just before the transition (Fig.7c). The observed broadening might be due to Doppler shift in the reflectometer signals induced by an $E \times B$ poloidal velocity rather than an increase of density fluctuations. The significant increase of the $E \times B$ velocity before the L-H transition inside the separatrix is consistent with the detected increase of the radial electric field (E_r) at the edge, as will be discussed in section 3.2 (see Fig. 8); the distinct behaviour at different radial positions suggests the existence of a highly sheared $E \times B$ flow leading to better confinement through the decorrelation of the turbulent fluctuations, the accepted scenario to trigger the L-H transition.

3.2. Detection of density profile modifications during the L - H transition

In the spectral content of the reflected signals a clear low-frequency oscillation (≤ 500 Hz) is observed around the L-H transition; it is caused by movements of the reflecting layer associated with radial displacements of the layer during the density profile build-up associated with confinement improvement.

In Fig. 8 b, the low pass filtered reflectometry signal obtained from the raw data of Fig. 8 a (referring to layer $n_e \sim 2.58 \times 10^{19} \text{ m}^{-3}$, LFS) is shown. Periodic oscillations start at $t \sim 1.69$ s, coinciding with the slow increase of the radial electric field E_r before the transition; this rise in E_r is inferred from changes in the fluxes of ripple-trapped charge exchange (CX) neutrals [4], (Fig. 8e), in parallel to the edge pressure gradient, revealing an improved confinement still in the L phase (with increasing $n_{e,edge}$ (Fig.8c), and with the presence of ELMs (Fig.8d)).

After the L-H transition ($t \sim 1.704$ s), a fringe with high amplitude is observed revealing a radial displacement outwards of the probed layer (towards the receiver antenna), corresponding to the profile build-up during a time interval of ~ 2.5 ms. On the same time interval a fast increase of E_r occurs (Fig. 8e), consistent with the build-up of the edge transport barrier following the abrupt drop in turbulence.

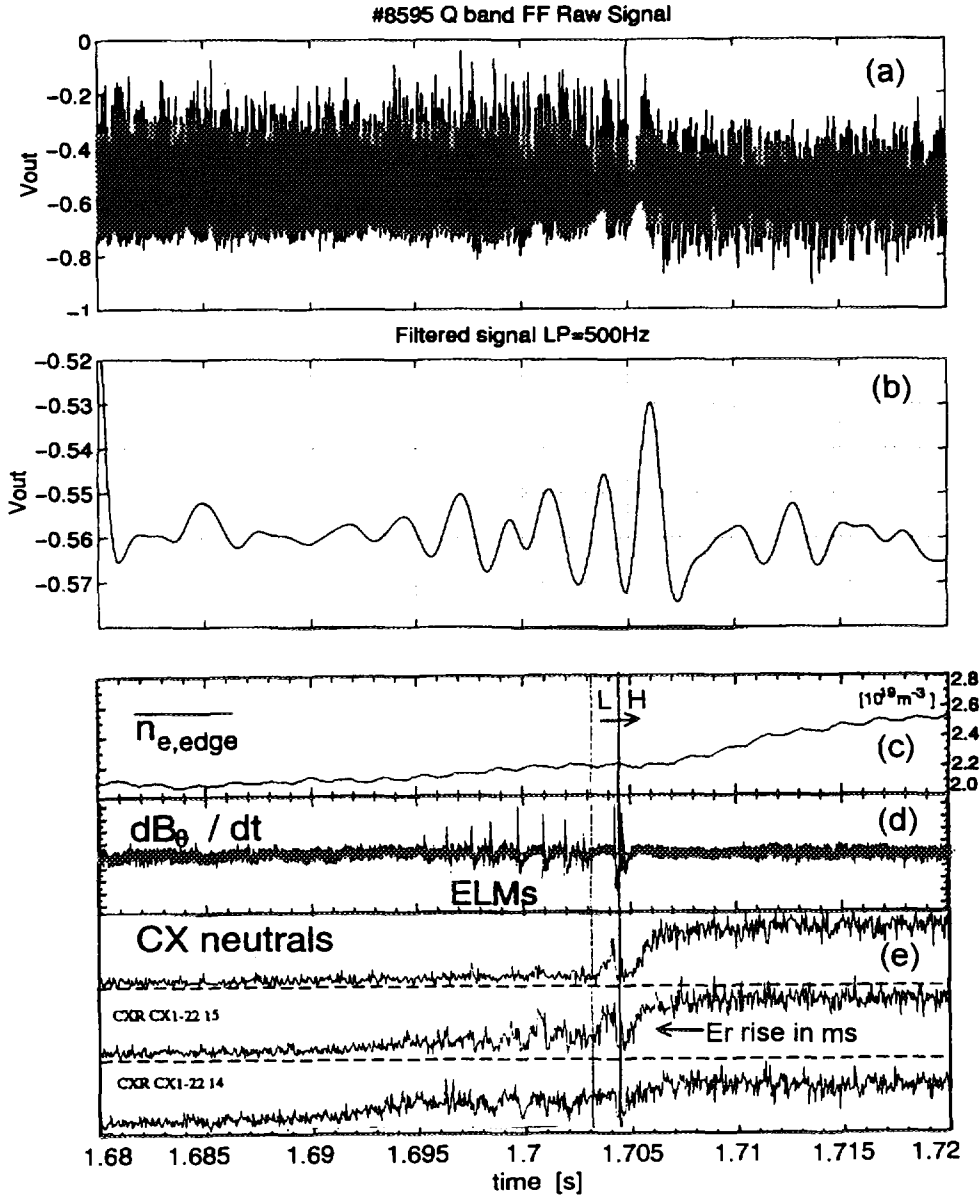


Fig. 8

The profile evolution at the edge can be inferred by estimating the incremental displacements of the layer. Using a numerical code [5] which takes into account the antenna-plasma geometry of the reflectometry system and assuming the shape of the evolving density profile (with increasing mean density and no global radial displacement), the estimated displacement of the reflecting layer (ΔR_c) corresponding to one fringe variation is ~ 0.6 cm; a similar result is obtained through the relation $\Delta R_c \cong \lambda_0 \Delta \phi / (4\pi \bar{N})$, with the mean refractive index $\bar{N} = 0.6$. Assuming as an initial profile the one from Li-beam at 1.7s, a radial displacement of 1.2cm (2 fringes) between 1.703 s and 1.708 s will lead to a steepening of the edge gradient from $\sim 0.6 \times 10^{21} \text{ m}^{-4}$ to $\sim 1.0 \times 10^{21} \text{ m}^{-4}$.

The impact on the density profile of the full development of the transport barrier might therefore be tracked with the “continuous” temporal probing of several density layers (from the edge up to the bulk plasma), as foreseen for the next measuring campaign (with probed densities up to $\sim 14 \times 10^{19} \text{ m}^{-3}$). However, an heterodyne detection system for the direct measurement of the phase will be important in order to overcome ambiguities that might occur with fringe detection when the plasma layers move back and forth (as in the profile changes caused by ELMs).

4. Discussion and concluding remarks

Broadband results

A new data analysis method was applied to broadband reflectometry which unfolds the energy associated with the reflection from the plasma and the energy scattered by fluctuations, giving its particular location in time (density) and frequency.

From the point of view of profile evaluation this is very important because it avoids the use of narrow digital filtering and therefore retains details of the group delay curve that may be important for profile accuracy. It also “smooths” errors that occur when a significant part of the energy is scattered by fluctuations and the spectral peak deviates from the average beat frequency. Profiles were measured in ASDEX Upgrade showing that during an ELM, the profile flattens inside the separatrix coinciding with the rise of the D_α signal; for $t \geq 500 \mu\text{s}$ the profile is already peaking and continues until a new ELM occurs. The detailed profile changes in each density layer and the evolution of the local energy spectrum of plasma perturbations were obtained from the history of the energy spectrum in each window of analysis. Strong perturbations were observed during ELMs and between ELMs in the middle region of the plasma, and also at the onset of the ELM, in the inner zone where the profile flattening occurs.

Further and more detailed experiments (with sweeps of $20 \mu\text{s}$, spaced by $30 \mu\text{s}$) are foreseen to determine if the observed perturbations can be attributed to MHD activity.

Fixed frequency results

In addition to information about the abrupt decrease of turbulence and about the increase of plasma rotation at the L - H transition, the spectral content of the reflected signals was also used to obtain insight about density profile changes. By low-pass filtering the spectra of the reflected

signals, fringes due to radial displacement of the density layers during the profile build-up can be identified. With this technique the incremental shift of the position of the reflecting layer can be estimated with an accuracy in the millimetre range.

A new reflectometry channel has been recently installed for monitoring the L - H transition on ASDEX Upgrade, to operate in fixed frequency independently of the other channels [6]. Simultaneous measurements with fixed frequency and broadband operation in the same discharge (as foreseen for the next measuring campaign on ASDEX Upgrade), will provide density profile measurements with high temporal and spatial resolutions and further indication about the absolute position of the layers probed in fixed frequency. The potential of a such a highly performant reflectometry diagnostic suggests the possibility of tracking continuously the motion of plasma layers associated with important physical phenomena where fast profile changes occur (such as L-H transition, ELMs and MARFES).

Acknowledgments

This work has been carried out in the frame of the Contract of Association between the European Atomic Energy Community and "Instituto Superior Técnico" and has also received financial support from "Junta Nacional de Investigação Científica e Tecnológica" and PRAXIS XXI.

References

- /1/ A. Silva et al., Rev. Sci. Instrum. 67 (12), 1996.
- /2/ B. Porat , Digital Processing of Random Signals, Prentice-Hall, Englewood Cliffs, 1994
- /3/ J. Santos et al., (1997), III Reflectometry Workshop for Fusion Plasmas, Madrid, 1997.
- /4/ W. Herrmann et al., Phys. Rev. Lett. 75, 4401, 1995.
- /5/ T. Grossmann et al., this Conference, III Reflectometry Workshop for Fusion Plasmas, Madrid, 1997.
- /6/ A. Silva et al., III Reflectometry Workshop for Fusion Plasmas, Madrid, 1997.

**NEXT PAGE(S)
left BLANK**

DUAL FREQUENCY O-MODE HETERODYNE REFLECTOMETER ON TORE SUPRA TOKAMAK

Ph. Moreau, F. Clairet, J.M. Chareau, M. Paume, C. Laviron
and, G. Leclert*

Association Euratom-CEA sur la fusion controlée / CEA Cadarache
13108 St Paul-Lez-Durance cedex, FRANCE

*LPMI URA CNRS 835 / Université Henri Poincaré
54506 Vandoeuvre, FRANCE

Introduction

A new heterodyne dual frequency reflectometer has been installed on Tore Supra. It combines high dynamic sensitivity and fast frequency sweeping potentiality. It works over the 26-36 GHz frequency band, so that its performances can be directly compared with the actual O-mode homodyne reflectometers [1]. As it measures simultaneously phase and amplitude, this new system should also be able to provide more valuable information for understanding the role of plasma turbulence upon the reflected signal of the homodyne system.

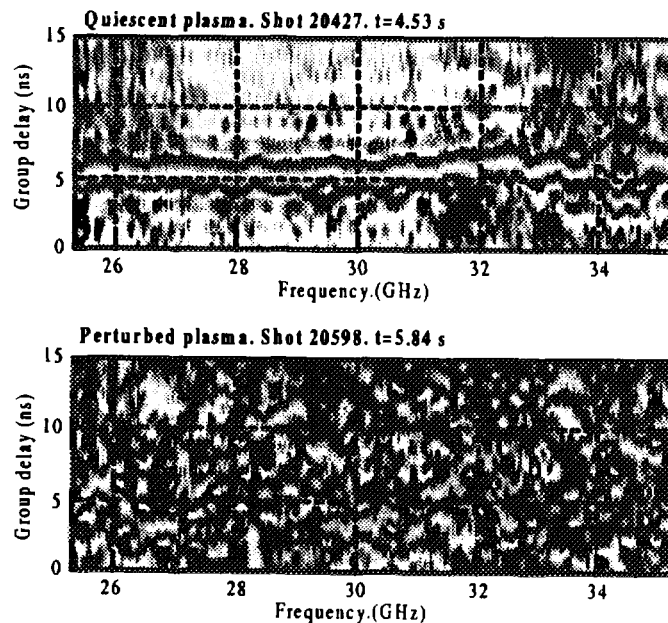


Figure 1 : Sliding FFT of the signal obtained with the O-Mode 25-35 GHz homodyne reflectometer for 2 different plasma conditions.

The X axis is the frequency launched into the plasma (sweeping time= t ms),
the Y axis is the group delay (or the beat frequency)

On Tore Supra, the phase delay is determined using sliding FFT method [1]. Typical results obtained with this technique applied on the O-Mode homodyne reflectometer are presented Figure 1a. On this first image, the plasma echo versus the frequency launched into the plasma is well defined, so the corresponding density profile is easily determined. But, sometime, the plasma information is completely lost (cf. Fig. 1b). With such results, it is very difficult to recover the time delay and finally a density profile having a physical sense. Up to now, the transition between these two cases have not been well understood. That's why we have developed a new O-Mode heterodyne reflectometer.

Experimental system

Until now, the reflectometry means on Tore Supra were composed of three homodyne O-mode reflectometers, with a frequency range covering 25 to 75 GHz (density cut off from 0.8 to $6.9 \cdot 10^{19} \text{ m}^{-3}$), and one X-mode homodyne reflectometer covering 78 - 118 GHz. The new dual frequency O-mode heterodyne reflectometer which has recently been installed on Tore Supra is presented figure 2.

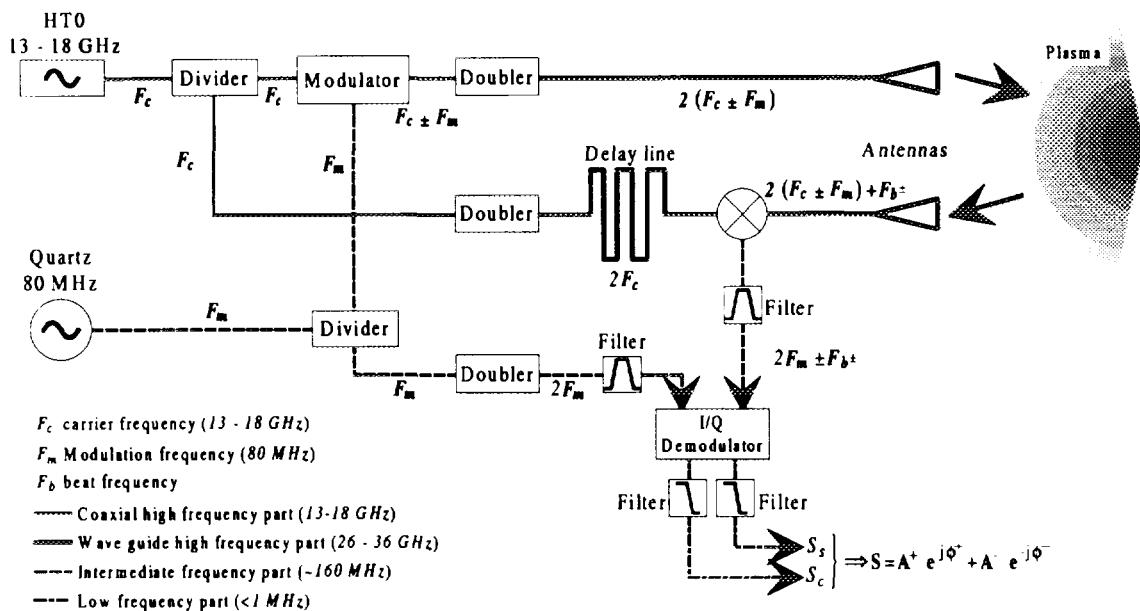


Figure 2 : Schematic view of the new dual frequency O-Mode reflectometer on Tore Supra.

The frequency band covered is 26-36 GHz providing edge density measurements from 0.8 to $1.6 \cdot 10^{19} \text{ m}^{-3}$. The frequency source used is a Hyperabrupt Tuned Oscillator (HTO 12000, 12-18 GHz). These solid sources offer numerous advantages over the BWO in the way that they are more stable, more reproducible, they can be rapidly full band swept as fast as $10 \mu\text{s}$ and they are conveniently driven with low voltage (0-20V) power supplies. A linear frequency versus time sweeping is provided with a 12 bits synthesised arbitrary waveform voltage generator (Wavetek 395). The HTO microwave signal is split into two parts with a 3 dB power divider. The first one is modulated at $f_m=80 \text{ MHz}$ with a quartz local

oscillator and then frequency doubled with an active frequency doubler. Therefore, two frequencies separated by 320 MHz ($2F+2fm$ and also $2F-2fm$) are launched into the plasma through 4 m of fundamental wave guides. The other part is used as phase reference with a line delay to allow to compensate for phase differences of the probing wave due to the propagation into the emitter and receiver wave guides. To emit and receive the signal, two closely separated rectangular antennas ($49 \times 37\text{ mm}^2$ 20 dB gain) are used.

When the plasma and reference wave are mixed the resulting signal is at twice the modulation frequency $2fm=160\text{ MHz}$ and contains information from the two cut off layers as two beat frequencies noted f_{b+} and f_{b-} . Finally, the detection is completed using an *I/Q* mixer providing in-phase and 90° -phase signals and allowing absolute phase and amplitude detection for both frequencies launched into the plasma. The demodulation is performed with the same quartz oscillator **providing no need of phase locking system.**

The key point in this heterodyne reflectometer, is the modulator to frequency convert the probing wave. In a first prototype, the modulation has been done with a single side band modulator (SSBM) supposed to provide only one frequency $F+fm$. It then would have been possible to perform density profile as well as density fluctuation measurements. But after active doubling, the lower side band $2(F-fm)$ reached a non negligible intensity (10dB) below the $2(F+fm)$ of interest. The lower band level was not satisfactory so, we have replaced the SSBM with a simple mixer providing identical side bands.

The dynamic range of such heterodyne detection typically lies around 60 dB (to be compared to $20\text{-}30\text{ dB}$ for homodyne detection).

Data acquisition system

We have made numerous sweeping time tests to study the turbulence influence on the phase detected. When the sweeping time decreases, the beat frequency is proportionally increased, needing to adapt the acquisition system.

The first plasma experiments were done with 1 ms sweeping time, the beat frequency was of the order of 200 kHz , and the acquisition was performed with a CAMAC 6810 (12 bits resolution, sampling frequency 1 MHz , memory 1 Mo).

The results down to $100\mu\text{s}$ sweeping time providing beat frequencies up to 2 MHz were recorded with ICM101 acquisition modules with 4 MHz sampling frequency and 12 bits resolution.

Recently, $10\mu\text{s}$ sweeping time (beat frequency 20MHz) has been achieved using a LeCroy 334 oscilloscope (resolution : 8 bits; max. sampling frequency : 500 MHz ; digital memory : 512 kB) as data acquisition system.

Detected signal

Since two frequencies are simultaneously launched into the plasma, the reflected signal carries information from both cut-off layers with different beat frequencies. The detected signal can then be written :

$$S = A_{2(F+f_m)} \exp \left[j \phi_{2(F+f_m)} \right] + A_{2(F-f_m)} \exp \left[j \phi_{2(F-f_m)} \right]$$

A typical real part of the signal is presented on figure 3a and the Fourier transform of the complex signal taken on Tore Supra backwall is shown figure 3b. On this spectrum, the positive frequencies correspond to the upper probing frequency $2(F+f_m)$ and the negative ones to the lower probing frequency $2(F-f_m)$. The amplitude difference between these two parts of the spectrum is mainly due to the couple SSBM-active frequency doubler which generate two frequencies band of different level.

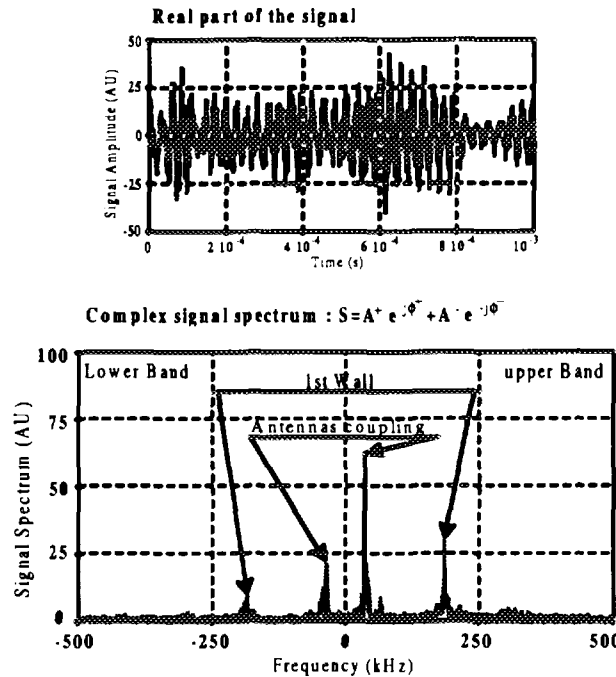


Figure 3 : Example of results obtained on the Tore Supra backwall. (a) is the real part of the signal, (b) is the spectrum of the complex signal. These results have been obtained with the SSBM as modulator, that's why the two frequency band levels are different.

Focusing on the positive part of the spectrum the first beat frequency has been identified as an antennas coupling. This point is very interesting because this reflection is used as phase reference with a calculated propagation length of 5 cm. The other beat frequency correspond to the Tore Supra backwall.

Comparison of homodyne vs. heterodyne reflectometers

Comparison between the homodyne 25-35GHz and the new heterodyne reflectometers have been done by simultaneous measurements on plasma for 1ms sweeping time.

An example of such a comparison is represented figure 4 : while the homodyne reflectometer is unable to give a clear representation of the phase variation to lead to a good reconstruction of the time delay evolution, the heterodyne reflectometer clearly detects the cut-off layer. These features observed between both types of system is mainly due to their sensitivity difference (20 dB for the homodyne and 60 dB for the heterodyne). More over, the homodyne reflectometer cannot differentiate between phase and amplitude as the detected signal is : $S=A.\cos\Phi$. It is then important to state whether the loss of information is due to a loss of the signal dynamic or whether it arises from any phase scrambling. It is shown on ref [2] how both effects are due to the plasma turbulence.

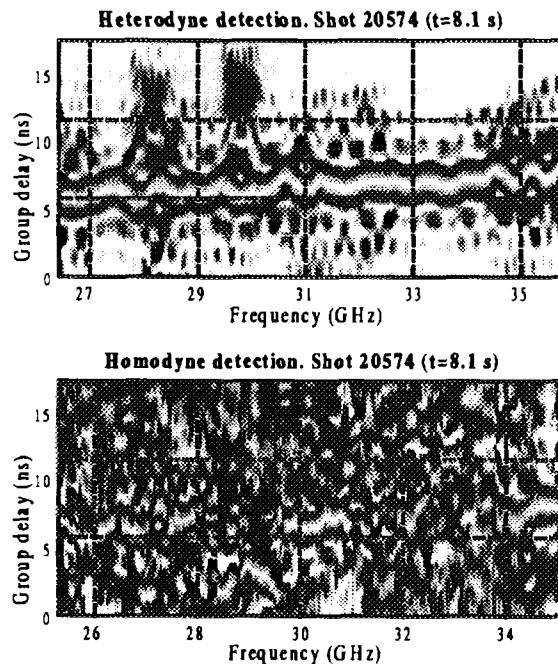


Figure 4 : Sliding FFT of the signal obtained with heterodyne (a) and homodyne (b) system for the same shot at the same time.

The X axis is the frequency launched into the plasma (or the time), the Y axis is the group delay (or the beat frequency)

Fast sweeping operations

With this setup, sweeping times down to $100 \mu\text{s}$ are easily achieved, and $10 \mu\text{s}$ has been performed owing to a dynamic correction of the calibration curve [3]. Figure 5 represents two density profiles obtained with $100 \mu\text{s}$ and $10 \mu\text{s}$ sweeping time for two similar plasmas. With this figure, we see a real improvement of group delay and profile determination with very fast sweep.

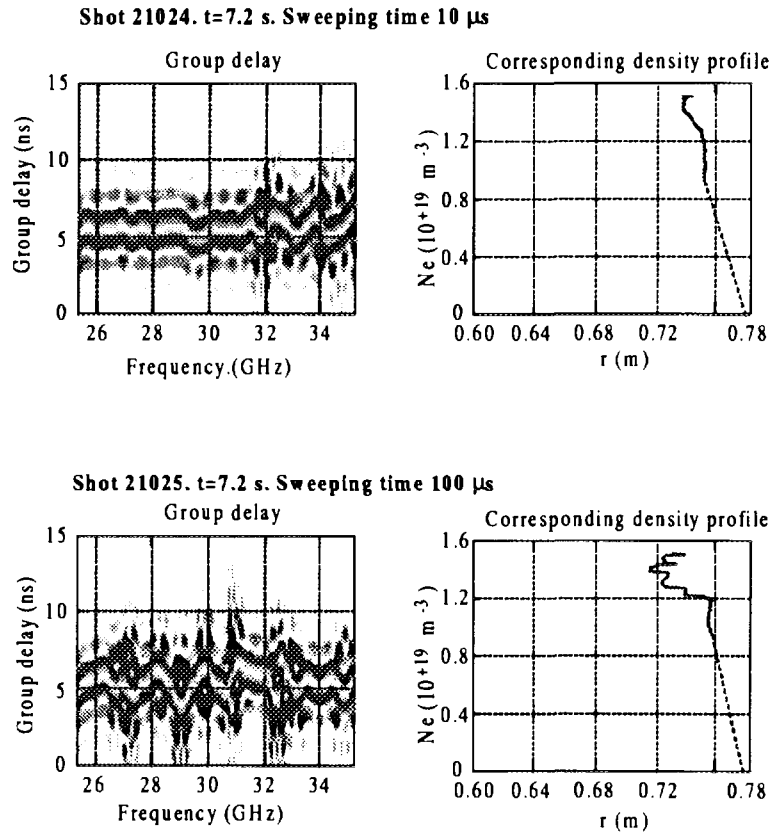


Figure 5: Group delay and corresponding density profile comparison with sweeping times of $10 \mu\text{s}$ and $100 \mu\text{s}$ for two similar plasmas.

Conclusions

A new O-Mode dual frequencies heterodyne reflectometer has been installed on Tore Supra, introducing improvement from high dynamic heterodyne detection, and ultra fast sweeps.

Comparing homodyne and heterodyne results, it seems that the homodyne detection problems principally come from its sensitivity, the signal being still present but with such a low level that the homodyne detection fails. The heterodyne detection has a higher dynamic, so it is less sensitive to this problem.

The use of a solid state source HTO provides an ultra fast sweeping time ($10 \mu s$). We have compared results with different sweeping times and we can conclude that the profile determination is greatly enhanced with faster sweep.

This new reflectometer launches two frequencies into the plasma, amplitude and phase being measured separately for each one. This particularity provides numerous physical studies as developed in [2].

- [1] M. Paume, J.M. Chareau, F. Clairet and X.L. Zou, Proc. IAEA Tech. Comm. Meeting on microwave reflectometry for fusion plasma (Abingdon 1992) 21.
- [2] F. Clairet, Ph. Moreau, J.M. Chareau, M. Paume and G. Leclert, this workshop.
- [3] C. Laviron, Ph. Moreau, F. Clairet J.M. Chareau and M. Paume this workshop.

**NEXT PAGE(S)
left BLANK**

REFLECTOMETRY MEASUREMENTS ON THE TORE SUPRA TOKAMAK

F. Clairet, P. Moreau, J.M. Chareau, M. Paume, C. Laviro
and, G. Leclert*

Association Euratom-CEA sur la fusion contrôlée / CEA Cadarache
13108 St Paul-Lez-Durance cedex, FRANCE

*LPMI URA CNRS 835 / Université Henri Poincaré
54506 Vandoeuvre, FRANCE

Introduction

Among the diagnostics measuring the electron density profiles, the reflectometry offers the advantages of low cost, low maintenance, low access need, no sensitivity to radiation and provides a good spatial resolution. However, this technique, based on phase delay measurement of the reflected wave, suffers phase perturbation due to the plasma turbulence. Despite numerous works, theoretical as well as experimental, the effects are still not well understood. So we are still facing questions like : What is the turbulence? What is its origin? How to characterise the perturbation? How localised is the reflectometry measurement? And finally, how to get rid of the problem?.

Data processing: FFT technique vs. Phase unwrapping

The challenge of reflectometry as a radar technique is to measure the phase delay experienced by a wave launched into a plasma :

$$\phi(F) = \frac{4\pi F r_c}{c} \int_a^{r_c} N(r, F) dr - \frac{\pi}{2}$$

where $N(r, F)$ is the refraction index, r_c is the cut-off position and a is the plasma edge.

By linearly sweeping the frequency with respect to the time, the density profile reconstruction is performed with the experimental determination of the time delay of the wave propagating through the plasma up to the cut-off layer. This time delay is related to

the derivative of the phase : $\tau = \frac{1}{2\pi} \frac{d\phi}{dF}$.

For homodyne detection we are used to performed sliding FFT analysis⁽¹⁾ to determine the group delay evolution versus the frequency sweeping, assuming the amplitude signal being constant and the phase varying slowly with respect to the analysed frequency interval. According to these hypothesis, the detected signal can be written as :

$$\text{Homodyne: } S(t) = A(t) \cdot \cos(\phi(t)) \approx A \cdot \cos\left(\frac{d\phi(t)}{dF} t\right) = A \cdot \cos(2\pi(F)F)$$

The heterodyne I/Q detection allows to extract directly the phase of the reflected signal⁽²⁾, therefore, we can perform the instantaneous time derivative to obtain the instantaneous group delay information.

$$\text{Heterodyne: } S(t) = A(t) \cdot e^{i\Phi(t)}$$

On figure (1), both techniques are compared showing how FFT analysis can conveniently average out the group delay. Also, even if

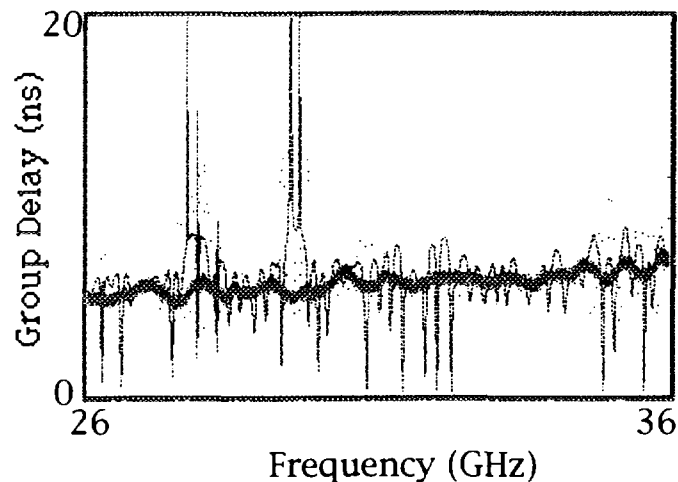


Figure 1 : comparison between sliding FFT analysis (broad curve) (signal: 1024 points width:64pts; sliding:4pts) and instantaneous group delay measurement (thin curve).

the localisation of the reflection occurs in the millimetre range, the instantaneous group delay experimental determination points out the effect of the plasma fluctuations (backscattering or oscillating mirror effect) over the exact location of the cut-off layer. Then, the question of the resolution is mostly a matter of how these fluctuations disturb the measurement.

Localisation of the measurement

The dual frequency reflectometer launches two frequencies separated by 320MHz into the plasma so that two close cut-off layers can be probed simultaneously. Figure (2) represents the sliding FFT analysis for the $F+fm$ and $F-fm$ reflected signals, and the distance between these two layers depends on the density gradient and ranges between 2mm to 1cm in this case. It is surprising to see how localised can be the perturbation and how a strong deviation of the group delay occurs. For example, at 31.5GHz the upper band ($F+fm$) alone is perturbed although the radial separation with the ($F-fm$) cut-off is only about 5mm. The instantaneous group delay calculation shows that, there is a strong and rapid modification in the phase response as well as in the amplitude. More generally, it is observed that a rapid change of the group delay always occurs with a strong decrease of the amplitude of the signal.

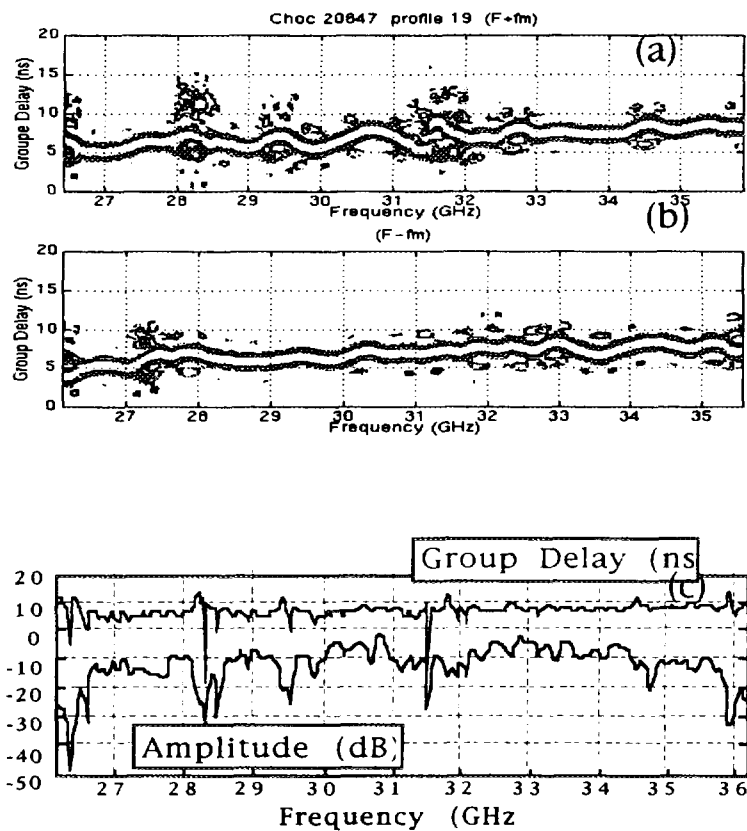


Figure 2 : (a) and (b) Group delay determination by sliding FFT analysis for the two probing frequencies $F+160\text{MHz}$ and $F-160\text{MHz}$. (c) Instantaneous group delay (upper curve) and amplitude signal (lower curve).

Influence of the sweeping time

It has recently been observed that decreasing the sweeping time leads to an improvement of the density profile determination⁽³⁻⁵⁾. We have studied the effect of the decrease of the sweeping time for identical ohmic plasma discharges, between 1ms and 100 μ s, and, between 100 μ s and 10 μ s. On figure (3), the instantaneous group delay and the amplitude of the signals are plotted with different sweeping times, for the upper frequency ($F+f_m$). Rapid turbulent events still occur but they are less numerous. In some sense, we can state that the turbulence has been frozen. So the effects show how is greatly reduced the effects of plasma turbulence upon the instantaneous group delay evaluation.

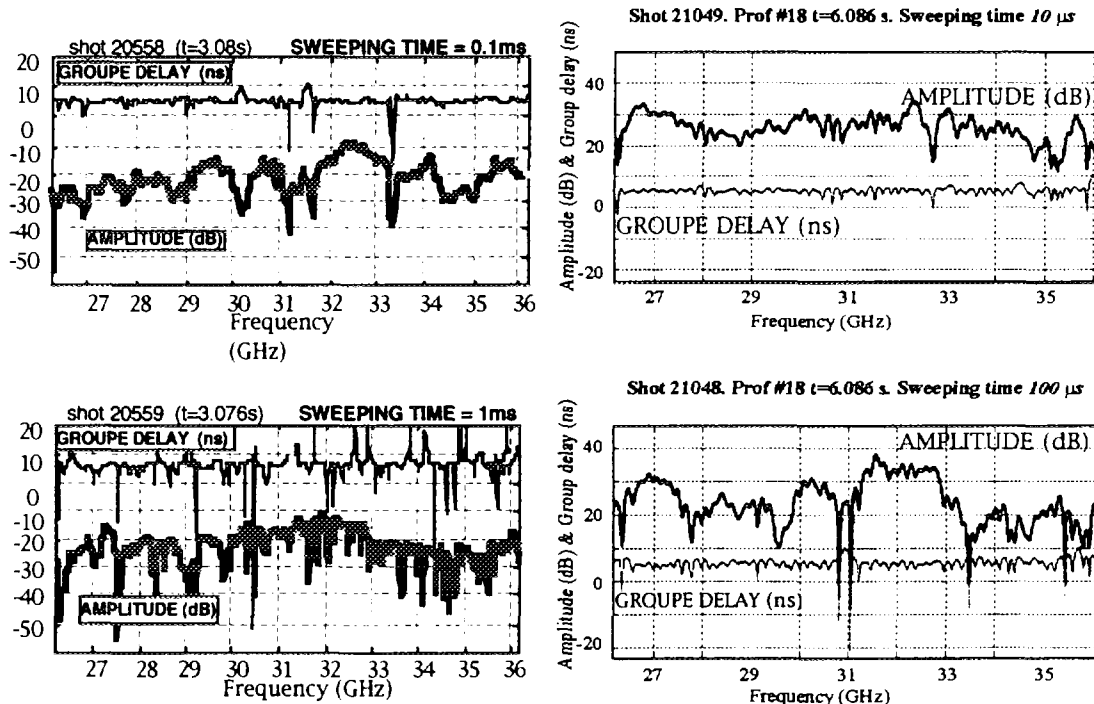


Figure 3 : Instantaneous group delays and amplitudes. Sweeping time comparisons between 1ms and 100 μ s (left), and, between 100 μ s and 10 μ s (right).

However, if by decreasing the sweeping time, the phase jumps are less numerous, their characteristics remain similar in the fact that we are still observing events with strong decrease in the amplitude of 40 to 60 dB.

When we compare the beat frequency spectra (figure (4)) between the 1ms and the 100 μ s reflected signals for two identical plasma discharges, they exhibit the same spectral width (approximately 200kHz). Therefore, since as we decrease the time sweeping, we increase the absolute beat frequency, it means that in terms of group delay the jumps are relatively attenuated.

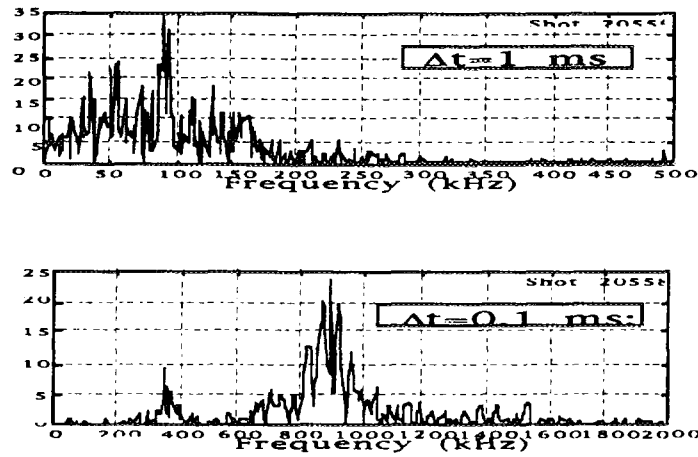


Figure 4 : Beat frequency spectra for 1ms and 100 μ s sweeping time of reflected signals on two identical plasma discharges.

Origin of the turbulence: plasma parameters

The definition of a turbulent plasma needs to be clarified from the reflectometrist point of view, i.e. when the group delay exhibits more and more jumps⁽⁶⁾. From highly turbulent plasma discharges, it appears that the relevant phase information is definitively lost. Numerous theoretical investigations have developed in order to understand this problem, but codes suffer from a lack of knowledge of the turbulence itself in terms of geometrical configuration and dynamical behaviour. In order to get some insight in the origin of this turbulence, we have created a database from several ohmic shots looking at how perturbed was the reflected signal of the edge homodyne reflectometer signal (which is the most sensitive to the turbulence), and, we have tried to correlate this phenomenon to physical plasma parameters. On figure (5), we have ordered three classes of plasmas : high, medium and low turbulent plasma. It came out from this study that the collisionality is the relevant plasma parameter for triggering and increasing the turbulence rather than simply a radius effect.

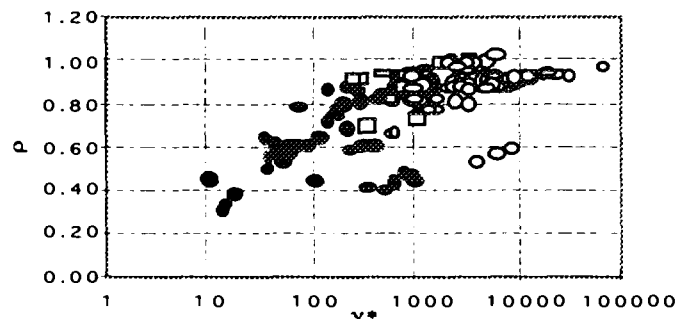


Figure 5 : Statistic between perturbed (closed circles), slightly perturbed (squares), and, non perturbed (open circles) plasma discharges as function of the effective collisionality (ν^*), and, the normalised plasma radius (ρ). (data from the 25-35GHz homodyne reflectometer).

Conclusion

Heterodyne I/Q detection combines high sensitivity with phase and amplitude separation. Both characteristics allow a better understanding of the reflected signal : phase jumps occur very rapidly, of the order of few microseconds, and simultaneously with a strong decrease of the amplitude signal (as much as 60dB). Ultra fast sweep technique considerably improves the group delay measurements. These features considerably help to perform accurate and reliable density profile measurement by reflectometry.

Reflectometry measurement is very localised and the turbulence may perturb the reflected signal very locally within few millimetres. Strong jumps in the group delay values show how the fluctuations limit the resolution of the density profile measurement. However, if the physical characteristics of the turbulence needs be clarified, the high localisation as well as the resistivity dependence suggest that a low wave number and resistive MHD type turbulence rather than a microturbulence; However, the apparent intermittent and small scale behaviour of the perturbed reflected signal may not be sufficient to describe the turbulence since reflectometry look at the plasma in a closely one dimensional geometry.

- (1) M. Paume, F. Clairet, X.L. Zou, et al. : Proceedings of the 1st IAEA Technical Meeting on Microwave Reflectometry for Fusion Plasma Diagnostics Abingdon (1992).
- (2) P. Moreau, F. Clairet, M.Paume, et al : these proceedings.
- (3) T. Tokuzawa, A. Mase, N. Oyama, et al. : Rev.Sci. Instrum. 68, 443 (1996)
- (4) K.W. Kim,E.J. Doyle,T.L. Rhodes, et al. : Rev.Sci. Instrum. 68, 466 (1996)
- (5) A. Silva, M.E. Manso, L. Cupido, et al. : Rev.Sci. Instrum. 67, 4138 (1996)
- (6) F. Clairet, M. Paume, X.L. Zou, et al. : Proceedings of the 2nd IAEA Technical Meeting on Microwave Reflectometry for Fusion Plasma Diagnostics Princeton (1994).

Investigation of Density Profile Perturbations by means of Pulsed Radar Reflectometry

P.C. de Vries¹, A.J.H. Donné¹, S.H. Heijnen¹ ‡, C.A.J. Hugenholtz¹,
A. Krämer-Flecken², F.C. Schüller¹ and G Waidmann²

Partners in the Trilateral Euregio Cluster

¹ FOM-Instituut voor Plasmafysica 'Rijnhuizen', Association EURATOM-FOM,
P.O.Box 1207, 3430 BE Nieuwegein, The Netherlands

² Institut für Plasmaphysik, Forschungszentrum Jülich GmbH.,
Association EURATOM-KFA, P.O. Box 1913, 52425 Jülich, Germany

Abstract. Density profile perturbations due to large rotating $m/n = 2/1$ magnetic islands have been studied by means of a four channel pulsed radar reflectometer in TEXTOR-94. The flight time of the microwave pulses was strongly effected by the shallow density gradients over the magnetic islands. A detailed analysis showed the existence of secondary reflection layers inside the magnetic island, which is an indication of a strong density peaking. This may be explained by assuming that the particle transport is reduced inside the magnetic island.

1. Introduction

A tokamak [1] is a toroidal device in which a hot plasma is confined by means of magnetic fields in order to study thermonuclear fusion. The equilibrium magnetic field configuration consists of magnetic field lines which are toroidal helices and lie on radially nested toroidal surfaces with constant magnetic flux. The helicity is given by the safety factor q [1]. Because the transport in a tokamak along field lines is much faster than in perpendicular, or radial, direction the pressure is constant on these flux surfaces. The set of flux surfaces is the magnetic structure which confines the plasma.

Major points of interest in tokamak plasma research are the quality of confinement and the stability of the magnetized plasma. Various magnetohydrodynamic (MHD) instabilities are thought to perturb the ideal magnetic structure. On surfaces with a rational helicity, $q = m/n$ (m and n are integer numbers) the magnetic field lines are closed in themselves. These flux surfaces may tear and reconnect, forming so-called magnetic islands and perturbing the

‡ Present address: IRCTR, Univ. of Technology Delft, The Netherlands

§ Contribution to the 3rd Workshop on Reflectometry for Fusion Plasmas, Madrid (1997)

equilibrium [1, 2]. Magnetic islands are helical perturbations of the flux surfaces characterized by a poloidal and toroidal mode number, m and n , respectively and a radial extension or width, w . Around the centre, or O-point, of the magnetic island a new set of closed magnetic flux surfaces is found. This set of reconnected flux surfaces of the magnetic island short-circuit radially separated points, which were located before the generation of the magnetic island on separated flux surfaces. This may lead to a local flattening of the pressure profile [3] and thereby causing a degradation of plasma confinement. It is thought that the destruction of magnetic flux surfaces due to small magnetic islands may cause an enhancement of energy and particle transport [4, 5]. A complete loss of confinement can be caused by the growth of magnetic islands, leading to a disruption of the tokamak discharge [6]. Therefore many theoretical and experimental studies are devoted to these perturbations.

The distribution of the temperature and density inside the magnetic island is determined by the balance of transport along the flux surfaces and that perpendicular to them. Although the transport coefficients along the field lines are much larger than the perpendicular ones, perpendicular fluxes may still be larger because the gradient length is smaller. It has been shown that over small magnetic islands the perpendicular transport still dominates yielding a temperature and density gradient over the full magnetic island width [3, 7]. A critical width, w_c , exists above which the density or temperature will be a flux function inside the magnetic island. For the density one finds [3],

$$\frac{w_c}{r_s} = \left(\frac{D_{\perp}}{D_{\parallel}} \right)^{1/4} \left(\frac{1}{\epsilon_s s_s n} \right)^{1/2}, \quad (1)$$

where r_s , ϵ_s and s_s are the position of the $m/n = 2/1$ magnetic island, the local aspect ratio, r_s/R_o , and the local shear, respectively. If one assumes the parallel diffusion, D_{\parallel} to be determined by the parallel conductivity and that in the perpendicular direction, D_{\perp} , to have the same anomalous value as in the plasma outside the magnetic island, one finds for TEXTOR-94 that $w_c \approx 8.5$ cm. Similarly, using the heat transport coefficients, the critical width for the temperature to become a flux function inside the magnetic island can be found. If no heat sources are present inside a magnetic island, the temperature is expected to flatten over a $m/n = 2/1$ magnetic island larger than 2.3cm [3, 8].

Because of plasma rotation the perturbations due to magnetic islands appear as oscillations on the time traces of the various diagnostics. Alternating the O-points and the knots of the magnetic island, X-points, are observed. Magnetic pick-up coils, located outside the plasma provide little information on the local structure of the magnetic islands. Observation of local temperature profile perturbations, by means of Electron Cyclotron Emission (ECE) diagnostics, may reveal this information. The width and position of the magnetic island have been determined at TEXTOR-94 by means of temperature profile measurements with a good radial resolution [8].

Previously it has been shown that a local temperature maximum exists inside the O-point of large magnetic islands in TEXTOR-94, which shows that a nett heat source may be present and that energy is confined inside [8]. The question arises how the density profile is perturbed over the magnetic island.

In this paper measurements of density profile perturbations will be shown, which have been performed by means of pulsed radar reflectometry. First the diagnostic will be described briefly after which the measurements will be presented. In the last section the effect of shallow

density gradients on the pulsed radar reflectometer signals will be discussed in order to reveal information on the density gradient inside the magnetic island.

2. Pulsed Radar Reflectometry at TEXTOR-94

Local measurements of the plasma density cannot be performed easily. Interferometry can be used to determine density profiles, however, this technique has its limitations because of the line-integrated nature versus the localized dynamic behaviour of density profiles. Local measurements can be achieved by means of reflectometry [9]. A four-channel pulsed radar reflectometer which was originally developed for the RTP tokamak has recently been installed at TEXTOR-94 ($R_o = 1.75\text{m}$, $a = 0.46\text{m}$ and $B_T = 2.25\text{T}$) [9, 10, 11, 12].

The pulsed radar reflectometer launches short microwave pulses ($FWHM = 1.5\text{ns}$) with four different frequencies (29, 33, 36 and 39GHz) into the plasma with a repetition rate of 125kHz. The microwaves are in ordinary mode, i.e. the electric field wave vector is parallel to the magnetic field in the plasma. The refractive index of the plasma determines the propagation of the waves. A cut-off for these microwave pulses is found at the plasma frequency, ω_{pe} , which is determined by the plasma density. Each pulse is reflected in the plasma where its frequency matches the local plasma frequency. The flight time of the reflected pulse is measured, hence the position of the density layers with $n_e = 1.0, 1.4, 1.6$ and $1.9 \cdot 10^{19}\text{m}^{-3}$ are probed. If no reflection layer is present in the plasma, because the density is too low, the pulse is reflected at the vessel back-wall. For the measurements presented in this letter the flight time of a back wall reflection in vacuum is defined to be zero. The flight time is determined by the distance to the reflecting layer and the group velocity of the pulse. Because the pulse moves slower in a dense plasma, the flight time will be longer in this situation compared to that in the vacuum case. The effect on the group velocity is also important in the analysis of reflections by plasma density layers. Especially in the case of non-monotonic density profiles, as can be expected in the presence of magnetic islands, one should interpret the data with great care. When a pulse is reflected at a density layer, with a shallow density gradient just before it, the flight time may be much longer than that of pulses with slightly higher frequencies, reflecting from density layers further inside the plasma [12, 13]. Secondary effects on the time-of-flight measurement could be caused by pulse broadening and refraction in regions with a shallow density gradient. Because of the finite pulse width (1.5ns) all frequency components of the pulse will reflect at slightly different density layers. In severe cases the reflected pulse might become too spread out to be detected.

3. Observation of Magnetic Islands

Large magnetic islands have been observed in TEXTOR-94 with a typical width of several cm. Flux surface perturbations of this amplitude can be detected by the pulsed radar reflectometer. An example of the observation of MHD modes by means of pulsed radar reflectometry can be illustrated by a specific discharge. During this discharge the current was ramped-up to 475kA ($q_a = 2.7$) which led to a minor disruption at $t = 0.528\text{s}$ and a major one at $t = 0.560\text{s}$. The central density rose to $2.5 \cdot 10^{19}\text{m}^{-3}$ as shown in Fig. 1. In the same figure the time-of-flight of one of the pulsed radar reflectometer channels is pictured. In the early phase of the discharge,

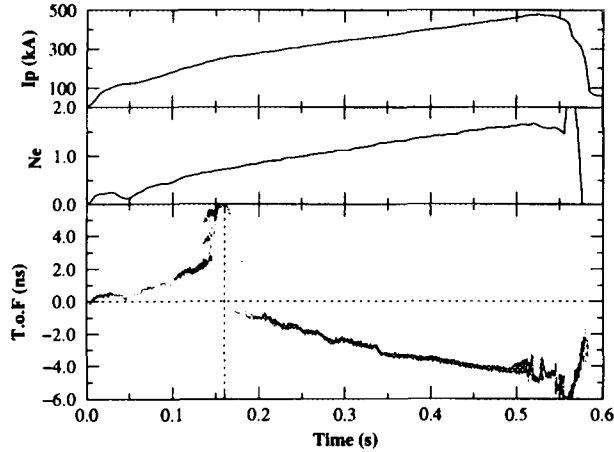


Figure 1. The upper two graphs show the ramp-up of the current and line integrated density of discharge 66159. The lower graph shows the time-of-flight (*T.o.F.*) of 33 GHz pulses ($n_c = 1.4 \cdot 10^{19} \text{m}^{-3}$). The vertical dashed line indicates the time when the central density equals the critical density for this frequency. The vacuum flight time to the vessel wall and back is defined to be zero.

when the density is still below critical, the flight time to the back wall increases because the group velocity of the pulse decreases. During a short phase, $t = 0.15 - 0.16 \text{ms}$, when the critical density is in the central part of the plasma, the pulse probes a region of the profile with a very small density gradient. As a result the pulse becomes too broadened and cannot be properly detected. At $t = 0.160 \text{ms}$ the central density is larger than the critical density for this channel, $n_c = 1.4 \cdot 10^{19} \text{m}^{-3}$. The pulses are now reflected by a density layer which moves slowly towards the outside of the plasma due to the still increasing density. As a precursor to the disruptions an $m/n = 2/1$ tearing mode has been observed. The island width in the temperature profile grows to $w = 7 \pm 1 \text{cm}$ just before the disruption.

In Fig. 2a-b the MHD oscillations are shown, for the same discharge as in Fig. 1, from two specific pulsed radar channels monitoring the surfaces with a density of $n_e = 1.4$ and $1.0 \cdot 10^{19} \text{m}^{-3}$, respectively. The two surfaces lie on opposite sides of the rational q surface, which can be concluded from the fact that the oscillations are in counter phase. The HCN interferometer, which measures the line integrated density over 9 vertical lines through the TEXTOR-94 plasma, also observes MHD oscillations. The phases of these MHD oscillations reverse also sign for interferometer channels on opposite sides of $q = 2$ surfaces. The interferometric value for the density in the vicinity of the rational q surface was found to be between 1.0 and $1.5 \cdot 10^{19} \text{m}^{-3}$. Remind, however, that the Abel-inversion of the line integrated interferometer data may be erroneous in the presence of these highly deformed density profiles. For comparison the MHD oscillation in the local temperature is given in Fig. 2c.

The MHD oscillation amplitude grows on both pulsed radar channels. One has to be careful deducing a magnetic island width from this amplitude as possible flat density regions may considerably change the group velocity of the pulse. The 29GHz-channel (Fig. 2b), monitoring a density layer in front of the magnetic island, is not effected by small density

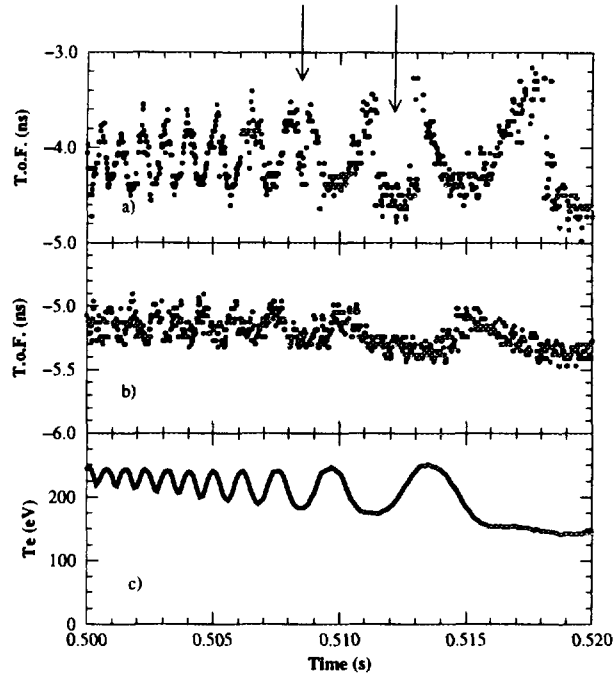


Figure 2. Specific time window from Fig. 1. In a) and b) the flight time of the 33GHz and 29GHz, respectively (1.4 and $1.0 \cdot 10^{19} \text{m}^{-3}$) are plotted. Both MHD oscillations are in counter phase. The two arrows indicate the observed interruptions of the MHD oscillation. For comparison a time trace of the local temperature is given in c). Note that this diagnostic is on a different toroidal position.

gradients and has a maximum oscillation amplitude of 0.4ns . Assuming that the group velocity is roughly $\frac{1}{2}c$ a density layer shift on one side of the island of about 3cm can be calculated. This is in agreement with the observed magnetic island width. However, the 33-GHz-channel (Fig. 2a), which pulses reflect from a density layer behind the magnetic island, a shallow density gradient results in an oscillation of about 1.5ns . A group velocity of $\frac{1}{2}c$ would result in an unrealistic large shift, hence a much lower averaged velocity is expected.

A striking phenomenon concerning the density profile over the magnetic island is observed on the 33GHz-channel (Fig. 2a). As soon as the O-point passes at $t = 0.508\text{s}$, as the magnetic island is about $w = 5 \pm 1\text{cm}$, the oscillation is interrupted and the flight time is suddenly shortened. During the next period, as the width of the magnetic island has increased, the effect becomes even stronger. Similar observations have been made in all discharges with large ($w > 5\text{cm}$) $m/n = 2/1$ magnetic islands, provided that the density in the vicinity of the rational q surface was in the range of the pulsed radar system.

A nice example of this phenomenon is shown in Fig. 3. The pulses launched from the low-field-side are reflected by a layer behind the slowly rotating magnetic island. However, as soon as the O-point appears a secondary reflection layer in front of the first layer is observed. This shows that the density profile is peaked inside the magnetic island. On specific interferometer channels, observing through the magnetic island, non-harmonic MHD oscillations have been found. It was previously shown that non-harmonic oscillations on ECE time traces indicated

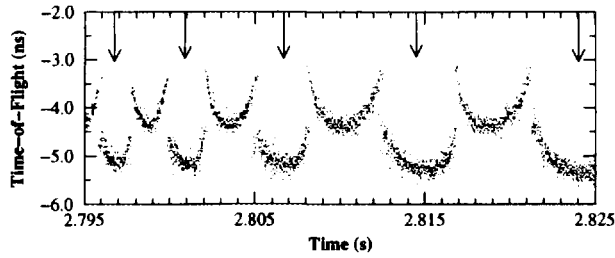


Figure 3. *Two reflection layers are observed by this pulsed radar channel. If the X-point of the slowly rotating magnetic island passes the pulsed radar antenna the pulses are reflected at a layer behind the magnetic island while as the O-point, indicated by the arrows, comes in front of the diagnostic the pulses are reflected from within the magnetic island.*

that the temperature was a flux surface function inside the magnetic island [8].

4. Analysis & Conclusions

Peaking indicates that the density is a flux function inside the magnetic island. However, under the assumption that the perpendicular transport inside the magnetic island is equal to the rest of the plasma, this can only be expected for magnetic islands larger than $w_c = 8.5\text{cm}$. The critical width for which the density becomes a flux function inside the magnetic island can be used as a figure-of-merit for the transport properties inside the island. A decrease of the critical width from 8.5 to 5 cm may indicate a decrease of the perpendicular transport coefficient with almost one order of magnitude (see equation 1).

Additional information on the transport properties may be revealed from the density gradient inside the magnetic island, since it determines via the group velocity the flight time of pulses reflected at the O-point. Hence, different density gradients, will reflect in different measurements. To gain more insight in the measurements, calculations have been performed of the flight time for reflection inside magnetic islands with a specific density peaking. The density peaking is defined as the percentage increase of the density from the separatrix of the magnetic island to its centre. Two different cases are shown in Fig. 4 for a density peaking of 10% and 1%, respectively. The first case approaches the measurements shown in Fig. 2a.

In figure 5 the flight time of pulses reflected at the O-point and X-point are compared for different density peaking inside the magnetic island. It has been assumed in the calculation that the pulses should always reflect in the magnetic island as observed in the experiments. If the density gradient is too low the flight time to the reflection layer at the O-point will be longer than that to the X-point. This is, however, not in agreement with the experimental observations. A reasonable density peaking will be in the order of 10%.

A possible source for the density peaking is the particle pinch[14]. It is believed that such a pinch operates in tokamaks. The inward flux should balance the particle outflow losses. The magnetic island, which may confine particles inside the new nested flux surfaces around the O-point, can be compared with the whole plasma. A comparison between the particle diffusion properties of the magnetic island, \bar{D} , and those of the whole plasma, D , can be made, which

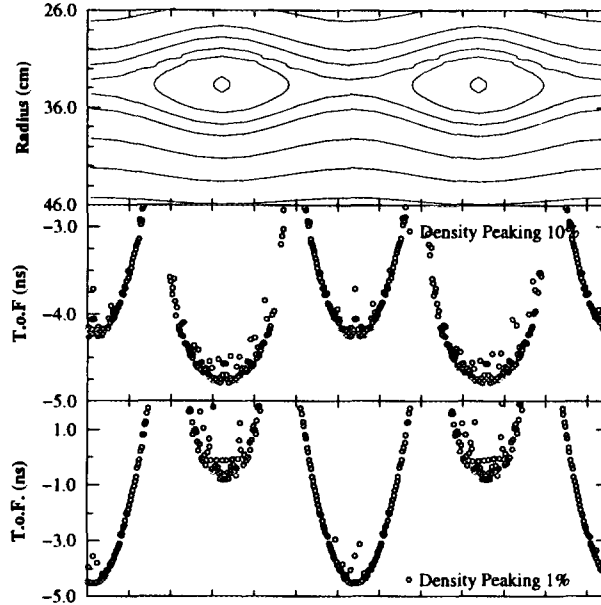


Figure 4. The flight time of a microwave pulse with a single frequency component is calculated. The density profile is perturbed due to the presence of a magnetic island ($w = 6\text{ cm}$) as shown by the density contour plot of constant density at the top. All parameters are identical to the experimental situation from Fig. 1. A parabolic profile, with a maximum determined by the peaking factor, over the magnetic island was assumed. The first case, with a peaking of 10%, can be compared with the ones in Fig. 2 and 3. In the second case, with a peaking of 1% the flight time towards the reflection layer inside the magnetic island is increased which is not in agreement with the observations.

gives [14],

$$\frac{\tilde{D}_{\perp}}{D_{\perp}} \simeq \frac{n_o}{\tilde{n}} \left(\frac{w/2}{a} \right)^2, \quad (2)$$

where n_o is the central density and \tilde{n} the increase of the density from the separatrix to the centre of the magnetic island. It is easily calculated that, if the transport properties are equal both inside and outside the magnetic island, the density peaking, \tilde{n} , can be not more than 1% for magnetic island widths of about $w = 6\text{ cm}$ in TEXTOR-94. In figure 5 the density peaking for an anomalous perpendicular particle diffusion is indicated. It is not in agreement with the observations. To explain the larger observed density peaking one must again conclude that the perpendicular particle diffusion inside the island is lower ($\tilde{D}_{\perp} < D_{\perp}$) by one order of magnitude.

It has recently been reported that in TEXTOR-94 the temperature is found to increase inside $m/n = 2/1$ magnetic islands [8]. Along with the density peaking this provides a strong indication that the confinement inside magnetic islands is improved compared to the overall plasma. Similar indications have been found for the confinement properties inside $m/n = 1/1$ magnetic islands at JET after pellet injection [14]. The present four-channel reflectometer

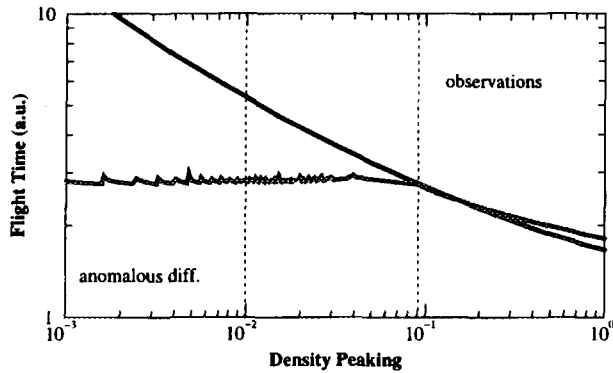


Figure 5. Calculations of flight times of pulses reflected at the O-point or the X-point of a magnetic island $w = 6\text{ cm}$) as a function of the density peaking, i.e. the internal density gradient. The density peaking expected from a anomolous diffusion and the experimental observation are indicated.

system will be upgraded to a 12-channel system. Detailed analysis of half of the density profile may reveal better information on the flux surface perturbations due to magnetic islands in the near future [15].

Acknowledgments

We are acknowledged to *M. de Baar* and *H. van der Meijden* for their advice and technical assistance. This work has been performed under the EURATOM-FOM and EURATOM-KFA association agreements with financial support from NWO, KFA and EURATOM in the framework of the Trilateral Euregio Cluster.

References

- [1] J.A. Wesson, *Tokamaks* (Clarendon University Press, Oxford 1987).
- [2] H.P. Furth, J. Killeen and M.N. Rosenbluth, *Phys. Fluids* **6** 495 (1963).
- [3] R. Fitzpatrick, *Phys. Plasmas* **2** 825 (1995).
- [4] N.J. Lopes Cardozo, *et al.*, *Phys. Rev. Lett.* **73** 256 (1994).
- [5] N.J. Lopes Cardozo, *Trans. of Fusion Tech.* **29** T183 (1996).
- [6] F.C. Schüller, *Plasma Phys. Contr. Fusion* **37** A135 (1995).
- [7] B. Ph. van Milligen, *et al.* *Nucl. Fusion* **33** 1119 (1992)
- [8] P.C. de Vries *et al.*, *Plasma Phys. Contr. Fusion.* **39** 439 (1997).
- [9] C Laviron *et al.*, *Plasma Phys. Contr. Fusion* **38** 905 (1996).
- [10] C.A.J. Hugenholtz and S.H. Heijnen, *Rev. Sci. Instrum.* **62** 1100 (1991).
- [11] S.H. Heijnen, *et al.*, *Rev. Sci. Instrum.* **66** 419 (1995).
- [12] A.J.H. Donné, S.H. Heijnen, C.A.J. Hugenholtz, to be published in *Fusion Eng. and Design*.
- [13] S.H. Heijnen, *Pulsed Radar Reflectometry* (Thesis University Utrecht, Utrecht 1995).
- [14] J.A. Wesson, *Plasma Phys. Contr. Fusion* **37** A337 (1995).
- [15] C.A.J. Hugenholtz *et al.*, *Proceedings of this conference*.

MULTI-CHANNEL PULSED RADAR SYSTEM FOR THE TEXTOR TOKAMAK

C.A.J. Hugenholtz¹, J.F.M. van Gelder¹, A.J.H. Donné¹, B.S.Q. Elzendoorn¹, G.P. Ermak³,
W. Kooijman¹, H.A. van der Laan¹, G. Land¹, H.J. van der Meiden¹, A.J. Putter¹,
H.J.F. van Ramele¹, P.C. de Vries¹, G. Waidmann², F. Wijnoltz¹

Trilateral Euregio Cluster

¹*FOM Instituut voor Plasmafysica 'Rijnhuizen', Association EURATOM-FOM
P.O. Box 1207, 3430 BE Nieuwegein, The Netherlands*

²*Institut für Plasmaphysik, Forschungszentrum Jülich GmbH., Association EURATOM-KFA,
P.O. Box 1913, 52425 Jülich, Germany*

³*Institute of Radiophysics and Electronics of the Ukraine,
Ak. Proskura st. 12, Kharkov 310085, Ukraine*

Abstract

A ten-channel pulsed radar reflectometer is under development for the TEXTOR Tokamak. The frequency range is 18 GHz to 57 GHz corresponding to pulse reflections at layers with critical densities between 4×10^{18} and $4 \times 10^{19} \text{ m}^{-3}$. Two variable frequency channels (35 - 36 GHz and 49 - 51 GHz), in combination with two fixed frequency channels (36 GHz and 51 GHz), are available to perform correlation measurements on density fluctuations.

All sources have an individual modulator to produce a 1 ns radar pulse and a 20 ns LO-pulse. The 20 ns LO-pulse selects a time window for the corresponding radar channel. Profile measurements with an accuracy of 70 ps will be possible with a 2 MHz repetition rate, giving 64 Mb of data points. Correlation measurements will run at a 10 MHz repetition rate. An embedded controller in VME will store the data with a speed of 20 Msamples/s. A custom-made pulsed radar controller will manage the system. Remote operation with a data link to FOM-Rijnhuizen will be possible.

Introduction

In pulsed radar reflectometry, short microwave pulses in the order of 1 ns are launched into the plasma [1,2]. Depending on the radar frequency and the plasma parameters, the pulse is reflected by a critical density layer and received again by the diagnostic equipment. The basic quantity that is measured by the pulsed radar diagnostic is the flight time of the microwave pulse between transmission and detection.

Although the physical mechanisms underlying the various reflectometry techniques are basically the same, each technique has some specific merits and drawbacks. With the new set-up, an upgrade of the four-channel pulsed radar described by Heijnen [3], the amount of drawbacks is reduced. The number of channels is increased to ten and two variable frequency channels are

added to the system. The two variable frequency channels can be used in combination with two fixed frequency channels to perform correlation measurements and to study MHD modes [4]. The pulse repetition frequency has been increased from 500 kHz for four channels to 2 MHz for ten channels in the upgraded system. The flight time is recorded with an accuracy of 70 ps, corresponding to a spatial resolution of 1 cm when reflected from a metal mirror. The accuracy can be further improved to 35 ps. One of the drawbacks of the pulsed radar technique is the fact that fluctuations and shallow density gradients give additional pulse broadening, which has an effect on the flight time measurement. The chosen pulse length of 1 ns is a compromise between the accuracy of the time of flight measurement and the pulse broadening. In the present system, the flight time is measured between the 50% level of the leading edge of the transmitted and received pulse. By clocking also the 50% level of the falling edge a measurement of the pulse width could be obtained. This would provide additional information on the density gradient.

Microwave hardware

The outline of the microwave system of the TEXTOR pulsed radar reflectometer is given in Fig. 1. The system consists of three main parts:

- two homodyne channels at 18 and 24 GHz in K-band waveguide,
- four heterodyne channels at 29, 33, 36, and 39 GHz in Ka-band waveguide,
- four heterodyne channels at 47, 51, 54, and 57 GHz in U-band waveguide.

The Ka-band sources will act as LO-oscillator for the U-band receiver and the U-band sources will act as LO-oscillator for the Ka-band receiver. The Ka-band and U-band frequencies are alternately used as RF-pulse and LO-pulse. After mixing, the heterodyne channels give an 18 GHz IF-pulse. Two channels with variable frequencies around 36 and 51 GHz are added to the system to perform correlation measurements with the corresponding fixed frequency channels. The properties of these systems will be described later.

The microwave sources are Impatt oscillators with an output power of approximately 200 mW in the K-band, 200 to 400 mW in the Ka-band, and 100 mW in the U-band. All sources have an individual pulse forming modulator. The advantage (a.o.) is the possibility to choose for a high repetition frequency. The modulator consists of a circulator and a varactor diode. For both the 1 ns RF-pulse and the 20 ns LO-pulse, special drivers have been constructed that can produce pulses with a repetition frequency of 20 MHz. The 1 ns pulse is Gaussian shaped. The pulsed LO selects a certain time window in which the heterodyne receiver is active. The output voltage of the LO driver pulses are individually adjustable, which gives the possibility to tune the amplitude of the IF-pulses to the same level at the video detectors. The modulators need a driver voltage of 5-10 V. The 1 ns and 20 ns drivers are combined in a single device with a 50 Ohm output impedance and a DC level control. This level control (0 V to -1 V) can be used to tune the various modulators to a maximum isolation in the off-state. An isolation of 30 dB for the lower frequencies (29 GHz - 47 GHz) and 25 dB for higher frequencies (51 GHz - 57 GHz) is possible. The insertion loss of the modulators varies from 1.2 dB to 2 dB.

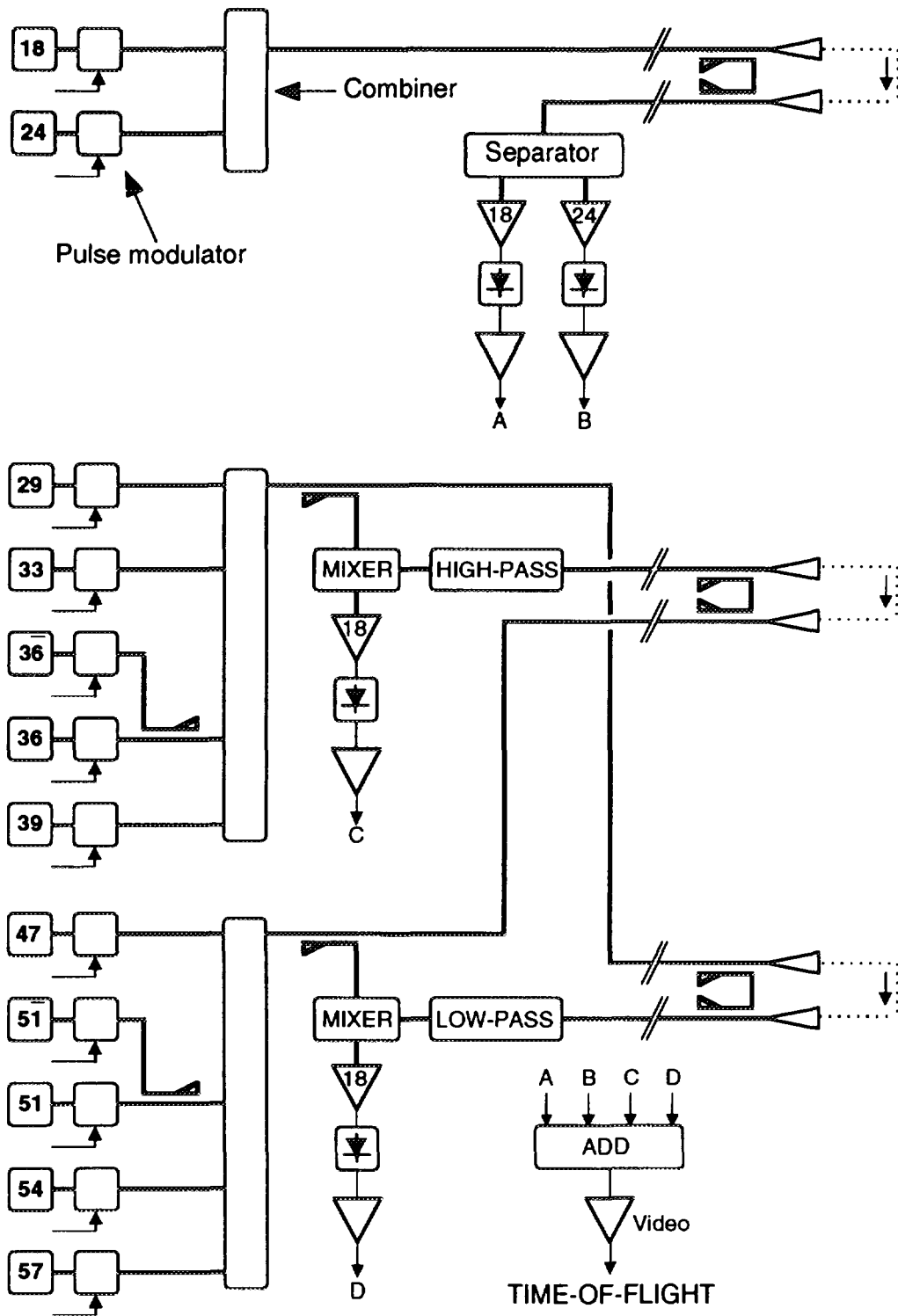


Fig. 1: Block diagram of the ten-channel pulsed-radar diagnostic, extended with two channels for correlation measurements. All frequencies are in GHz. The sweepable sources are indicated with a minus sign.

The channels in the three different sections are merged by means of combiners. The combiner consists of resonant cavities and circulators. As an example, the schematic of the Ka-band combiner is shown in Fig. 2. The main advantage over conventional directional couplers is the very low insertion loss of approximately 1.5 dB. The frequency bandwidth of the different input channels is approximately 2 GHz. In the original RTP set-up [3] a single-pole four-throw PIN-switch was used. This switch has an insertion loss of 5 dB and cannot be used at the high repetition frequency of 20 MHz.

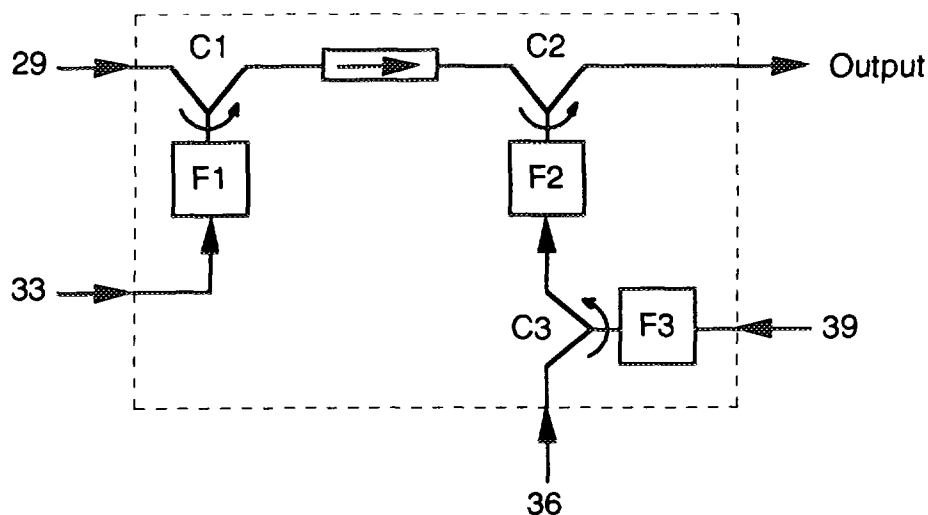


Fig. 2: Schematic of the Ka-band combiner to merge the 29, 33, 36, and 39 GHz channels. C1, C2, and C3 are circulators. F1, F2, and F3 are filters.

For the K-band system homodyne detection is chosen because of the relatively high pulse power of 150 mW and the lower waveguide losses as opposed to the Ka-band and U-band systems. Frequency selectivity is obtained with a frequency sensitive separator in combination with 18 GHz and 24 GHz amplifiers¹. Both amplifiers have a bandwidth of 1 GHz. In the Ka-band and U-band systems heterodyne detection takes care of frequency selective reception. The conversion loss of the Ka-band mixer² is 7 dB for 29 GHz to 36 GHz and 12 dB for 39 GHz. The 12 dB loss may be too high and should be improved. The conversion loss of the U-band mixer³ varies from 5 dB at 47 GHz to 7.5 dB at 57 GHz. The IF-amplifiers in the two heterodyne systems have a gain of 30 dB⁴ for the Ka-band and 38 dB⁵ for the U-band. Both amplifiers have a noise figure of 4 dB. Detection is performed with Schottky barrier detectors⁶. A simple antenna and waveguide system is chosen using separate transmitter and receiver antennas and oversized X-band waveguides. Oversized waveguides are necessary to keep the losses and the pulse broadening as low as possible.

¹) MITEQ: AFS6-18001900-40-10p and AFS4-24502550-40-10p

²) MILLITECH: MCP-28C-020L

³) FARRAN: BMF-19/28S

⁴) MITEQ: AFS5-15002000-40-10p

⁵) AVANTEK: AAMT-20036

⁶) MILLITECH: DXP-42-01

The distance from the antennas to the radar set-up is about 10 meters. Two echo pulses will be received from each transmitted radar pulse. The first one is a start pulse travelling via the bypass and the second one is the stop pulse reflected at the critical density layer. Jitters in the electronics are irrelevant in this set-up. The minimum time between the two pulses is 4 ns which is determined by the constant fraction discriminator (CFD) in the video section of the set-up (Fig. 3). The longest time delay is obtained from reflections at the far wall when the density rises to near the critical density (n_c). The time delay with plasma densities near n_c is about 6 ns longer than the time delay without plasma. Calibration is performed using the TOF of the reflected pulse at the far wall. The bypass consists of two 10 dB directional couplers, an attenuator and a short section of waveguide. The position of the bypass must be chosen in such a way that the start and stop pulse coincide with the 20 ns LO-pulse. Tuning is possible by adjusting the length of the waveguide. The attenuator must be set such that the start and stop pulse have approximately the same power level. After detection, the four video channels (A, B, C, and D) are pre-amplified with pre-settable amplifiers. The four signals are added and then amplified to a level of about 5 Volts and fed to a constant fraction discriminator (CFD)⁷. The two output pulses will start and stop a time-of-flight counter (TOF), developed at Rijnhuizen using eight parallel gated counters [3,7]. The data produced by the TOF-counter is fed to a data acquisition system built in VME. The data handling, storage etc. will be described in a separate section.

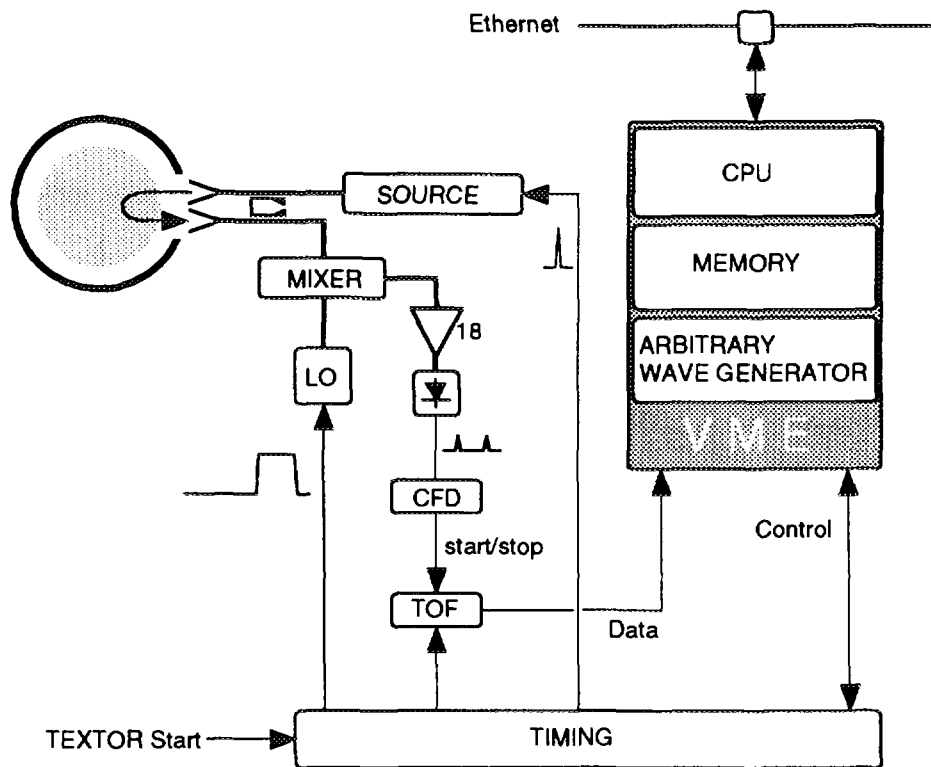


Fig. 3: Timing, control and data storage.

⁷) EG&G ORTEC, Model 9307

Timing and measurements

A number of measuring modes are available. The first mode is a profile measurement with ten channels. Figure 4 shows the timing diagram. From this diagram it can be seen that the timing unit is quite complex.

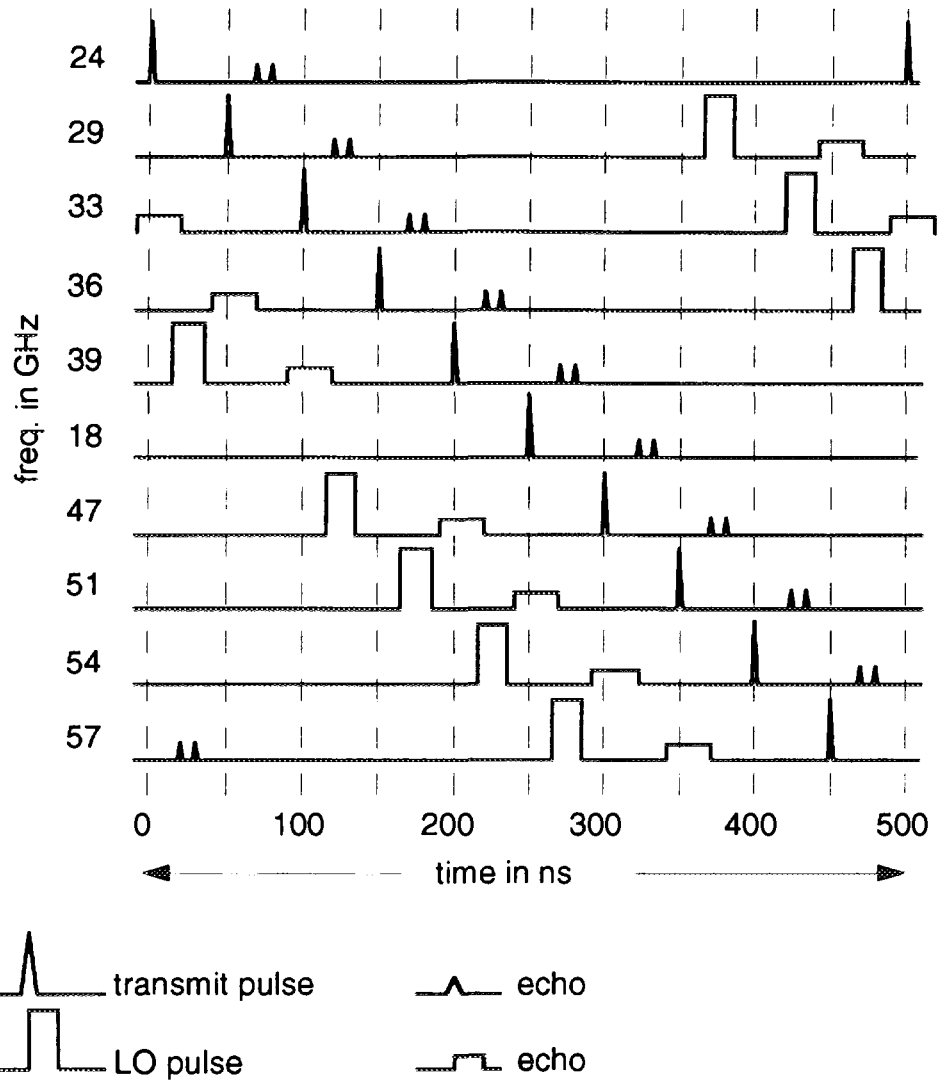


Fig. 4: Timing diagram for a 10-channel profile measurement.

Each radar and LO pulse can be tuned individually by means of programmable time delay settings. During the existence of a LO pulse only one pair of matching start and stop pulses is present (e.g. the 29 GHz LO pulse matches with the 47 GHz radar pulses). False mixing may occur when a transmitted pulse acts as LO at a time an echo from the original 20 ns LO-pulse coincides in time. However, all these mixing products fall outside the bandwidth of the 18 GHz IF-amplifier. For safety, a low-pass filter, with a cut-off frequency of 40 GHz, in the receiver of the Ka-band, and a

high-pass filter in the U-band receiver are added. The storage capacity of the memory is 64 Mb corresponding to a maximum measuring time of 3.2 s at a sampling frequency of 20 MHz. This 3.2 s time interval can be chosen freely within the TEXTOR discharge, which can last as long as 10 s. It is also possible to run at a sampling rate of 10 MHz or 5 MHz and measure over 6.4 s or 12.8 s. Other measuring modes are possible when only one group of four channels is used (e.g. 47, 51, 54, and 57 GHz). One measuring cycle will only take 200 ns in the four channel modes. Real quick-firing of pulses occurs in the correlation mode, where only two channels are involved (Fig. 5).

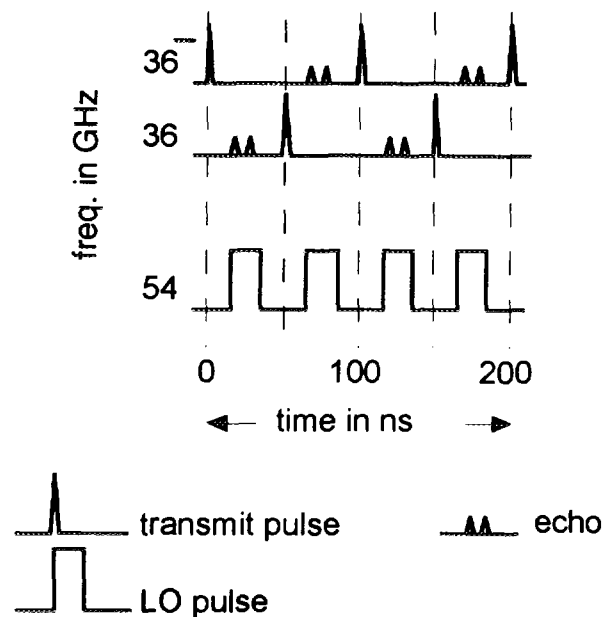


Fig. 5: Timing diagram for the 36 GHz and 36' GHz correlation measurement.

For the correlation measurements two sweepable sources are available (36 and 51 GHz) with a sweep range of 1 GHz. The fixed and variable source alternately transmit a 1 ns radar pulse. These pulses are processed in the same way as in the profile measurements. For both sources the same LO is used. During the discharge the variable source can be swept by tuning the driver voltage. This voltage is generated by means of an arbitrary wave generator (AWG). The number of frequency steps (max. 64), the number of samples per step, the sweep frequency, and the start and stop frequency can be chosen freely within the limits of the clock frequency and the electronic hardware.

Software for control, data handling, and storage

The pulsed radar diagnostic will be regarded as a subsystem of TEXTOR. This means that the diagnostic should be synchronised with the TEXTOR control system. Four timing stages are distinguished:

- inter-pulse (diagnostic can be used),
- pre-pulse (all devices are initialised and ready to accept a pulse),
- start-pulse (radar start),
- post-pulse (the data in the memory module can be stored in a database).

There is a possibility to work stand alone for test purposes. The data acquisition of the pulsed radar diagnostic is (whenever possible) built up from commercially available components like a Solaris v2.4 operating under UNIX with a VME-bus system (Fig. 6). The embedded controller⁸ clocks the data via the RS485 input into a dual-port memory. A VSB VME-bus is the connection between the modules. In this way the memory-module acts as a memory extension of the UNIX system. The pulsed radar controller and the arbitrary waveform generator are developed by FOM-Nieuwegein.

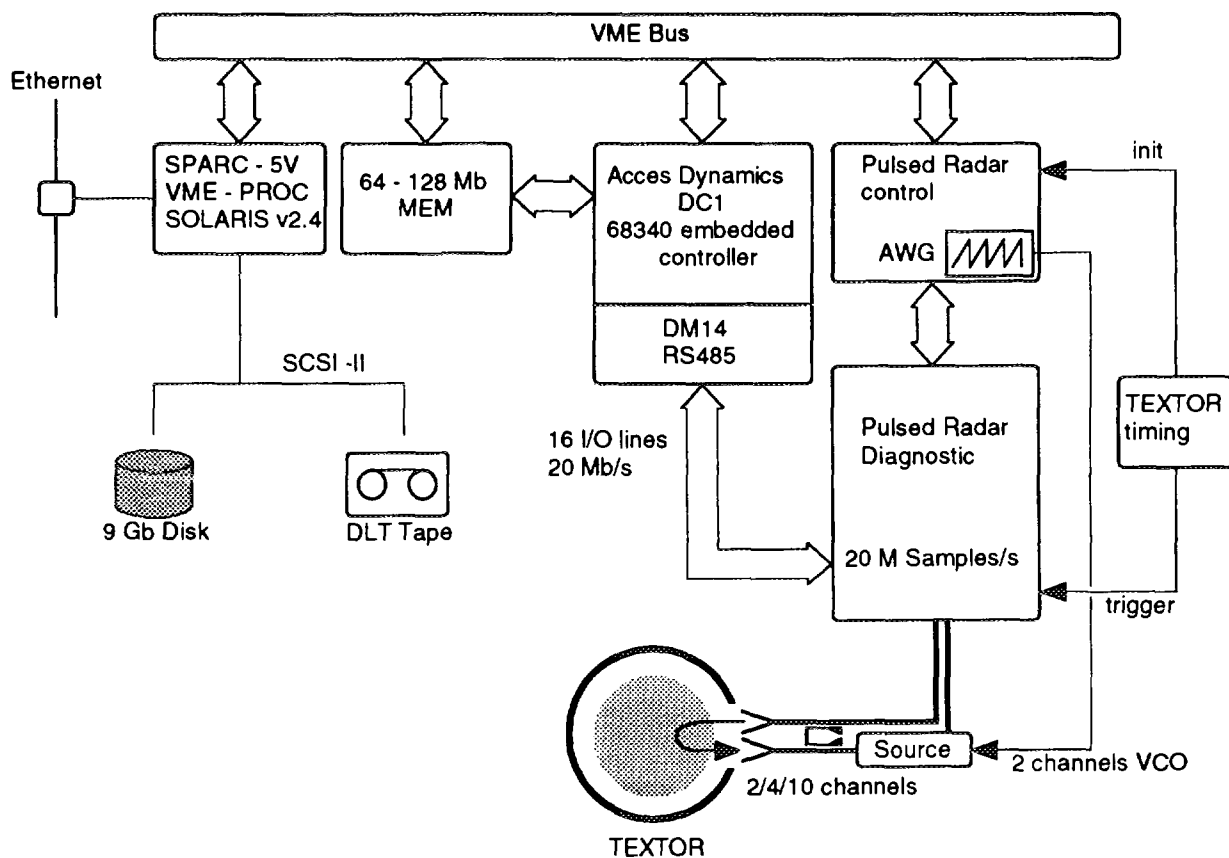


Fig. 6: Control, data handling, and memory systems.

⁸) Acces Dynamics, DC1.

The software for the user application will be in IDL (Interactive Data Language). This language is used for several reasons: FOM-Nieuwegein and IPP-Jülich both have experience with this tool. It is easy to make menus and buttons, to visualise the data, to do calculations with the IDL-standard library, and to make connections with software written in FORTRAN or C.

The communication between the existing local area network (LAN) in Jülich, and the FOM-Nieuwegein LAN is necessary for the intended Remote Control Room. A demonstrator for this project is being developed at the University of Utrecht. Because of the remote control room, the data will be distributed over several sites. CORBA-standardisation will be used to connect the different computer systems (CORBA: Common Object Request Broker Architecture). CORBA is a strongly object-oriented protocol. The basic idea is that CORBA transforms objects to the local formats and takes care of the transport to other computer systems. This communication and data-conversion is hidden from the user. The data will be stored in an Object Oriented Distributed Database. By standardisation of the data handling system, extension of the subsystems with new application software will be relatively simple.

Acknowledgement

The work described in this paper was performed as part of a research programme of the 'Stichting voor Fundamenteel Onderzoek der Materie' (FOM) with financial support from the 'Nederlandse Organisatie voor Wetenschappelijk Onderzoek' (NWO) and EURATOM.

References

- [1] C.A.J. Hugenholtz and S.H. Heijnen, *Pulsed radar technique for reflectometry on thermonuclear plasmas*, Rev. Sci. Instrum. **62** (1991) 1100.
- [2] V.F. Shevchenko *et al.*, *Plasma study at T-11M tokamak by microwave pulse radar reflectometer*, Proc. 20th Conf. on Contr. Fusion and Plasma Phys., Lisbon (1993), Part III, p. 1167.
- [3] S.H. Heijnen, *Pulsed Radar Reflectometry*, Thesis University of Utrecht, Utrecht (1995).
- [4] A.J.H. Donné, S.H. Heijnen, C.A.J. Hugenholtz, *Fusion Engineering and Design* (1997), Accepted for publication.
- [5] S.H. Heijnen *et al.*, Rev. Sci. Instrum. **66** (1995) 419.
- [6] P.C. de Vries *et al.*, Submitted to Phys. Lett.
- [7] M.J. van de Pol, S.H. Heijnen, C.A.J. Hugenholtz, Proc. of the IAEA Technical Committee Meeting on Microwave Reflectometry for Fusion Plasma Diagnostics, JET (1992) p. 228-235.

**NEXT PAGE(S)
left BLANK**

AM Reflectometer Density Profile Measurements on TdeV

D. Pinsonneault,^{a)} B. Quirion,^{b)} J.L. Lachambre,^{c)} C. Legros^{d)}

Centre canadien de fusion magnétique, 1804 Boul. Lionel-Boulet, Varennes, Québec, Canada J3X 1S1

Abstract

The TdeV AM reflectometer measuring edge electron density profiles from the X-mode upper cut-off layer has recently been modified. In addition to the original reflectometer channel operating at 33-50 GHz and amplitude modulated at 201 MHz, a second at 50-75 GHz with a 200 MHz amplitude modulation is now operational. The first channel probes the scrape-off layer (SOL) while the second extends the spatial coverage up to typical values of $r/a \sim 0.9$. Densities of $1 \times 10^{18} \leq n_e (\text{m}^{-3}) \leq 3 \times 10^{19}$ can be measured for 1.8 T operation. These two channels are coupled to a single transmission line with one set of antennae. Two distinct modulation frequencies were adopted to enable simultaneous detection. Although these modulation frequencies correspond to plasma measurements with two slightly different sideband spatial separations, good agreement between the two channels has been found. The reflected envelopes, carrying the time delay information, are downconverted to a 1 MHz IF signal to facilitate narrow-band filtering and phase detection. To improve the performance of the detection system, low-noise amplifiers and limiting amplifiers are presently being used. Additionally, filters with 1 kHz bandwidths presently allow for faster fullband sweeps. As a result, density profiles for various plasma conditions have recently been measured. Also, reflectometry data, such as the density scale length and the density at the separatrix, are provided as boundary conditions for the inversion of FIR interferometer data to obtain accurate density profiles. The design and construction of the AM reflectometer will be described and recent experimental results will be presented.

1. Introduction

The AM reflectometer¹ operating on TdeV has recently been modified to accommodate the geometry of the upgraded TdeV-96². TdeV-96 is a divertor tokamak which now operates with higher toroidal fields up to 2.0 T and with smaller major and minor radii of 0.83 m and 0.22 m respectively. The divertor was redesigned for higher power handling capability and to allow for a more flexible divertor geometry. For biasing purposes, the divertor plates are electrically insulated from the vacuum vessel. For the results presented here the 1.3 MW lower hybrid system which is generally used for both heating and current drive was not operational. The X-mode upper cut-off layer is used. To investigate fully the edge region under these new operating conditions, a second channel covering the frequency range of $50.0 \leq f (\text{GHz}) \leq 75.0$ and amplitude modulated at 200 MHz has been added to the existing first channel operating at $33.0 \leq f (\text{GHz}) \leq 50.0$ with a 201 MHz amplitude modulation. The first channel probes the scrape-off layer (SOL) while the second extends the spatial coverage up to typical values of $r/a \sim 0.9$. Densities of $1 \times 10^{18} \leq n_e (\text{m}^{-3}) \leq 3 \times 10^{19}$ can be measured for 1.8 T operation. Additional modifications to the detection system have also been made; low-noise amplifiers and limiting amplifiers considerably improve the power dynamic range and filters

^{a)}INRS-Énergie et Matériaux, Varennes, Québec, Canada.

^{b)}Décatron, St-Bruno, Québec, Canada.

^{c)}Hydor-Québec, Varennes, Québec, Canada.

^{d)}Inspectech 2000, St-Sulpice, Québec, Canada

with 1 kHz bandwidths presently allow for faster fullband sweeps. In vessel calibration checks proved to be essential for optimizing the final detection stage. The two channel reflectometer will be described in detail and recent experimental results will be presented.

2. AM reflectometer

A block diagram of the two channel AM reflectometer is shown in fig. 1. Two BWO sources operating in the frequency range of 33-50 GHz and 50-75 GHz are modulated in amplitude by two separate PIN diode modulators at 201 and 200 MHz respectively. Two distinct modulation frequencies were adopted to enable simultaneous detection. The additional 200 MHz source needed is obtained by mixing signals from the 201-MHz generator with that of a 1-MHz reference and by filtering the resulting signal (BW:400 kHz at 200 MHz). Each PIN modulator operates with a DC bias of +10V and a RF modulation signal of 13 dBm leading to an average carrier insertion loss of 6 dB. At the cut-off, these frequencies yield a radial separation between the carrier and the sidebands of the launched AM spectra of the order of 1 mm for typical plasma conditions. For each channel, the carrier frequency is determined by applying a control voltage to the appropriate BWO power supply and is accurately measured by monitoring the high voltage biasing of the helicoidal grid of the BWO head. This frequency control technique is valid for sweep rates ≥ 25 ms. To ensure measurements along the same line of sight, the two channels are coupled through a diplexer to a single WR-22 waveguide run. Isolators are introduced between the PIN modulators and the diplexer to prevent modulation crosstalk between the channels in the vicinity of 50 GHz. As the BWOs, the isolators were shielded to avoid stray magnetic fields, while the PIN modulators proved to be insensitive to these fields. Two separate standard 25-dB gain antennae are used, one as a launcher and the second as a receiver. The apertures are aligned vertically on each side of the torus midplane at ~ 23 cm from the last closed flux surface and are oriented to enable measurements from reflections on the midplane. A 0.09 mm thick silica window provides the vacuum seal. The total emitted power is approximately -10 dBm averaged over the full bandwidth and coupling losses of ~ 25 -30 dB between the antennae were measured with a metallic reflector. At the receiving antenna, the two reflected signals are separated into their respective bandwidths by a diplexer and detected with two distinct DC biased detectors. A 110 μ A biasing current is applied to optimize the output signal level. These signals are filtered and pre-amplified immediately after detection to minimize sensitivity to EM pickup. A shielded coaxial cable carries the resulting signals to the electronics located 8 m from the machine.

The detected signals are frequency-downconverted to 1 MHz for final detection with low-frequency limiting amplifiers and phase detectors. This frequency downshift is performed by simply mixing the detected 201-MHz signal with the 200-MHz reference source for the 33-50 GHz channel and by mixing the detected signal at 200-MHz with that from the 201-MHz oscillator for the 50-75 GHz channel. At this point, these signals are separately filtered with a BP filter (BW: 1 kHz at

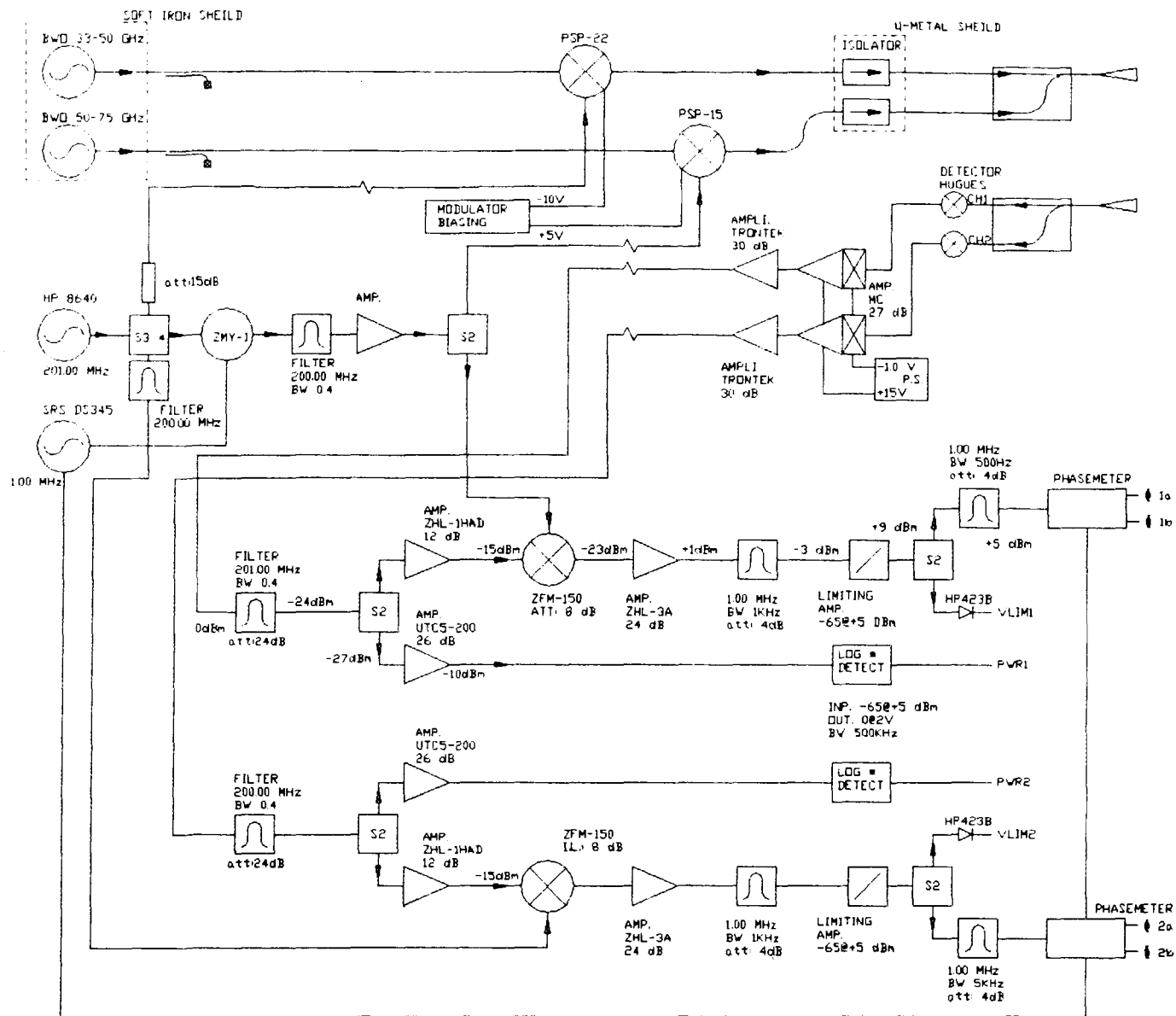


Figure 1: Block diagram of the amplitude modulation reflectometer installed on Tdev-96.

1 MHz). In order to drive the phasemeters with nearly constant amplitude signals, high precision limiting amplifiers have been implemented with a dynamic range of -65 to +5 dBm and with an overall phase variation $< \pm 3.0^\circ$. Also, a logarithmic amplifier detector with an identical dynamic range presently monitors the RF reflected power to verify that the limiting amplifiers operate in their constant-phase regime. Finally, for each channel, two phasemeters measuring out of phase (Φ and $\Phi + \pi$ outputs) allow precise phase reconstruction at $0-2\pi$ phase transitions. At these modulation frequencies, the plasma phase excursions are of the order of 1 fringe. The phase outputs are digitized at a sampling rate a few times higher than the IF bandwidth (5 kHz).

3. Calibration

A frequency calibration was performed by changing the voltage at the input of each BWO power supply while accurately measuring the frequency at the output of the BWO heads with a frequency meter and by monitoring the corresponding high voltage. These measurements were performed in both fixed and swept frequency modes; for frequency ramps at different sweep rates, the frequency uncertainty was within 0.2 GHz. These meters will be permanently incorporated into the system for rapid frequency checks.

Phase calibration measurements made against the inner vacuum wall graphite limiter are used to determine the phase delay measurements due to propagation through the waveguide runs and electronics. Accurate measurements are necessary because the measured plasma phase shifts are usually very small. Calibration checks were made with a movable retractable mirror which can be positioned closer to the antennae, at distances comparable to the lowest frequency cut-off position. This mirror was also used to adjust the overall power gains as well as to verify near field phase measurements. Together these measurements provide the extreme values of the reflected power and phase fluctuation levels caused by multiple reflections between the antennae and the reflecting

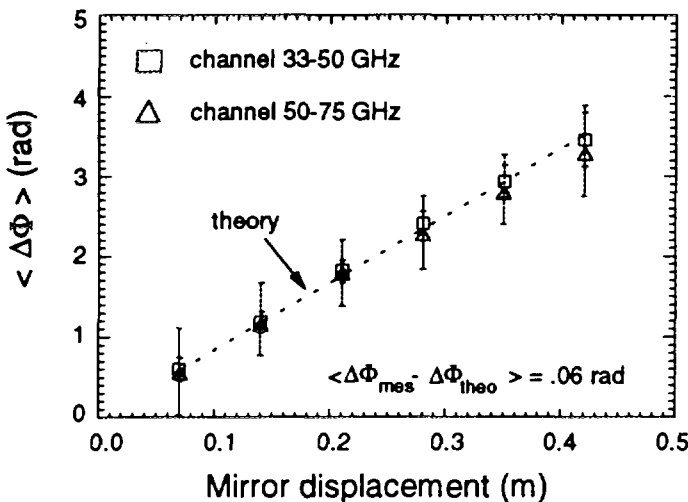


Figure 2: Total phase shifts for different mirror positions.

surfaces. The accuracy of the phase measurements was determined by measuring the reflection from a mirror located inside the vacuum vessel at different radial positions from the antennae. For each mirror position, the BWO's were swept over their full bandwidths. The phase shifts relative to the position closest to the antennae were then averaged over the swept bandwidth and are plotted for different mirror positions in figure 2. The resulting phase varies linearly with mirror displacement as predicted by

$\Delta\phi_{\text{theo}} = 2\Omega\Delta L/c$ (Ω is the modulation frequency and ΔL is the mirror displacement). The error bars shown are the RMS value of the phase shifts around their mean values. These large error bars are believed to be due to interference between the antennae and the mirror at the carrier frequencies. Fortunately, during a fullband sweep, the number of these interferences is large; their average phase value is close to zero and therefore do not influence the overall profile reconstruction but create spurious structure on the profile and thus must be reduced. The maximum phase error obtained from these error bars is about 17° , but since the interferences are largely removed by low pass filtering before profile reconstruction the effective phase error is estimated to be less than 5° .

The overall power response of the final detection stage was determined by introducing a phase calibrated variable attenuator which provided 0-80 dB attenuation with a phase error $< 2^\circ$. The output of the phasemeter showed an almost flat phase response ($\pm 3^\circ$) from 0 dBm down to -60 dBm, a value approaching the limiting amplifiers lower limit of operation, thus yielding a power dynamic range of about 60 dB for the entire system.

4. Results

Examples of the reflectometer signals are given in figure 3. Signals from the two phase detectors measuring out of phase are shown for both channels during a single fullband sweep. A total phase shift of about 1 fringe is often measured with a $0-2\pi$ transition somewhere during the sweep. This transition is accurately corrected for by using the other phase output which shows no transition at the same time. As expected, larger phase noise is apparent at low frequencies on the 33-50 GHz channel (figure 3c) since fluctuation levels increase towards to edge region.

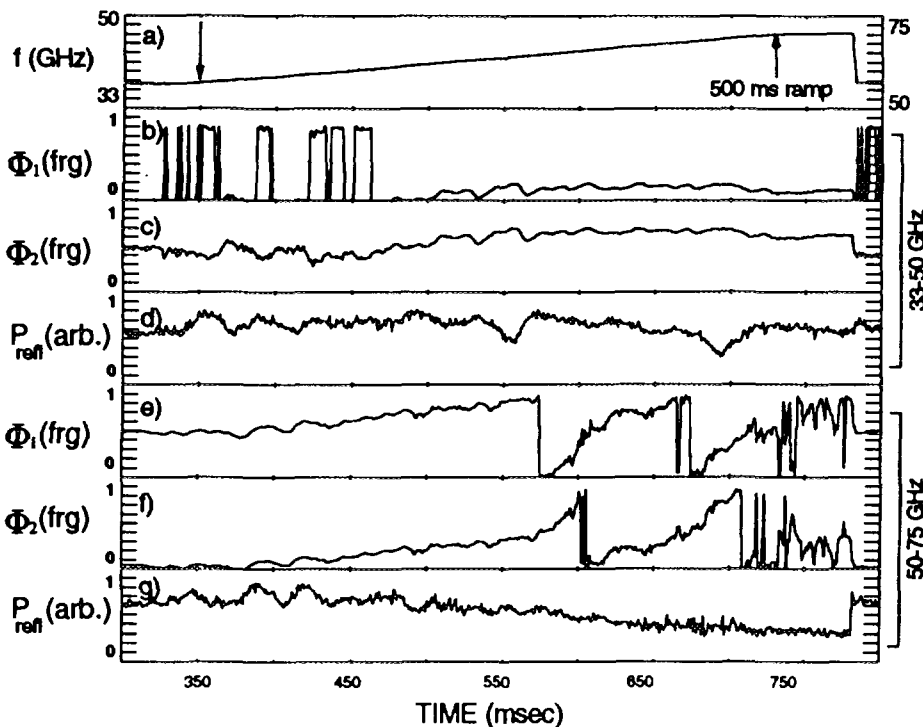


Figure 3: AM reflectometry measurements during an ohmic discharge, pulse 30361 ($I_p=219\text{kA}, B_T=1.6\text{T}$) showing overall behaviour during (a) 500 ms frequency ramp: (b),(c) and (e),(f) phase shifts Φ_1 and Φ_2 measured with the two phase detectors out of phase for the 33-50 GHz and the 50-75 GHz channels respectively, and (d), (g) power measurements P_{ref} with variations due to density fluctuations and interferences.

A shot to shot calibration against the inner wall graphite limiter, located 76.0 cm in front of the antennae, provide phase delay measurements due to propagation through the waveguide runs and electronics. The plasma phase shift is obtained by subtracting this calibration signal from the total measured phase shift and is shown in figure 4a.

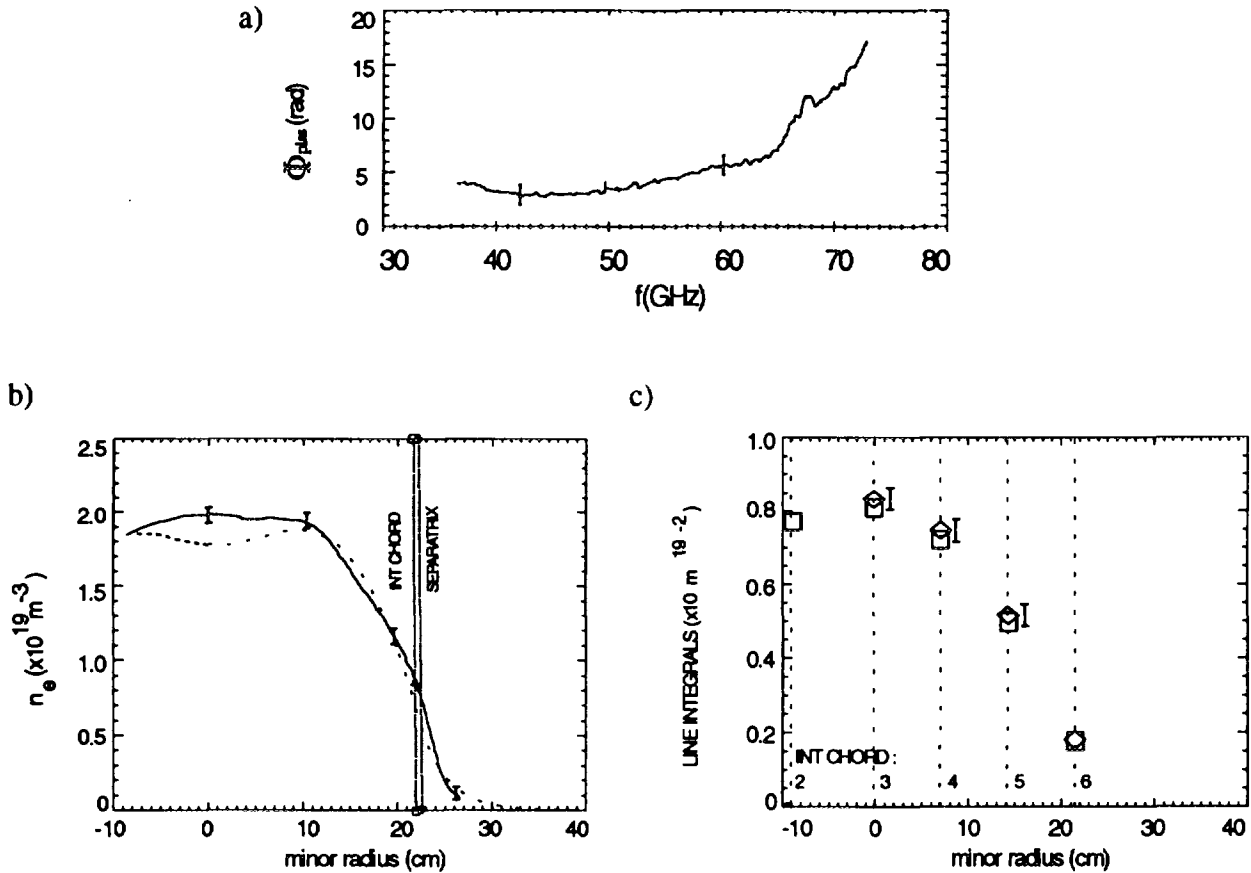


Figure 4: (a) Plasma phase shifts Φ_{plas} as a function of the carrier frequency for the two channels, pulse 30361 ($I_p=219$ kA, $B_T=1.6$ T, $n_e=1.6 \times 10^{19} \text{ m}^{-3}$), (b) reconstructed reflectometer density profile (full line) and the interferometer profile (dotted lines). The vertical lines show the position of the outermost interferometer chord and the plasma minor radius. (c) Reflectometer line integrals (lozenges) calculated at the positions of each interferometer chords are shown for comparison with the measured interferometer line integrals (squares). No error bar is shown at the position of the interferometer's outermost chord which is used to position the reflectometer profile.

Figure 4a clearly shows the fine phase continuity at 50 GHz where the two independent channels overlap. This phase information allows for density profile reconstruction as described in detail in reference [4]. The uncommon feature in our inversion procedure is that the inversion starting point is chosen so that the line-integrated density along a vertical chord, calculated with the flux surface

topology given by an equilibrium code, is the same as that inferred from the outermost chord of the submillimeter interferometer⁵, located at $r=0.22$ m (for $R_0=0.83$ m). The resulting density profile is illustrated in figure 4b along with the interferometer density profile. These were the only available diagnostics for edge density profiles during this measurement campaign. Also, these density profiles shown were measured at a low magnetic field of 1.6 T and an average density of $1.6 \times 10^{19} \text{ m}^{-3}$, conditions under which the reflectometers radial measurements extend inwardly beyond the magnetic axis allowing for a more interesting comparison. The general agreement between the two profiles is satisfactory. Moreover, the reflectometer profile shows no hollow at the magnetic axis, a feature often obtained on the interferometer profile. Also, a clear change in the density gradient is observed about the separatrix, demonstrating a sudden change in transport parameters (and mechanisms) when moving from closed to open flux surfaces. A more in-depth comparison between the calculated line integrals obtained by inverting the reflectometer profile with the interferometer line-integrated data (accuracy of 1%) is shown in figure 4c. Differences of less than 3% are obtained for all interferometer chords intercepted by the reflectometer profiles. This gives us confidence in the overall phase measurement system. At the other extreme, figure 5 shows density profiles at a higher density ($B_T=1.6$ T, $n_e=7.0 \times 10^{19} \text{ m}^{-3}$), in which case the measurements from the reflectometer scarcely reach the position of the interferometer's outermost chord.

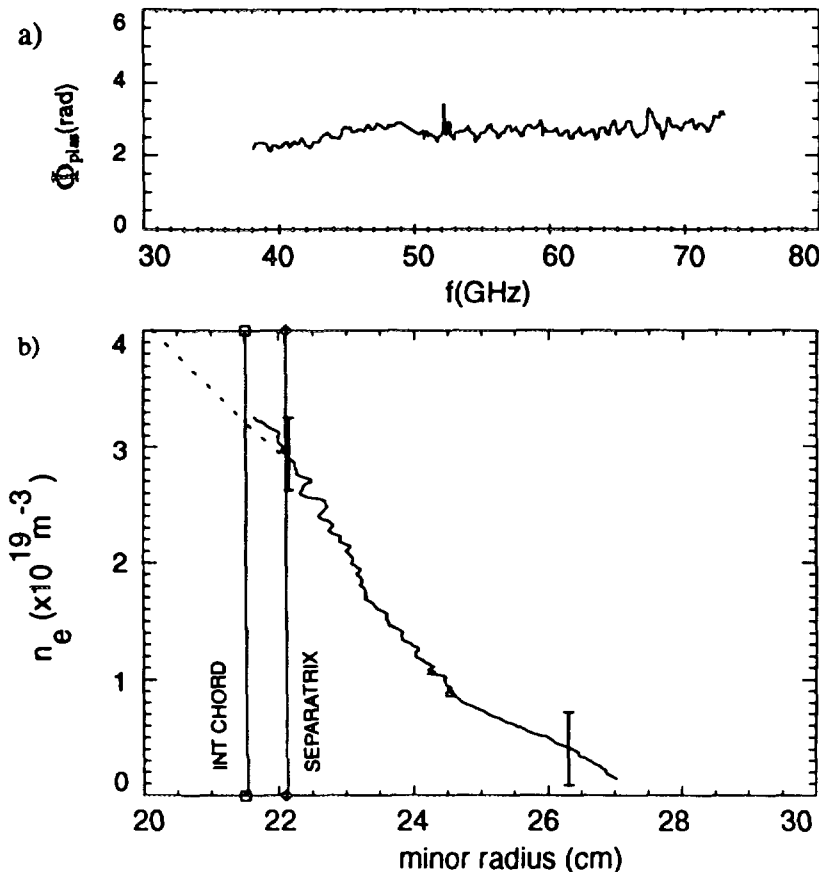


Figure 5: (a) Plasma phase shifts Φ_{plas} as a function of the carrier frequency for the two channels, pulse 30359 ($I_p = 219$ kA, $B_T=1.6$ T, $n_e=7.0 \times 10^{19} \text{ m}^{-3}$). (b) reconstructed reflectometer density profile (full line) and the interferometer profile obtained using reflectometry data (dashed lines). The vertical lines show the position of the outermost interferometer chord and the plasma minor radius.

Finally, to illustrate the sensitivity of the reflectometer measurements, density profiles for three divertor plate biasing voltages are given in figure 6. For negative biasing, a significant drop in the edge plasma e-folding length is observed. This is consistent with similar measurements previously made with the lithium ablation diagnostic⁶. A pronounced discontinuity at around 0.17 m is also observed on all three reflectometer profiles. This is caused by a large spurious structure present on the phase signal at 68 GHz which is the cut-off frequency corresponding to this radial position. This structure is most probably related to undesirable interferences from multiple reflections at the antennae. More experiments will be needed to investigate biasing effects on density profiles inside the separatrix.

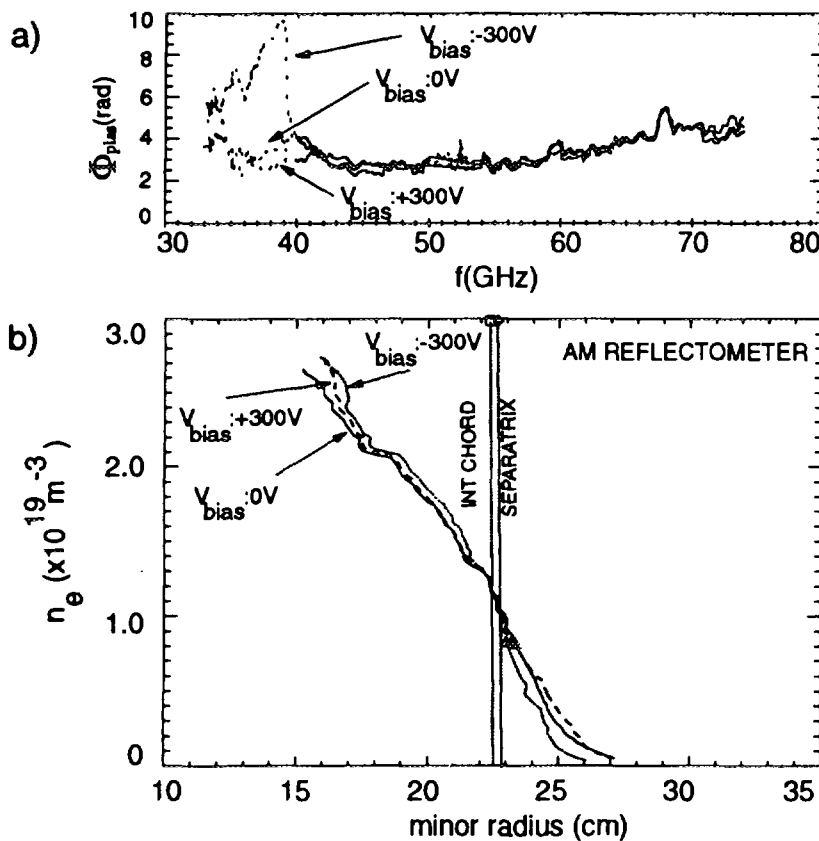


Figure 6: Plasma measurements Φ_{plaz} for three different biasing voltages on the divertor plates showing (a) overall phase shifts: full line (0 V, shot 30622), dotted lines (-300 V, shot 30620, dashed lines (+300 V, shot 30621) and (b) corresponding reflectometer density profiles: note the clear change in the scrape off layer length with negative biasing.

5. Conclusions

Density profiles for various plasma conditions have been obtained. The calculated line integrals compare well with those measured by the interferometer chords. Densities $n_e \geq 10^{18} m^{-3}$ can be measured despite large density fluctuations and good agreement between the two channels have been found. The use of high-precision limiting amplifiers have significantly reduced the large phase and amplitude fluctuation levels without the need of narrow filters allowing for faster fullband sweeps. Large undesirable interferences from multiple reflections at the antennae create spurious structure on the profiles. Efforts are aimed at reducing these interferences.

Acknowledgements

The authors are grateful to Dr. G. R. Hanson of Oak Ridge National Laboratory for guidance and stimulating discussions during the initial developing stages of the reflectometer. Also, we wish to thank Dr. A. E. Hubbard of Alcator C-Mod, Dr. F. Skiff and Dr. Derek Boyd of IPR University of Maryland for continuous discussions and encouragement. We acknowledge the contribution and support of the TdeV team. This work was funded by the Government of Canada, Hydro-Québec, and the Institut national de la recherche scientifique.

References

- ¹D. Pinsonneault, B. Quirion, J.-L.Lachambre, *Rev. Sci. Instrum.*, **68**, 990(1997)
- ²R. Décoste et al., *Proceedings of the 16th IAEA International Conference, Canada, 1996* to be published
- ³J. Sanchez, B. Branas, E. De la Luna, and T. Estrada, *Rev. Sci. Inst.*, **64**, 487 (1993).
- ⁴H. Bottollier-Curtet and G. Ichtchenko, *Rev. Sci. Instrum.*, **58**, 539 (1987)
- ⁵J.L. Lachambre and M. Gagné, *Rev. Sci. Instrum.*, **65**, 3428 (1994)
- ⁶J.L. Lachambre et al., *Nuclear Fusion*, **34**(11),1431(1994)

**NEXT PAGE(S)
left BLANK**

Automatic linearisation of swept microwave sources for density profile reflectometry

C. Laviron, P. Moreau, F. Clairet, J.M. Chareau and M. Paume

Association Euratom-CEA sur la fusion contrôlée, CEA/Cadarache,
F-13108 Saint Paul-lez-Durance Cedex, France

Introduction

When reflectometry relies on a frequency sweep technique for density profile reconstruction, often named FM-CW (frequency modulation continuous wave), a group delay is calculated through the relation $\tau = \frac{1}{2\pi} \frac{d\phi}{df}$. In order to avoid any error due to variations of the term df along the frequency sweep, it is necessary to precisely know the time evolution of the frequency during the sweep to correct for any non linearity, or, better, linearise the frequency sweep through an advanced procedure.

A standard method consists to calibrate the source by using a frequencymeter. But this calibration is static, and, due to the dynamics of the sweep, the effective frequencies launched to the plasma may be different during a measurement, the more so for ultra fast sweep systems.

We present here a dynamic technique, which allows a proper linearisation for any sweep speed because this linearisation is made in the same conditions as for the plasma measurements. In a first part, this dynamic linearisation will be presented on a theoretical point of view, followed with numerical simulations. In a second part, examples of applications on the reflectometers of Tore Supra will show the efficiency of this technique, in particular allowing very good results for 10 μ s sweeps.

Principle of dynamic linearisation

A linear frequency sweep means that the frequency increment is constant for each time step: $f(t_i) = f_0 + kt_i = f_0 + k i \Delta t$.

Usually, the frequency generator is driven by an external voltage control, through an arbitrary function generator. In order to get a good linearity, this controller should apply an adequate voltage for each time step. As the relation between voltage control and frequency output is not linear, the set of voltage values has to be defined for each step. For a standard static linearisation, this is made with a frequencymeter. For this operation, the frequency cannot

be swept continuously: it has to be stabilised at each step, therefore inducing some time for the overall measurement.

A non perfect set of voltage control values (voltage vector) for each frequency step would correspond to a linear frequency sweep plus an error vector $e(t)$:

$$f(t) = f_0 + kt + e(t)$$

the time vector t being taken as linearly spaced $t = t_i = i \Delta t$. If we apply a linear voltage control $V(t)$ to the source, this expression can also be written:

$$\begin{aligned} f(t) &= f_0 + f'V(t) + e(t) && \text{with } f' = df/dV \\ &= f_0 + f'V't + e(t) && \text{with } V' = dV/dt \\ &= f_0 + At + e(t) && \text{with } A = df/dV \cdot dV/dt = df/dt = \text{agility of the source} \end{aligned}$$

Using this vector $V(t)$, we can sweep over a fixed mirror and record the beat frequency to detect the phase shift for each time step (figure 1). This phase shift can be written

$$\varphi(t) = 2\pi f(t) \frac{2d}{c}$$

d being the path difference between the mirror and the reference. This phase shift includes all the information concerning the error $e(t)$.

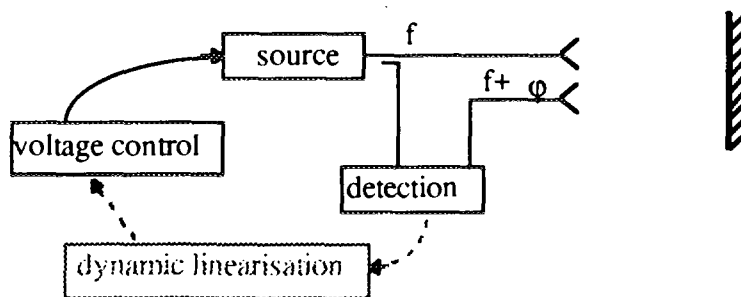


Figure 1 - Schematic of dynamic linearisation

The beat frequency f_b (proportional to the group delay) can be obtained through different numerical techniques (fringe counting, sine fit, Fourier transform, wavelet analysis, ...). For an ideal linear sweep, f_b should be constant through the whole sweep, i.e.

$$f_b = \frac{2d}{c} \frac{df}{dt} = \frac{2d}{c} A$$

If f_b is not constant, the error on the frequency of the source can be determined through

$$e(t) = \int \left(\frac{c}{2d} f_b(t) - A \right) dt$$

To avoid this integration, another way is to directly determine the phase through the Hilbert transform, which is valid when the amplitude of the measured signal varies slower than the phase. The phase should be linear during the whole sweep, so any non linearity allows to correct for the voltage control.

The correction is made for each time step, as shown on figure 2. At time step t_2 , frequency f_2 has been obtained instead of an optimal frequency f_1 (as explained above, this can also be calculated directly on the phase, replacing f_1 and f_2 by φ_1 and φ_2). The voltage V_1 which generated f_1 (or φ_1) should therefore be applied. To improve the precision, interpolations can be made if the time step is not small enough.

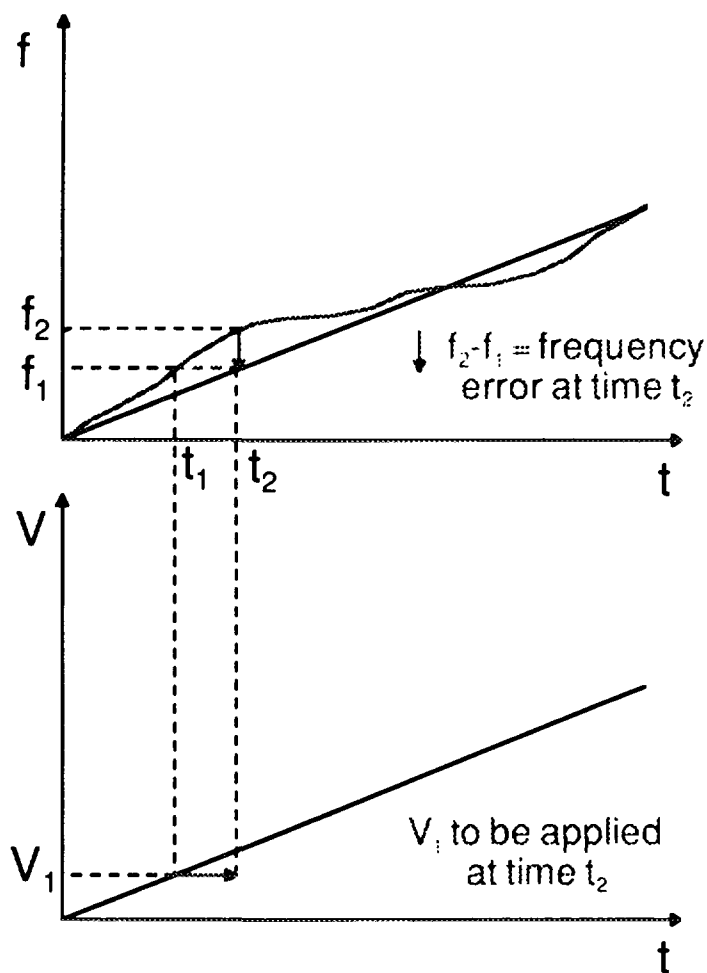


Figure 2 - Determination of the voltage correction on a step-by-step basis

Numerical simulations have been made to validate this concept, before any implementation on the reflectometers. Figure 3 shows an example of such a simulation: for errors extending over few hundred MHz (fig. 3, left), the beat frequency (fig. 3, right) is broad (dash-dotted line) and its value cannot be precisely defined. After linearisation, a sharp peak is obtained (dashed line), exactly placed compared to the ideal linearity (plain line).

This example shown on figure 3 allows to obtain a S/N ratio of about 25 dB after linearisation (dashed line), although the theoretical perfect linearity should give 40 dB (plain line). To improve it, if necessary, the operation could be iterated using the new voltage control vector as initial conditions.

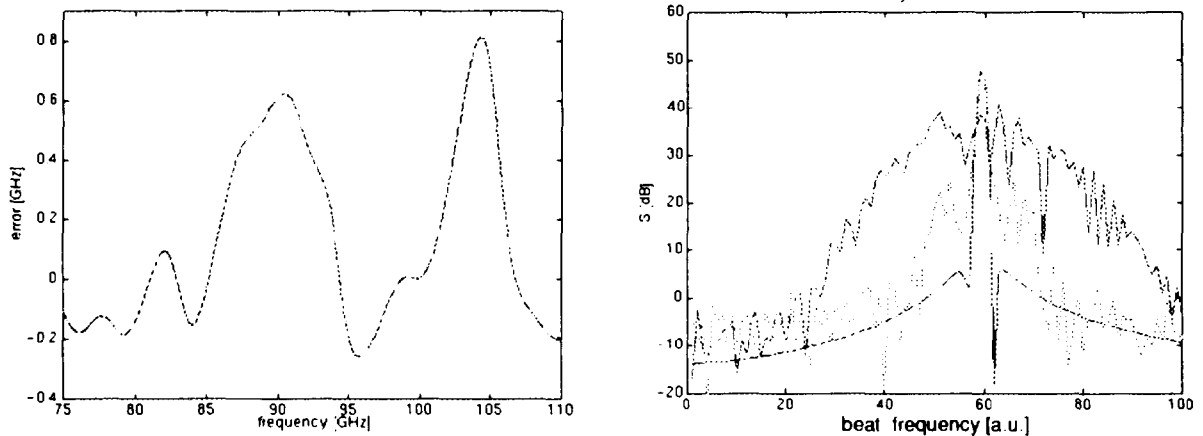


Figure 3 - Numerical simulation of linearisation in the W band (75-110 GHz): simulated error (left), and beat frequency (right) without linearity error (solid line), with simulated error (dashdotted) and after linearisation (dashed).

Simulations show that when the starting conditions are too far from the optimum linearity, the correction may induce a drift through successive iterations. This drift is due to frequency edge effects (f_{min} and f_{max} through V_{min} and V_{max}) and to the fact that the exact position of the mirror is not perfectly known: a calculated distance d_{calc} , obtained from the average of the measurements, has to be used for d . To avoid this drift, we can impose no edge correction for V_{min} and V_{max} . A better constraint is to impose d from previous measurements (i.e. $V_{max} - V_{min} = \text{constant}$). In any case, it is better not to iterate and to linearise from "not-too-bad" conditions. A preliminary static linearisation can be used as a starting point, which allows to obtain a good linearity in a single pass, without iteration.

Application to Tore Supra reflectometers

This technique has been successfully applied, in laboratory tests as well as on Tore Supra, for the standard O-mode reflectometers [1], as well as for the new heterodyne system [2]. The Tore Supra backwall is used as a reflecting mirror. First experiments have

shown that starting from a linear voltage sweep does not allow to linearise easily, as expected from simulations. Therefore, a preliminary static linearisation with a frequency meter is necessary to ensure optimised initial conditions. Then, the dynamic linearisation is made with the same conditions (sweep speed, data acquisition) than for the reflectometry frequency sweep on a plasma. Figure 4 shows the obtained echoes in both conditions (static and dynamic linearisation) for a 10 GHz frequency sweep (26-36 GHz) in 1 ms for the heterodyne reflectometer. As detailed in [2], this reflectometer simultaneously launches two frequencies toward the plasma, the main one corresponding on the figure to positive beat frequencies. The peak at about 130 kHz corresponds to the mirror reflection (the one used for optimising the linearity), and the other one (~40 kHz) to the antenna coupling. It can be seen on the backwall reflection that the dynamic linearisation (fig. 4, right) provides a sharper peak than the static one (fig. 4, left), therefore providing better measurements from plasma reflections.

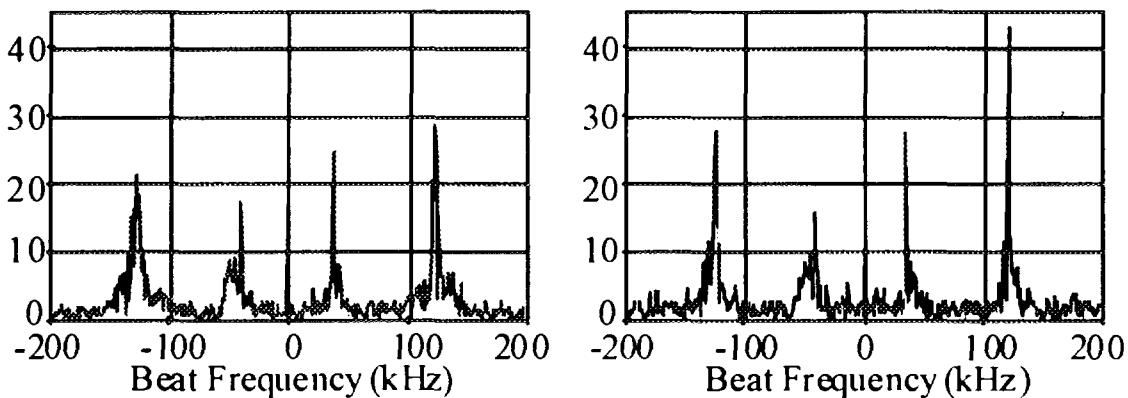


Figure 4 - Comparison between static (left) and dynamic (right) linearisations for a 1 ms frequency sweep.

For a faster frequency sweep (100 μ s) in the same frequency range (figure 5), the improvement is even better. This shows that the frequency generator (here an HTO) has a voltage vs frequency relation which varies with the agility. And for a 10 μ s sweep (figure 6), the mirror reflection is quite good from the dynamic linearisation, while the static technique provides a very poor response. This active linearisation technique might be one of the keys points for a successful fast frequency sweep [2].

It is interesting to note that the correction from static to dynamic linearisation is much smaller than the correction from a linear voltage sweep. In figure 7, the obtained frequency, measured statically from a frequency meter is represented as a function of the applied voltage control, and shows that the relation is far from being linear. On this same graph, the additional correction obtained from dynamic linearisation would not be seen as it is of the order of 1% of the applied voltage (figure 8).

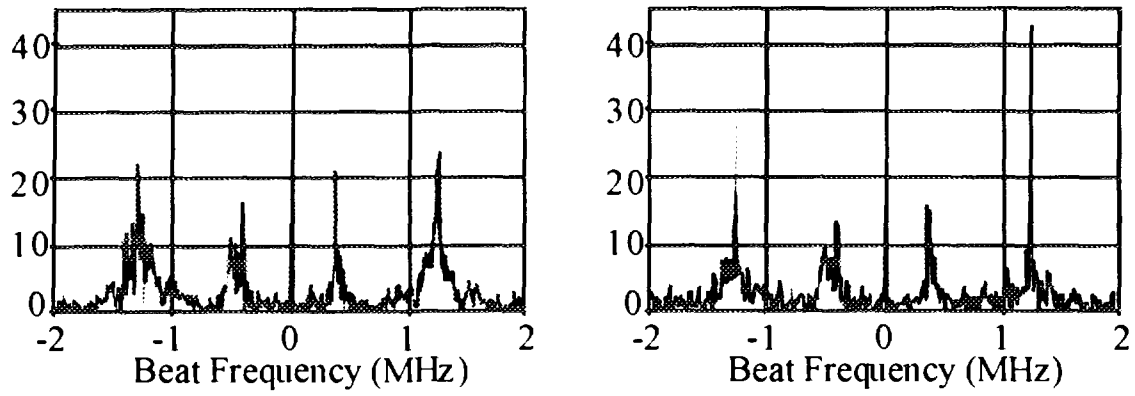


Figure 5 - Comparison between static (left) and dynamic (right) linearisations for a 100 μ s frequency sweep.

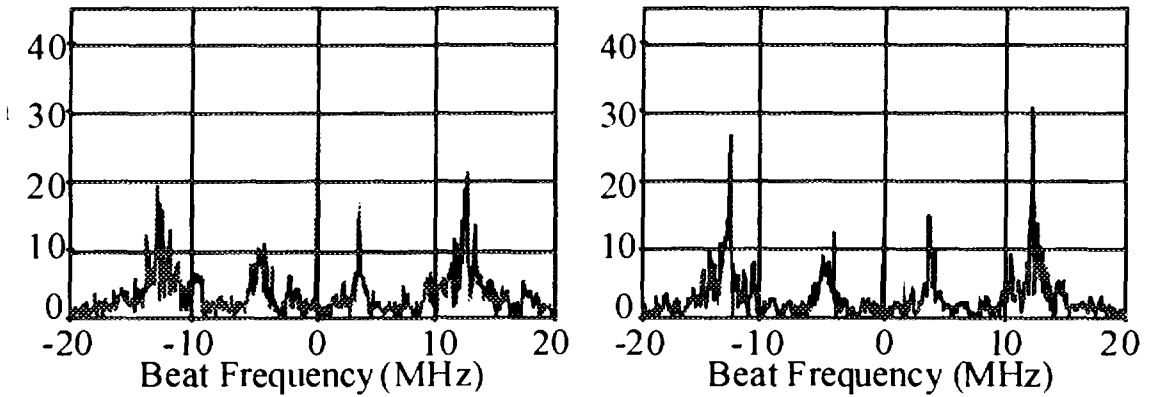


Figure 6 - Comparison between static (left) and dynamic (right) linearisations for a 10 μ s frequency sweep.

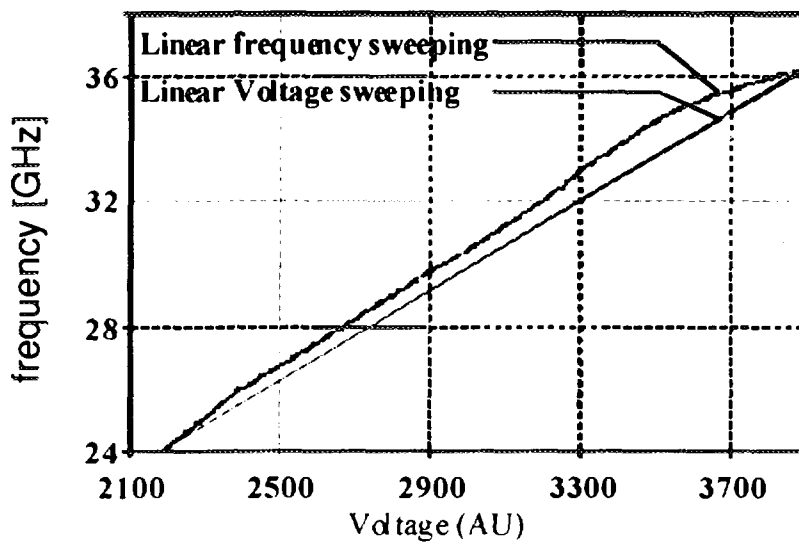


Figure 7 - Relation between frequency of the heterodyne reflectometer source (HTO and doubler) and voltage control.

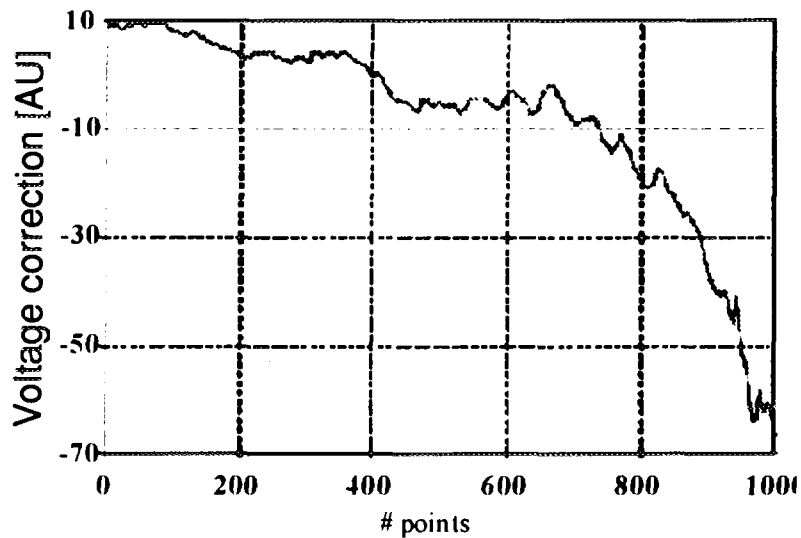


Figure 8 - Additional correction from a dynamic linearisation for a 100 μ s sweep.

Conclusion

For linearly swept FM reflectometry, the principle of dynamic linearisation consists to sweep the source in real experimental conditions and record the echo from a fixed reflector. Then, for each frequency, the beat frequency (or group delay, or directly the phase), computed supposing a perfect linearity, is compared to the theoretical one. The difference allows to compute a correction to apply to the control of the frequency sweep. Numerical simulations have shown the efficiency of this technique, but also the constraints on the extremities of the frequency range.

This technique is now successfully and routinely applied on Tore Supra, using the first backwall as a reference. To ensure better results, the correction has to be small and a static linearisation used as initial conditions. Excellent results have been obtained on the new heterodyne reflectometer with 10 μ s sweeps, showing that this active linearisation technique might be one of the key points for successful ultrafast sweeps.

References

- [1] M. Paume, J.M. Chareau, F. Clairet and X.L. Zou, Proc. IAEA Tech. Comm. Meeting on Microwave Reflectometry for Fusion Plasmas (Abingdon, 1992) 21
- [2] P. Moreau, F. Clairet, M. Paume, J.M. Chareau, C. Laviron and G. Leclert, this workshop

**NEXT PAGE(S)
left BLANK**

New developments of the ASDEX Upgrade Tokamak microwave reflectometer

A. Silva, L. Cupido, B. Kurzan*, J. Santos, P. Varela, S. Vergamota, M. Manso, F. Serra and
W. Suttrop*

Associação EURATOM/IST, Centro de Fusão Nuclear, 1096 Lisboa Codex, Portugal

**Max-Planck-Institut für Plasmaphysik, EURATOM Association, D-85748 Garching, Germany*

1 - Introduction

The broadband reflectometry system for the ASDEX Upgrade tokamak uses frequency modulation of a continuous wave (FM-CW) [1]. The monostatic antenna configuration, is optimised for eliminating spurious reflections (Fig. 1). A combination of solid state microwave sources Hyperabrupt Tuned Oscillators (HTO) with active and passive doublers are used. The detection is homodyne up to V band (75 GHz) operating in broadband and fixed frequency.

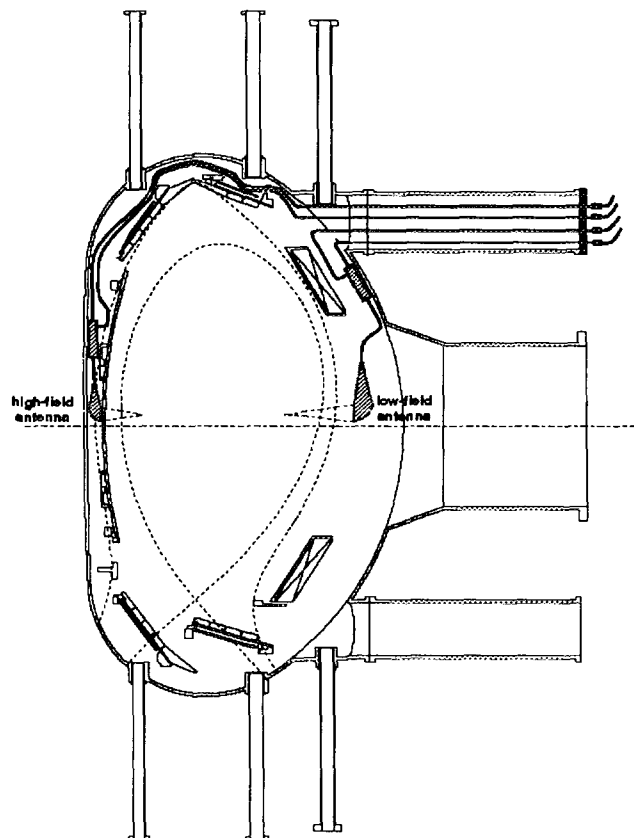


Fig. 1 - Schematic of the inside vessel microwave circuit.

Advanced digital signal processing techniques were applied to obtain density profiles. The diagnostic is capable of measuring 1000 electron density profiles each in 20 μs and with separation of 10 μs [2].

During the recent shutdown period, a new W band channel was installed at the low field side (LF) to extend the probed densities up to $1.5 \times 10^{20} \text{ m}^{-3}$. A broadband heterodyne detection was implemented for the V and W bands, with the capability of a full band sweep in 10 μs . A new Q band channel with fixed frequency operation was installed for on-line fast monitoring the L-H transition based on the reduction of the plasma density fluctuations.

At the present the system have at the high field side (HF) four O mode channels covering density range 0.3 to $6.76 \times 10^{19} \text{ m}^{-3}$ (sectors 5 & 6). At the LF we have five O mode channels with a density ranging from 0.3 up to $15 \times 10^{19} \text{ m}^{-3}$ (sector 6), plus a fluctuation monitor channel (sector 4), and two X mode channels frequency range 33 to 74 GHz (sector 6). There is also one X mode channel inside the ICRH antenna (50 to 74 GHz) (sector 4). The accessibility regions for a typical ASDEX Upgrade plasma is shown in figure 2.

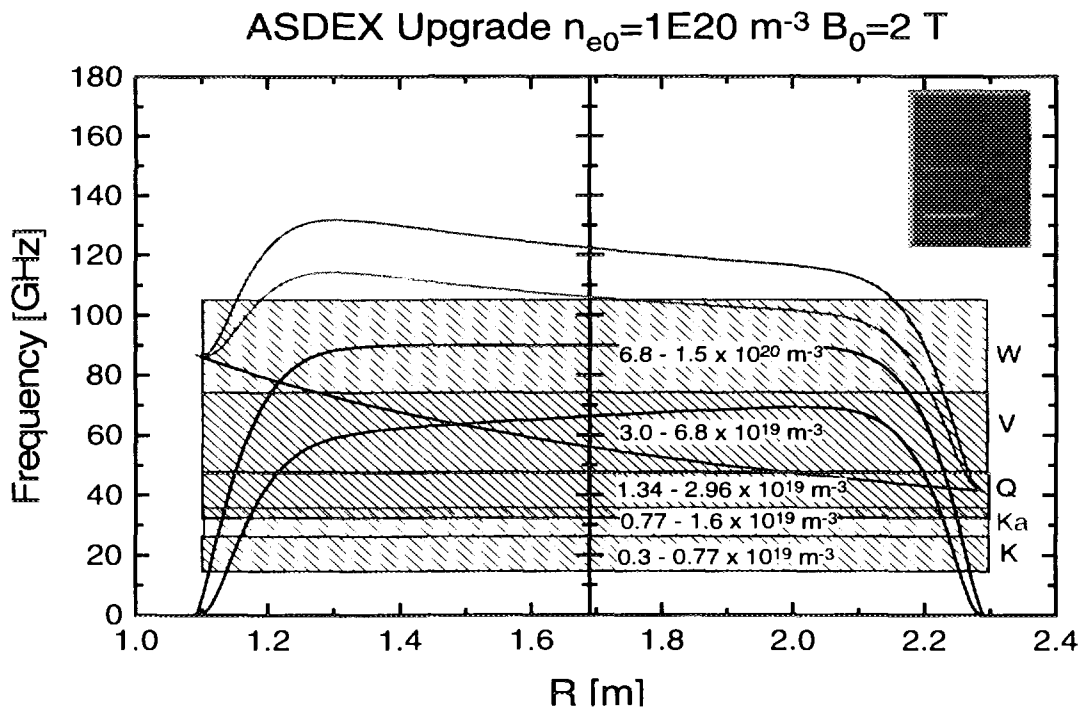


Fig. 2 - Regions of accessibility for a typical plasma configuration. The probed regions with O-mode for each band are marked. The curves are: F_{pe} plasma frequency, F_{ce} electron cyclotron frequency, F_{uco} upper cutoff, F_{lco} lower cutoff, F_{uh} upper hybrid frequency.

2 - The heterodyne detection

When the probing frequencies are above 50 GHz, the conjunction of high waveguide losses with low power available from the microwave sources, makes the use of a homodyne detection very difficult. For the homodyne system the sensitivity is limited by the waveguide detector tangential sensitivity (TSS) and the detector load will set a compromise between bandwidth and sensitivity.

With a heterodyne detection the sensitivity can be close to the theoretical maximum, and the dual side band (DSB) noise figure of the mixer will limit the receiver performance. This technique requires a local oscillator that tracks precisely the main signal (Fig. 3). Sets of two oscillators are phase locked to each other with an offset frequency (the intermediate frequency, IF), this produces clean signals but has complex phase locked loop (PLL) and electronics. The detection is done at IF after amplification and could be single ended, as in homodyne detection. This assures compatibility with the pin reference scheme. Quadrature detection can also be used and full phase and intensity variation can be obtained. This can always be implemented as an upgrade of a single ended circuit.

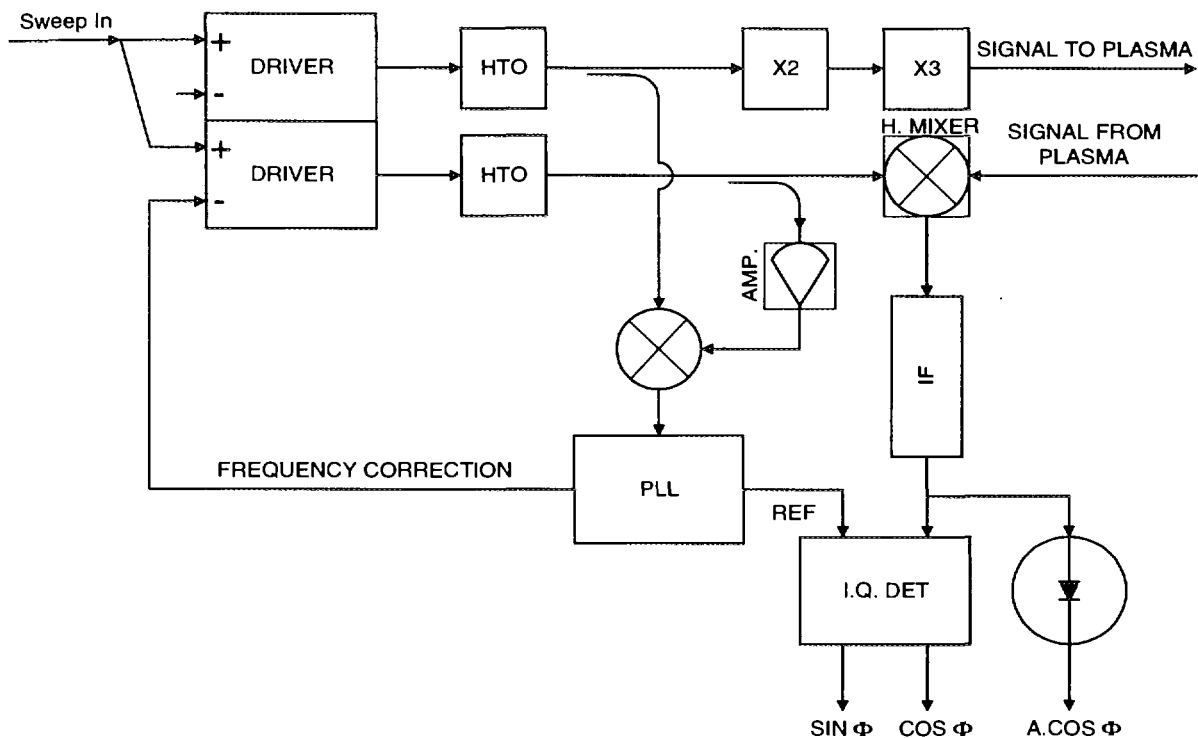


Fig. 3 - Schematic of the heterodyne system.

Laboratory tests showed an improvement of 42 dB for V band and 30 dB for W band when compared with homodyne detection. The PLL capture range in IF exceeds 4 to 700 MHz, with an acquisition time below 50 ns, and a sensitivity of -10 dBm at 192MHz during lock state condition. Both systems can perform a full band sweep in 10 μ s.

3 - Fluctuations monitor for the L-H transition

A Q band antenna was installed on sector 4, at the low field side. This channel operates in fixed frequency (O mode), probing a fixed density layer of the plasma. The frequency can be changed in the range 33 to 50 GHz.

A set of band pass filters select the fluctuations spectrum to be monitored. The output signal is proportional to the fluctuations amplitude, providing a way to on-line fast monitoring the L-H transition (Fig. 4), where an abrupt decrease of the fluctuations is observed [3].

This channel will be operated independently from the other reflectometer channels, and will run for the complete discharge. The signals can be used for simultaneous measurements of

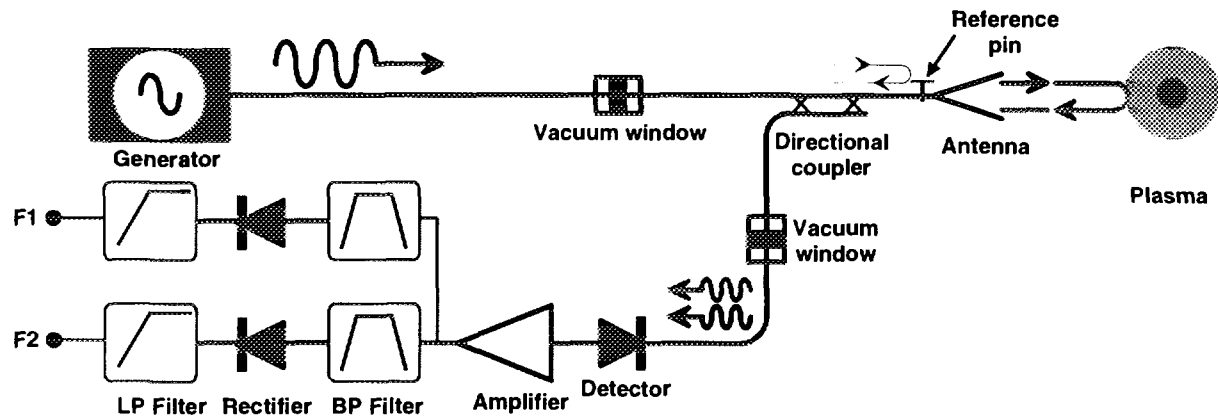


Fig. 4 - Schematic for the L-H transition fluctuations monitor

electron density profiles and density fluctuations.

A simulation was made using real reflectometer data and implementing by software the band pass filter, rectifier and low pass filter. The results are compared with D_{α} signal and the transition can be clearly resolved by the reflectometer data (Fig. 5).

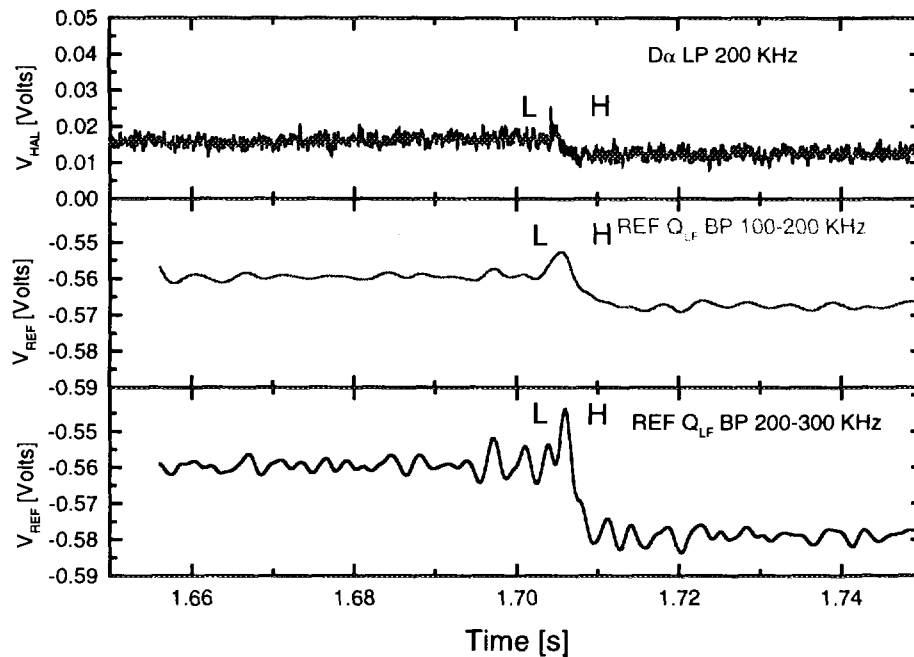


Fig. 5 - Simulated data for the L-H transition fluctuations monitor

4 – Conclusions

With the present setup a density profile can be measured every $30 \mu\text{s}$, covering the range of 0.3×10^{19} to 15×10^{19} , when O-mode is used.

An heterodyne system for the V and W bands was developed and will allow fast sweeping ($10 \mu\text{s}$) with improved S/N. A similar system can be used on other reflectometers like the one under construction for TJII or for the planned ITER reflectometers.

A fixed frequency channel will give the possibility to monitor the L-H transition with high temporal resolution. Machine operation engineers can use the output signals to control in real time some of the processes involved with the L-H transition, like the additional heating needed to achieve the power threshold of the transition..

- [1] – A. Silva, L. Cupido, M. Manso, F. Serra, et al., Proceedings of 17th Symposium on Fusion Technology, edited by C. Ferro, M. Gasparotto and H. Knoepfel (North-Holland, Amsterdam, 1992), Vol. 1, p. 747.

- [2] – A. Silva, M. E. Manso, L. Cupido, M. Albrecht, F. Serra, P. Varela, et al., *Rev. Sci. Instruments* 67, 4138 (1996).
- [3] – Recent results, this Workshop.

A Novel Fast Frequency Modulation Scheme for the JET Multi-channel Reflectometer

N Deliyankis

JET Joint Undertaking, Abingdon, Oxon, OX14 3EA, UK

1. INTRODUCTION

Several different modulation schemes are employed in reflectometer systems to determine the group delay time required for density profile measurements (Laviron *et al*, 1996). The JET multi-channel reflectometer uses slow, narrow-band sweeps of the microwave frequency in each of the channels (Sips and Kramer, 1993). 10 channels of the original system are currently in operation, spanning the range from 18 to 70GHz, in the O-mode. Three problems are associated with this approach: First, the frequency sweep is slow (6ms) in comparison to the time-scale of most plasma fluctuations, whether turbulent or coherent. Second, the corresponding phase change is measured by fringe counters which rely on the signals being continuously present during the sweep. Third, the exact frequency excursion depends on the characteristics of the microwave sources. These circumstances result in frequent loss of profile information, or in relatively large errors in the position of the density profiles, as well as errors in their shape, though the latter are partially corrected by making use of the phase evolution during the fixed-frequency intervals between sweeps. These limitations are significant in measurements of edge density gradients and densities, both important in the study of high-confinement (H-mode) plasmas in JET (Deliyanakis *et al*, 1994). On the other hand, the present system can perform *simultaneous* measurements of density fluctuations at 10 radial positions: such measurements were crucial in identifying the so-called outer modes, external kink modes limiting the performance of H-mode plasmas (Smeulders *et al*, 1995). The present system is also able to function in conjunction with the long waveguide runs needed at JET.

To eliminate the problems discussed above and improve the general performance of this diagnostic, whilst retaining the advantageous aspects of the present system, a novel scheme relying on fast frequency modulation has been designed and is being implemented. This paper discusses the underlying theory and technical aspects of this novel system. These will be illustrated with examples of preliminary measurements.

2. Theory

In the fast-frequency modulation (FFM) scheme,‡ the microwave sources are frequency-modulated by a stable oscillator at 65MHz. The time dependence of the wave launched by each source is given by

$$S(t) = A \cos(2\pi f_c t + m \sin 2\pi f_m t), \quad (1)$$

where f_c is the carrier frequency and f_m is the modulation frequency, and m is the modulation index. The modulation bandwidth is comparable to the modulation frequency, that is, the modulation index is small. It should be noted that this scheme is similar, in terms of the launched microwave spectrum, to amplitude modulation or differential-phase schemes, but is simpler to implement technically as it does not involve any modifications to the microwave components of the existing system. In the present scheme, the bandwidth of the launched microwave power is limited by the IF bandwidth. In general, however, one can increase this bandwidth for an FM system, by increasing the modulation index for a fixed modulation frequency. Some models (Vayakis, 1995) suggest that the robustness of the measured group delay against density fluctuations is enhanced when the bandwidth exceeds the correlation bandwidth of the fluctuations.

The modulation frequency has been chosen to be much higher than the plasma fluctuation frequencies (typically up to 1MHz), but low enough to eliminate phase ambiguity (the largest displacement within the JET cross-section is approximately 2m, corresponding to an optical path change of 4m, whereas the wavelength of the modulating signal is 4.6m). The phase measurement is now performed at the modulation frequency, which depends on the stable oscillator and not on the microwave sources. The group delay time is given by

$$\tau_G = \frac{\phi_m/2\pi}{f_m}, \quad (2)$$

within one period of the modulating signal, for a phase ϕ_m between 0 and 2π . Because there is no phase ambiguity, a measured phase corresponds to a single value for the group delay time, and such a measurement can in effect be performed instantaneously. A spatial resolution of 1cm in vacuum entails a phase resolution (and stability of the corresponding group delay time in the instrumentation) of 1.6° .

3. Technical aspects

To measure the group delay time, the received microwave signal is down-converted to an intermediate frequency (IF) of approximately 300MHz, using the heterodyne receiver

‡ many authors of reflectometry articles use the term *frequency modulation* to refer to frequency sweeping; in this paper, this term is used in the sense usual in communications

of the existing system; the modulating signal is recovered from the limited IF signal using a frequency discriminator; and its phase, relative to the reference signal from the master oscillator, is measured using an IQ demodulator.

Shown in figure 1 are the microwave components and electronic instrumentation for one of the 10 channels of the reflectometer. Both transmitter and local oscillator are varactor-tuned Gunn oscillators. A single oscillator at 65MHz and individual, variable-gain amplifiers are used to modulate the transmitter oscillators. The local oscillator operates at a fixed frequency and the need for a phase-lock loop is obviated. Should the transmitter or local oscillator sources drift in frequency, the resulting drift in frequency of the IF signal would not affect the phase measurement at the modulation frequency; nevertheless, a slow compensating circuit (not shown) has been included to maintain a constant intermediate frequency. The IF signal from the heterodyne receiver is limited in power, by means of a feed-forward gain control loop. This uses a Schottky power detector controlling a PIN-diode attenuator, and has its bandwidth limited to 1MHz, this being sufficient to eliminate power variations in the IF signal due to the plasma. This arrangement is preferable to a limiting amplifier, because of its linearity and group delay stability (phase variations in the IF signal are of course unimportant). Following this section, is a frequency discriminator which recovers the modulating signal by mixing the incoming modulated signal with a delayed version of itself (the delay is such that the carrier is eliminated or considerably attenuated). Finally, an IQ (in-phase/quadrature) demodulator is used to extract the phase information from the recovered modulating signal centred at 65MHz. The 65MHz signal from the master oscillator is used as reference; if the oscillator is stable, there is no need for a delay line. The two video signals produced by the IQ demodulator are digitized, at 5kHz and 250kHz, and are used for the calculation of the group delay. The group delays from the 10 channels are then used in an Abel inversion procedure to obtain the density profile. Naturally, certain assumptions have to be made about the variation of the group delay between successive channels, and also below the lowest density that is probed.

Also shown in figure 1, is a secondary circuit which generates a homodyne signal, by mixing the IF signal originating in the plasma with a corresponding signal from the reference waveguide of the existing system. This homodyne signal, which clearly responds to the phase and amplitude of the microwave carrier, is used for density fluctuation measurements.

The frequency discriminator and IQ demodulator have both been specifically developed for this application, the main design object being to optimize the group delay stability of the discriminator and the phase resolution of the IQ demodulator. The latter has been optimized by careful design of the video amplifiers, and by biasing the 90° hybrid and the two mixers of the circuit.

4. Simulations

The modulation system described above has been simulated by a code which models, in the time domain, both coherent and turbulent fluctuations in the plasma, and the imperfect electronic components of the modulation and detection circuits. Shown in figures 2 and 3, are the power and phase spectra of the detected modulating signal generated, respectively, in the absence of plasma, and from a plasma with coherent fluctuations, resulting in fluctuations in both the phase and amplitude of the reflected signal. Shown in figure 4, are the temporal variations of the group delay, obtained from the phase of the detected signal, and of the power of the latter. It is clear that, despite the artificially introduced imperfections, the position and movement of the plasma reflection layer can be accurately reconstructed. Shown in figure 5, is the effect of a spurious reflection (10% of the incident power): such a spurious reflection can result in a distortion of the movement of the reflection layer, and also manifests itself in a modulation of the power of the detected signal.

5. Preliminary measurements

The hardware described above has been installed and commissioned satisfactorily, with the exception of the discriminator circuits (these include the gain-control loop); the latter have been developed but not delivered. Preliminary experiments were carried out using a commercially obtained limiting amplifier in the place of the gain-control loop. Figure 6 shows the power spectra of the launched microwave and down-converted IF signals for one of the channels of the system. Clear from these figures is the structure of the FM spectrum, with a carrier and only two sidebands (because of the low modulation index). Figure 7 shows the recovered signals at the modulation frequency of 65MHz, in the absence of plasma (reflection from the back wall of the vessel), and with plasma. The effect of plasma fluctuations in this signal is evident. It should be noted that, whilst the power at the centre frequency is attenuated (by about 4.5dB), the peak remains sharp. Finally, figure 8 shows the equivalent vacuum displacement of the reflection layer as obtained from the measured phase of the recovered modulating signal, and the corresponding movement of the plasma boundary (LCFS) as obtained from a magnetic reconstruction code (XLOC). Whilst the measured phase clearly exhibits the movement of the plasma, the latter is grossly overestimated (by a factor of about 15). This serious difficulty has been attributed to the limiting amplifier used, and has led to the design of the gain-control loop described above. Two further solutions to this problem will be considered, should this approach fail. First, the limiting process may be eliminated; the simulation shows that good resolution in position can be obtained even in the presence of large power variations. Second, amplitude modulation can be implemented

instead of frequency modulation, with relatively few changes to the existing system (PIN modulators would have to be included in the four microwave bands of the instrument).

References

- Deliyanakis N *et al* 1994 The VH-mode at JET *Plasma Phys. Control. Fusion* **36** 1159
- Laviron C *et al* 1996 Reflectometry techniques for density profile measurements on fusion plasmas *Plasma Phys. Control. Fusion* **38** 9
- Sips A C C and Kramer G J 1993 Analysis of reflectometry density profile measurements in JET *Plasma Phys. Control. Fusion* **35** 743
- Smeulders P *et al* 1995 Influence of MHD instabilities on JET high performance *Controlled Fusion and Plasma Physics, Proc. 22nd Eur. Conf. (Bournemouth, 1995)* vol 19C IV-061
- Vayakis G 1995 A model of the effect of Plasma Turbulence on Time Delay Measurements by Reflectometry *JET Report JET-P(95)76*

Figure captions

Figure 1. Schematic diagram of the microwave components (bold lines) and electronic instrumentation of the fast frequency modulation (FFM) system, for one of the 10 channels of the JET reflectometer (KG3)

Figure 2. Power and phase spectra of recovered modulation signal at 65MHz, as simulated in the absence of plasma

Figure 3. Power and phase spectra of recovered modulation signal at 65MHz, as simulated for a plasma with coherent fluctuations at 2MHz

Figure 4. Temporal variation of group delay (in fringes) and power of recovered modulation signal, as determined by simulated IQ demodulation. The group delay is compared to the corresponding delay calculated directly from the position of the reflection layer. The mean position and movement are accurately reconstructed.

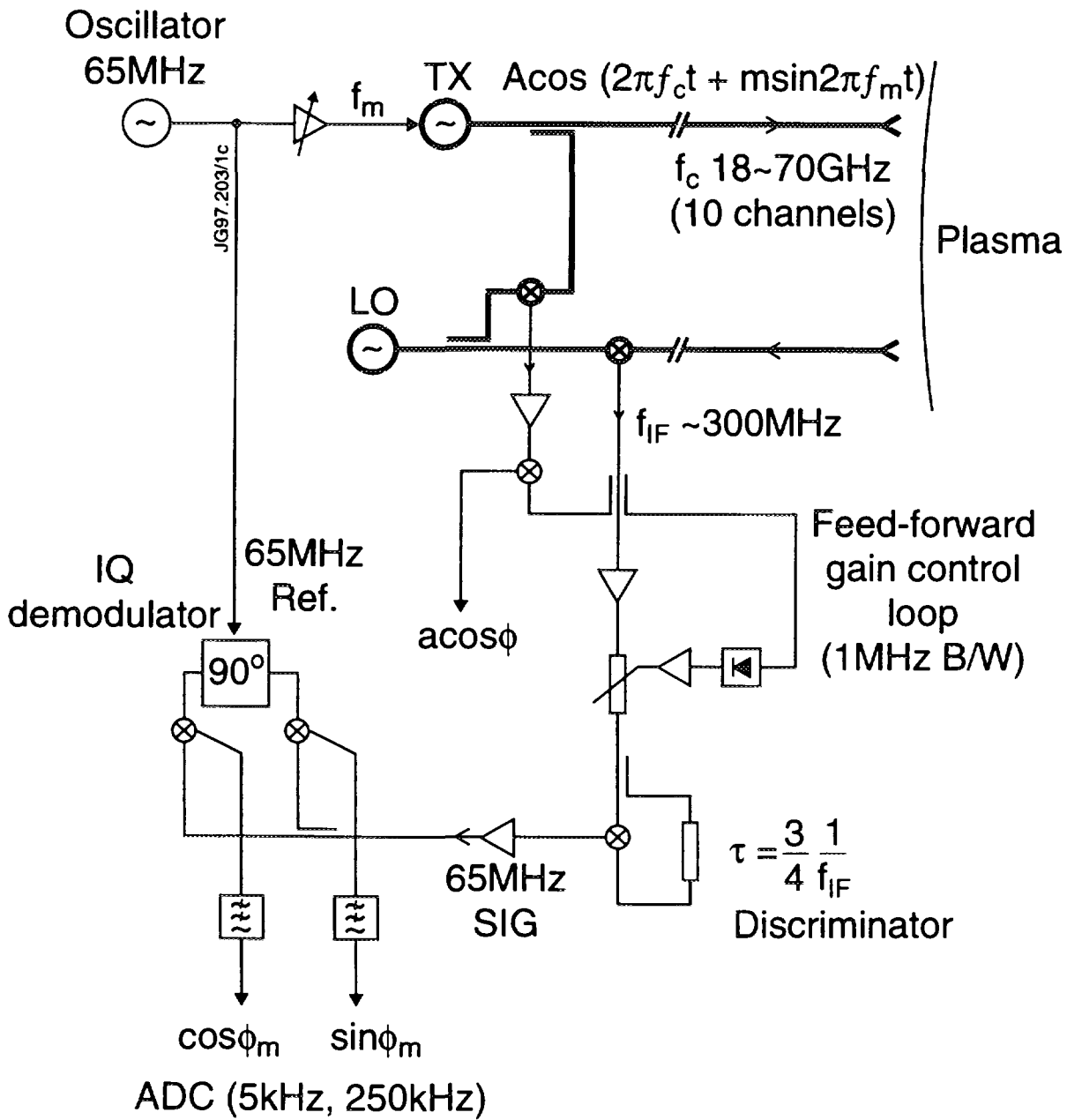
Figure 5. As figure 4, but with a spurious reflection of 10% of the launched power. The movement of the reflection layer is distorted, but the mean position is not affected; the power of the detected signal is strongly modulated.

Figure 6. Power spectra of (a) launched microwave from channel 3, centred at 29.0GHz; and (b) down-converted IF signal, centred at 316MHz. The two sidebands arising from the frequency modulation are separated from the carrier by the modulating frequency of 65MHz. (The wider peaks in the microwave spectrum correspond to spurious mixing products.)

Figure 7. Power spectra of recovered modulating signal at 65MHz, obtained (a) without plasma (back wall reflection), and (b) with plasma.

Figure 8. (a) Equivalent vacuum displacement of reflection layer corresponding to channel 3 (29.0GHz), as obtained from the measured phase of the recovered modulating signal; (b) Corresponding movement of plasma boundary from magnetic data.

KG3 FFM System



REFERENCE & DETECTED SPECTRA

NO PLASMA

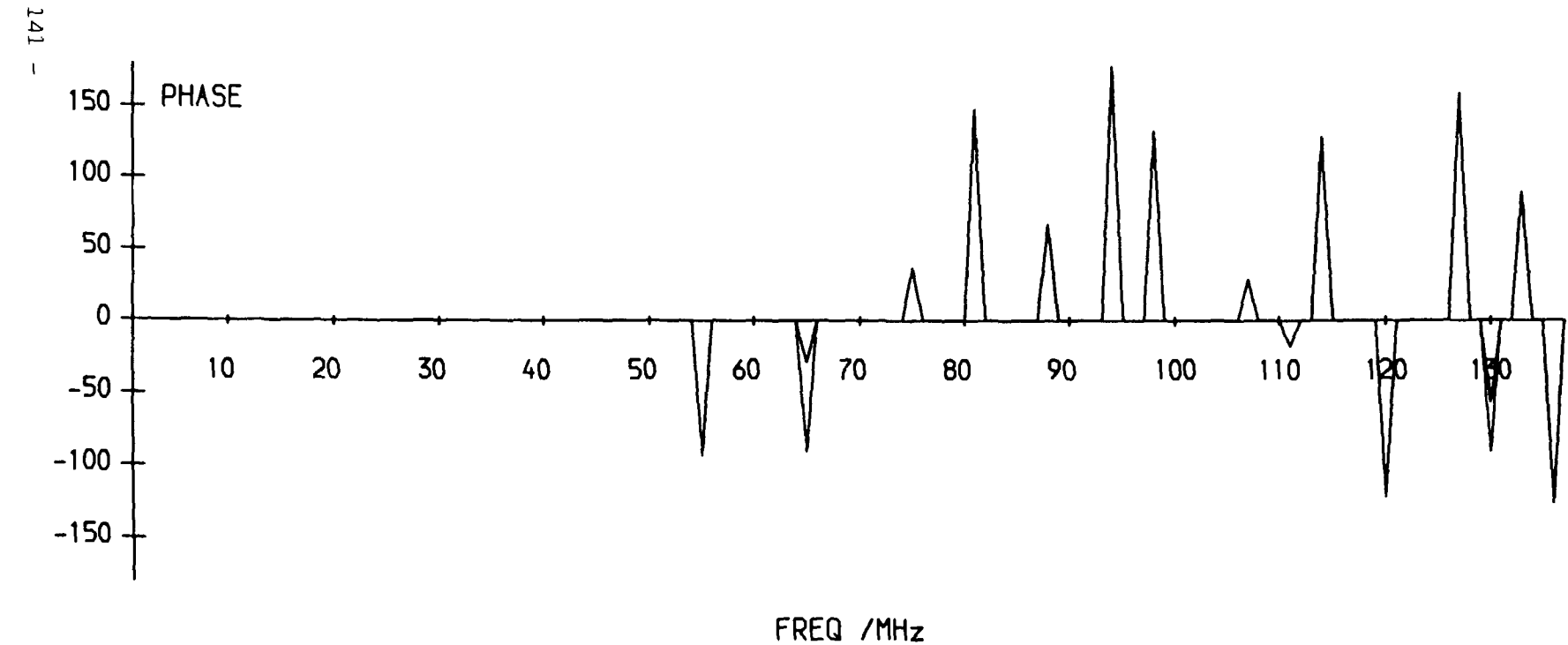
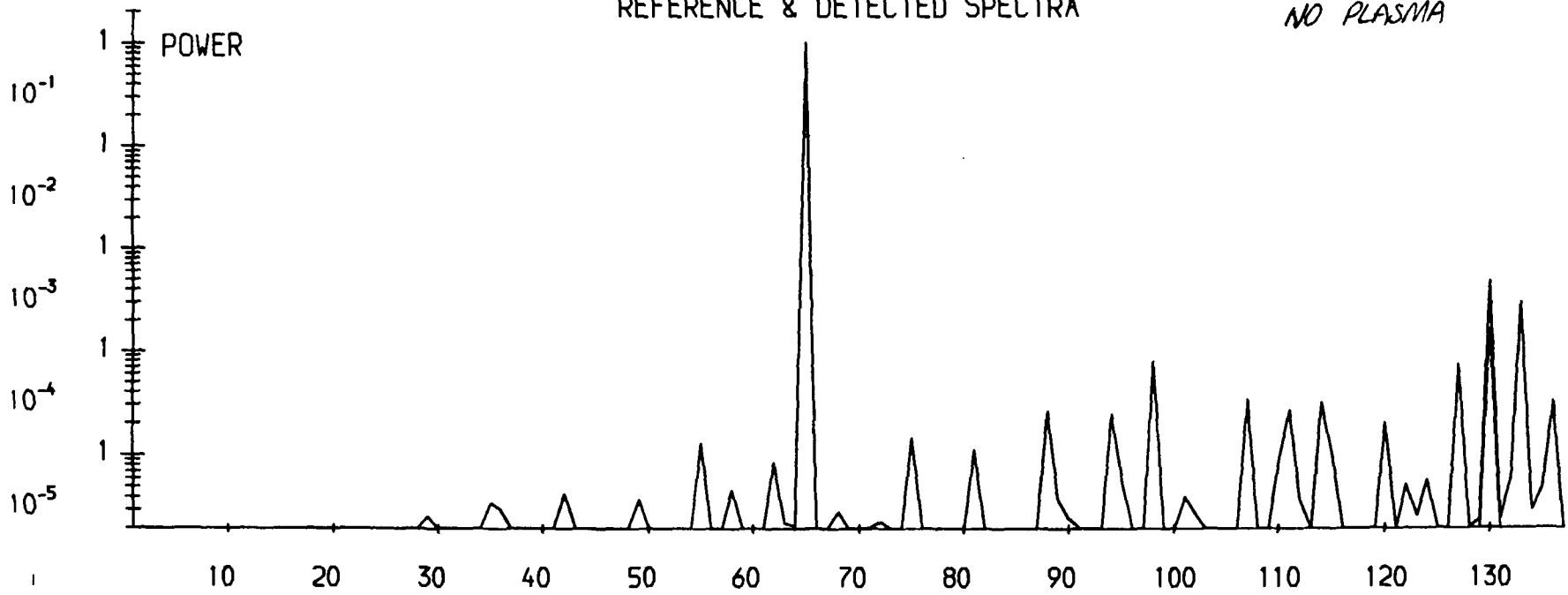


fig. 2

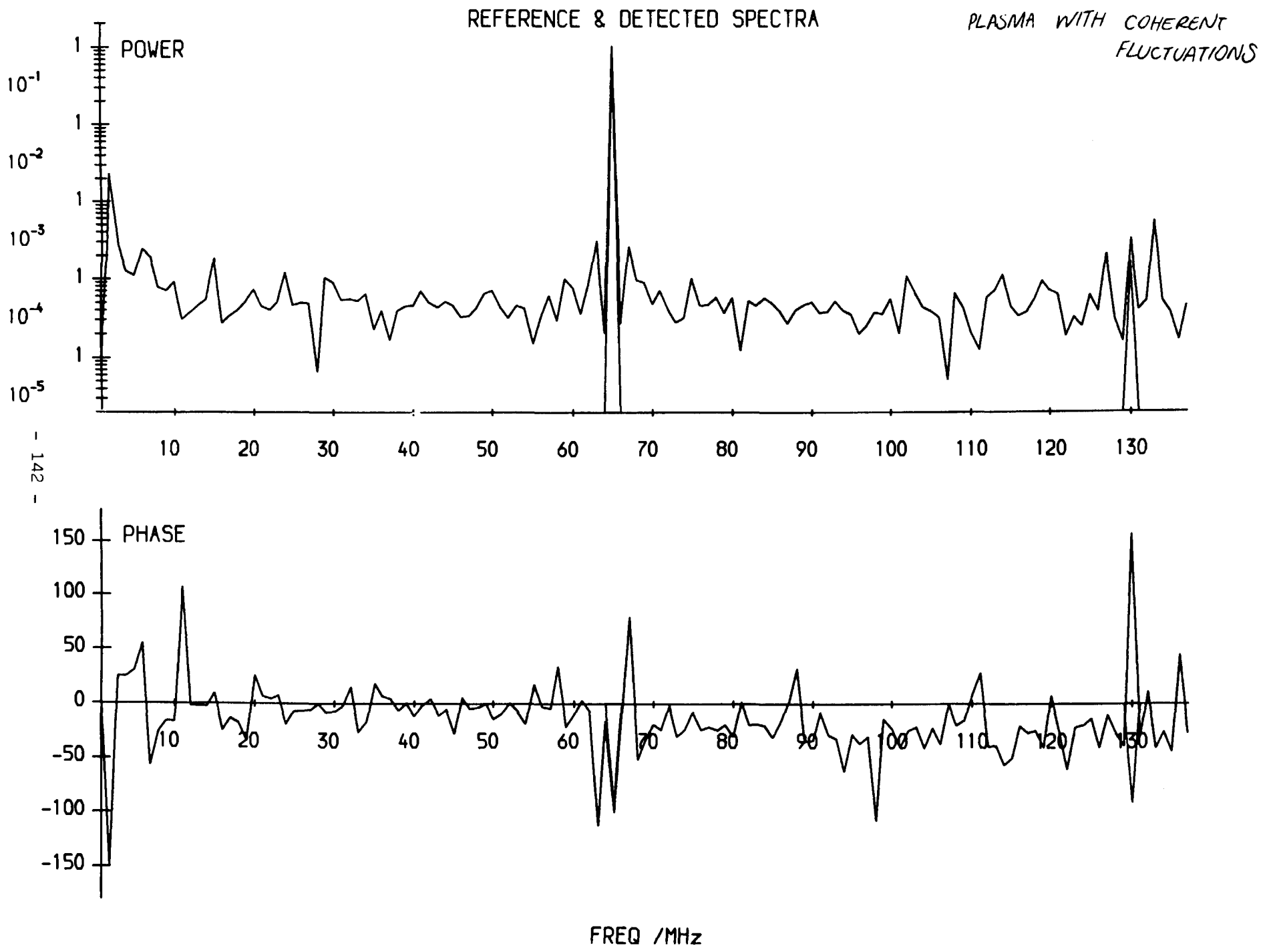
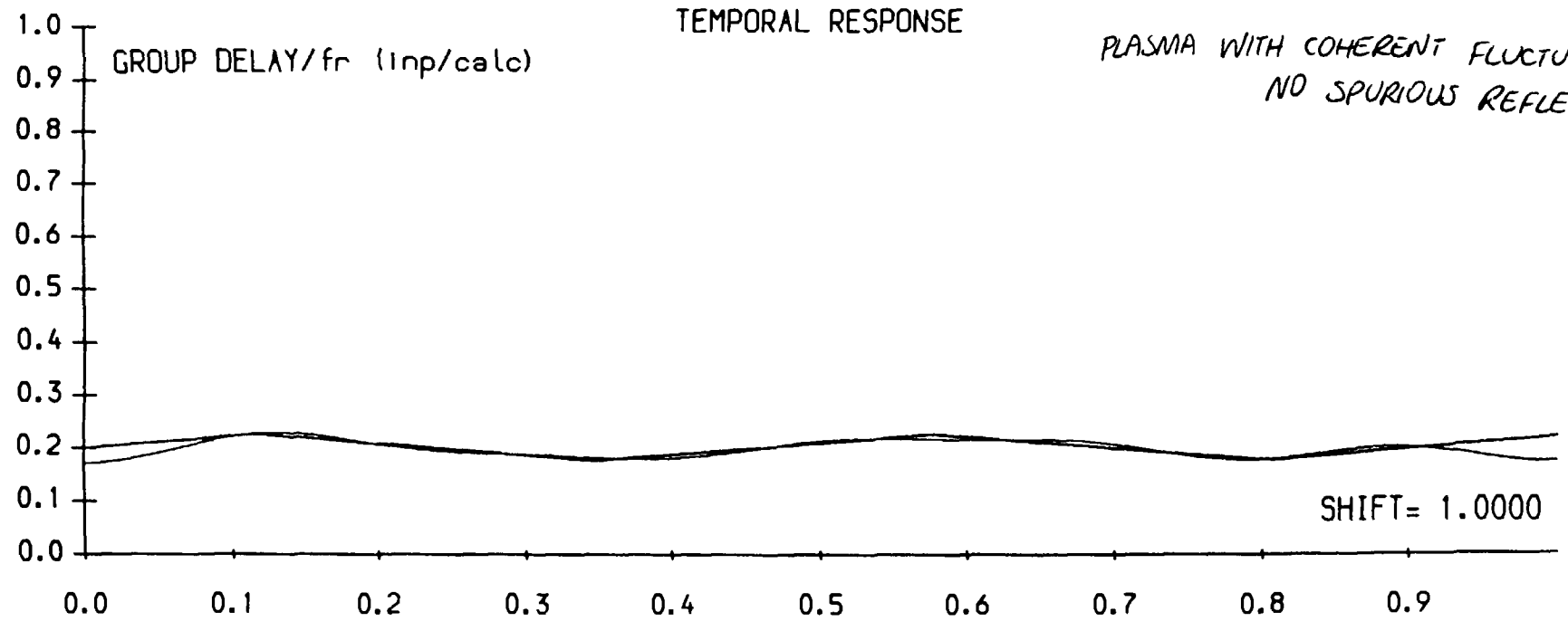


fig. 3

TEMPORAL RESPONSE

PLASMA WITH COHERENT FLUCTUATIONS
NO SPURIOUS REFLECTION



1.72

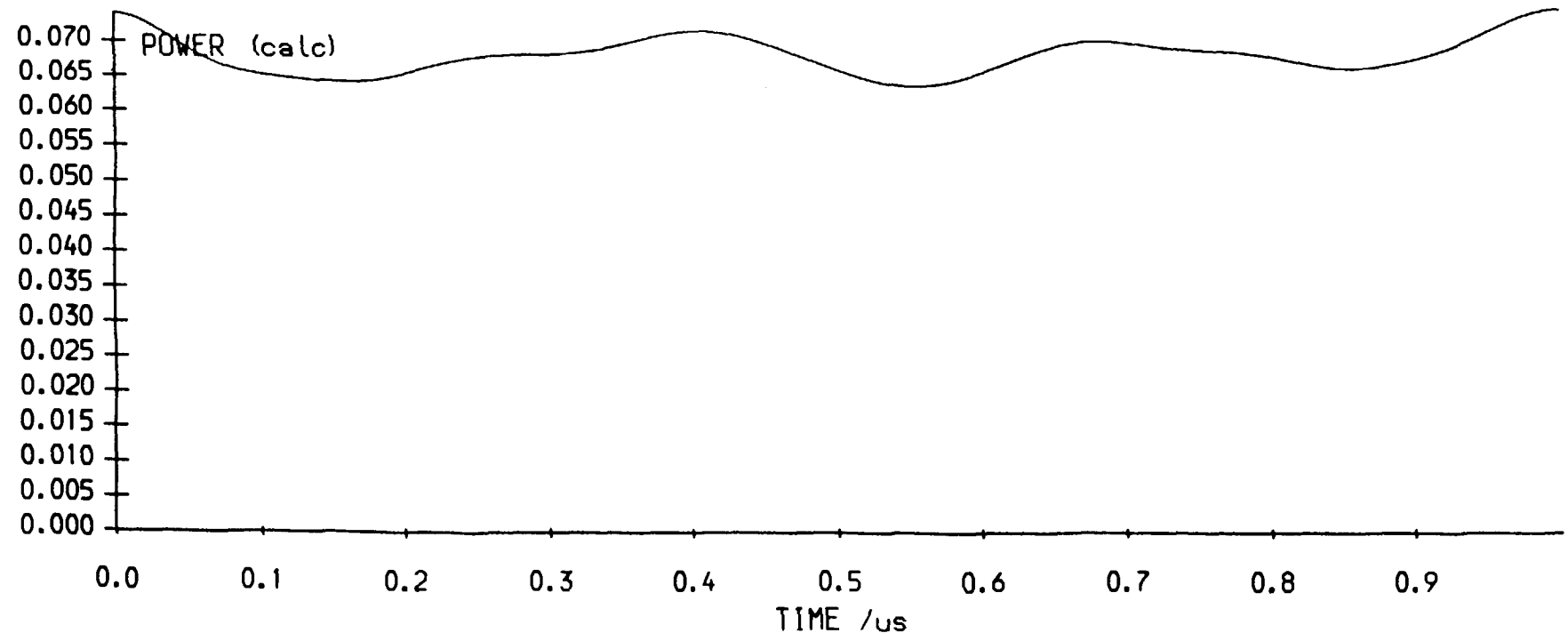
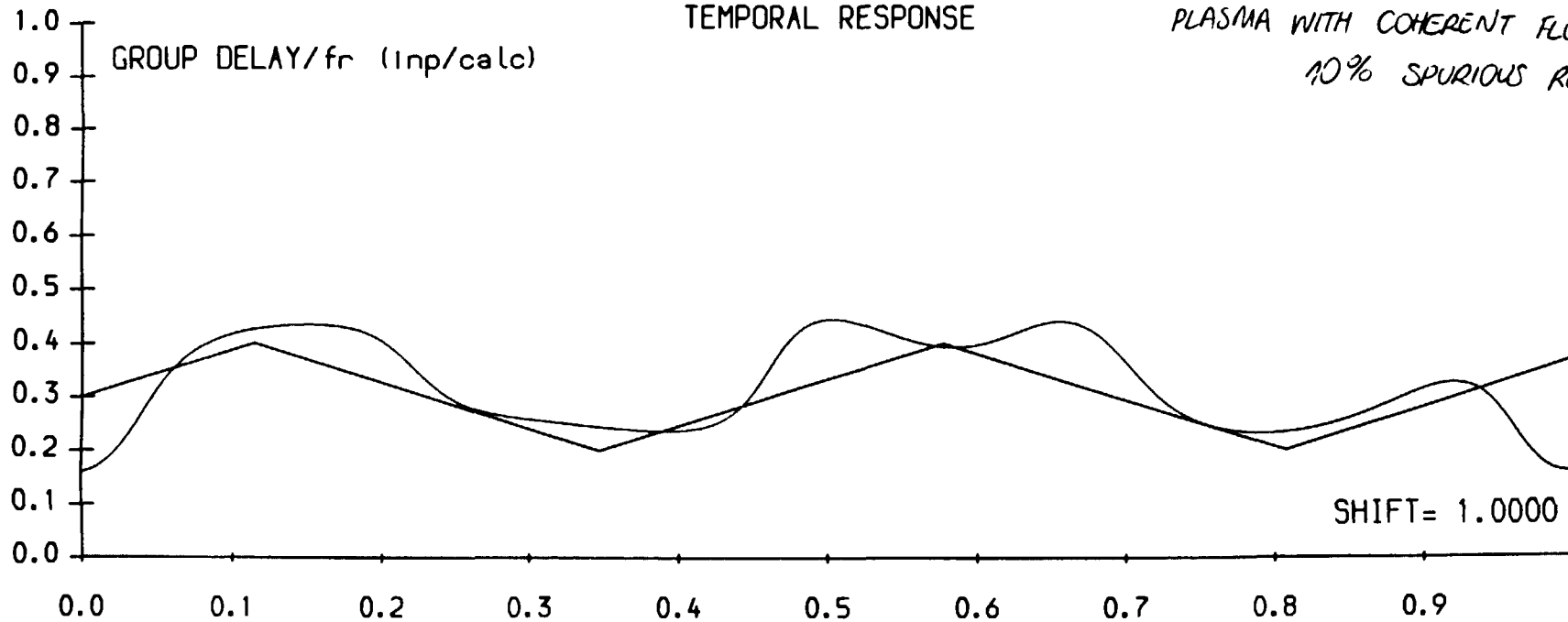


fig. 4

TEMPORAL RESPONSE

PLASMA WITH COHERENT FLUCTUATIONS
10% SPURIOUS REFLECTION



- 144 -

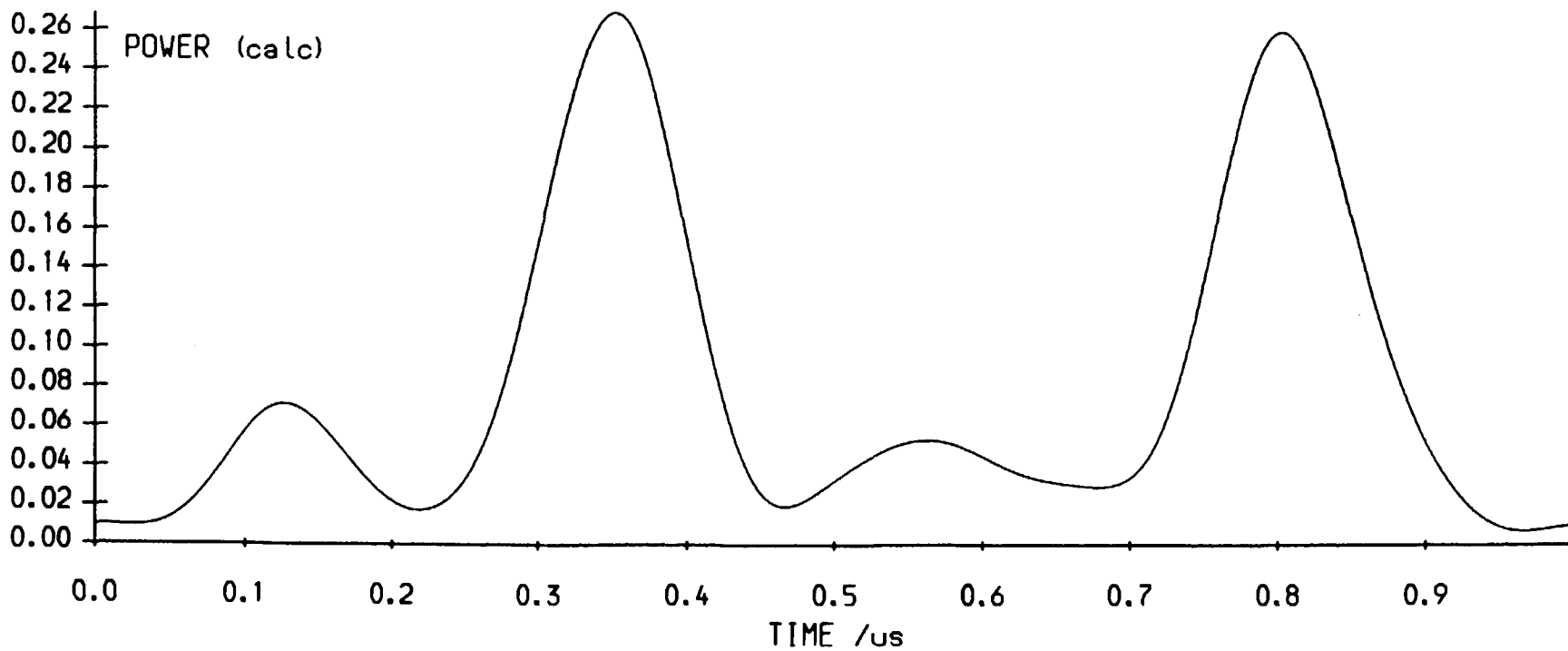


fig. 5

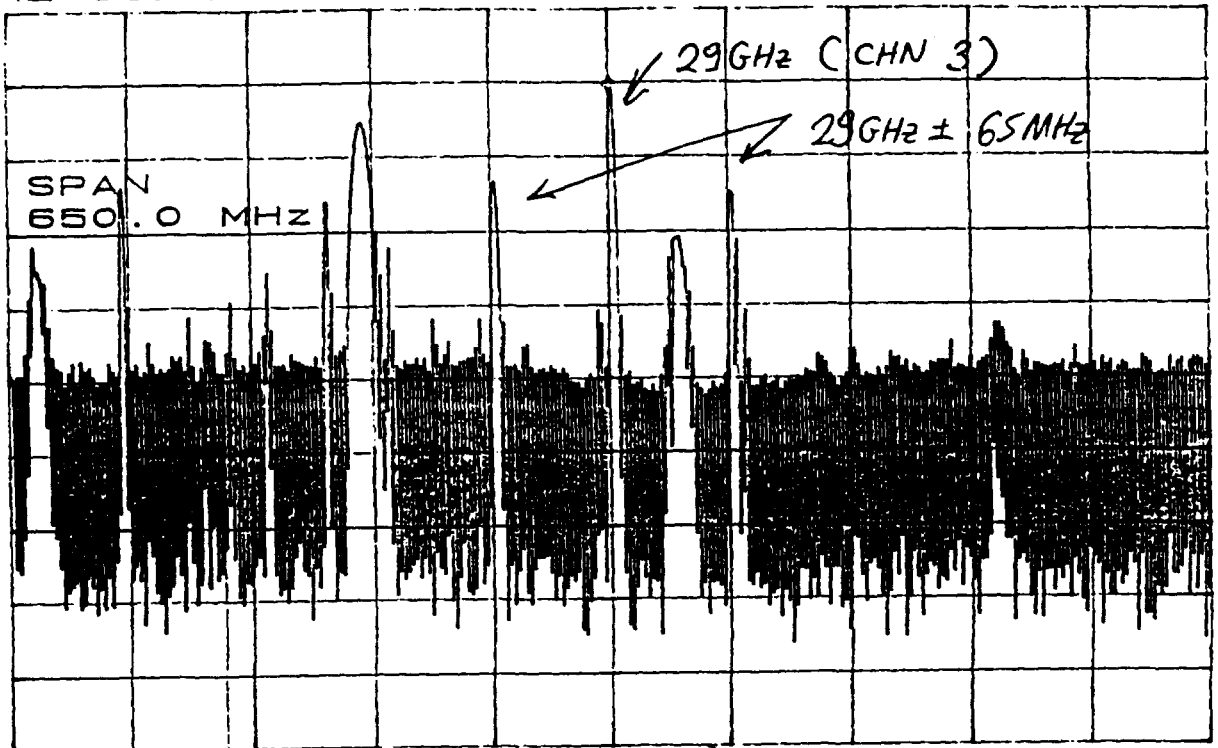
MICROWAVE SPECTRUM

CL 30.0dB
RL 0dBm

10dB/

MKR -11.33dBm
29.0091GHz

(a)



CENTER 29.0080GHz
RBW 2.0MHz

VBW 3.0MHz

SPAN 650.0MHz
SWP 50ms

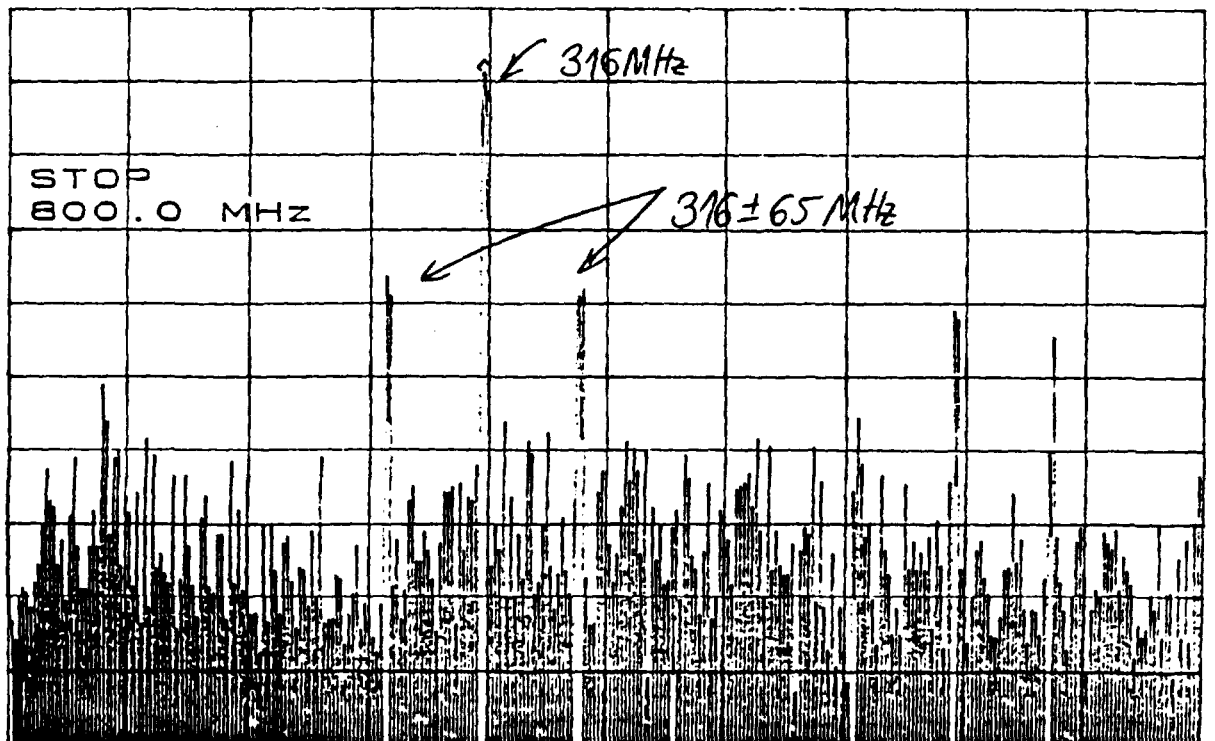
IF SPECTRUM

ATTEN 30dB
RL 18.4dBm

5dB/

MKR 13.82dBm
316.0MHz

(b)



START 0Hz
RBW 2.0MHz

VBW 3.0MHz

- 145 - STOP 800.0MHz
SWP 50ms

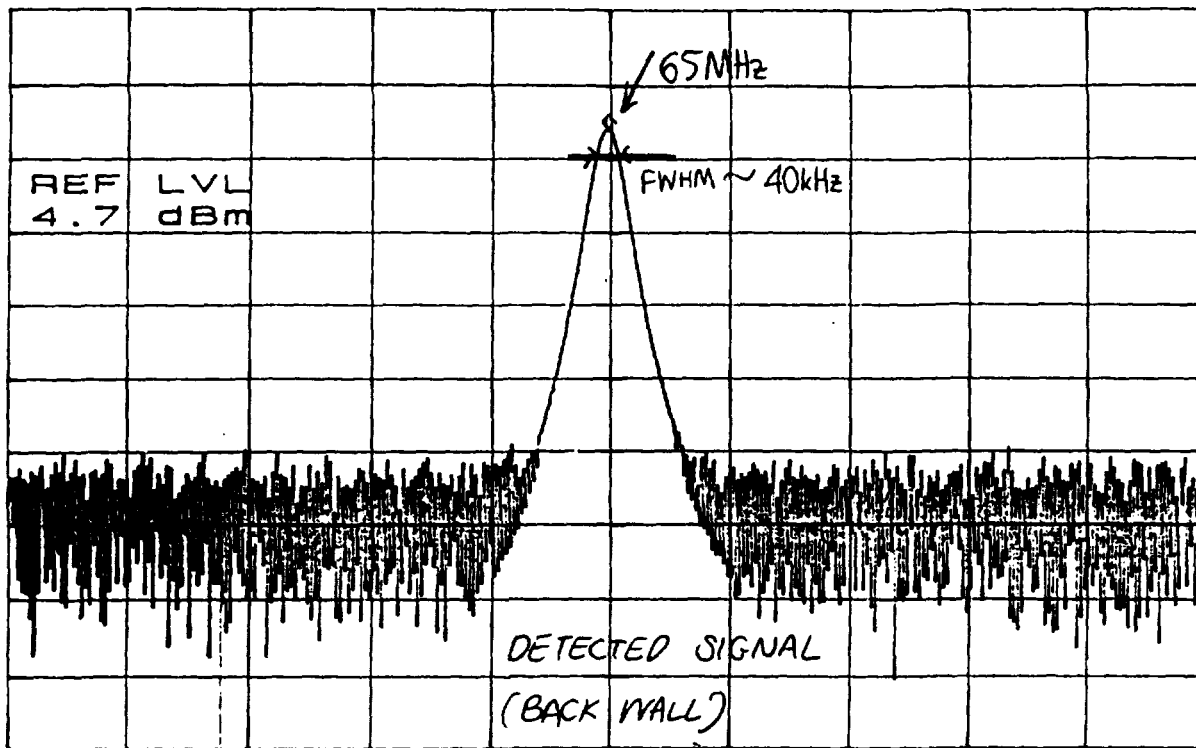
fig. 6

ATTEN 20dB
RL 4.7dBm

10dB/

MKR -11.13dBm
65.010MHz

(a)



CENTER 65.013MHz

SPAN 2.000MHz

RBW 30kHz

VBW 30kHz

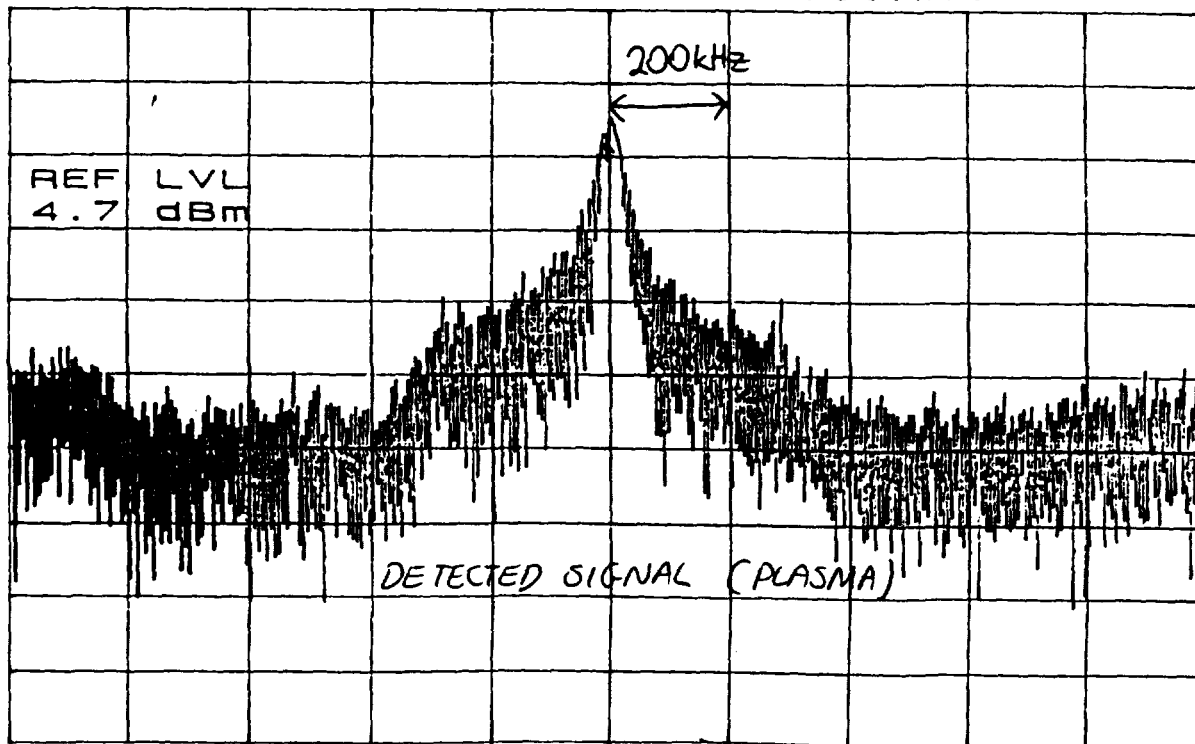
SWP 50ms

ATTEN 20dB
RL 4.7dBm

10dB/

MKR -15.63dBm
65.010MHz

(b)



CENTER 65.013MHz

SPAN 2.000MHz

RBW 30kHz

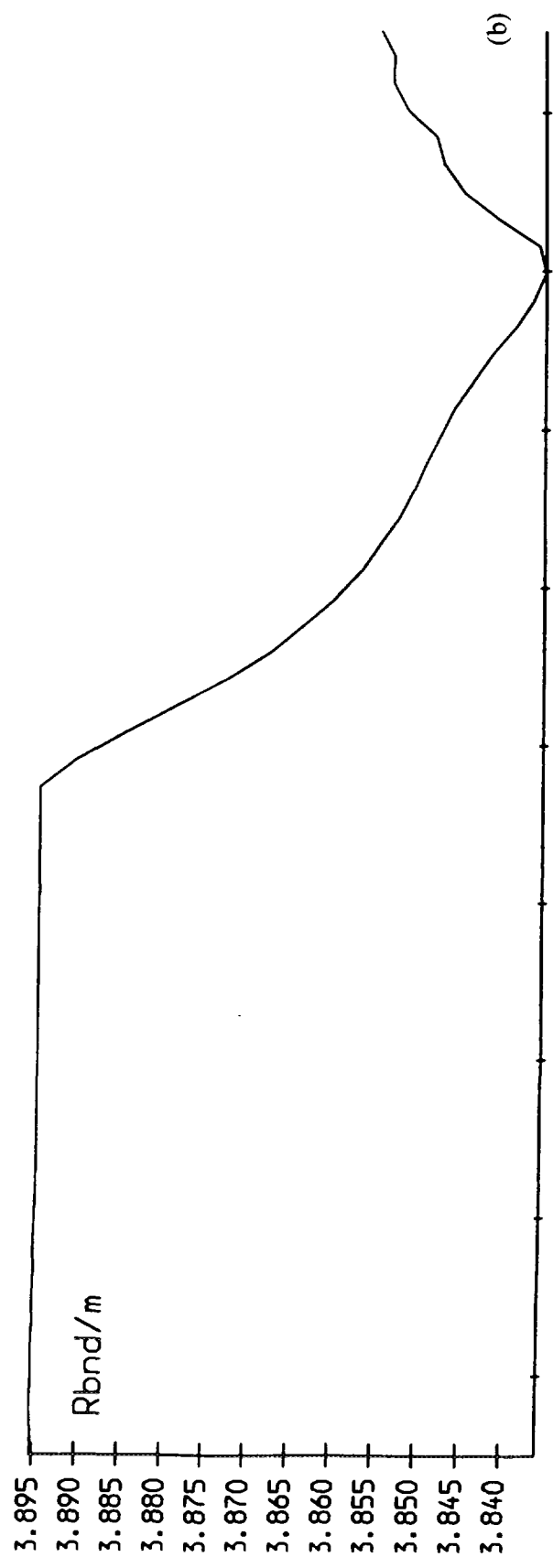
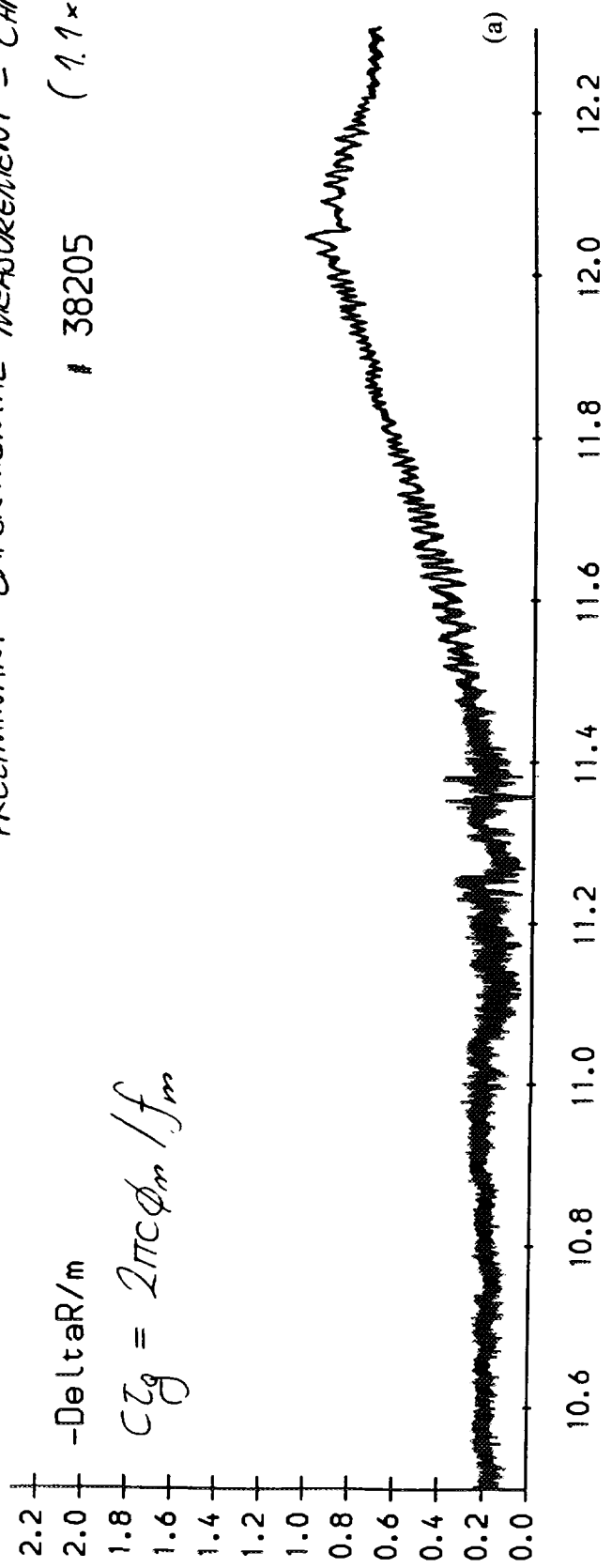
VBW 30kHz

SWP 50ms

PRELIMINARY EXPERIMENTAL MEASUREMENT - CHN 3
 # 38205 ($1.1 \times 10^{19} \text{ m}^{-3}$)

$$-Delta R/m$$

$$C_{Tg} = 2\pi C \phi_m / f_m$$



NEXT PAGE(S)
 left BLANK

10.6 10.8 11.0 11.2 11.4 11.6 11.8 12.0 12.2 TIME/S

fig. 8

Effects of Turbulence in Profile Reflectometry

J. Sanchez, T. Estrada, V. Zhuravlev, M. Francés, B. Brañas, E. de la Luna

Asociación Euratom-CIEMAT, 28040 Madrid Spain.

Abstract

Reflectometry for density profile measurements uses typically beams with several cm diameter but mm probing wavelengths. The beam is reflected in a corrugated critical layer with structures which have a typical wavelength of several cm. Under these conditions (extended beam with short wavelength) WKB -2 dim ray tracing can give a good description to the interference phenomena arising. This approach requires less computing time than Full Wave 2-dim calculations and therefore it allows for a more comprehensive analysis of the effect of the density fluctuations on the reflectometry signal, either in fluctuations or profile studies.

The 2-dim WKB code [1] has been used to simulate the reflectometry signals in profile measurements under turbulent conditions. The signal for a given reflectometry system (AM, FM, Pulse) can be synthesized. Special attention has been paid to the effect of rotating structures, which lead to phase runaway effects and can have a clear impact on the profile measurements. Comparison between AM (pulse radar behaves in a similar way) and swept FM reflectometry is made for different rotation speeds and turbulence levels.

Introduction

One of the limiting factors in reflectometers when trying to measure the density profile in fusion plasmas is the existence of a fraction of experiments where the measurement becomes impossible: very noisy signals leading to nonsense density profiles. Those so called "bad shots" are usually linked with strongly turbulent plasmas and the remaining problem is to be able to assess "a priori" if the data coming from a given experiment will correspond to a normal profile or if they will be meaningless.

The effect of turbulence in the reflectometer signal is twofold, temporal and spatial. The temporal effect is seen in swept frequency systems which use consecutive measurements to determine the time delay ($\partial\phi/\partial f$) function: the profile changes locally during the measurement (false fringes in frequency swept homodyne systems). These effects are usually overcome in the experiments by sweeping fast (frequency sweep rate in the order of 1 GHz/ μ s have been achieved, leading to clean results).

The spatial effects come from the fact that the reflecting layer is a corrugated surface: both phase and amplitude of the reflected beam become affected by interference effects and the perturbation cannot be avoided by sweeping fast.

Under strong turbulence the reflectometer will aim to determine the average density profile but due to the several nonlinear magnitudes involved (phase, time delay) the achievement of this goal is not guaranteed. The main question here is whether or not this average profile can be determined and how the different techniques are affected.

Simulation process

In order to compare the ability of the different techniques (AM, FM, Pulse) to provide an acceptable average profile we have developed a simulation procedure:

A steady state profile is assumed and a 2-dimensional distribution of turbulence is added. Now, with a propagation code we obtain the transfer function for each relevant cutoff frequency: amplitude $A(f)$ and phase $\phi(f)$. Once we have these functions, we can synthesize the different reflectometers, obtain the averaged time delay function $\langle \tau \rangle(f)$, perform the profile inversion (by a simple 1 d reconstruction algorithm) and compare with the original unperturbed profile.

The wave propagation is simulated with a 2-dimensional WKB code (multi-ray tracing): many rays are launched for each relevant frequency and those collected at the receiving antenna interfere to give a resulting phase and amplitude. The use of the WKB approximation is based on the fact that we have a short wavelength beam with a diameter similar to the size of the dominant turbulent structures. The main advantage over full-wave codes is the shorter computing time required, this is important because typically 2000 frequencies are launched to simulate a profile measurement.

The model for the turbulence is made up by addition of localized perturbations, with some random distribution of amplitudes and locations (within 50% of the average values). The correlation length is about 4 cm and the poloidal and radial dimensions are equal and the ratio of turbulence wavelength to vacuum wavelength of the incoming beam (Λ/λ) is kept between 6-15 in order to guarantee applicability of the WKB assumption.

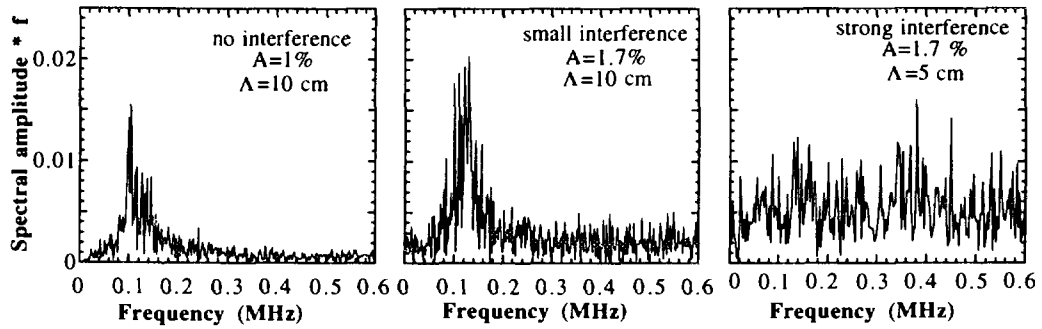


Fig.1. Spectra of the phase of the reflected beam for fixed frequency operation in the W7AS geometry.

Results

First simulations were performed at fixed frequency for the geometries of the W7AS stellarator and ITER and for different turbulence parameters (amplitude and dominant wavelength of the turbulence). Fig.1 shows the results for a small size machine (W7AS stellarator, reflection point $r/a=0.75$, 80 GHz X-mode): we move from a spectrum without interference, which is very similar to the actual spectrum of the density fluctuations, to a very noisy spectrum just by going to a factor 2 higher turbulence level or shorter turbulence wavelength. If we analyze the results for the parameters of ITER ($r/a=0.93$, 125 GHz X-mode) we see (fig.2) that the noisy spectrum appears for

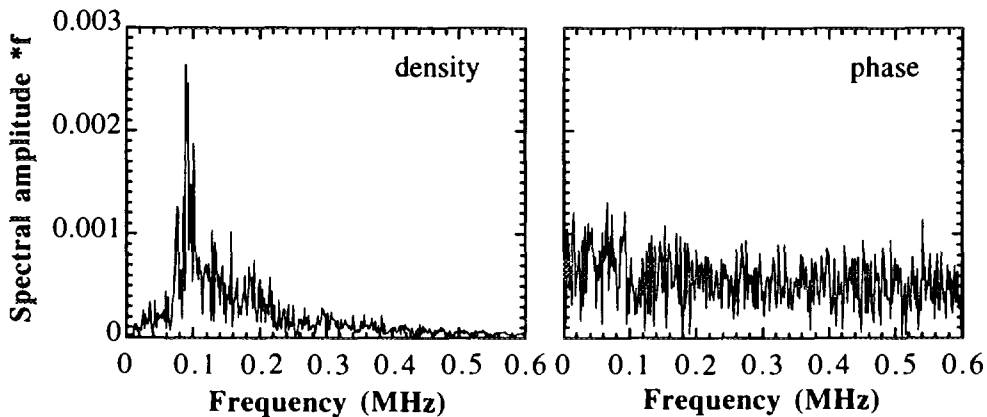


Fig.2. Spectra of the phase of the reflected beam for fixed frequency operation in the ITER geometry.

turbulence parameters which were showing good behaviour in the case of the smaller device. This results is in part due to the shorter wavelength but also due to the larger

distances involved [1] and it shows that in devices like ITER the level of perturbation in the phase will be large.

Simulations were performed for fast swept FM heterodyne, Amplitude Modulation and Pulse Radar reflectometers. The phase delay $\phi(f)$ and amplitude $a(f)$ of the reflected signal were computed as a function of the carrier frequency and from these data the measurements of each reflectometer were simulated. The frequency step was 20 MHz for all simulations, that means, for different device parameters. In all cases the turbulent structure was kept constant during the sweep ("frozen" plasma).

For the Pulse Radar, pulses were reconstructed by backward Fourier transform of the spectrum of the reflected pulse, including the effects of phase and amplitude changes. The pulse width was about 1 ns, its frequency components were reflecting in the plasma within a radial extension shorter than the correlation length. The time delay was defined as the time between the maximum power of the reflected and launched pulses. The maximum power of the reflected pulse suffered variations more than 20 dB due to turbulence. Shapes of many reflected pulses were distorted due to the interference of rays reflected in different points of plasma.

For the AM reflectometer, the time delay was computed from the phase differences in the 3-component spectrum, with 200 MHz distance between components. Results were averaged over 0.01 of full range of frequency sweep. In this case the frequency resolution of the AM reflectometer became close to that of the Pulse Radar. In real AM reflectometers this vector averaging is done by IF filter. This averaging eliminates short splashes of the measured time delay due to interference, accompanied usually by a fall of the signal amplitude.

For the FM homodyne system, a given interval of the signal (corresponding to the selected range of microwave frequencies during the sweep) is converted to its frequency spectrum by FFT, then we take the frequency of the maximum as the instantaneous beat frequency. This FFT method produces a kind of vector average (since it takes for the FFT both phase and amplitude of the homodyne signal) and the results in the reconstruction of the profile are better than with the fringe detection system or directly using the phase signal (heterodyne system).

In order to check the effects of the 2-dimensional interference on the density profile measurements, the parameters of the turbulence were chosen such to produce a noisy spectrum in the fixed frequency operation. Simulations were done for the periphery of an ITER-like plasma. The amplitude of the turbulence was chosen 1.5% (rms) of the central density, constant along the radius, the turbulence average size was 6 cm. The results of the simulation of the time delay and amplitude of the reflected beam, evaluated with the above described procedures, are shown for the Pulse Radar (fig. 3a), Amplitude Modulation (fig. 3b), FM homodyne technique with fringe detection (fig. 3c) and FM homodyne with FFT for transformation to a pulse (fig. 3d). The FM-fringe detection

simulation has been shown without smoothing. Turbulence causes strong, more than 20 dB, modulation of power of reflected signal of AM reflectometer and pulse radar, for the FM homodyne system the amplitude oscillations during the sweep were smaller. The corresponding density profile reconstruction is shown on fig. 4 As we can observe, the

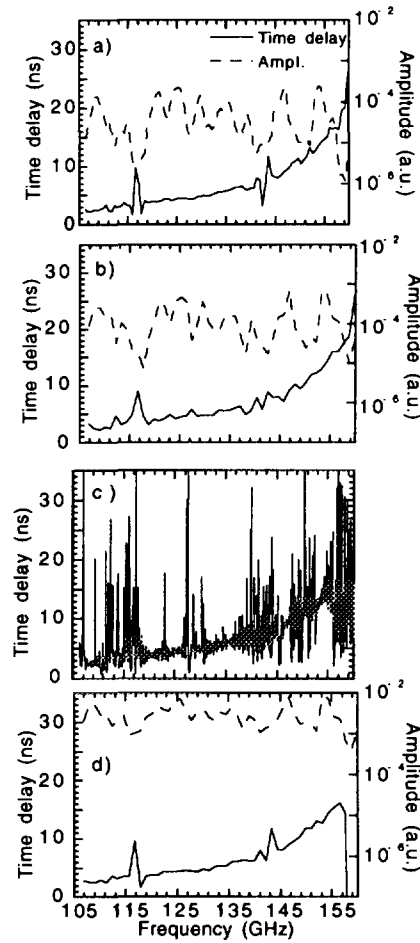


Fig.3. Simulated time delay and amplitude of the reflected beam for the different techniques: pulse (a), AM (b), FM-fringe detection (c), FM-FFT (d)

FM homodyne system with fringe detection (presently used very seldom in the experiments) leads to accumulated errors and produces an unacceptable density profile. On the other hand, Pulse Radar as well as AM and FM (FFT technique) are able to produce a good approach to the original unperturbed profile, which is an encouraging result towards the operation of reflectometers in large devices under turbulence.

Simulations done for the parameters of W7-AS also showed good agreement between the different reconstructions and the original average profile. Even for the fringe detection simulation good profiles were obtained in most cases.

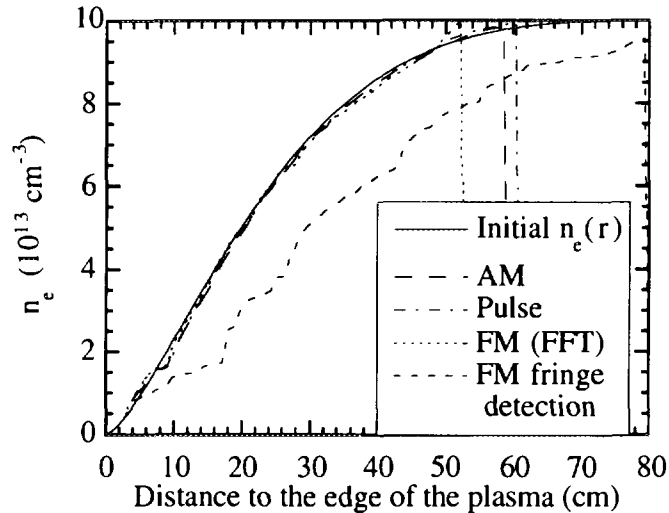


Fig.4. Original average and reconstructed profile using the different techniques (simulation for ITER).

The clue to understand how we can get reasonable profile reconstructions even from noisy phase data is the concept of "vector average": either during the frequency sweep or during a fixed frequency observation of a evolving plasma the signal has some instants with destructive interference (as a result the amplitude of the received signal is low and the phase random) and some others with large amplitude and meaningful phase, due to constructive or absent interference. If we first obtain the phase and then take the time average, the result includes errors, if we instead take the average of the electric field at the receiver (phase & amplitude) then the random values corresponding to strong interference are less weighted (because of the smaller amplitude) and the final average becomes free of error. The vector average is done by hardware at detection in the AM and Pulse radar technique (the pulse radar naturally averages the over many frequencies whereas the AM system performs the average at the last filter). FM systems perform the average by post detection processing (FFT technique means the same averaging as in pulse radar).

These results were obtained for a plasma frozen during the time of sweep. Now we want to analyze the effects of rotating plasmas which in addition to slight antenna tilting lead to phase-runaway phenomena, observed in the experiments (unidirectional phase drift which depends on tilting angle and rotation speed [2]).

We have chosen as relative speed parameter "v": the number of turbulence wavelengths passing in front of the antenna during the (linear) sweep time. For example, $v=2.5$ corresponds to a sweep rate of 4 GHz/ μ s with 200 kHz turbulence. In the simulations,

the antennae were tilted 5° . The results of the simulations for the FM technique with FFT analysis are shown on fig. 5a. For small values of the parameter ν the effect of the rotation is small in the reconstructed density profile. With increasing ν the systematic error increases, reaching unacceptable levels. Opposite direction of rotation leads to the inversion of the error. The same calculations for the AM reflectometer with $\nu=12.5$ have shown no such errors due to the plasma rotation (fig. 5b). This result could be expected being the AM measurement an instantaneous measurement of the time delay (with the three spectral components reflecting simultaneously in the plasma).

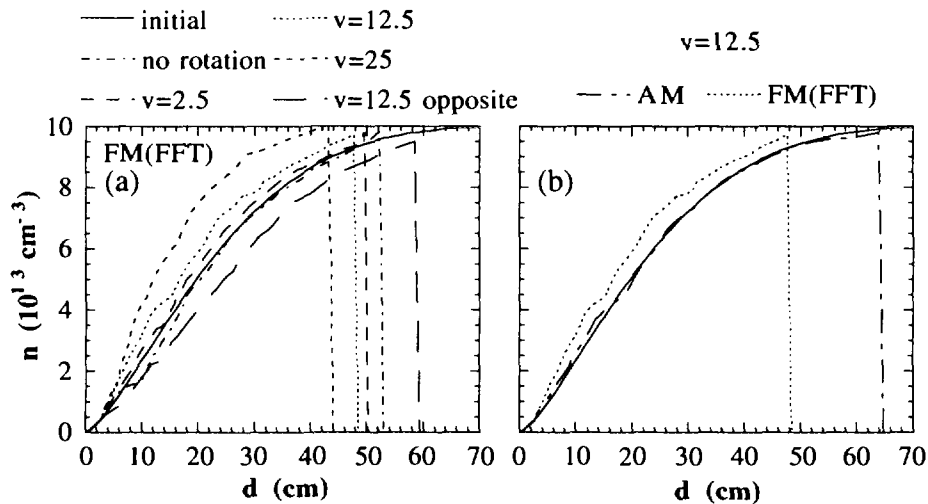


Fig.5. Reconstructed density profiles for different rotation speeds (ITER geometry).

Conclusions

The 2-dim WKB code, able to compute interference effects, was used for qualitative investigation of the perturbations in reflectometry measurements induced by turbulence. Different reflectometry techniques: AM, Pulse Radar, FM (FFT method), are able to measure the density profile in a turbulent ITER size plasma with acceptable accuracy. Plasma rotation together with non-perpendicular reflection that cause no additional errors in the results of the AM reflectometry measurements, lead to systematic errors for the FM reflectometer. Those errors could be eliminated by extremely fast frequency sweep (frequency sweep times shorter than the characteristic rotation times).

References

- [1] V. Zhuravlev, J. Sánchez, E. de la Luna. Plasma Phys and Contrl. Fusion 38 , 2331 (1966).
- [2] B. Brañas et al, these Proceedings.

**NEXT PAGE(S)
left BLANK**

The challenge of reflectometry on ITER

G.Vayakis and the ITER JCT and Home Teams*

ITER JCT, San Diego JWS, 11025 N. Torrey

Pines Rd., La Jolla, CA92037, U.S.A.

Abstract. In present day devices, reflectometry has evolved into a useful plasma diagnostic, both for the measurement of profiles and for the measurement of transient events and fluctuations. Reflectometry is in principle a reactor friendly diagnostic, and as such is counted on to provide a wide range of measurements for ITER. The first part of this paper is a short summary of the role that reflectometry is expected to play on ITER, and the constraints imposed by a reactor grade device on the implementation of the system designs. A brief report of the status of each system is given, with emphasis on the progress in the optimisation process which balances the desired system functions and performance with the realities of incorporating the corresponding front end into the machine. Despite the difficulties, it appears that the ITER measurement requirements can be met.

1. Introduction

Reflectometry has evolved into a useful plasma diagnostic, both for the measurement of profiles and for the measurement of transient events and fluctuations. Reflectometry is also relatively "reactor friendly": It needs, in principle, comparatively small penetrations through the first wall and neutron shield, and the signal can be routed in complex paths to minimise neutron streaming. In addition, the front end requires little or no maintenance, because it is resistant to damage from the plasma, and essentially immune to neutron irradiation effects. For these reasons it is planned to deploy a substantial number of reflectometry systems on ITER.

Nevertheless there are significant problems to overcome: access to the plasma through the plasma facing components, access to the front end for installation and maintenance, calibration to provide immunity to machine movements during the long pulses planned, long transmission lines and relatively ambitious frequency ranges. Although it is fair to state that most of these problems have to be dealt with on present generation tokamaks, ITER presents an unusual challenge in that the problems occur simultaneously. In particular, the access to the plasma is restricted to an unusual degree, due to the stringent thermal and mechanical requirements on the first wall and neutron shield structures.

The paper outline is as follows: in section 2 we examine the measurement role of reflectometry in the ITER diagnostic system. In section 3 we outline the implementation constraints that apply to all the ITER reflectometry systems. Sections 4, 5, and 6 contain a summary of the present state of the design of the systems, with an emphasis on the relation between the system functions and the front end distribution for each system and the solutions adopted to the problems outlined above. Finally, section 7 draws some conclusions and outlines future work on the systems.

*Special acknowledgements to D. Wagner, L. deKock, A. Costley, T. Ando, E. Martin, C. Lippert and to the members of the Reflectometry Working Group: N. Bretz, E. Doyle, V. A. Vershkov, A.J.H. Donn e, J. Irby, M.E. Manso, A. Mase, J Sanchez, V.F. Shevchenko, and C.I. Walker.

Table 1: List of measurements for which reflectometry is expected to be the primary diagnostic.

Measurement	Category
Shape and Position (long pulse)	1b
Divertor Density	1b
Edge Density Profile	1b
ELMs	1b
Density fluctuations	2

2. The role of reflectometry on ITER

One way of prioritising measurements on ITER is by their probable relevance to the control of the machine. This divides measurements into three types: basic machine control (1a), that is, measurements essential to control any plasma pulse; advanced control (1b), that is, measurements that are integrated in the control loop for specific programs, or to access particular regions of operating space; finally, measurements for performance evaluation and physics studies (2). For each measurement we have selected a primary diagnostic system. Reflectometry is expected to be the main diagnostic for the measurements of Table 1. In addition, it is expected to provide supplementary information for a great number of other measurements, such as MHD modes, TAEs, core density profile, and possibly divertor plate erosion.

The measurement list leads naturally to the implementation of three reflectometry systems: a reflectometer for the main plasma, whose main function is the measurement of the density profile, a plasma position reflectometer, able to measure the plasma shape and position in such a way that it can be integrated in the control system, and a divertor reflectometer to measure the density profile in the divertor. The desired measurement capability for each plasma region is based on the target measurement requirements reported in [1,2]. The corresponding frequency ranges are summarised in [3]. In general, it appears possible to meet the measurement requirements [3-6] for all plasma regions, with the possible exception of the 3 mm density resolution target in the divertor region, although predictions for this region are hampered by the lack of relevant experimental results.

3. General implementation constraints

The constraints imposed on the reflectometry systems by the machine are generic in nature, although the solutions vary for each system. Starting from the front end they are:

Access through the first wall / target: Two factors restrict the aperture size that can be provided: the neutron leakage through the first wall and shield, (which must be minimised to ensure hands-on access as close to the machine as possible), and the additional heat loads imposed on the first wall by the presence of the aperture. The latter requirement turns out to be the most restrictive in practice.

Ability to withstand neutron and EM radiation heat loads: The radiative load on parts of the first wall can reach (locally) 0.5 MW/m^2 . For the divertor this figure can be an order of magnitude higher. The neutron first wall loading is $\sim 15 \text{ W/cc}$ for stainless steel. Thus, careful analysis of the cooling requirements must be performed for all the front end components.

Transmission through the first vacuum boundary: The requirements on the pressure handling capability, temperature range and remote handling of the first window are not very different from the present

Table 2: List of the measurement functions of the main reflectometer system

Measurement	Comment	Category
Density profile	• high time and spatial resolution edge profiles	1b
Locked modes	Island size, Te amplitude	1b
ELMs	• high time and space resolution edge profiles	1b
MHD modes, sawteeth, disruption precursors	radial structure	1b
Fishbones and TAEs	• radial structure	2
Density fluctuations		2
<i>Line average density</i>	+	<i>1a</i>
<i>q(r)</i>	+	<i>1b</i>
<i>Plasma rotation</i>	+	<i>1b</i>

A bullet (*) indicates measurement capabilities not shared by other systems.

A cross (+) indicates an indirect or synthesised measurement.

Italics indicates that reflectometry is not the primary system for this measurement.

generation of D-T capable machines. However, the window is usually in a restricted and not readily accessible region. These factors imply that the consequences of window failure on operating time will be severe.

Movement compensation: The transitions between operating states, and thermal effects during the plasma pulse, result in relatively large movements (several cm) between machine components (blanket / vacuum vessel / bioshield). These movements have to be taken up in the transmission line, without disturbing the measurement.

Calibration: One consequence of the machine movements during the pulse is that reference time delays for the reflectometers have to be provided in real time. This is in contrast to the requirements on existing reflectometers, (although real time schemes are implemented on a number of machines).

Location and maintenance of the electronics: Outside the bioshield, the mm-wave electronics are only accessible during maintenance periods, unless extremely long (>100 m) transmission lines are used to bring the signals to the diagnostic hall. This is usually impractical, so that the equipment has to be designed to operate completely unattended for long periods of time, and placed closer to the machine. This results in transmission line lengths of order 30 m, not very far removed from present operational experience.

4. The main reflectometer

(a) Accessibility summary and measurement functions

The accessibility of the main plasma cutoff layers for the standard ITER scenarios has been reported elsewhere [4-6]. In brief, determining the position of the plasma edge and measuring the low density edge plasma profile requires the use of the X-mode upper cutoff (X-u). This can also measure beyond the steep

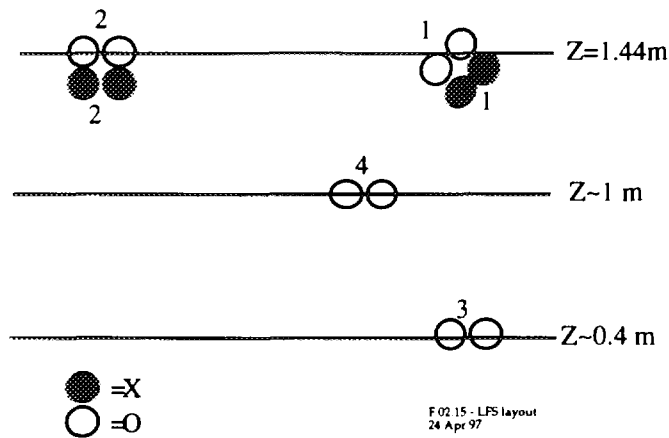


Figure 1: The arrangement of the low field side antennas, viewed from the plasma.

edge density gradient region in H-mode plasmas, but will not reach the plasma centre under standard conditions. O-mode reflectometry partially fills this gap for any temperature profile in the gradient region above a minimum density. Access to the core for flat or slightly hollow density profiles requires the use of the X-mode lower cutoff (X-1), launched from the high field side. For these regions (edge / gradient / core) there are a number of measurements required. These are summarised in Table 2.

(b) The low field side system

In order to meet the requirements implied by Table 2 for the majority of ITER operating conditions and plasma shape, a number of distinct front ends are required. To keep the total number of transmission lines and windows low, the approach is to use relatively few, but broad band, front ends. Based on current operational experience, we are considering bistatic antennas. The arrangement (shown in Figure 1) is optimised for profile performance and MHD measurements for plasmas with Z in the range 0.1-1.75 m. Small scale fluctuation measurements share the same antennas and have affected the design mainly in the grouping of O and X-mode antennas.

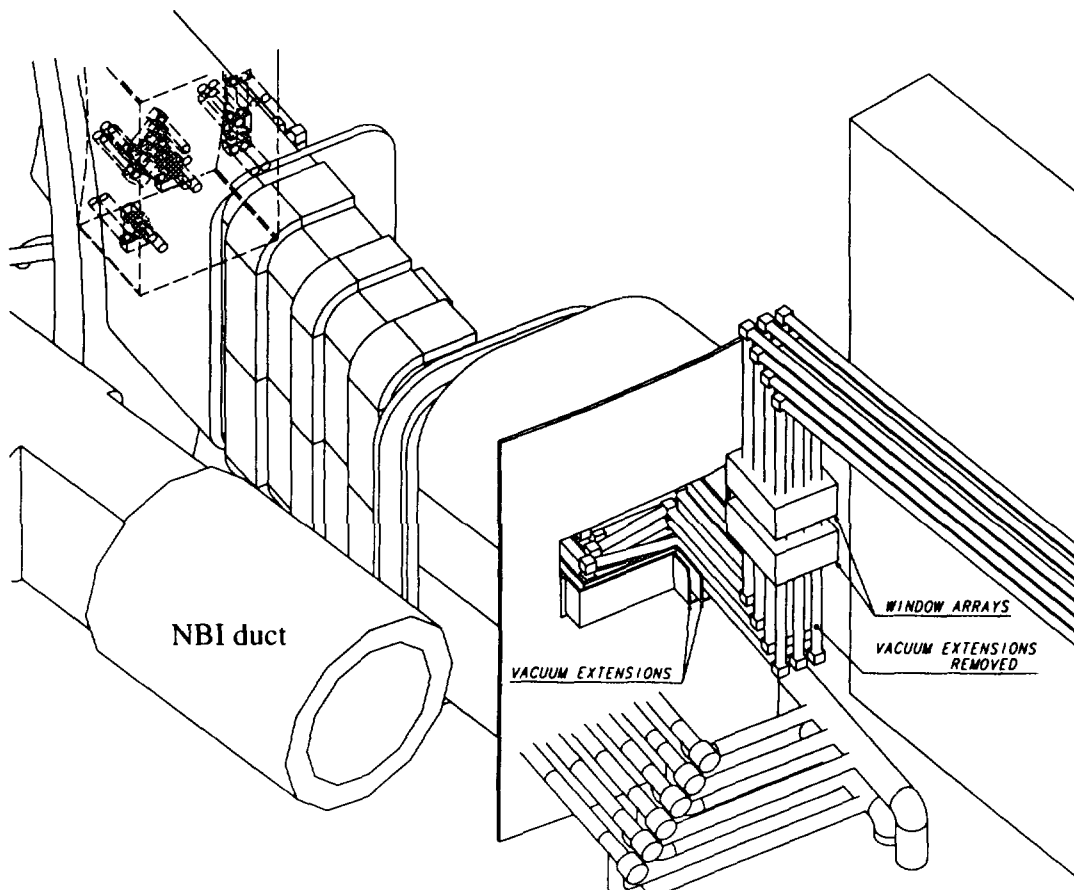
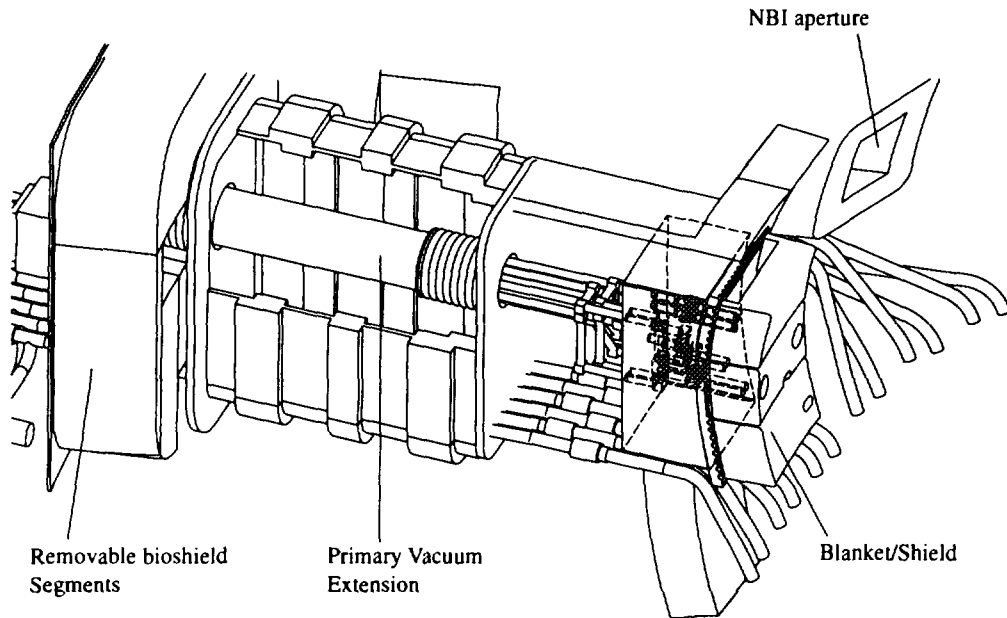
The nominal function of the front ends for O-mode is as follows: *Pair 1*: gradient region profiles for full aperture plasmas, gradient region, 1-point MHD measurements and 1-point density fluctuation measurements. *Pair 2*: Back-up of pair 1 and 2-point MHD measurements in the toroidal direction with pair 1. *Pair 3*: gradient region profiles for start-up plasmas, and 2-point MHD measurements in the poloidal direction with pair 1. *Pair 4*: gradient region profiles for plasmas in the Z range 0.8-1.2 m, and 2-point MHD measurements with any other pair.

The X-u mode system is anticipated to be used only near the edge [4,5], making it less sensitive to vertical displacement. This means that two front ends are sufficient to cover most plasmas (but not the start-up phase). Their functions (refer again to Figure 1 for the numbering scheme) are as follows: *Pair 1*: Scrape-off/gradient profiles for all plasmas, 1-point MHD measurements and 1-point density fluctuation measurements in the edge. *Pair 2*: back-up of pair 1 and 2-point MHD-scale measurements with pair 1.

This tentative arrangement has been used to investigate the possibility of implementation on port #7, which is partially occluded by a tangential neutral beam injector (Figure 2). Some key points are:

- The antennas (at present truncated circular waveguide pairs) are grouped to view the plasma through 4 penetrations, each less than 300 mm in the longest dimension. They need to be optimised (beam pattern, beam overlap, relative inclination) to balance performance in the plasma with minimising the aperture.

Note that standard blanket modules are shown in the figure, but in practice a special first wall module would be necessary to accommodate the penetrations shown.



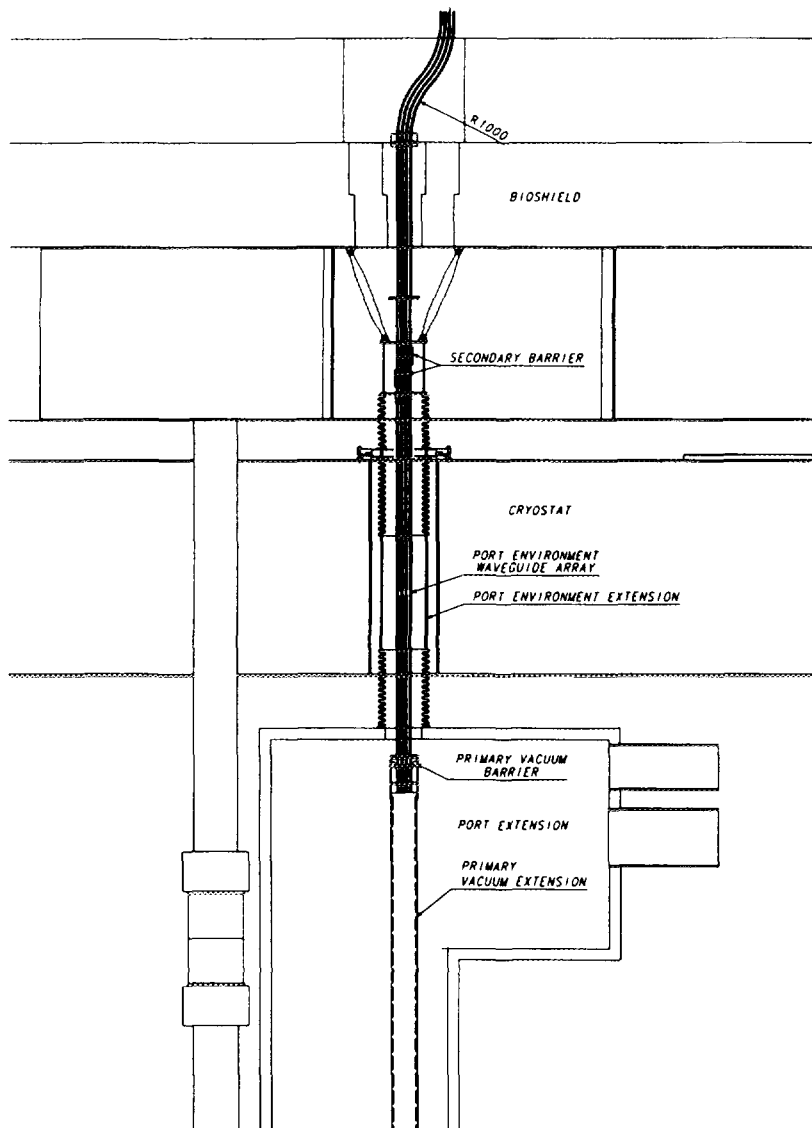


Figure 3: Schematic of the access of microwave guides through a preliminary version of the vertical port for high field side launch (position control and main reflectometer systems). Note the sliding joints beneath the first and second vacuum boundary.

Figure 2: View of the low field side part of the main reflectometer system, from the plasma side (top) and from the Neutral Beam cell (bottom).

- The plasma-antenna distance is of order 1 m. This make the front ends relatively easy to design from the thermal standpoint and confines them to the diagnostic block, which is removed from the outside as a unit.
- In order to provide relatively easy access to the windows, the vacuum boundary has been brought out to the Neutral Beam cell, which in practice forms a tertiary boundary. (There is an additional window on exiting the NB cell.)
- The transmission line is oversize circular corrugated waveguide, with mitre bends. The waveguides are grouped to ease maintenance. The distance between electronics and the front end is of order 40 m.

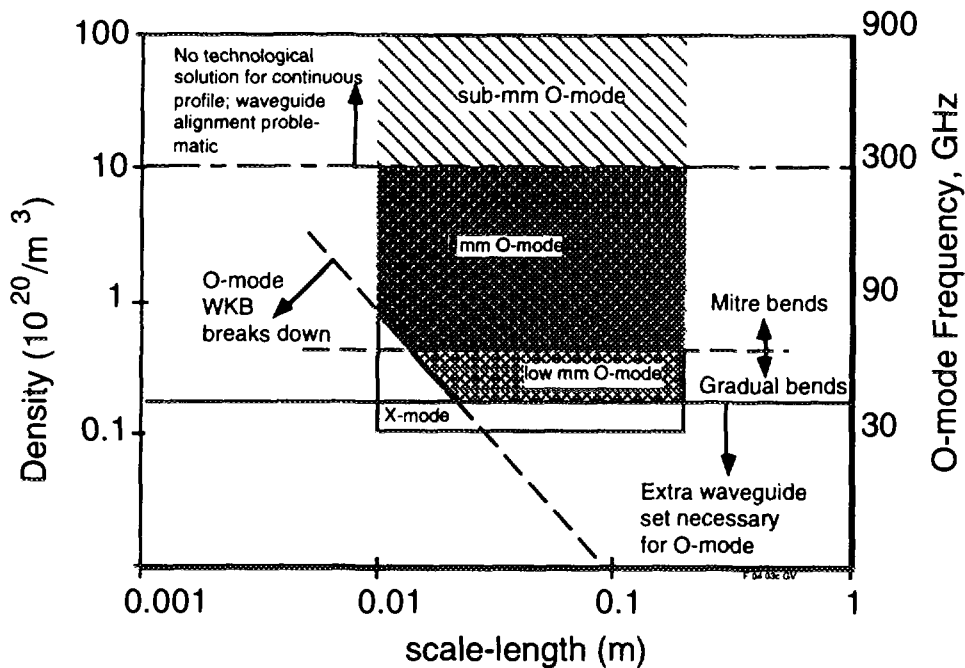


Figure 4: Divertor operating space, deduced from simulations. The x-axis represents the local density scale length.

- The movements between the diagnostic block (supported by the vacuum vessel) and the bioshield are taken up in a dog-leg/sliding joint structure, similar to the one shown in [3]. This is at present embedded in the bioshield.
- The calibration of the system is at present envisaged to be by reflection at the first miter bend using a grating designed to have little effect in band [7].

(c) The high field side system

Because of the physical constraints on the HFS waveguide and antenna construction, it is not possible to design an antenna system that can operate adequately over the full frequency range. For the HFS X-1 mode, two antenna pairs are necessary, one to cover the range 10-40 GHz, and a second for the range 40-110 GHz. For the O-mode front end, the corresponding ranges are 15-60 GHz, and 60-155 GHz. It is anticipated that the antenna pairs will be staggered toroidally, to allow MHD-scale toroidal wavenumber/propagation studies. We are at present attempting to incorporate these antennas into the backplate and blanket structure, with the following constraints and guidelines:

- The antennas fit in the gap between the blanket shield modules, which is nominally 20 mm wide. They are cooled by radiation only. This tends to favour relatively thin structures made out of refractory materials. Each front end is bistatic, and has to be optimised for plasma-antenna distance varying from a few cm to 1.5 m.
- The transmission line is rectangular cross-section (20x20 or 20x10 mm OD) plain copper waveguide for the low frequencies, with a special taper and curve for the final approach before the antenna. For the high frequencies, 25 mm ID corrugated waveguide is used, with a mitre bend before antenna. These waveguides are placed between the blanket shield modules and the backplate.

Table 3: Measurements possible using the divertor waveguide set, and the corresponding waveguide under the assumption that 10% loss per bend is tolerable.

Measure- ment	Band and Polarisation	Suggested Waveguide size (mm), tor x pol	Bend type in poloidal plane	Bend type in toroidalplane
Reflectometry for profiles	mm X	10 x 60	Mitre	None
	low mm O	10 x 10	Hyp. Secant or other special bend	
	mm O	10 x 20	Mitre	None
ECA	mm/sub mm X	10 x 60	Mitre	None
Interfero- metry, Plasma Dispersion Measurement (including peak density)	sub-mm O	10 x 20 *	Mitre	Mitre

* For these measurements, ohmic losses, (rather than mode conversion at the bends), influence the waveguide choice

- The first and second vacuum barrier are in a vertical port. Movement compensation is effected by sliding joints and large radius waveguide flexing. The distance between electronics and the front end is approximately 30 m.
- The calibration is provided by a controlled leak between the transmit and receive waveguide, sufficiently close to the front end that the calibration does not get significantly affected by thermal expansion. In practice it can be up to one or two metres behind the antenna; alternatively, the coupling at the antenna mouth can be exploited.

5. The plasma position reflectometer

This diagnostic is designed to act as a stand-by position/shape measurement system, in order to correct or supplement the magnetics for plasma position control. It likely to be essential during pulse operation exceeding 3×10^3 s, where the position deduced from the magnetic diagnostics could be subject to substantial error due to drifts. This is an advanced control measurement (category 1b).

Clearly, no measurement of a simple plasma quantity can be an exact substitute for the magnetic measurements for the location of the outer flux surfaces. Nevertheless, measurement of the location of contours of a plasma quantity, such as density, can supply sufficient information to control the plasma shape. For the purposes of machine protection, such a measurement has the advantage of providing a direct estimate of the gap between the plasma and the wall. To keep the system as simple as possible, we have chosen an O-mode system located at several (of order 8) points around the main plasma chamber. The relevant frequency range is 15-60 GHz [3]. For an O-mode reflectometer, the accuracy of the estimate of the edge gap improves by measuring the group delay for cutoff densities below the chosen control density, because of the initialisation requirement in the inversion process. 15 GHz corresponds to $3 \times 10^{18}/\text{m}^3$ and

Table 4: Provisional assignment of waveguides for a notional sightline through the divertor leg,

Measurement	Band and polarisation	Number of waveguide lines per sightline	Waveguide size (mm)
Line integral density	sub mm O-mode	2 (in transmission)	10 x 20
Peak density		1 (in reflection)	10 x 20
Profile width, or higher moments		-	-
Low density profile from target side, monostatic (or bistatic)	low mm O-mode	1(or 2)	10 x 10
Profile from target side, bistatic	mm O-mode	-	-
Low density profile from target side, bistatic	mm X-mode	2 (in reflection)	10 x 60
ECA	sub-mm X mode	1 (in transmission)	10 x 60

should ensure more than sufficient accuracy for full performance (and hence dangerous for the first wall) plasmas. At low densities the accuracy degrades, although it is likely to remain reasonable for monotonic edge profiles.

The position control reflectometer shares the implementation problems and features of the low frequency component of the HFS main reflectometry O-mode, and its engineering implementation is being investigated in parallel with that system. The antenna distribution, however, is a distinct optimisation problem. To illustrate the access path for both systems, Figure 3 shows a schematic of the features of a transmission line taken through a nominal vertical port. Optimisation of the transmission line will depend on the final layout and maintenance procedure for the vertical port, at present under modification.

6. The divertor reflectometer

(a) System functions; location and function of the antennas

The divertor reflectometer is mainly a density profile measurement system. The resolution target is 3 mm across the divertor leg, and 10 cm along the leg, and the time resolution requirement is 1ms [3]. An additional function for this system may be determining the ionisation front location in the semi-detached divertor operating regime. In addition to the difficult access within the cassette, the challenges in designing the divertor system lie in two areas:

1) The divertor operating space. This is illustrated in Figure 4, To show the consequence of the consequent frequency operating space requirements, we consider first the choice of waveguide near the front end, where the toroidal size is fixed at around 10 mm. Table 3 shows suitable types of waveguide given the frequency ranges shown in Figure 4, and a requirement for mode conversion less than 10%/bend. We have assumed here that X-mode ECA measurements can use the same waveguide as X-mode

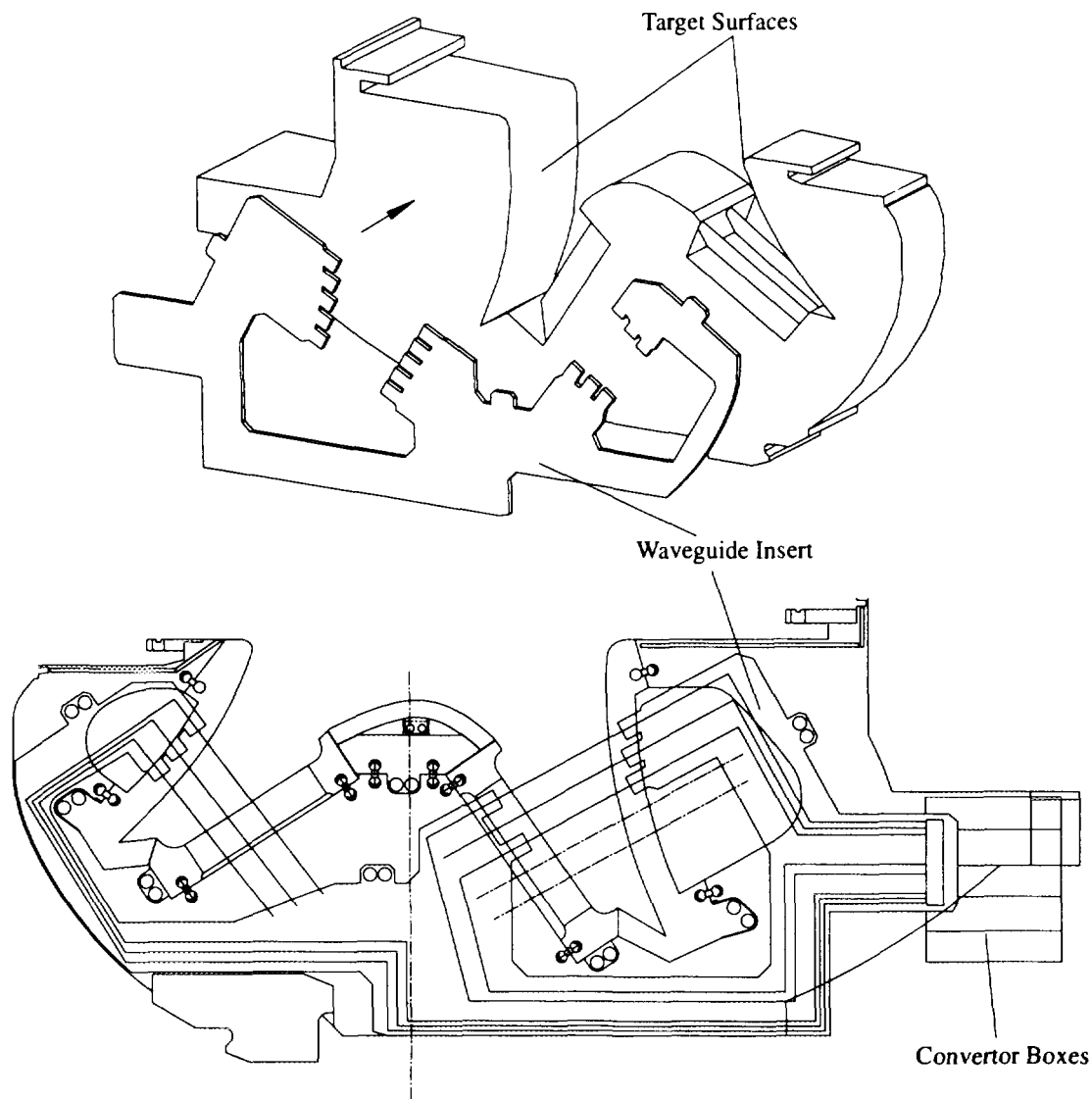


Figure 5: Top: The principle of attaching a pre-assembled waveguide insert onto a divertor cassette. Bottom: The arrangement for the left hand side of port # 18, showing the partial utilisation of 6 sightlines.

reflectometry (in transmit mode) and that robust line integral, peak density and plasma dispersion measurements can be performed using any opposing pair of waveguides.

2) The wide range of possible measurement geometries. For example within reflectometry, one can measure from the private flux or target side, using monostatic or bistatic antennas, in O-mode or X-mode, with a choice of sightlines. In addition ECA, interferometry and plasma dispersion techniques requiring transmission through the plasma will have to share the access space. The present design choice is for multiple sightline, low transmission line diversity system. In order to estimate the number of possible sightlines in such a system, we have to consider the possibilities for waveguide sharing between measurements. To make progress we have assigned high priority to "robust" measurements that have been demonstrated on the present generation of machines. This is shown in Table 4.

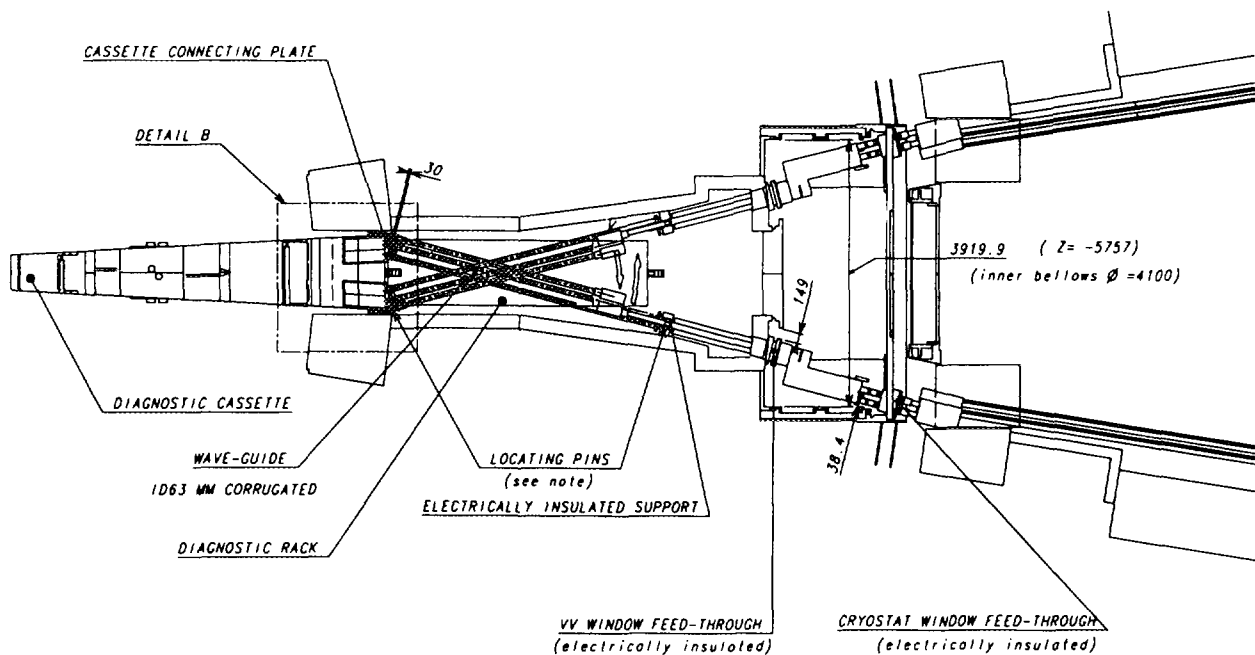


Figure 6: Plan view of the proposed divertor reflectometer arrangement

(b) Transmission line layout

More work is necessary to determine the viability of the more difficult schemes of Tables 3 and 4 before determining a final configuration. In the meantime, since the ITER divertor cassette design is considerably advanced we were able to determine the regions within the divertor cassette where waveguides could be placed with some confidence. This resulted in a concept of using a semi-independent insert to house and cool the front end waveguides and antennas (Figure 5, top). The antennas have to view the plasma through the gaps between target plate (10-25 mm). Any other solution produces unacceptable local heat loads on the divertor target. Providing a reference point for calibration, and resolving plasma reflections (the plasma - antenna distance ranges from a few cm to ~0.5 m, depending on the sightline) is complicated by parasitic reflections in the gap between the cassettes. The details of the antenna for each function and frequency range will require extensive study.

Taking the 8 waveguides per sightline implied by Table 4, for a reasonable 5 outer leg sightlines and 3 inner leg sightlines results in a total of 56 waveguides. The maximum number of waveguides that we can route out of the machine is constrained by the space available in the diagnostic ports. For reasonable waveguide size (40-90 mm dia corrugated), we can fit 40 waveguides in two ports. In practice due to additional restrictions imposed by the cassette, not all configurations are possible at all sightlines. For example no more than two 10 x 60 waveguides can be routed to the inner leg for each cassette used.

Figure 6 shows the complete transmission line layout for one of the divertor ports. Some key points are:

- Most of the transmission line, including the first and second vacuum barriers, is permanently installed in the divertor port. There is a remotely handled folding section which allows quick removal of the cassette.

- The transition between the oversize corrugated waveguide and the rectangular waveguide within the cassette is performed quasi-optically, in a set of assemblies ("convertor boxes" in Figure 5) attached to the divertor cassette. The distance between the electronics and the front end is about 40 m.
- Movement compensation is provided by a dog-leg and sliding joint assembly located in the interspace between the vacuum vessel and cryostat seal plates. This has to be removed to allow access to the windows on the vacuum vessel flange.
- **7. Conclusions**

Reflectometry is expected to be routinely useful in ITER for a wide range of measurements, many of which are required to form part of real-time control loops used to operate the machine. As a result we have planned for thorough coverage of all plasma regions. There are great differences in the details of the implementation of each system, but also some common themes (not all of which have been explored in this paper), which will form the backbone of future work on these systems:

One common theme is the requirement for *optimisation of a limited number of antennas for a wide range of functions*. This optimisation depends both on the antenna distribution, which must be sufficient for the coverage of expected plasmas, and the *optimisation of individual front ends for the full frequency and radial range expected* with the minimum disturbance to the first wall or target and neutron shield structures. In principle, solutions have been found for this key problem of access through the first wall for all the systems, but much work remains, including a *reliable assessment of the likely effect of fluctuations on front end performance*. Another common element is the need for rugged calibration schemes that will allow the real time reference of the density profile to a hardware feature of the machine (backplate, vacuum vessel or divertor cassette). Again, this is linked to the detailed optimisation of the front end. For all systems there is a need to mitigate the effects of parasitic reflections that arise from the close fitting apertures through which the antenna views the plasma. It is a common observation in complex mm-wave systems that the performance of the whole system depends on interactions between the components, which sometimes produce undesirable and unpredicted results. Given the effort required to place diagnostics with a machine such as ITER, it is expected that prototype transmission lines will have to be thoroughly tested for all the systems before installation.

Acknowledgement

This report has been prepared as an account of work performed under the Agreement among the European Atomic Energy Community, the Government of Japan, the Government of the Russian Federation, and the Government of the United States of America on Cooperation in the Engineering Design Activities for the International Thermonuclear Experimental Reactor ("ITER EDA Agreement") under the auspices of the International Atomic Energy Agency (IAEA).

References

- [1] A. Costley et al, in "Diagnostics for Experimental Thermonuclear Fusion Reactors", P.E. Stott, G. Gorini and E. Sindoni Eds., Plenum Press, New York and London 1996, p. 23 ff
- [2] K. Young et al, Rev. Sci. Instrum. 68 (1), 1997, p. 862
- [3] G. Vayakis et al, *ibid.* p. 435
- [4] M.E. Manso et al, in "Diagnostics for Experimental Thermonuclear Fusion Reactors", P.E. Stott, G. Gorini and E. Sindoni Eds., Plenum Press, New York and London 1996, p. 133 ff
- [5] V.A. Vershkov, *ibid.* p. 143 ff
- [6] E.J Doyle et al, *ibid.* p. 117 ff
- [7] L. Empacher et al, to appear in Proceedings 10th Joint Workshop on Electron Cyclotron Emission and Electron Cyclotron Resonance Heating, Ameland, the Netherlands April 1997.

Phase runaway effects on Wendelstein 7-AS

B. Brañas, M. Hirsch*, V. Zhuravlev, J. Baldzuhn*, J. Sánchez, T. Estrada, T. Geist*, H.J.

Hartfuß*

Asociación EURATOM-CIEMAT, Madrid, Spain

**Max-Planck-Institut für Plasmaphysik, EURATOM-Ass, 85748 Garching, Germany*

Abstract. The phase runaway phenomenon has been studied using the W7-AS heterodyne reflectometer. The phase evolution is intermittent, changing rapidly in certain time intervals that show a strong level of amplitude fluctuations. There is a clear dependence of the value of the runaway phase $\langle d\phi/dt \rangle$ with the local and global plasma parameters. Several authors have proposed that the phase runaway is due to rotation of turbulent structures provided that some asymmetry between these structures and the reflectometer axis exists. The relation between the phase runaway and plasma rotation has been confirmed at W7-AS. The radial profile of the runaway qualitatively corresponds with the plasma poloidal rotation profile. Besides, the observed phase drift can be inverted by inverting the toroidal magnetic field of the stellarator, thus changing the rotation direction of the plasma. This result implies that the necessary asymmetry is independent on the direction of plasma rotation. 2D WKB simulations of the reflection on a poloidally rotating turbulent plasma for the W7-AS reflectometer and plasma parameters reproduce qualitatively the experimental features (intermittent phase drift, relation between phase and amplitude changes) of the measured phase signal.

I. Introduction

Under turbulent plasma conditions a drift of the measured reflectometer phase is observed which can not be explained by a realistic radial movement of the cut-off layer due to density changes. This so called "phase runaway", that complicates and in occasions impairs completely the density measurements, has been observed for many plasma conditions with almost all reflectometers able to follow such a phase drift [1-6].

The phase runaway can affect the density profile measurements performed by some reflectometry techniques. The relevant magnitude to be measured for obtaining the density profile is the time delay $\tau(F) = 1/2\pi (d\phi/dF)$, where F denotes the microwave frequency. Techniques like FM reflectometry measure the time delay from the time derivative of the phase as the frequency is swept with time. Under these conditions the phase runaway directly affects the measurements since it simply adds to the actual phase derivative. The problem can be overcome by sweeping the frequency fast enough or by using techniques like Pulse Radar or Amplitude Modulation (also differential phase techniques) which determine the time delay from simultaneous measurements of the phase at neighboring frequencies.

Concerning the density turbulence measurements, the time scales of the phase excursions that give rise to the phase drift and that of the turbulence induced phase fluctuations are similar. This makes the separation of both parts of the signal very difficult and sometimes impossible. On the other hand, the phase runaway itself is a consequence of the plasma density turbulence. An understanding of this phenomenon is therefore essential for the correct interpretation of the reflectometer signal in terms of plasma density turbulence. With this aim experiments and simulations have been carried out at W7-AS.

It has been suggested that the phase runaway represents the Doppler shift of the probing radiation reflected from rotating cut-off layer disturbances [2,4,5]. Either these disturbances are asymmetric [2,4] or a misalignment of the reflectometer axis with respect to the normal at the cut-off

layer exists [5]. A two dimensional full wave simulation [7] of the interaction between the mm-wave and poloidally propagating oscillatory modes in this situation predicts the appearance of a phase runaway. However, so far no direct comparisons of the runaway phase with an independent plasma rotation measurement have been done.

In this paper we first describe the reflectometer system (section II). Section III deals with the characteristics of the observed phase drift. In section IV the experiments to investigate the relation of the phase runaway with plasma rotation at W7-AS are described. 2D WKB code calculations are presented in section V. The possible origin of the phase runaway at W7-AS is discussed in section VI.

II. System description

W7-AS is a low shear modular stellarator with a major radius $R=2$ m and an average minor radius $a<17$ cm. The reflectometer installed at this machine [8,9] uses X-mode propagation in the W-band (75-110 GHz) for probing radial positions corresponding to densities between 1 and $6 \cdot 10^{19} \text{ m}^{-3}$ (for a magnetic field on axis $B_0=2.5$ T) or between 4.5 and $10 \cdot 10^{19} \text{ m}^{-3}$ ($B_0=1.25$ T). Corrugated horns in combination with elliptical mirrors are used as emitting and receiving antennas. Their pattern is characterized by gaussian beams (nearly flat wave front approaching the plasma) with a waist of 2 cm in vacuum at a focal distance of 50 cm. The experimental setup is shown in Fig. 1. The cut-off surfaces are slightly tilted (2.6°) with respect to the probing direction.

Heterodyne detection with a dynamic range of more than 60 dB allows to decouple phase and amplitude fluctuations. The phase is detected by a sin/cos phase meter operating at 60 MHz and the signal amplitude is measured at the input of the phase detector with a wideband detector diode (3 dB bandwidth of 4-5 MHz). An Amplitude Modulation system [9] integrated in the reflectometer

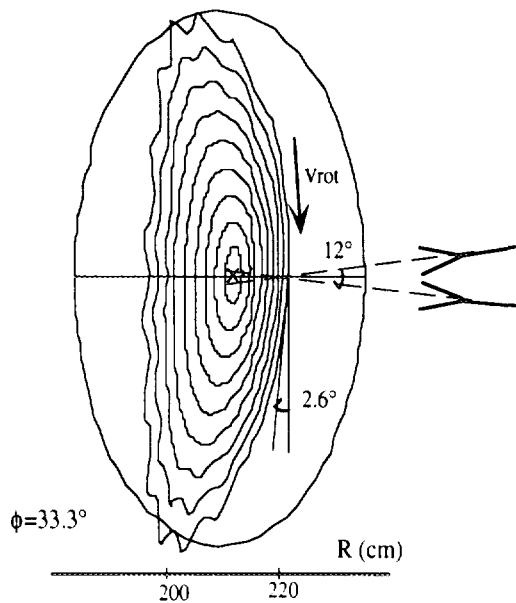


Fig. 1: W7-AS reflectometer setup.

provides a time delay measurement which is used to obtain density profile information. All signals: carrier phase, time delay and amplitude, are sampled at 10 MHz.

Instrumental effects can be excluded to be responsible of the observed phase drift. Phase changes up to at least 5 MHz can be properly measured. Nevertheless, in order to increase the signal/noise ratio, the 3 dB bandwidth of detection was restricted to 1 MHz by a bandpass filter immediately before the phase meter. For the complete reflectometer

system, including oscillators, mixers and electronics, the dynamic range is 60 dB and the overall phase noise is around 0.1 rad in all the range of mm-wave frequencies. It has been checked that the electronics, even for very small signal levels, does not introduce any apparent drift of phase.

III. Description of the "phase runaway" at W7-AS

An example of the evolution of the reflectometer phase during stationary plasma conditions of a typical plasma discharge at W7-AS is shown in Fig. 2a. A detail of 10 μ s is given in Fig. 2b.

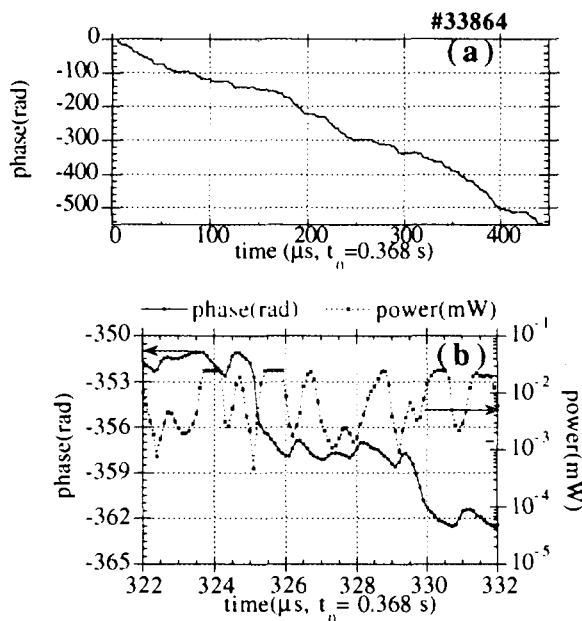


Fig. 2: a) Evolution of the reflectometer phase for a constant microwave frequency ($F=85$ GHz, $r_{cut-off}=0.135$ m) during stationary plasma conditions (origin of time trace 0.368 s after beginning of discharge). b) Detail of reflectometer phase (solid line) and reflected power (broken line) signals for the same conditions as in fig 2a).

is shown in Fig. 2b): the phase increases faster than it decreases, with the minima in the amplitude produced during the fastest phase change. During these periods of low amplitude, the phase shows sometimes excursions of the order of 2π , not recovering to its previous value, causing in the long term a drift in negative direction.

The minimum measured power is around -40 dBm, well above the limit for a correct measurement of the phase detector (the minimum power at the entrance of the phase detector required for a phase measurement with an accuracy of 3° is -70 dBm). When the phase drift is not too strong, amplitude and phase signals are coherent for all frequencies higher than 50 kHz with the phase shift between them very close to $\pi/2$. This agrees with observations at JET and simulation predictions [10,11]. On the other hand, when the phase runaway is large, the phase spectra have a $1/f$ shape and amplitude and phase signals show low coherence in the whole frequency range. The $1/f$ shape of the phase spectrum has also been observed experimentally in TFTR during discharges with high power NBI heating [12] and in ohmic discharges on CCT [13].

The phase evolution is intermittent. There are time regions without phase drift and small time intervals (5-30% of the time) in which the phase increases or decreases very rapidly ($(2\pi)^{-1}d\phi/dt$ of several hundreds kHz). These phase excursions (between 4 and 15 radians typically) tend to occur preferentially in one direction giving rise to an average phase runaway $(2\pi)^{-1}\langle d\phi/dt \rangle$ of the order of some tens of kHz. A 10 MHz sampling rate is required to measure properly the fast phase changes. The phase excursions are accompanied by fluctuations in the returned mm-wave power and a clear correspondence exists between the power minima and the fastest phase changes. Typically, all phase increments faster than 2 rad/ μ s are related to a drop of power of the order of 20 dB. The observed phase fluctuations are often asymmetric (an example

Although fluctuations in the time delay measured with the AM system are observed, the phase of the AM envelope is typically within a range of 1-2 rad, also during periods which exhibit a drift of the carrier phase. This indicates that the phase evolution is very similar over the radial range probed by the spectral components of the AM wave and thus the drift is canceled by the differential phase measurement.

The magnitude $(2\pi)^{-1}\langle d\phi/dt \rangle$ of the observed runaway shows a characteristic radial profile: it is positive, i.e. the reflected signal is "blue shifted", outside the separatrix, negative within the confinement region with a maximum net frequency shift of a few 100's kHz and it decreases towards the plasma centre. This radial dependence has been observed in a wide range of plasma conditions with ECH, NBI, at different heating power and electron densities.

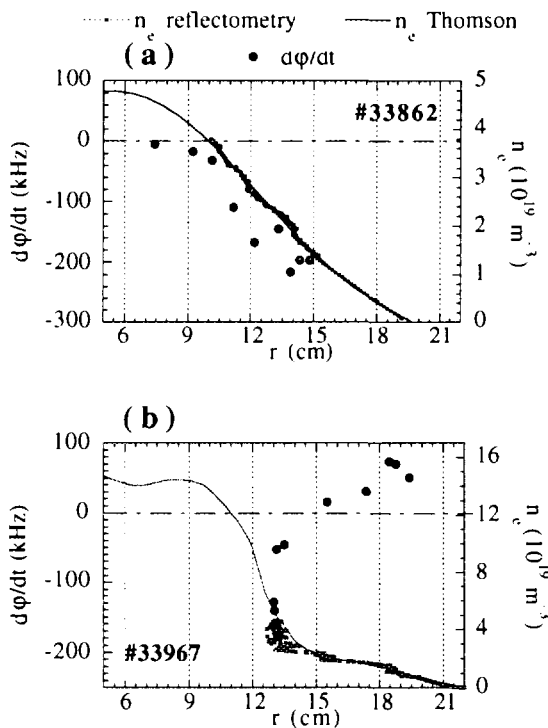


Fig. 3: Dependence of the phase runaway (black dots) with radial position a) 400 kW ECH heating, $\langle n_e \rangle = 3.5 \cdot 10^{19} \text{ m}^{-3}$ and b) for a high density separatrix-dominated (1.8 MW NBI heating, $\langle n_e \rangle = 1.2 \cdot 10^{20} \text{ m}^{-3}$) discharge. The density profiles, obtained using the reflectometer time delay signal during the ramp down following the stepwise sweep and Thomson data, are also included. Position of the LCFS is around 16 cm and 13 cm in Figs. 4a and 4b respectively.

Fig. 3a shows the runaway radial profile during an ECH discharge. As an example of the positive values of the phase runaway observed outside the LCFS, Fig. 3b shows the runaway and electron density profiles during a discharge with high density ($\langle n_e \rangle = 1.2 \cdot 10^{20} \text{ m}^{-3}$) and heating power (1.8 MW NBI), for which the radial positions accessible for the reflectometer are more external with respect to the separatrix.

For a given microwave frequency, the phase runaway strongly depends on variations of plasma conditions such as the heating scenario or fuelling. Changes in the value and sign of the runaway phase drift are observed a few tens of ms after the ECH or NBI heating are switched on or off. These variations are associated with the change of the electron density profile that results in a shift of the probed radial position. For some plasmas with balanced NBI heating no runaway was observed while it was present with co or counter injection alone. The most striking effect is the sudden disappearance of the phase runaway at the transition to the H-mode[14,15]. This can be seen in Fig. 4a, which shows the phase of the signal reflected at a position within the transport barrier together with the H_α signal for comparison. Figs. 4b and 4c show the Fourier spectra of the carrier phase and power signals in time windows corresponding to L and H-mode respectively. The

runaway was observed while it was present with co or counter injection alone. The most striking effect is the sudden disappearance of the phase runaway at the transition to the H-mode[14,15]. This can be seen in Fig. 4a, which shows the phase of the signal reflected at a position within the transport barrier together with the H_α signal for comparison. Figs. 4b and 4c show the Fourier spectra of the carrier phase and power signals in time windows corresponding to L and H-mode respectively. The

phase spectrum during L-mode shows the typical $1/f$ behaviour and the phase and power fluctuations are incoherent. When going into the H-mode, a decrease of fluctuations in the phase and power signals is observed for the full frequency range. During this regime, amplitude and phase fluctuations are coherent, being the phase shift between them very close to $\pi/2$ for all fluctuation frequencies.

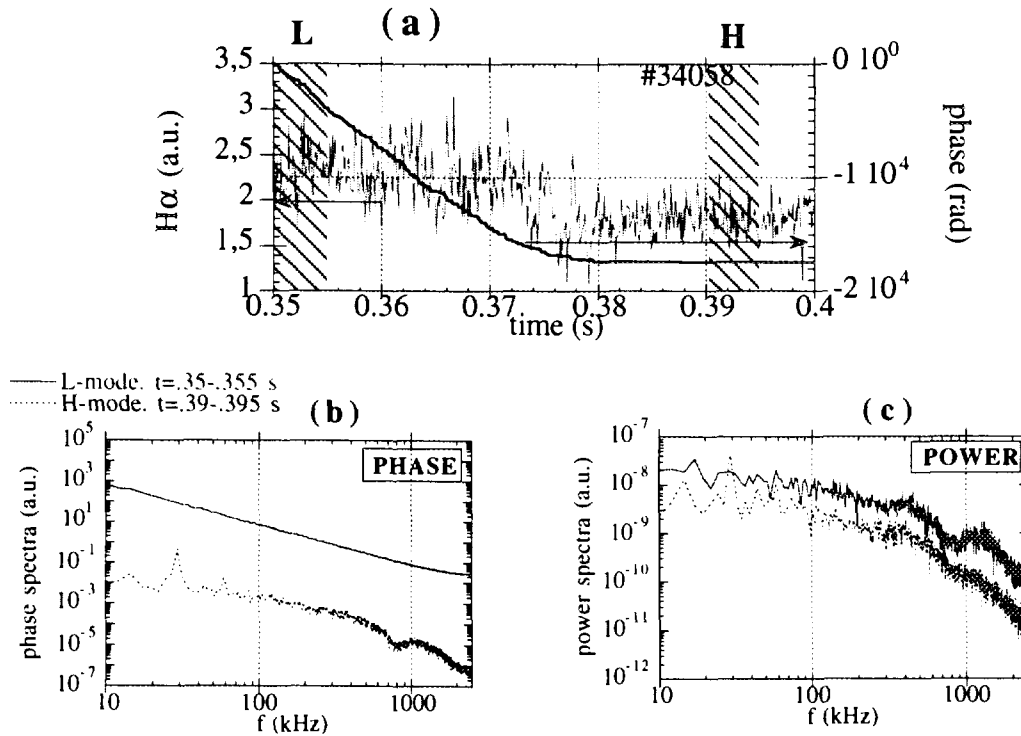


Fig. 4: (a) Reflectometer phase and $H\alpha$ signals during an L-H transition. Probing frequency is 86.8 GHz and corresponds to a position $r=0.16$ m, inside the transport barrier. Power spectra of (b) carrier phase and (c) signal power in L and H-mode.

The disappearance of the runaway is observed at all radii except for the most external ones, outside the transport barrier. ELMs and dithers are accompanied again by rapid phase excursions.

IV. Experiments on plasma rotation

The correlation between the phase runaway and poloidal plasma rotation of the electrons has been investigated at W7-AS. The observed change of sign of the runaway at a position close to the LCFS (and to the velocity shear layer) suggests a relation between these parameters. This has been studied in detail in two types of discharges which display different rotation profiles (Fig. 5): (5a) ECRH heating 400 kW off-axis + 400 kW on-axis and (5b) ECRH 400 kW off-axis only. The poloidal plasma rotation was obtained as a sum of the $E \times B$ and diamagnetic drifts. The radial electric field has been measured from the Doppler shift of impurity emission lines (boron IV) and the pressure profile has been obtained from Thomson scattering data. Fig. 5 shows that for the two plasma conditions the radial profile of the phase drift qualitatively corresponds with the poloidal plasma rotation profile. The electron density and temperature profiles are also displayed in this figure. For the case of pure off-axis heating (Fig. 5b) the electron temperature and its gradient have moderate values inside the heating position ($r \sim 0.1$ m). Therefore the diamagnetic contribution to plasma rotation in this region is very low, a feature that is also observed in the phase runaway values. In this

experiment positions outside the LCFS could not be reached with the reflectometer and no positive values of the runaway were found.

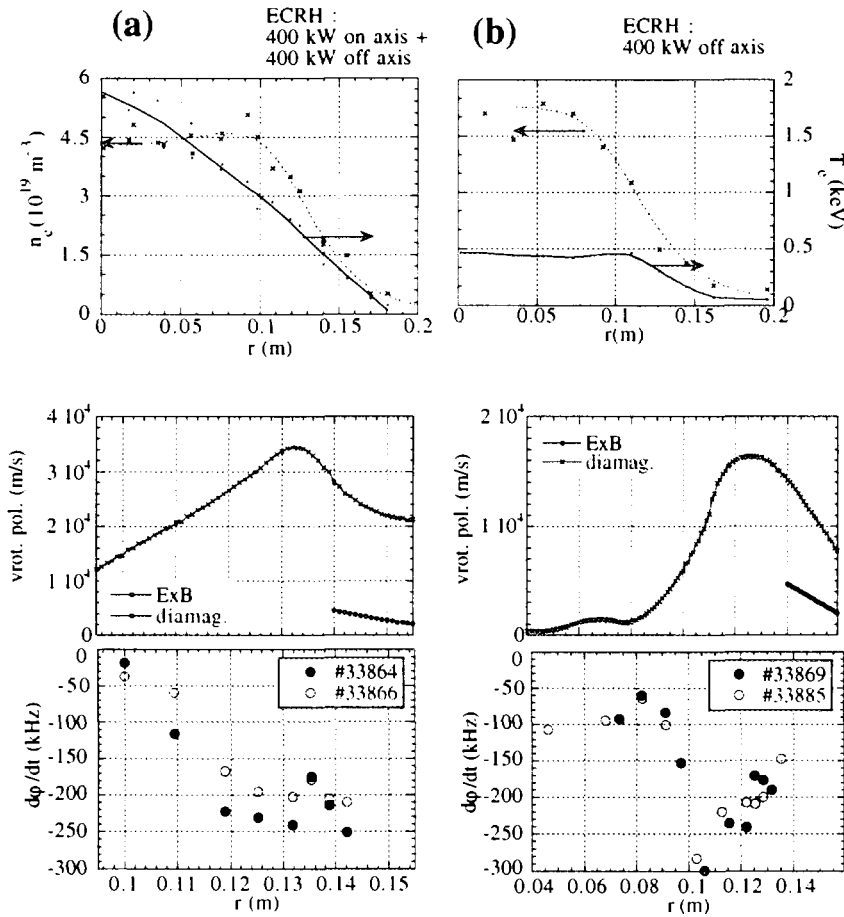


Fig. 5: Radial profiles of electron density and temperature, electron poloidal rotation and phase runaway. (a) ECRH heating 400 kW off axis + 400 kW on axis, (b) ECRH 400 kW off axis only. For each case, the values of the runaway in two identical discharges are shown.

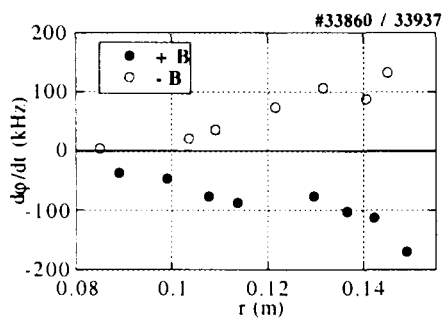


Fig. 6: $d\phi/dt$ as a function of radius in two symmetrical plasma configurations. All plasma parameters are kept constant while magnetic field and rotation have opposite sign in both.

To confirm the relation between the phase runaway and plasma rotation, the stellarator magnetic field has been inverted for a series of ECRH heated discharges keeping all other plasma parameters constant.

The electron density profile (measured with Thomson scattering, reflectometry and Li-beam) and the electron temperature profile (measured with Thomson scattering and ECE), do not change as the magnetic field is reversed. Impurity rotation changes sign

confirming the inversion of the ExB velocity.

Fig. 6 shows the radial profile of the phase drift for positive and negative magnetic field: for all probed radial positions the drift is inverted as the plasma rotation is reversed. Nevertheless, for some

discharges, the absolute values of the drift differ by up to a factor of two, specially for the lower microwave frequencies. A detailed observation of the phase signal shows that not only the runaway but also the shape of the temporal behavior of the phase fluctuations is inverted. This can be observed in Fig. 7, that represents a detail of the phase and amplitude of the reflected microwave signal for two discharges with different magnetic field directions.

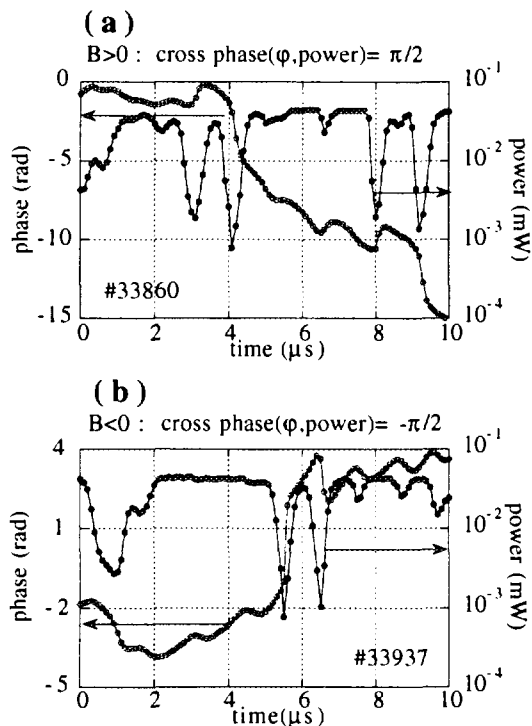


Fig. 7: Phase and amplitude time traces of a reflectometer signal for a) positive and b) negative magnetic fields. Probed position is $r \sim 0.1$ m.

and $14 \cdot 10^{19} \text{ m}^{-3}$, rotational transform 0.3/0.5). No change in the magnitude and sign of the runaway phase was observed when using the upper or the lower antenna for launching the microwaves.

V. Simulation

To analyze the possible effects of poloidally propagating density structures, a two dimensional WKB simulation has been carried out for the W7-AS plasma and reflectometer parameters (antenna aperture= 2.3° , distance antenna-plasma=50 cm, microwave wavelength $\lambda=2.7\text{-}4$ mm). Previous 1D calculations [16] have shown that for the microwave wavelengths used and the expected fluctuation wavelengths (1.5 cm at the plasma edge, 3 cm at the most internal probed positions) the WKB method can be considered a good approximation to the full wave treatment. Diffraction effects are not taken into account in the WKB approximation. However, given the high directivity of the antenna-mirror arrangement, for a probing direction close to perpendicular most of the diffracted signal should not return to the receiving horn and thus reflected components should dominate the measured signal. For the turbulence, a simple model consisting of a series of hills and valleys superimposed to the average density distribution is used [17,18]. The amplitude A_s of each hill or depression and the distance between them vary randomly in both radial and poloidal directions within 50% of their mean

For the data of Fig. 7, that correspond to an internal position ($r \sim 0.1$ m), the coherence between phase and amplitude signals is high in the range $50 \text{ kHz} < f < 2 \text{ MHz}$, and the phase shift between both signals is $\pm\pi/2$ for positive and negative magnetic field respectively.

Note that in base of these experiments, a Doppler shift induced by radially moving density bursts can be excluded to be the main origin of the phase runaway.

To find out whether the use of two poloidally separated horns had any influence in the phase runaway, emitting and receiving transmission lines were interchanged between reproducible discharges by means of waveguide switches. This was done for a wide range of plasma conditions (toroidal magnetic field of 1.25 / \pm 2.5 T, heating with 400/800 kW ECH and 1/2 MW NBI, average density between 2

values. The average size Λ_s of the turbulence is the average distance between tops of the hills. Calculations were made for a range of Λ_s corresponding to $\tilde{n}/n \sim 0.1-6\%$ (typical \tilde{n}/n measured at W7-AS from phase signals that presented no runaway are 1-6%) and for $\Lambda_s \sim 0.1-20$ cm.

In accordance with the experimental findings, the simulated phase signal shows sudden phase changes combined with drops in the signal amplitude. This occurs when 1) the amplitude of the density turbulence A_s is greater than some threshold A_{thr} , where $A_{thr} \sim \lambda/8 \times \text{gradn}$ and 2) the average poloidal size of the turbulence is comparable to the spot size. These two conditions imply that phase shifts of the order of π can exist between rays that are reflected at different poloidal positions in the antenna pattern. These rays interfere at the receiving antenna giving rise to strong amplitude fluctuations and rapid phase changes of the resulting signal. The coherently reflected signal is lost and the phase of the resulting wave is not related linearly with the density fluctuations. In this situation, a net drift of the phase appears if the geometry of the emitting horn, the rotating cut-off layer and the receiving horn is not symmetric. The asymmetry may be present in the turbulent structures or may be caused by non perpendicular probing with respect to the cut-off layer. It must be mentioned that a method has been proposed recently to extract the density turbulence characteristics from the ratio of the coherent and incoherent parts of the reflected signal[19].

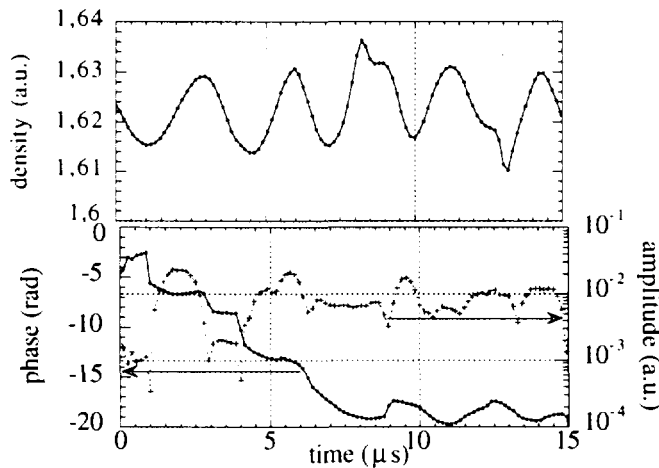


Fig. 8: Results of 2D WKB simulation with the horn axis 11° misaligned from the equatorial plane. Turbulence parameters used: $\tilde{n}/n=0.8\%$, $\Lambda_\theta=3\text{cm}$. a) Density fluctuations. b) Reflectometer phase and amplitude.

As an example, Fig. 8 shows the simulated phase and amplitude fluctuations and the corresponding density signal when the antenna axis is misaligned by 2° in the poloidal plane. Large phase and amplitude variations are observed. In the long run the phase changes are unbalanced and lead to phase runaway. In agreement with the experimental results presented in section III, the minima in the amplitude correspond to the fastest phase changes.

If the average size of the turbulence is much smaller than the spot size the probability of completely destructive interference decreases and so does the resulting phase runaway (but note that if $A_s > A_{thr}$ reflection is incoherent and phase and density fluctuations can not be related). No phase runaway occurs either in the other limit, when the spot includes only a small fraction of an average

wavelength. For intermediate values of A_s and provided the necessary condition $A_s > A_{thr}$ is fulfilled, the resulting runaway is larger the larger is the amplitude of the density turbulence A_s . For large A_s , strong fluctuations in the signal amplitude that are incoherent with the phase oscillations appear and the phase spectra have a $1/f$ behaviour. (even when no asymmetry exists [18]). For low values of A_s the phase runaway $\langle d\phi/dt \rangle$ is lower, phase fluctuations correlated with density fluctuations can be distinguished from the phase of the incoherent signal and the phase spectra are different from $1/f$. This is consistent with the experimental observations that were described in section III and coincides also with the predictions of the random phase screen model [12,20] for low and high turbulence cases when the measurement takes place beyond the diffraction scale length for the phase screen.

The wavelengths of the fluctuations are supposed to be much larger in toroidal than in poloidal direction [21]. If this is the case, the effect of the toroidal pattern of the cut-off layer on the resulting amplitude and phase signals should be much smaller than the effect of the poloidal pattern. This is the reason why the toroidal rotation has not been considered in the simulation.

In conclusion, the simulations confirm that a drift in the phase can appear when there are poloidally rotating structures in the plasma provided some asymmetry exists. The drift is due to the existence of a rough cut-off surface ($A > A_{thr}$) and the finite spot size. Recently, a 2D full wave code has been developed [16] and its predictions will be compared to the ones of the WKB code.

VI. Conclusions

The reflectometry system at W7-AS has been used to investigate the phase runaway effect observed at most reflectometer devices. Due to the dynamic range and bandwidth of the system an instrumental origin of the phenomenon, e.g. due to intermittent loss of the reflected signal, can be excluded. Besides, the measured phase runaway strongly depends on plasma conditions.

It has been proposed [7,2,4,5] that the phase runaway can be explained by a Doppler shift of the reflected radiation caused e.g. by plasma rotation and either a non-perpendicular line of sight or poloidally asymmetric density structures at the cut-off layer. The relation of the phase runaway with plasma rotation in W7-AS has been confirmed by a comparison of the runaway radial profile with the plasma poloidal rotation profile as obtained from impurity spectroscopy. In addition, it has been demonstrated that the direction of the phase drift can be inverted by inverting plasma rotation. Therefore, an explanation based on the existence of asymmetric density structures would require that the asymmetry be independent on the rotation direction. For example, velocity shear induced asymmetries should be excluded. The most plausible explanation of the asymmetry in W7-AS would then be a tilt of the antenna axis with respect to the plasma.

2D WKB simulations of reflection on a rotating plasma made for the W7-AS plasma and reflectometer parameters show that for the expected turbulence conditions a phase runaway can appear due to the slight tilt of the antennas (2.6°) with respect to the normal to the cut-off surfaces. Moreover, the simulations reproduce qualitatively some of the experimentally observed features of the phase runaway: the $1/f$ phase spectra and the correspondence between minima in the amplitude of reflected signal and the fastest phase changes. Quantitative results cannot be deduced from these

simulations as the phase response is very sensitive to the particular parameters of plasma turbulence and the antenna-plasma geometry. In particular the orientation of the cut-off surfaces at the plasma edge of the low shear stellarator W7-AS can change due to the neighbourhood of island structures and thus depends on the edge rotational transform.

It is difficult to extract information about the plasma rotation velocity from the mean phase runaway measurements, as the phase drift depends on turbulence parameters (amplitude and wavelengths) which are usually unknown. Besides, the observed intermittent phase evolution complicates even more the interpretation of the phase runaway in terms of plasma rotation. This behaviour can in principle be explained by the non-linear response of the phase measurement to the local density fluctuations at the reflecting layer (small changes in the amplitude and wavelength characteristics can produce a completely different phase response). However, the intermittency could also be the result of a real intermittent behaviour of the plasma : the appearance and disappearance of small turbulent structures or a sudden change in their characteristics. It is worth to be mentioned that given the high instantaneous $d\phi/dt$, great care must be taken when measuring the profiles with FM techniques.

Based on the comparison between the experimental results and the 2D WKB simulation we can state that the observation of a phase runaway is a consequence of the 2-dimensionality of the reflection process (which under turbulent plasma conditions is modified by refraction, diffraction and scattering phenomena). The absence of the phase runaway is a necessary but nevertheless not sufficient condition to state that 2D effects do not affect the fluctuation measurement (e.g. runaway is not present in cases without asymmetry or with very broad antenna pattern). However, for plasma regimes where the phase signal shows no runaway and fluctuations of the reflected signal amplitude are low - like in the H-mode - the measured phase can be related with the density at the cut-off layer following a 1D scheme.

Acknowledgements

The authors would like to thank G. Kühner for the Thomson scattering data and Ch. Konrad for help with the data acquisition.

References

- [1] Sips A C C 1991 *Ph. D. Thesis Eindhoven Holland*
- [2] Aleksandrov V O, Bulanin V V, Korneyev D O, Sergeev A A, 1992 *Proc. 19th Eur. Conf. on Controlled Fusion and Plasma Physics (Berlin) vol 16C 1 111*
- [3] Hanson G R et al. 1992 *Nucl. Fusion* 32 1593
- [4] Sánchez J, Estrada T, Hartfuß H J 1992 *Proc. 1st IAEA Tech. Comm. Meeting on Microwave Reflectometry for Fusion Plasma Diagnostics (Abingdon) 133*
- [5] Bulanin V V, Korneev D O 1994 *Plasma Physics Reports* 20 (1) 14
- [6] Ejiri A, Kawahata K, Tanaka K and JIPP TII-U group 1995 *Proc. Toki Conference*
- [7] Irby J H, Horne S, Hutchinson I H, Stek P C 1993 *Plasma Phys. Control. Fusion.* 35 601
- [8] Hartfuß H J, Estrada T, Hirsch M, Geist T, Sánchez J 1994 *Rev. Sci. Instrum* 65 (7) 2284
- [9] Hirsch M, Hartfuß H J, Geist T, de la Luna E 1996 *Rev. Sci. Instrum.* 67(5) 1807
- [10] Conway G D. "2D Physical optics simulation of fluctuation reflectometry". *These proceedings*
- [11] Conway G D, Vayakis G, Bartlett D V. "Reflectometer fluctuation and correlation studies on JET". *These proceedings*
- [12] Nazikian R, Mazzucato E 1995 *Rev. Sci. Instrum.* 66 392

- [13] Rhodes T L. "Comparison of Density Fluctuation Measurements from Reflectometry and Langmuir Probes". *These proceedings*
- [14] Brañas B, Hirsch M, Zhuravlev J, Sánchez J, de la Luna E, Estrada T, Geist T, Hartfuß H J 1995 *Proc. 22nd Eur. Conf. on Controlled Fusion and Plasma Physics (Bournemouth)* vol. 19C IV 161.
- [15] Hirsch M et al 1996 *Plasma Physics and Controlled Nuclear Fusion Research (Proc. 16th Int. Conf. Montreal)* IAEA-F1-CN-64/CP 26
- [16] Grossmann M T, Holzhauer E, Hirsch M, Serra F, Manso M.E., Nunes I. "A 2D Code for the Analysis of Microwave Reflectometry Measurements in Fusion Experiments". *These proceedings*
- [17] Zhuravlev V, Sánchez J, de la Luna E 1995. *Proc. 22nd Eur. Conf. on Controlled Fusion and Plasma Physics (Bournemouth)* vol. 19C IV 433.
- [18] Zhuravlev V, Sánchez J, de la Luna E 1996 *Plasma Phys. Control. Fusion* 38(12A) 2231
- [19] Conway G D, Schott L, Hirose A 1996 *Plasma Phys. Control. Fusion* 38 451
- [20] Mazzucato E, Nazikian R 1995 *Rev. Sci. Instrum.* 66 1237
- [21] Rudyj A et al 1989 *Proc. 16th Eur. Conf. on Controlled Fusion and Plasma Physics (Venice)* vol. 13B I 27.